Electronic Structure and Dynamics of Quasi-One Dimensional Materials

Christopher W. Nicholson

Im Fachbereich Physik der
Freien Universität Berlin
eingereichte Dissertation
zur Erlangung des Grades
eines Doktors der
Naturwissenschaften (Dr. rer. nat.)

Freie Universität, Berlin
August 2017

This work was done between August 2012 and August 2017 in the group of Prof. Dr. Martin Wolf at the Fritz Haber Institute of the Max Planck Society in Berlin.

Berlin, August 2017

Erstgutachter: Prof. Dr. Martin Wolf

Zweitgutachter: Prof. Dr. Martin Weinelt

Drittgutachter: Prof. Dr. Thierry Giamarchi

Datum der Disputation: 26.03.18

Abstract

This thesis explores the electronic structure and ultrafast dynamics of quasi-one dimensional (1D) materials by means of high resolution angle-resolved photoemission spectroscopy (ARPES) and femtosecond time-resolved ARPES (trARPES) respectively. Confining electrons to quasi-1D environments induces a range of broken symmetry ground states and emergent properties that result from the increased inter-particle couplings and reduced phase space that such a confinement enforces. Investigating the energy relaxation and transfer between electrons and other degrees of freedom enables fundamental insights into the microscopic mechanisms behind these novel behaviours; for example by reference to characteristic time scales. Furthermore, since quasi-1D objects always interact with a higher dimensional environment, it is also of fundamental interest to investigate the influence that these interactions have on such phases, and whether they play a role in stabilising them. In this work, a number of model quasi-1D systems have been analysed to explore the coupling of 1D objects to a 3D environment, as well as the ultrafast dynamics of photoexcited broken symmetry phases.

The bulk 1D compound $NbSe_3$ is found to show behaviour consistent with a dimensional crossover from 1D to 3D as a function of decreasing energy and temperature, resulting from the coupling between individual 1D chains. Intriguingly, residual 1D behaviour is found to persist even in the 3D regime. Additionally, charge density wave gaps in the electronic structure are observed at low temperatures. The candidate 1D system Ag/Si(557) is investigated to reveal its electronic dimensionality. While the doped Fermi surface reveals predominantly two-dimensional behaviour, the influence of the stepped Si substrate anisotropically induces replica states. The atomic nanowire system In/Si(111) is well known to undergo concomitant structural and metal-to-insulator transitions. By resolving the dynamics of multiple individual electronic states following photoexcitation, a detailed picture of the electronic structure evolution is obtained. An impressive agreement between theory and experiment is obtained, allowing important microscopic insights into this system. Finally the spin density wave phase transition in thin films of Cr is driven by photoexcitation, highlighting the role of electron-electron scattering as the mechanism behind this phase. The applicability of an equilibrium-like order parameter is found to be appropriate in this ultrafast transition.

Deutsche Kurzfassung

Die vorliegende Arbeit untersucht die elektronische Struktur und die ultraschnelle Dynamik von quasi-eindimensionalen (1D) Materialien mittels hochauflösender winkelaufgelöster Photoelektronenspektroskopie (ARPES) und mittels femtosekundenzeitaufgelöster ARPES (trARPES). Die Einschränkungen, denen Elektronen in quasi-1D-Umgebungen unterliegen, induzieren eine Reihe von Grundzuständen mit gebrochener Symmetrie und emergenten Eigenschaften, die sich aus den erhöhten Wechselwirkungen und dem reduzierten Phasenraum ergeben, den eine solche Beschränkung erzwingt. Die Untersuchung der Energierelaxation und des Energietransfers zwischen Elektronen und anderen Freiheitsgraden ermöglicht fundamentale Einblicke in die mikroskopischen Mechanismen hinter diesen neuartigen Verhaltensweisen, beispielsweise mit Bezug auf charakteristische Zeitskalen. Da quasi-1D-Objekte immer mit einer höherdimensionalen Umgebung in Wechselwirkung stehen, ist es auch von grundlegender Bedeutung, den Einuss zu untersuchen, den diese Wechselwirkungen auf diese Phasen haben, und ob sie eine Rolle bei deren Stabilisierung spielen. In dieser Arbeit wurde eine Reihe von quasi-1D Modellsystemen analysiert, um die Kopplung von 1D-Objekten an eine 3D-Umgebung sowie die ultraschnelle Dynamik photoangeregter Phasen mit gebrochener Symmetrie zu erforschen.

Das 1D-Volumenmaterial $NbSe_3$ zeigt bei Abnahme von Energie und Temperatur ein Verhalten, das mit einem Dimensionsübergang von 1D zu 3D konsistent ist und welches sich aus der Kopplung zwischen einzelnen 1D-Ketten ergibt. Faszinierenderweise bleibt ein Rest-1D-Verhalten auch im 3D-Regime bestehen. Darüber hinaus werden bei niedrigen Temperaturen Ladungsdichtewellen-Energielcken in der elektronischen Struktur beobachtet. Das potentielle 1D-System Ag/Si(557) wird untersucht, um seine elektronische Dimensionalität zu bestimmen. Während die dotierte Fermi-Oberfläche vorwiegend zweidimensionales Verhalten zeigt, induziert der Einuss des gestuften Si-Substrats anisotrope Replikatzustände. Das atomare Nanodraht-System In/Si(111) ist für seinen simultanen strukturellen und Metall-zu-Isolator-Übergang bekannt. Durch die zeitliche Auflösung der Dynamik mehrerer einzelner elektronischer Zustände nach der Photoanregung erhält man ein detailliertes Bild der Entwicklung der elektronischen Struktur. Es wird eine eindrucksvolle Übereinstimmung zwischen Theorie und Experiment erzielt, welche wichtige mikroskopische Einblicke in dieses System ermöglicht. Schließlich wird der Spindichtewellen-Phasenübergang in dünnen Cr-Filmen durch Photoanregung getrieben, wobei die Rolle der Elektronen-Elektronen-Streuung als Mechanismus hinter dieser Phase hervorgehoben wird. Interessanterweise ist eine akkurate Beschreibung dieses ultraschnellen Phasenübergangs mittels eines gleichgewichts-ähnlichen Ordnungsparameters möglich.

Contents

List of Figures

1 Introduction

Electrons at the Nanoscale

The continuing scientific interest in low dimensional materials is fuelled not only by the desire to acquire a fundamental understanding of the intricacies of the physical world, but also by the idea that nanoscale devices may help solve some of the great challenges faced by humankind in areas such as energy, medicine and computing. One of the great opportunities, at the same time one of the greatest challenges, when working at the nanoscale is the increased importance of quantum effects and many-body interactions when electrons are strongly spatially confined. By restricting electrons to nano scale objects – for example two dimensional (2D) layers or one-dimensional (1D) chains – the Coulomb interaction between electrons can be enhanced due to the reduction of electronic screening. As a result the complex interplay between electronic, lattice and spin degrees of freedom in low dimensional materials leads to a number of intriguing emergent behaviours such as high temperature superconductivity and giant magnetoresistance (Nobel prizes in 1987 and 2007 respectively). At the same time the reduction of scattering phase space in these reduced spatial environments means that collective effects are also heightened. Particularly interesting in these regards are 1D or quasi-1D systems, comprised of either a bulk of linear chains held together by van der Waals forces, or isolated atomic wires self-assembled on a surface. The confinement of electrons to 1D chains has resulted in the observation of a range of phenomena such as metal-to-insulator transitions, charge density waves (CDWs) and have hinted at the existence of the Tomonaga-Luttinger liquid phase, to name a few examples. The self-assembly of atomic wires is itself an important topic, as it may allow for the controlled growth of nanostructures with novel and even tailored properties.

The focus of this work is on quasi-1D materials, both at equilibrium and on ultrafast time scales following photo-excitation. Quasi-1D is differentiated from "true 1D" by the existence of weak couplings to a higher dimensional environment, originating for example from inter-chain interactions or coupling to a bulk 3D substrate. It is somewhat intuitive that a purely 1D system is a theoretical construct, and that in real physical systems such couplings will always be present to some extent. The study of quasi-1D physics therefore also includes an investigation of these couplings, which are often critically involved in stabilising the long-range ordered phases such as those described above. The investigation and quantification of this "quasi"-1D character is therefore fundamental to understanding the microscopic origins of broken symmetry phases in real 1D systems, and low dimensional materials in general. An example pertinent to the implementation of nanoscale phenomena to devices is knowledge of the flow of energy, both within the structure itself and also to its surroundings. This is also central to understanding the mechanisms that drive phase transitions between phases, and for chemical reactions.

The Method: Photoemission Spectroscopy

In order to study the physics of quasi-1D systems this work addresses the electronic band structure at equilibrium, and following optical excitation on ultrafast time scales. High resolution photoemission spectroscopy (Nobel prize 1981), especially angle-resolved photoemission spectroscopy (ARPES), is now a mature and important technique for addressing the occupied part of the band structure, due to its ability to measure the single particle spectral function in momentum space including many-body effects [Hüf95, Dam03]. This is highly relevant since the electronic structure within $\sim k_B T$ of the Fermi level determines a wide range of phenomena. Modern light sources such as third generation synchrotrons offer high resolution and high photon flux over a widely tunable energy range, allowing for efficient band mapping down to temperatures of a few Kelvin.

More recently time-resolved ARPES (trARPES) has combined the momentum and energy resolution of ARPES with ultrafast optical excitation, giving access to the *unoccupied* band structure, as well as dynamic processes occurring on femtosecond (10^{-15} s) time scales. Since many of the microscopic scattering processes, such as electron-electron or electron-phonon scattering, are determined by strong interactions, they therefore occur on very short time scales: typically from atto- (10^{-18} s) to pico-seconds (10^{-12} s). Therefore trARPES is ideally placed to investigate out of equilibrium changes to the band structure, including energy transfer processes and bottle necks, magnetisation dynamics and phase transitions that may be induced by laser excitation. Such out-of-equilibrium dynamics are highly relevant for further developing our fundamental understanding of low dimensional materials, as well as for technological progress at the nanoscale.

trARPES Hardware Development

One of the key aims achieved during this thesis was the construction of an ultra high vacuum (UHV) chamber for trARPES measurements at the Fritz Haber Institute in Berlin, as well as the development of *in situ* growth capabilities and recipes for quasi-1D nanowires. This involved the construction of chambers and components, the calibration of equipment for photoemission spectroscopy measurements, and the design of some specialised pieces for molecular beam epitaxy (MBE) sample preparation. The setup is presented in detail in chapter 4 in conjunction with a novel 500 kHz XUV laser system, which was developed as the doctoral thesis of another PhD student (Michele Puppin). The joint system has been utilised for the investigation of In/Si(111) nanowires, as presented in this thesis.

The Materials: Model Quasi-1D Systems

As outlined above, quasi-1D systems often exhibit a range of intriguing properties, which may be inter-related or even competing. Therefore in order to investigate the many facets of quasi-1D physics, it is often instructive to focus on model systems. Typically these are well studied materials, with an extensive literature from which information obtained from multiple techniques can be drawn. This facilitates a more comprehensive analysis of data obtained by new experimental methods, which in turn offer complementary insights. The systems investigated in this work have been

chosen both for their interesting, and also model quasi-1D properties, in an attempt to elucidate new insights into the basic physics of quasi-1D materials.

An outline of this work is as follows. A brief theoretical introduction to the physics of 1D systems and the photoemission technique are given in chapters 2 and 3 respectively. An overview of the various setups used during the course of this thesis, and of the preparation of samples is presented in chapter 4. The experimental chapters are divided by material. Equilibrium ARPES studies of $NbSe_3$ (chapter 5) and Ag/Si(557) (chapter 6) investigate the question of electronic dimensionality and coupling to higher dimensional environments in quasi-1D materials. Subsequently time-resolved studies in chapters chapter 7 and chapter 8 focus on the dynamics of photo-induced phase transitions in quasi-1D systems; specifically the multiple time scales of the structural phase transition in In/Si(111) nanowires (chapter 7) and the melting and recovery of the spin density wave in Cr/W(110). A more complete introduction to each individual topic is given below.

In addition to the main projects of the thesis, related studies on low dimensional materials that have been performed partially as part of the thesis work are presented briefly in the appendices. Measurements of the recently discovered quasi-1D superconductor $K_2Cr_3As_3$ with ARPES have been carried out in collaboration with the group of Moritz Hoesch at Diamond Light Source in the UK. A strong spectral weight depletion close to the Fermi level is revealed, with a temperature scaling relation that hints at the elusive Luttinger liquid behaviour A. Layered 2D compounds from the family of transition metal dichaolcogenides (TMDCs) have been investigated with trARPES using the Artemis user facility in the UK, investigating the production of spin polarized excited states in bulk WSe_2 B, and revealing important insights into the formation mechanism of the CDW in $TiSe_2$ C.

ARPES study of the dimensional crossover in bulk quasi-1D $NbSe_3$

Quasi-1D systems are characterised by a coupling of atomic chains to a higher dimensional environment, the energy scale of which sets a crossover scale E_C above which excitations exhibit 1D character, while low-energy excitations behave as in a higher dimensional Fermi Liquid. A dimensional crossover is also a prerequisite for a 1D system to enter an ordered phase, as occurs in a number of quasi-1D materials [Grü88, Grü94b]. To date, how strong one-dimensional correlations are imprinted on the low-temperature phase remains poorly understood [Gia04].

A high-resolution ARPES study of $NbSe_3$ single crystals is presented. $NbSe_3$ is among the most investigated quasi-one dimensional materials and its transport and diffraction results serve as a benchmark for many other studies. Evidence of a dimensional crossover from 1D to 3D is observed as a function of decreasing energy and temperature. Additionally, spectral features of CDWs gaps are observed at low temperatures, occurring consistently with x-ray data and reproduced by theoretical simulations. At high temperatures a clear deviation of spectral weight from a that of a typical metal is observed, suggestive of 1D behaviour. A crossover energy scale is extracted based on a tight-binding model, which is corroborated by an analysis of the density of states. This allows a quantification of the quasi-1D nature of this material, and will likely be useful in other systems.

ARPES investigation of the dimensionality of Ag/Si(557) nanowires

Metal wires on semiconducting substrates are important model systems for low dimensional materials. Not only do some of these systems exhibit well defined quasi-1D metallic band structures [Cra04, Sni10] but through variation of parameters such as the terrace width or by doping, a degree of control over electronic confinement and interactions may be achievable which is difficult to obtain with bulk 1D crystals. Metallic states are of particular interest as 1D electrons have the potential to exhibit exotic electronic properties, but the number of such systems is rather limited. Here, ARPES is used to investigate the electronic structure of Ag/Si(557) nanowires for which a strong anisotropy in the plasmon dispersion observed has been interpreted as evidence for quasi-1D behaviour [Kri13]. However measurements of the Fermi surface reveal a strongly two-dimensional surface, with the only influence of the anisotropic substrate being the production of weak 2D replica states. The lack of observation of confined 1D behaviour is linked to real space inhomogeneities and the wide terraces intrinsic to this system.

trARPES study of the ultrafast phase transition in quasi-1D In/Si(111) nanowires

A key concept in structural transitions and chemical reactions is that the system evolves along a Born-Oppenheimer (BO) potential energy surface from reactants to products; or in the case of phase transitions, from phase 1 to phase 2. The BO surface is determined by the electrons: in particular the transient electronic band structure and its occupation. This naturally suggests trARPES as a tool for elucidating microscopic insights of the dynamics of phase transitions, and for better informing theory about realistic conditions during such reactions.

trARPES is used to investigate the photo-induced phase transition in a model quasi-one dimensional (1D) surface system: In/Si(111) [Yeo99, Sni10]. By resolving the dynamic evolution of multiple individual electronic states, the phase transition is found to develop on three distinct time scales, including temporally separated metal-to-insulator and structural transitions. Molecular dynamics simulations reproduce these distinct time scales and highlight the role played by photo-excited holes in the reaction mechanism. In addition, excited state mapping in both phases is carried out over multiple Brillouin zones to highlight the distribution of photo-excited carriers. Finally an analysis of bonding strengths and orbital distributions during the phase transition links the dynamics band changes in momentum space with the ultrafast formation of specific bonds in real space. The insights obtained during this work represent a significant step forward in the understanding both of In/Si(111) and of the combination of experiment and theory during photo-induced phase transitions.

trARPES study of the ultrafast SDW transition in Cr/W(110) thin films

In ultrafast pump-probe measurements, the transfer of energy from the laser pulse can lead to the population of excited states and a transient increase of the electronic temperature. An open question is to what extent the electronic temperature alone can be said to govern ultrafast changes, particularly for phase transitions, due to the strongly non-adiabatic nature of pump-probe experiments and the possibility of exciting non-thermal electron distributions on short time scales. Such a description

is further complicated in many correlated materials such as high-T_c superconductors, charge density waves (CDWs) and ferromagnets, in which lattice degrees of freedom play an important role.

In contrast to the above mentioned phases, the antiferromagetic SDW in Cr thin films [Faw88, Rot05, Rot08] is investigated, which stems from purely electronic correlations [Ove62]. Although Cr is a bulk 3D material the SDW in the system itself results from a quasi-1D coupling. The idea is to investigate the role played by the electronic temperature in driving materials from one phase to another under non-equilibrium conditions. It is found that the order parameter of the SDW is governed by the transient electronic temperature, implying an intimate link between electronic temperature and spin ordering as the driving mechanism of the SDW in Cr, thus demonstrating that equilibrium thermodynamic concepts can still survive on ultra-short time scales, in cases where the temperature of a single sub-system governs the behaviour of an ordered phase.

The insights afforded by the above electronic structure studies into the model systems presented above provide fundamental insights into quasi-1D materials; in particular on the topics of the interplay between 1D structures and their higher dimensional environments, and the dynamics of 1D systems during phase transitions.

2 Theoretical Background: 1D Physics

2.1 The Problem of Interacting Electrons

At the heart of condensed matter physics is the interaction of electrons and atomic nuclei in solids. In principle these interactions are simple and well understood as originating from the Coulomb interaction between charges. By writing down the Schrödinger equation, one in principle captures all relevant interactions (excluding spin) and one could therefore describe it as a "Theory of Everything" [Lau00] for matter:

$$i\hbar\frac{\partial\Psi}{\partial t} = \hat{H}\Psi \tag{2.1}$$

where the Hamiltonian, $\hat{H}$ is:

$$\hat{H} = -\sum_{j}^{N_e}\frac{\hbar^2}{2m}\nabla_j^2 - \sum_{\alpha}^{N_i}\frac{\hbar^2}{2M_\alpha}\nabla_\alpha^2 - \sum_{j}^{N_e}\sum_{\alpha}^{N_i}\frac{Z_\alpha e^2}{|\boldsymbol{r_j}-\boldsymbol{R_\alpha}|} + \sum_{j<k}^{N_e}\frac{e^2}{|\boldsymbol{r_j}-\boldsymbol{r_k}|} + \sum_{\alpha<\beta}^{N_i}\frac{Z_\alpha Z_\beta e^2}{|\boldsymbol{R_\alpha}-\boldsymbol{R_\beta}|} \tag{2.2}$$

Here Z_α and M_α are the atomic number and mass of the α^{th} nucleus, R_α is the location of this nucleus, e and m are the electron charge and mass respectively, r_j is the location of the j^{th} electron, and $\hbar$ is the reduced Planck's constant. When confined to a system containing only a very small number of particles, this equation is found to agree in impressive detail with experiments [Gra86, Wol95]. In principle then we already know, or can work out, everything there is to know about objects made of electrons and nuclei. However, a system containing only a few particles is clearly a hopeless over simplification when it comes to solids, in which the number of particles is on the order of the Avogadro constant (10^{23}). Despite this, the single particle model with no interactions has been remarkably successful in explaining a wide variety of materials. This success is due largely to the insights provided by Landau in his Fermi Liquid (FL) theory [Lan57b, Lan57a, Lan59]. The basic idea of FL theory, which will be introduced further below, is to take the interactions between particles in a many-body system and include them as renormalised properties of particles in a non-interacting system.

However, even the FL concept cannot account for the behaviour of many solids. The reductionist approach appears to be fundamentally unable to predict or describe the considerable diversity of phenomena that occur as a result of many body interactions: termed *emergent phenomena*. These complex phenomena appear despite the fact that electrons and nuclei obey the simple rules given in Eq. 2.2. As we shall see the electron-electron interaction (4^{th} term) poses a particular problem; as ever, the difficulty lies in the detail. This emergence of complex properties within large systems that obey apparently simple rules was summed up by P. W. Anderson (Noble prize, 1977) as "more is different" [And72]. It is clear then that these emergent phenomena are many-body effects; in particular the interactions between

electrons play a key role. As a result strongly correlated electron systems have been, and continue to be, the focus of intense research. Such phenomena are among the most fascinating of modern physics and include high temperature superconductivity, fractional quantum Hall states and various forms of magnetism to name just a few.

The fact that interactions may be strongly enhanced by confining electrons to reduced dimensions means that low dimensional materials are a fertile environment for emergent phenomena. This is a result of the reduction of both the phase space for electron scattering and of the Coulomb screening of charges. In 2D, a number of fascinating phenomena have been intensively studied in recent years including cuprate high-T_C superconductors [Dam03], graphene [Cas09] and surface states of topological insulators [Has10]. Recently the family of layered Transition Metal Di-Chalcogenides (TMDCs) have received intensive interest (for reviews see e.g. [Wan12a, Che14, Kol16]) while the emergence of metallic states at surfaces [Mee11, SS11] and interfaces [Oht04] of oxide insulators has also sparked much research. Further reducing the dimension of a system to 1D results in a number of exotic behaviours unique to this highly confined regime: topological edge states including Majorana Fermions [Has10], spin-charge separation [Hal81] and spin and charge density waves [Grü88, Grü94b]. Due to the focus of the current work on 1D materials, a brief introduction to 1D concepts will be given in what follows, including the Tomonaga-Luttinger-Liquid (TLL) which is the 1D equivalent of the FL theory in higher dimensions. We therefore start with a short discussion of the FL.

2.2 From Fermi to Luttinger Liquids

2.2.1 Fermi Liquid Theory

The central idea of FL theory [Lan57b, Lan57a, Lan59] is to take the interactions between particles in a many-body system and include them as renormalised properties of particles in a non-interacting system. Here only the main arguments and results will be discussed; see also [Ash76, And81, Sch99b] for further discussions. The starting point is a system of non-interacting electrons – the free electron gas – for which one can write down the eigenstates. Interactions between electrons are then slowly turned on. The postulate is that there will be a one-to-one correspondence between the eigenstates in the interacting system with that in the non-interacting one. Thus although the wavefunctions and energies of the states may no longer be the same as in the non-interacting case, the quantum numbers that label the states remain good even once the interactions are fully switched on. This is often termed *adiabatic continuity* [And81]. As a result we still have fermionic particles and hole excitations around a Fermi level, with the same quantum numbers as in the free electron gas. Hence the Fermi-Dirac distribution is maintained, at least for non-interacting FL theory as just described. For interacting FLs there will be a discontinuity in the occupation at the Fermi wavevector as in Fig. 2.1b. However, the particles in question are no longer electrons, but *quasi-particles* (QPs) which have the interactions of the original system encoded in their properties. This changes the energetics of the states compared with their free-electron counterparts.

Interactions are encoded in two ways. The first is to account for the extra repulsion the interacting electrons now feel between each other making propagation through a

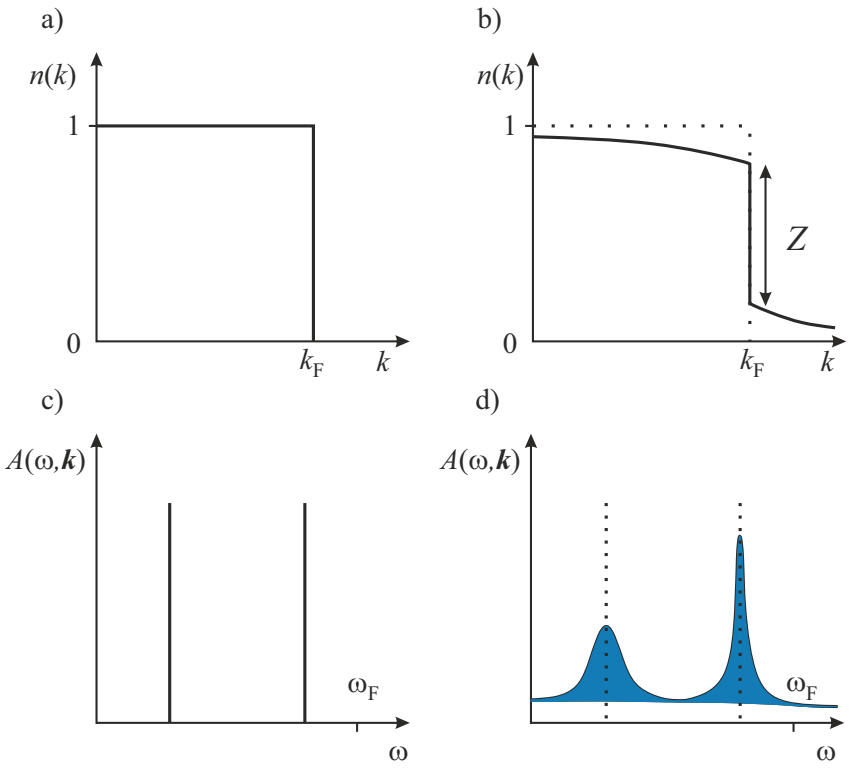

Figure 2.1: (After [Gia04]) (a) and (b) electron distribution functions as a function of momentum at $T = 0$ K for the non-interacting and interacting case respectively. The QP weight appears as a discontinuity at the Fermi wavevector ω_F. (c) and (d) the spectral function in non-interacting and interacting FL. The width of the peaks in (d) represents the lifetimes, which increases close to ω_F. Z is given by the area under the curve while the remainder of spectral weight $1 - Z$ goes into the incoherent background.

crystal more difficult, effectively making them heavier. Hence a renormalisation of the QP mass from m_e to m^* is required (this is separate to the renormalisation already caused by the interaction with the lattice or phonons). Secondly, QPs will scatter with one another in and out of energy levels which are no longer time-independent (stationary) eigenstates of the Hamiltonian, but rather have a finite spread of energy values around a central value. Landau included this effect with his "f-function" (Landau parameters). In principle if this scattering is strong enough it can lead to a break down of the FL picture altogether. The question is, when is the scattering rate small enough to allow the QP concept to survive? To answer this we first consider a filled Fermi sphere at $T = 0$ K which interacts with a single free electron with excess energy $\xi = E_1 - E_F$ above the Fermi level, where $E_1 = \hbar^2 k_1^2/(2m)$ is the free electron dispersion. This electron can only scatter with an electron below the Fermi level i.e. $E_2 < E_F$, since only these states are filled. Due to the Pauli exclusion principle, the two electrons can only scatter into unoccupied levels creating quasi-particles with energy $E_3, E_4 > E_F$. With the additional constraint of energy conservation we have:

$$\begin{aligned} E_2 < E_F, E_3 > E_F, E_4 > E_F \\ E_1 + E_2 = E_3 + E_4 \end{aligned} \tag{2.3}$$

If $E_1 = E_F$ Eq. 2.3 requires E_2, E_3, E_4 all to be E_F as well, which means there is

no phase space scattering volume for this process. As a result at E_F and $T = 0$ K the QP has infinite lifetime. Phase space for scattering becomes available when $E_1 > E_F$ within a shell with a thickness of the order $|E_1 - E_F|$ which leads to a scattering rate $\sim \xi^2$. The term is squared rather than cubed as a choice of E_2 and E_3 already defines E_4 due to energy conservation. Similarly finite temperatures add a contribution of $(k_B T)^2$ to the scattering rate. Thus the total scattering rate is given by [Qui58, Ash76]:

$$\frac{1}{\tau} = a\xi^2 + b(k_B T)^2 \tag{2.4}$$

This leads to stable QPs with long lifetimes at low temperatures and when the excitation is close to the Fermi surface. In particular the dependence of the scattering rate on ξ^2 means that at low excitation energies the scattering rate will always be small with respect to the excitation energy ξ, and the QP well defined. Far from the Fermi surface, the short lifetime will lead to a break down of the QP before the interactions are fully switched on, such that the adiabatic continuity is broken. We note that the relevant interaction between electrons is the *screened* Coulomb interaction; without screening the scattering rate would be so large such that single particle excitations would have vanishingly small lifetimes [Qui58].

In cases where adiabatic continuity is applicable, it should be possible to say something not just about QPs but also about electrons, since the one-to-one correspondence means a fraction of the original non-interacting particle wavefunction survives also in the interacting state. This fraction is know as the QP weight and is denoted Z. Electron excitations may be described by a spectral function $A(\omega, \boldsymbol{k})$ which measures the probability that an electron with momentum $\boldsymbol{k}$ will be measured to have energy ω. In a non-interacting system, single electrons are eigenstates (stationary states) of the Hamiltonian hence the spectral function is a delta function: $\delta(\omega - E_{\boldsymbol{k}})$ where $E_{\boldsymbol{k}}$ is the bare electron dispersion. In the interacting system, as we have seen, the QP may scatter into many other states and so there is a non-zero probability that one will find the electron at some other energy, hence the spectral function is spread in energy. For momenta close to the Fermi wavevector, k_F, there is a probability (Z) to find the QP in an eigenstate, with the result that the spectral function has a strong peak at the new QP energy with a width $\sim (\omega - \omega_F)^2$ resulting from the finite lifetime and an integrated area under the peak equal to Z; this is shown schematically in Fig. Fig. 2.1d. The spectral function will be discussed in further detail in Sections 3.3 and 2.5.3.

As a final comment, in the FL it is not only individual QP excitations that exist, but also a collective response of the charge or spin density. For charge in the presence of Coulomb interaction, this collective excitation would be a plasmon excitation.

2.2.2 The Tomonaga-Luttinger Liquid in 1D

As we have seen in the above, the phase space for single-particle scattering results in a well defined Fermi Liquid QP for small excitation energies close to E_F. This holds in 3D, but reducing the system to 1D produces a problem. Since in a 1D chain it is not possible to go around an object, for a particle to propagate it must also force all other particles in the chain to move. In fact at $T = 0$ K the scattering rate for the FL in 3D given in the previous section is altered to [Lut61]:

$$\frac{1}{\tau} = a\xi \tag{2.5}$$

Therefore there is no energy scale at which the lifetime is small compared with the excitation energy; the result being that single particle excitations are not stable in 1D and only *collective* density excitations can exist. For electrons that carry both charge and spin, this leads to two types of density excitations which can propagate at different velocities along the 1D chain. This is a clear breakdown of adiabatic continuity as the original electron has now been "split" into charge and spin carrying entities: the holon (charge) and spinon (spin). In addition, as we will see in Section 2.5 the 1D electron gas is unstable to a Peierls distortion and spontaneously forms a broken symmetry ground state [Pei55]. Clearly a different approach is required in 1D.

The collective excitations in 1D are superpositions of particle-hole excitations of electrons with momentum k being promoted above the Fermi level to a momentum state $k+q$ and are bosonic in 1D [Tom50], in contrast to the fermionic excitations in the FL. For small excitations around the Fermi level, where the dispersion is linear, all particle hole excitations at a fixed k have the same energy due to the particular shape of the 1D Fermi surface (see Fig. 2.3c). In higher dimensions this is not the case as the energy of an excitation depends both on the magnitude of q and the position of the excitation on the Fermi surface. The result in 1D is that the particle-hole excitations – the collective density modes – have well defined energy and momentum. In addition, close to the Fermi surface they fulfil a similar lifetime condition as in the FL and are therefore well defined [Gia04]. Collective excitations thus play the role of the QP in 1D, since they are well defined close to E_{F} as the fermionic QPs were in the FL. The basic idea of the Tomonaga-Luttinger Liquid (TLL) theory is very much in the spirit of the FL: to capture more complex scattering processes by a re-normalisation of a simpler system [Hal81]. Thus there is again a form of adiabatic continuity.

The Hamiltonian of the TLL system is separable into a part only containing charge excitations and a part with only spin excitations (the holon and spinon) [Gia04]:

$$\hat{H} = \hat{H}_\rho + \hat{H}_\sigma \tag{2.6}$$

where $\hat{H}_\nu(\nu = \rho, \sigma)$ has the form:

$$\hat{H}_\nu = \frac{1}{2\pi}\int dx \left[u_\nu K_\nu (\pi \Pi_\nu)^2 + \frac{u_\nu}{K_\nu}(\nabla\phi_\nu)^2\right] \tag{2.7}$$

where u_ν are the velocities of the excitations, $\phi_\nu(x)$ the density operators and $\Pi_\nu(x)$ is the conjugate momentum to $\phi_\nu(x)$. K_ν are dimensionless parameters that depend on the strength of interactions in the system. For spin rotation invariant systems, such as those investigated in Chapter 5, $K_\sigma = 1$, which leaves u_ρ, u_σ and K_ρ to completely characterise the 1D system. These are the 1D analogues of the Landau parameters in FL theory.

This all depends on the linearity of the dispersion close to the Fermi level, with excitations about a *single* Fermi point, either 0 or $2k_{\mathrm{F}}$. In reality there will also be scattering events between Fermi points and to higher energies where the dispersion is no longer linear. These additional scattering processes can in principle

remove the special 1D properties, voiding the model. The TLL starts from the Luttinger model [Lut63] which includes only small excitations about individual Fermi points in the linear dispersion regime. Additional scattering processes are then included in much the same way as the FL deals with scattering between QPs: by renormalising of the Luttinger parameters while maintaining a one-to-one link with the low energy excitations [Hal81]. The TLL therefore allows perturbative calculations to be carried out in the 1D regime where FL theory cannot be applied. See also [Voi94, Sch99b, Gia04, Gia03] for further details and discussions.

To see how spin-charge separation can occur in a 1D chain, we consider the situation of a 1D Mott insulator as in Fig. 2.2a in which electrons with an antiferromagnetic spin arrangement sit on a lattice. Suppose now that a single electron is removed from a lattice site by absorbing a photon (photoemission), leaving behind a hole. It is now possible for the electron on a neighbouring lattice site to hop onto the empty site. This would correspond to a spin excitation of the system as the now parallel arrangement of spins costs energy. Once this has occurred, other electrons are free to hop onto the sequentially vacated sites without further energy cost, as the antiferromagnetic ordering is maintained except at the point of the initial spin excitation. We can therefore end up in the situation as in the lowest panel where the hole has moved some distance compared with the spin excitation. In this way we see how it is possible for the holon and spinon to separate in a 1D chain. In higher dimensions this separation does not occur due to the additional energy cost caused by the magnetic frustration on parallel chains.

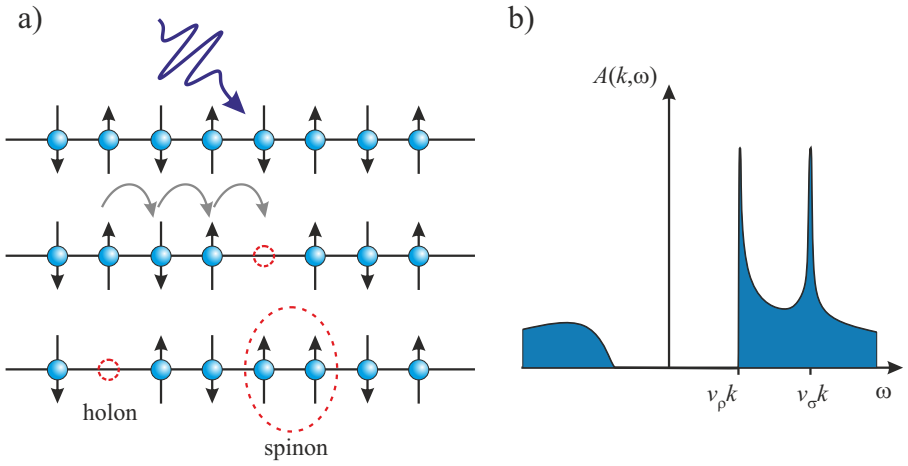

Figure 2.2: (a) Separation of spin and charge excitations in a 1D chain following photoexcitation of an electron (see text). (b) Spectral function in 1D revealing two peaks corresponding to the holon and spinon respectively. (After [Voi93b])

This double excitation can be seen in the single particle spectral function (Fig. 2.2b) which is contrasted to that of the FL phase (Fig 2.1d). The peaks occur at energies depending on the velocities of spinon and holon, $\omega = \nu_\rho$ and $\omega = \nu_\sigma$. The decay of the peak no longer has a Lorentzian width, but decays with a power law governed by the Luttinger parameter K_ρ. In fact, K_ρ is universal such that the decay of *all* correlation functions in a TLL are governed by it. The double peak feature corresponds to the creation of particles above the Fermi sea, while the (negative-energy) broad feature describes the annihilation of particles above the Fermi sea already present in the ground state [Voi93b].

In the case of the k-integrated spectral function – the density of states (DOS) – the power law exponent α describes the zero-temperature DOS of the TLL with the form $|E|^{\alpha}$. It is related to the microscopic parameters K_ρ and K_σ, by [Gia03]

$$\alpha = \frac{K_\rho + K_\rho^{-1} + K_\sigma + K_\sigma^{-1}}{4} - 1. \tag{2.8}$$

For spin-rotation invariant systems we have $K_\sigma = 1$, so $\alpha = (K_\rho + K_\rho^{-1} - 2)/4$ and we can deduce the value of K_ρ from the fitted exponent α:

$$n(E) \propto |E|^{\alpha} = |E|^{\frac{1}{4}(K_\rho + K_\rho^{-1}) - \frac{1}{2}} \tag{2.9}$$

$$K_\rho = 1 + 2\alpha - 2\sqrt{\alpha(\alpha+1)}. \tag{2.10}$$

In this case the integrated intensity goes to zero at the Fermi level, signifying again the lack of single-particle excitations in the 1D state. However the TLL is still a metal as the charge density excitations are capable of transporting charge. The above expression is utilised in Chapter 5 to analyse the density of states in the quasi-1D compound $NbSe_3$. As a side note, for large repulsive interactions between particles (compared with the kinetic energy), the 1D state can become an insulator: the Mott insulator [Mot90].

2.3 Interchain Coupling and the Dimensional Crossover

One of the key themes investigated in this thesis is that of dimensionality (see Chapters 5 and 6); in particular the extent to which materials behave as one dimensional (1D) objects in terms of their electronic structure. It is clear that a perfect 1D chain, as envisaged in the previous section is a theoretical construct. In real materials, even those that are strongly anisotropic are made of arrays of wires that can interact either with each other or with a 2D or 3D substrate. When discussing experimental systems we therefore often talk about quasi-1D systems, to differentiate them from the perfect 1D of theory. How interchain coupling leads to an effective change in the dimensional behaviour of a quasi-1D crystal is the subject of this section; more detailed discussions may be found in [Gia04, Gia03]. We note here that long-range ordered phases are not stable in a purely 1D system as a result of quantum and thermal fluctuations: the Mermin-Wagner theorem [Mer66]. Thus a dimensional crossover should be a prerequisite for a 1D system to enter an ordered phase, as occurs in a number of quasi-1D materials [Grü88, Grü94b] including charge and spin density waves. These details will be discussed in subsequent sections.

The quantity most relevant to the interchain coupling is the hopping of electrons from one chain to another. In the Hamiltonian this is included by a term:

$$\hat{H_\perp} = -\int dx \sum_{\langle\mu,\nu\rangle} t_{\perp,\mu,\nu}\ [\psi_\mu^\dagger(x)\psi_\nu(x) + h.c] \tag{2.11}$$

where $\langle\mu,\nu\rangle$ are pairs of chains and $t_{\perp,\mu,\nu}$ is the hopping integral between the two chains and $h.c.$ is the Hermitian conjugate. The hopping integral is determined by the overlap between orbitals on the chains. Such a description is relevant for many experimental systems in which there are anisotropic hopping integrals including

high-T_C superconductors [Cha93]. In the case that $t_\perp \ll t_\parallel$ ($t_\parallel$ is the overlap integral along the chains) there will be a well defined TLL regime, and a crossover to a higher dimensional phase in which the 1D properties of the TLL are no longer present. In a tight-binding picture the kinetic energy is given by:

$$E(k_\perp, k_\parallel) = -t_\parallel \cos(k_\parallel a) - t_\perp \cos(k_\perp b) \tag{2.12}$$

where a and b are the lattice constants parallel and perpendicular to the chain direction. The Fermi surface for three cases is shown schematically in Fig. 2.3: $t_\perp = t_\parallel$, $t_\perp \ll t_\parallel$ and $t_\perp = 0$. For an isotropic system we have a 2D Fermi surface, while in the other extreme ($t_\perp = 0$) the Fermi surface is perfectly 1D with two parallel lines. It is the intermediate regime ($t_\perp \ll t_\parallel$) that interests us, as this is exactly the case for many real materials and describes a system with a dimensional crossover. Here the role of interchain coupling is clear: at energy scales larger than that given by the warping of the Fermi surface the warping is smeared out and the Fermi surface becomes indistinguishable from the case of $t_\perp = 0$. It can therefore be considered as 1D as there is no coherent hopping of electrons between chains. Once the energy scale is reduced below the warping energy, coherent hopping becomes possible as the system sees a 2D (although still anisotropic) potential. The interchain hopping therefore sets the energy scale of the dimensional crossover.

Since this discussion of hopping parameters is very much a 2D picture, it is important to note that the restriction to 1D chains, and the interactions therein that lead typically to collective behaviour will renormalise the crossover energy. In the TLL single particle excitations are strongly suppressed and so the density of states for such a hopping process tends to zero. This will change the energy scale of the crossover to [Gia04]:

$$E^* \sim W \left(\frac{t_\perp}{W} \right)^{1/(1-\zeta)} \tag{2.13}$$

where $W = 4t_\parallel$ is the bandwidth along the wires and ζ is related to the Luttinger parameters K_ρ and K_σ.

For a non-interacting system $\zeta = 0$ and we recover $E \sim t_\perp$. On the other hand $\zeta > 0$ in the presence of interactions which will result in the energy scale of the

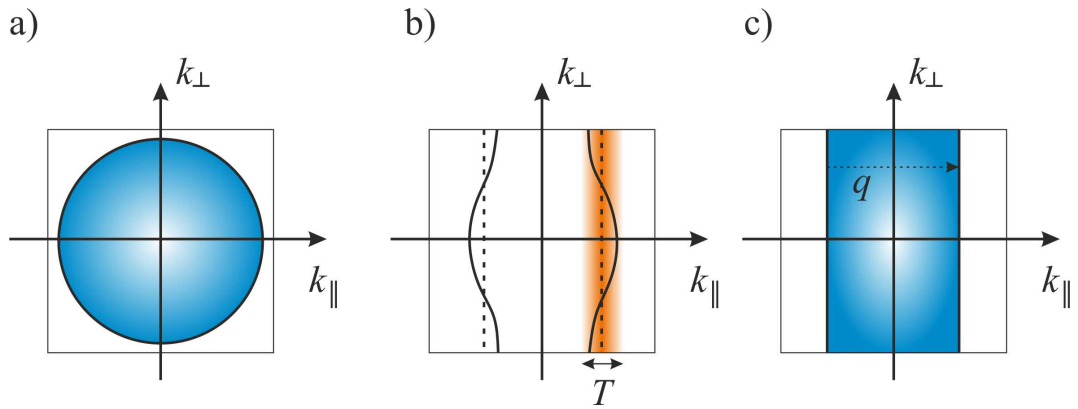

Figure 2.3: Schematic Fermi surface for the cases (a) $t_\perp = t_\parallel$ (b) $t_\perp \ll t_\parallel$ and (c) $t_\perp = 0$ (after [Gia04]). The nesting of the 1D Fermi surface with wavevector q is shown in (c).

dimensional crossover being reduced compared to that for non-interacting fermions. Thus interactions tend to stabilise the 1D system.

This leads to the question: if the energy scale is set to the scale of $t_\perp$ (e.g. by varying the temperature) how does the system behave? Do any of the TLL properties survive even when some higher dimensional processes are introduced, or are they killed immediately? Even in the case that the system really becomes 2D or 3D and can be described as a FL, it will most likely be an unusual FL, since it must originate from the high temperature phase with all its unusual properties. This may for example leave an imprint of the 1D phase in the correlation functions. Additionally since the hopping is not isotropic but depends on $k_\perp$ this may result in "hot spots" on the Fermi surface [Zhe95] and a variation of the resulting properties and dimensionality. To answer these questions on the dimensional crossover is not a simple task, but is one of the key motivations for current ongoing research into quasi-1D materials [Gia08, Ima09, Lak13, De 16, Fur16, Lic16, Nic17].

2.4 Quasi-1D Confined States

In some cases, it is possible to realise an intermediate regime between the quasi-1D case discussed above and a fully 2D or 3D system, as for example when electrons are confined to a nanoscale region. If this confinement occurs in only one direction the electrons can exhibit anisotropic behaviour that is sometimes also termed quasi-1D, although it can be quite different to that described in the previous section as the overall behaviour is rather 2D. Despite these differences, the mixing of confined and extended states in a single material is of relevance to understanding nanoscale behaviour and quasi-1D materials in general.

When an additional lateral potential is strong enough to efficiently confine electrons, the result is discrete quantum well states. On the other hand a weak potential introduces only a modulation to the electronic wavefunction resulting in a 2D super-periodicity, new zone boundaries and gaps in the spectral function at these new boundaries. Such states may be formed by step edges on vicinal surfaces of metallic single crystal, see Refs. [Bau04a, Bau04b, Ort05] and the references therein, or metal-semiconductor interfaces [Kim07, Rug10]. The strength of the confining potential therefore gives a route to quantifying the behaviour in these varied systems. Here a model for describing the strength of the confining potential is briefly introduced, which has been utilised in the case of Ag nanowires on a vicinal Si(557) surface in Chapter. 6.

A key concept in such systems is the potential barrier experienced by electrons at a step [Ort05], calculated within a 1D Kronig-Penney model [de 31]. This model considers a periodic array of rectangular potential barriers of width b and height V_0 as shown in Fig. 2.4.

In such a case in the limit $b \to 0$, $V_0 \to \infty$ Kronig and Penney showed that the solution of the Schrödinger equation becomes [de 31]:

$$cos(\alpha a) = cos(\beta a) + Q\frac{sin(\beta a)}{\beta a} \tag{2.14}$$

$\alpha = \frac{2\pi k}{L}$, a is the interpotential (interwire) distance, $\beta = \sqrt{\frac{2mV_0}{\hbar^2}}$ and $Q = \frac{mV_0 a}{\hbar^2}$.

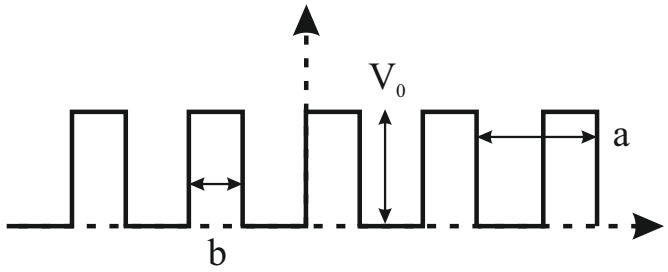

Figure 2.4: Form of the periodic potential in the Kronig Penney Model.

In the tight-binding limit where the strength of the potential is large i.e. $Q \gg 1$ the above equation can be expanded about the zeros and the eigenvalues become:

$$E = E_0 - 2J(1 - cos(ka)) \tag{2.15}$$

with $E_0 = \frac{\pi^2\hbar^2}{2ma^2}$ and $J = \frac{\pi^2\hbar^2}{2m^2a^3V_0}$. By performing a Taylor expansion and keeping only the first order term the cosine part of the disperion becomes:

$$cos(ka) \approx 1 - \frac{(ka)^2}{2}$$

i.e. a parabolic dispersion close to the band minima. By comparison to the free electron dispersion $E = \hbar^2k^2/2m$ this allows one to write:

$$m^* = \frac{m^2aV_0}{2\pi^2\hbar^2}$$

Therefore if the effective mass m^* is known, the barrier potential V_0 can be calculated.

2.5 Charge and Spin Density Waves

As we have already seen, due to the reduced scattering phase space in 1D, interactions can have a dramatic influence on the properties of materials. 1D materials are particularly susceptible to the formation of density waves (DWs) at low temperatures: broken symmetry ground states in which the charge (CDW) or spin (SDW) density varies periodically with the spatial coordinate $\boldsymbol{r}$ as a result of electron-phonon or electron electron interactions respectively. Of relevance is again the geometry of the Fermi surface in 1D, where large sections can be connected by a single momentum wavevector $\boldsymbol{q}$; in this case the Fermi surface is said to be "nested". Such a system is unstable towards the formation of a periodic modulation with period $1/\boldsymbol{q}$ through which it is able to reduce its energy by opening gaps at the Fermi level in the electronic dispersion at the new Brillouin zone boundaries. The transition to a DW ground state is therefore often framed as a metal-to-insulator transition. The energy driving this is the condensation energy $E_{con} = \frac{1}{2}n(E_\mathrm{F})\Delta^2$ where $n(E_\mathrm{F})$ is the density of states at the Fermi level and Δ is the gap for single-particle excitations caused by the transition to the DW state. Well-known examples of quasi-1D materials that display DW behaviour include transition metal-chalcogenides, transition metal bronzes, rare eart tellurides and inorganic linear chain compounds. What follows is a brief summary of the key concepts and results relevant for DWs, following the discussion in [Grü94a].

2.5.1 The Peierls Transition

As noted already, the Fermi surface of a 1D electron gas has only two points at $\pm k_{\mathrm{F}}$. This particular geometry responds very differently to an external perturbation compared with that in higher dimensions as captured by the Lindhard response function $\chi(\boldsymbol{q})$. In a free electron gas, the presence of an external time independent periodic potential with wavevector $\boldsymbol{q}$ induces a rearrangement of the charge density in real space $\phi(\boldsymbol{r})$:

$$\phi(\boldsymbol{r}) = \int_q \phi(\boldsymbol{q})\ e^{i\boldsymbol{q}\cdot\boldsymbol{r}} d\boldsymbol{r} \tag{2.16}$$

which is related to the perturbing potential by:

$$\rho^{ind}(\boldsymbol{q}) = \chi(\boldsymbol{q})\ \phi(\boldsymbol{q}) \tag{2.17}$$

The Lindhard response function therefore encodes how the system reacts to the external potential $\phi(\boldsymbol{r})$. In dimension d it has the form:

$$\chi(\boldsymbol{q}) = \int \frac{d\boldsymbol{k}}{(2\pi)^d} \frac{f(\boldsymbol{k}) - f(\boldsymbol{k}+\boldsymbol{q})}{E(\boldsymbol{k}) - E(\boldsymbol{k}+\boldsymbol{q})} \tag{2.18}$$

Here $f(T, \boldsymbol{k})$ is the zero temperature Fermi distribution. In $d = 1$ this integral can be evaluated to:

$$\chi(q) = -e^2\ n(E_{\mathrm{F}})\ ln\left|\frac{q + 2k_{\mathrm{F}}}{q - 2k_{\mathrm{F}}}\right| \tag{2.19}$$

which diverges at $q = 2k_{\mathrm{F}}$. This implies a divergent charge redistribution in response to a spatially varying potential with wavevector $q = 2k_{\mathrm{F}}$. Therefore at $T = 0$ K the 1D electron gas naturally forms a periodic ordering of the charge density with a wavelength of $\lambda = 2\pi/q = \pi/k_{\mathrm{F}}$. From Eq. 2.18 it is clear that in 1D this instability is the result of electron-hole pairs separated by $2k_{\mathrm{F}}$ of which there are many due to the strongly nested Fermi surface (see also Fig. 2.3). In higher dimensions many of these states are no longer connected and the singularity is removed. However depending on the Fermi surface shape it may still be possible to have large regions nested by a single vector, even in higher dimensions. Finite temperatures also have the effect of removing the explicit singularity, although the response function remains peaked at $q = 2k_{\mathrm{F}}$.

The CDW can be thought of as a frozen lattice distortion, with wavevector $q = 2k_{\mathrm{F}}$ as shown in Fig. Fig. 2.5. Clearly to move the ionic core lattice from their equilibrium positions will require energy, so how is it favourable for the instability in the electron density to occur? The answer is sketched in Fig. 2.5 which is again the situation for a 1D electron gas at $T = 0$ K. We assume a half filled metallic band such that states are filled up to $\pm k_{\mathrm{F}}$, far from the Brillouin zone boundary. By introducing a periodic potential with $q = 2k_{\mathrm{F}} = \pi/a$ the coupled electron-lattice system has a new periodicity and therefore new Brillouin zone boundaries appear at $\pm k_{\mathrm{F}}$ where gaps in the band structure open. The gap opening reduces the kinetic energy of the electrons, which compensates the cost of the lattice deformation. This additionally transforms the system from metallic to insulating; the Peierls metal-to-insulator transition [Pei55]. The strong relation between electronic and lattice systems is also

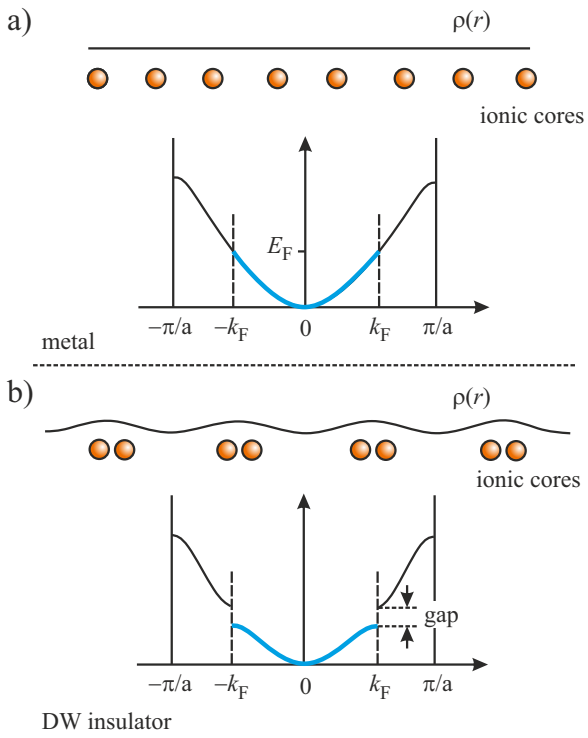

Figure 2.5: Schematic of the Peierls transition. (a) Metallic phase at half filling for constant charge density and (b) the insulating phase in which gaps have opened at the new Brillouin zone boundaries introduced by the modulated charge density (after [Grü94a]).

apparent from the Kohn anomaly where a dip in the phonon dispersion at $2k_F$ is observed [Koh59, Wol62].

Similar arguments apply for the spin density where electron-lattice interactions are replaced by an interaction between electrons of opposite spin. The result is that instead of the instability towards a charge redistribution, the system spontaneously forms a varying magnetisation along the 1D chains [Ove62]. Again the susceptibility is strongly peaked at $q = 2k_F$ for a 1D chain (Eq. 2.19), hence the magnetic (spin) order is a SDW with wavelength $\lambda = \pi/k_F$. Additionally as the electrons experience a varying magnetic potential with $q = 2k_F$, if we again assume a half filled band as in Fig. 2.5 the SDW leads to a metal-insulator-transition.

2.5.2 Mean Field Relations

In the weak coupling limit, where the single particle gap Δ is small compared with the Fermi energy, it is possible to describe the DWs with a mean field theory; in particular results derived in the BCS theory of superconductivity may be utilised. Such an approach can be applied to what are at first sight somewhat disparate phenomena – BCS superconductors, CDWs and SDWs – as it gives an average (mean field) description of the relevant interaction driving the broken symmetry ground state. The advantage is that the microscopic details of the interaction itself need not be explicitly specified, but are contained in the order parameter Δ [Grü94a, Mah00]. The specific ground state that develops is then dependent on the details of the interactions in a material. With such a mean field model the

temperature dependence of a number of parameters may be described, including that of the order parameter, which in the region close to the transition temperature becomes:

$$\Delta = 1.74\ \Delta_0 \sqrt{1 - \frac{T}{T_{\mathrm{DW}}}} \tag{2.20}$$

where Δ_0 is the zero temperature gap size and T_{DW} is the temperature at which the DW develops. The gap size and transition temperature are also predicted:

$$2\Delta_0 = 3.52\ k_{\mathrm{B}} T_{\mathrm{DW}} \tag{2.21}$$

$$k_{\mathrm{B}} T_{\mathrm{CDW}} = 1.14\ E_{\mathrm{F}}\ \exp\left(\frac{-1}{g\ n(E_{\mathrm{F}})}\right) \tag{2.22}$$

for CDWs, where g is the electron phonon coupling and $n(E_{\mathrm{F}})$ is the density of states at the Fermi level. A similar expression is found for SDWs:

$$k_{\mathrm{B}} T_{\mathrm{SDW}} = 1.14\ E_{\mathrm{F}}\ \exp\left(\frac{-1}{U\ n(E_{\mathrm{F}})}\right) \tag{2.23}$$

where U is the on-site Coulomb interaction.

2.5.3 Spectral Function in Mean Field Theory

A further use of the BCS mean field approach outlined above is to model the response of the spectral function to temperature, in order to compare directly with ARPES measurements. This has previously been shown to describe well the temperature dependent behaviour in a strongly correlated electron system displaying a CDW [Mon09, Mon10a, Mon10b]. Here we present briefly the final results; further discussions can be found in [Bar57, Mah00].

In the BCS Hamiltonian [Bar57, Mah00] spin-up and spin-down electrons interact resulting in an interaction term with four fermionic operators, which makes it very difficult to solve. In an ordered phase such as a BCS superconductor some of the operators relating to interactions need not be explicitly included and can be replaced by their expectation value. This is the essence of the mean field approach: it transforms the interacting particle system into one with non-interacting quasi-particles reducing a two particle interacting problem to a single particle in a modified potential – the mean field – represented by Δ (compare with the discussion on QPs in FLT given before). Once this has been achieved it is possible to apply a unitary transform that diagonalises the BCS Hamiltonian: the Bogoliubov transform [Bog58, Val58]. The transform creates new fermionic quasi-particle operators that are linear combinations of the original electron operators. The pre-factors $u(k)$ and $v(k)$ in the linear combination are defined by requiring the off-diagonal elements of the Hamiltonian matrix to be exactly zero. As discussed already, such a mean field approach is applicable beyond superconductors as the microscopic interaction is not specified; hence it can also be used for DWs.

The DW system may be described by a single electron band with a linear dispersion, which is subject to an interaction described in a mean-field manner by the order parameter Δ. The spectral function $A(k, \omega)$ is obtained from the retarded Green's function and in this model has the form [Mah00]:

$$A(k,\omega) = -\frac{1}{\pi}\text{Im } G^{\text{ret}}(k,\omega) = u(k)^2\delta(\omega - E(k)) + v(k)^2\delta(\omega + E(k)) \tag{2.24}$$

where $u(k)$ and $v(k)$ are the so-called coherence factors and $E(k)$ is the renormalised dispersion in the DW state. The renormalised dispersion is obtained from the poles of the retarded Green's functions and is given by:

$$E(k,T) = \pm\sqrt{\epsilon(k)^2 + \Delta(T)^2} \tag{2.25}$$

$\epsilon(k)$ is the bare (in this case linear) dispersion and $\Delta(T)$ is the temperature dependent order parameter, which is equal to half the gap size measured by photoemission. Please see also Chapter 3 for further discussion of the spectral function in relation to ARPES. In the gapped state, two renormalised dispersion branches appear, which carry spectral weight corresponding to:

$$u(k)^2 = \frac{1}{2}\left(1 + \frac{\epsilon(k)}{E(k)}\right),\ v(k)^2 = \frac{1}{2}\left(1 - \frac{\epsilon(k)}{E(k)}\right) \tag{2.26}$$

where $u(k)^2$ and $v(k)^2$ respectively describe the spectral weight transferred from the original bare band $\epsilon(k)$ to the back-folded band in the broken symmetry phase. The form of Eq. 2.26 is that required to ensure a diagonal Hamiltonian. These coherence factors are the residues of the poles of the Green's function [Mah00], which are themselves the projectors onto the corresponding energy eigenspaces. The projection operator (projector) gives the projection of a state into a particular basis i.e. it relates to the probability of measuring an electron in a particular state. In this way, $u(k)^2$ and $v(k)^2$ encode the probability of finding electrons in the renormalised dispersions i.e. their spectral weight (see also Fig. 8.8). In BCS theory $u(k)^2$ is the probability for a pair of orbitals to be empty, while $v(k)^2$ is the probability for them to contain a Cooper pair. Hence $u(k)^2$+$v(k)^2$=1 and $\sum_n v(k)^2 = N$ for a 2N electron system. This transfer of spectral weight can also be thought of as the coupling strength of an excitation, as for electron-phonon interaction. Since the DW is only a perturbation to the crystal potential i.e. weak, the spectral weight should therefore encode this. The renormalised dispersion is therefore observed as weak features often termed "shadow bands" [Voi00]. A model of the transfer of spectral weight in ARPES during DW formation is shown in Fig. 2.6.

The temperature response of the order parameter thus determines the response of the spectral function i.e. the redistribution of spectral weight that occurs due to an excitation of the amplitude mode and a closing of the gap. Combined with the relation for the order parameter as a function of temperature (Eq. 2.20), this allows us to simulate the spectral function at different temperatures. As will be shown in Chapter 8 this can also be applied on ultrashort time scales to track the order parameter in the SDW in Cr following pump excitation.

2.5.4 Collective Excitations

Since the DW ground state involves many particles and may be thought of as a condensate – a superposition of all electron hole-pair wavefunctions – excitations of the DW are collective excitations of the whole system. There are two possible excitation modes – amplitude and phase – which are described in the long wavelength

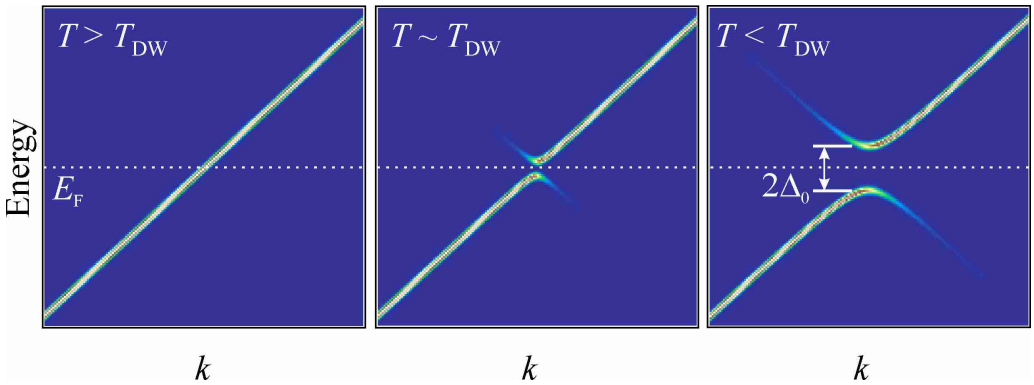

Figure 2.6: Model of spectral weight transfer in ARPES during formation of a DW phase, based on a mean field model (see text). No Fermi function is applied to highlight the dispersion also above E_F. Left panel: above the transition temperature (T_{DW}) a single linear band crosses E_F. Spectral weight is distributed evenly throughout the band. Central panel: close to T_{DW} the dispersion is renormalised into two branches with a gap at E_F. Only a small amount of spectral weight us transferred into the renormalised part of the dispersion, with the majority remaining in the original bands. Right panel: well below T_{DW} the gap grws as the order parameter approaches its zero temperature value (Δ_0).

limit of the Ginzburg-Landau theory. The amplitude mode corresponds to a change in the magnitude of the DW distortion shown in Fig. 2.7 for the case of a CDW. This directly affects the size of the gap in the electronic band structure. As a result trARPES may be used to excite and follow coherent oscillations and the dynamics of the order parameter in CDWs – see Refs. [Sch08, Ret14, Ret16] and Chapter 7 – and SDWs as shown in Chapter 8. In contrast the phase mode does not vary the size of the DW distortion but rather the spatial position of ionic cores. At $q = 0$ this would correspond to a rigid shift of all cores in the same direction. This leads to a transfer of charge (sliding DW [Bar82]) and therefore allows the DW condensate to conduct despite the presence of a gap in the single-particle spectrum. This occurs in both CDWs and SDWs.

The dispersion of the two modes is shown schematically in Fig. 2.7 close to $q = 0$. The similarity to a phonon spectrum with acoustic and optical modes is immediately apparent; the phase mode is a low energy mode with a linear dispersion (acoustic) while the high energy amplitude mode (optical) has a much flatter dispersion.

2.6 Fluctuations in 1D

In the above discussions on DWs we have assumed a system of weakly coupled chains, as introduced in the section on the dimensional crossover, rather than the pure 1D chain described in the TLL model. The reason for this is that a purely 1D system cannot develop long range order at finite temperatures due to the occurrence of fluctuations [Mer66]. Hence in order to be able to describe the phenomena of DWs that occur in many materials, it is necessary to use the mean field approach and neglect, for example, spin-charge separation effects. The occurrence of fluctuations and how they remove long range order in 1D can be seen from the following argument [Grü94a].

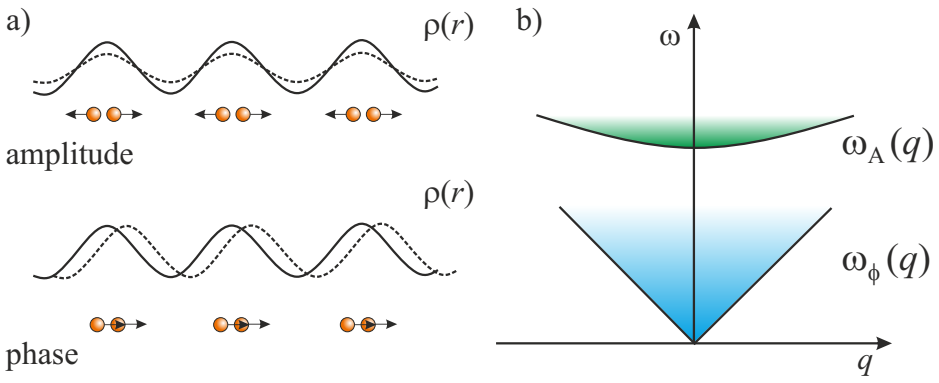

Figure 2.7: Schematic of the collective excitations in DWs: amplitude mode ω_A and phase mode ω_ϕ shown (a) in real space and (b) the dispersion in momentum space (after [Grü94a])

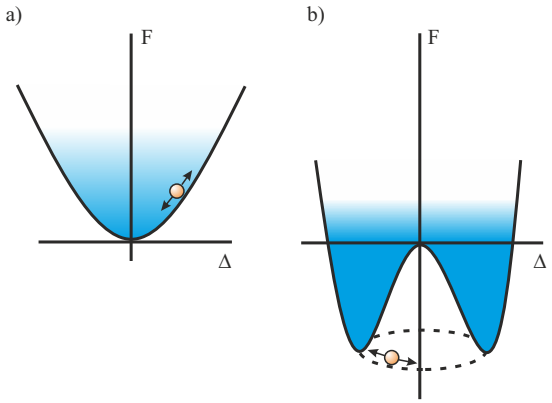

Figure 2.8: Schematic of the Free energy and order parameter fluctuations in (a) the metallic and (b) the DW states. After [Grü94a]

For a 1D chain the order parameter Δ is complex hence both fluctuations of amplitude and phase are possible. These fluctuations can be described by the Ginzburg-Landau formalism in which the Free energy in 1D is given by the functional:

$$F = F_0 + n(E_F) \int dx \left[a|\Delta^2| + b|\Delta^4| + c\left|\frac{d\Delta}{dx}\right|^2 \right] \tag{2.27}$$

The Free energy in the normal metallic phase is F_0 and Δ is the complex order parameter (gap size). The form of the Free energy as a function of the order parameter is shown schematically in both normal and DW phases in Fig. 2.8. Spatial fluctuations of Δ are given by the last term, which was neglected in the mean field approach described in the previous sections. For temperatures much larger than the mean field transition temperature (Eqns. 2.22,2.23) the amplitude of the order parameter fluctuates near $|\Delta| = 0$ as shown schematically in Fig. 2.8a. When T is well below the transition temperature $\Delta \approx \Delta_0$ and the amplitude fluctuations are removed. What remains are phase fluctuations, as Δ rotates around the bottom of the $F(\Delta)$ potential well Fig. 2.8b.

For a spatially varying phase $\phi(x)$ the order parameter fluctuations are given by:

$$\Delta \approx |\Delta_0| e^{-\frac{1}{2}\langle \phi(x)^2 \rangle} \tag{2.28}$$

In the case of DWs, a constant phase throughout space would correspond to a perfectly frozen-in distortion at $q = 2k_F$. Spatial fluctuations of the phase may be decomposed as a Fourier spectrum:

$$\langle \phi(x)^2 \rangle = \sum_{q-2k_F} \langle \phi^2_{q-2k_F} \rangle \, e^{i(q-2k_F)x} \tag{2.29}$$

The total energy in each of these fluctuation components (ϕ_{q-2k_F}) is given by:

$$n(E_F)(\hbar v_F(q-2k_F))^2 \langle \phi_{q-2k_F} \rangle = k_B T \tag{2.30}$$

through the equipartition theorem. Combining Eq. 2.29 and 2.30 we arrive at:

$$\langle \phi(x)^2 \rangle = \frac{k_B T}{n(E_F)\hbar v_F} \int_0^{\pi/a} \frac{e^{iq'x}}{(q')^2} \tag{2.31}$$

where $q' = (q - 2k_F)$ and the integral is performed over half of the Brillouin zone. This integral diverges meaning that the order parameter (Eq. 2.28) has a vanishingly small expectation value at small but finite temperatures. In other words, the long range ordered phase is destroyed by fluctuations in 1D. This would seem to remove any possibility of observing a DW, whereas experiments show that they do in fact occur in a number of quasi-1D materials [Grü88, Grü94b]. A consequence of this is that a dimensional crossover is required for a 1D system to enter an ordered phase, an example of which is presented in Chapter 5. Hence in order to describe DWs it is necessary to take an alternative approach to a "pure" 1D theory. We therefore argue that the system of weakly coupled 1D chains can be described by a mean field model, which gives a number predictions that can be tested experimentally. Such a quasi-1D system still fulfils to a large extent the nesting condition described above.

3 Theoretical Background: ARPES

The main experimental technique used in this thesis is angle-resolved photoemission spectroscopy (ARPES). This technique measures the energy and momentum of electrons ejected from a material following the absorption of light: the photoelectric effect. Since this gives access to the single-particle spectral function $A(\boldsymbol{k}, \omega)$ of metals and semiconductors, which measures not only the dispersion of electrons but also many-body interactions, ARPES has become a powerful technique in the investigation of solids. This chapter briefly reviews the historical development of photoemission, the theory of the photoemission process, and some of the experimental requirements for obtaining ARPES data. The time-resolved ARPES method will further be introduced, which has also been utilised in this thesis.

3.1 A Brief History of Photoemission

A detailed overview of the historical development of photoemission is contained in, for example, Refs. [Bon95, Hüf95, Rei05]. The first investigations of the photoelectric effect in solids – that electrons may be emitted from materials by ultraviolet radiation – were made by Hertz [Her87] and Hallwachs [Hal88] in the late 1880's. To put this in a historical context, the particle-like nature of the electron was not revealed until 1897 by the experiments of J. J. Thomson [Tho97]. Results obtained by Lenard [Len95, Len00, Len02] showed that the photoelectron kinetic energy did not depend on the intensity, but instead on the frequency of the incident light. Using these results in combination with the mathematical quantisation formalism introduced by Max Planck to explain black body radiation, Einstein was able to explain the photoelectric effect in both solids and gases by postulating that light exists as discrete packets of energy [Ein05], now known as photons. Einstein deduced a linear relationship between the maximum kinetic energy of the electrons and the frequency (ν) of exciting light:

$$E_{kin}^{max} = h\nu - \Phi \tag{3.1}$$

where h is Planck's constant and Φ is referred to as the work function of a material: the energetic barrier that electrons must overcome in order to escape a material. This was surprising within the paradigm of light as a purely wave-like phenomena, and it took some years before Einstein's theory was accepted by the physics community. The experiments of Millikan [Mil16] confirmed the theory and paved the way for Einstein's Nobel prize in 1921.

Modern photoemission developed from the 1960's onwards, building on the development of theoretical concepts such as the electronic band structure. The well-known three-step model of photoemission was introduced, in order to phenomenologically describe observed photocurrents [Ber64b]. Around the same time, the first angle-resolved experiments were carried out, investigating the band structure of semiconductors [All62, Ber64a, Gob64, Kan64] and metals [Wac72, Feu72]. The development of photoelectron techniques as a spectroscopy was notably influenced by

Kai Siegbahn, who discovered shifts of the photoelectron core level lines dependent on chemical environment [Nor57, Sie67]. Siegbahn was awarded the Nobel prize in 1981 for his contributions to high resolution photoemission spectroscopy.

The current availability of third generation synchrotron light sources [Wie03, Bil05] spanning from a few eV to the keV hard x-ray regime, with variable polarisation, allows for both high resolution valence band mapping and in-depth chemical studies, while ultra-high resolution measurements have become possible with laser-ARPES at low photon energies [Kor07, Liu08b, Ber11, Tam13, Bro15]. In addition, continuing developments in the field have added the possibilities of spin [Kir85, Hoe02, Hoe04, Ber10] and time-resolution [Eff84, Hai95, Sch08], opening up new avenues of exploration. Time-resolved ARPES will be introduced in more detail in following sections, as it has been one of the key techniques employed in this thesis. 2D electron detectors have further helped make band mapping efficient, while recent developments mean that high resolution 3D momentum mapping [Med17] or even 4D (with spin or time resolution) band mapping is possible [Tus15, Che15]. As a result of these developments, modern ARPES has become an important technique for the characterisation of electronic structure and electronic behaviour [Hüf95, Hüf07, Dam03]. With such a wealth of information available, it is no surprise that it continues to be a powerful and versatile tool for the understanding of solids.

3.2 The Photoemission Process

3.2.1 3-Step Model

Although photoemission itself is conceptually simple, extracting detailed information on the electronic structure from photoemission data can be a challenging task. To facilitate an intuitive understanding of the photoemission process, a three-step model is often used [Ber64b] which breaks photoemission into three separate processes: excitation to a final state in the solid; transport to the surface; transmission through the surface (see Refs. [Hüf95, Hüf07, Dam03, Dam04] for further details). These processes are illustrated schematically in Fig. 3.1a.

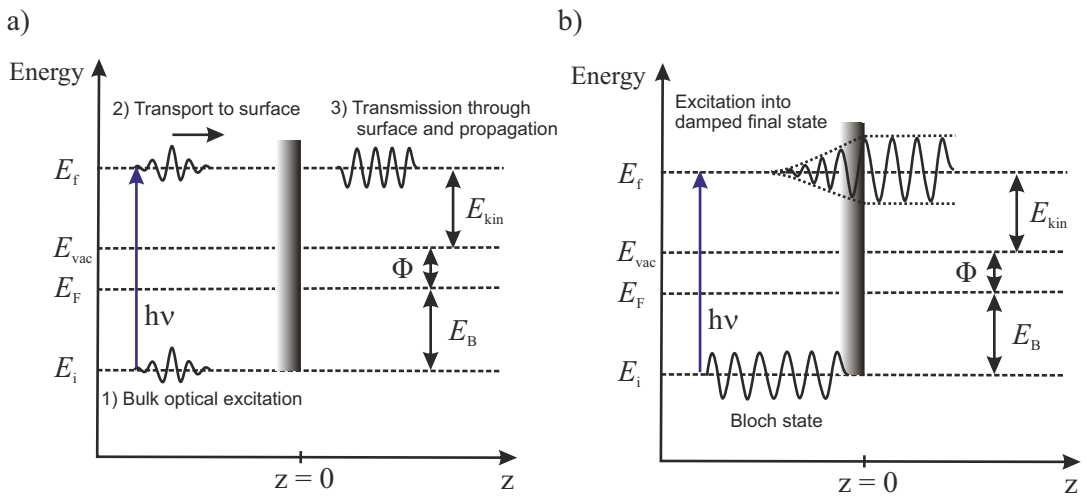

Figure 3.1: Schematic of (a) the 3-step and (b) the 1-step model of photoemission. The surface of the sample is at $z = 0$. Adapted from Ref. [Hüf95].

The first step is the optical excitation of the electron from an initial state ϕ_i to a final state ϕ_f, both states being Bloch states in the bulk of the solid. Due to the small photon momentum at energies below the keV scale this can be thought of as a vertical transition, which lifts the electron above the vacuum level and leaves a hole in the occupied states. The initial and excited states in Fig. 3.1a are visualised as localised wavepackets, with a spatial extent much less than the penetration depth of light in the solid. In this image E_i and E_f are the initial and final states energies respectively, E_{vac} is the vacuum level and E_{F} is the Fermi level. In order to be excited out of a solid, an electron requires requires a photon with energy $h\nu > \Phi$ where Φ is the work function of the material. The final state energy E_f will be measured in the detector, as the following two steps do not affect the energy distribution of the photoelectrons. Thus electrons will be detected with a kinetic energy:

$$E_{kin} = h\nu - \Phi - |E_B| \tag{3.2}$$

where E_B is the binding energy of an electron in the material with respect to the Fermi level. Due to the electrical connection between sample and detector the relevant workfunction will be that of the detector. In this way the energetic structure of electrons in a material can be accessed.

An additional relevant point is the role of the lattice in this step. A free electron cannot absorb a photon since it's dispersion ($E = k^2\hbar^2/2m$) does not support a vertical transition: it cannot conserve both energy and momentum. Therefore in order to conserve momentum in the photoemission process, a periodic potential (the lattice) is a requirement. The lattice is able to provide momentum with a reciprocal lattice vector $\boldsymbol{G}$ such that:

$$\boldsymbol{k}_f = \boldsymbol{k}_i + \boldsymbol{G} \tag{3.3}$$

Therefore rather than representing the ARPES process as a vertical transition in a reduced Brillouin zone scheme, it is more physical to use an extended zone scheme in which the lattice vector is explicitly included, and initial and final states are in different Brillouin zones.

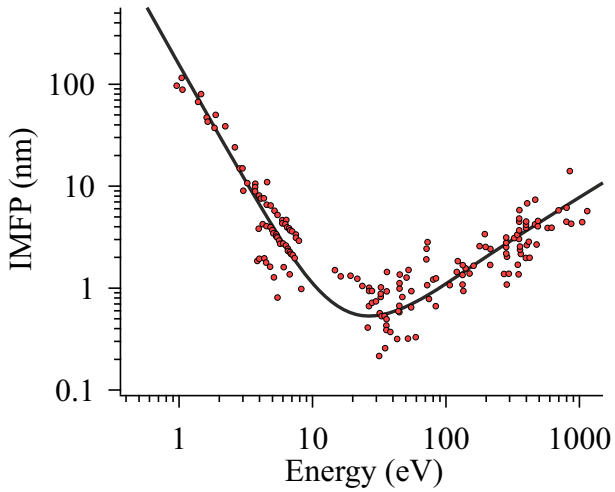

Figure 3.2: Compilation of the IMFP of various elements as a function of photon energy revealing the "universal" behaviour (data from [Sea79]).

The photoexcited electron must then be transported to the surface of the solid. During this step, electrons may undergo scattering processes, for example with other electrons, phonons or defects. Such scattering processes limit the depth from which photoelectrons can reach the surface without losing energy or momentum information. The typical time between electron-electron collisions τ can be estimated from the density of charge carriers, $\tau \sim 1/N_e$. This could also be phrased as how effectivly charges are screened in a material, expressed through the inverse plasma frequency $1/\omega_p \sim 1/N_e$. Since N_e is of the same order of magnitude in many elements, the time between collisions and therefore the inelastic mean free path (IMFP) in many materials falls on a "universal curve" shown in Fig. 3.2. Those electrons that do undergo scattering events contribute to an incoherent background.

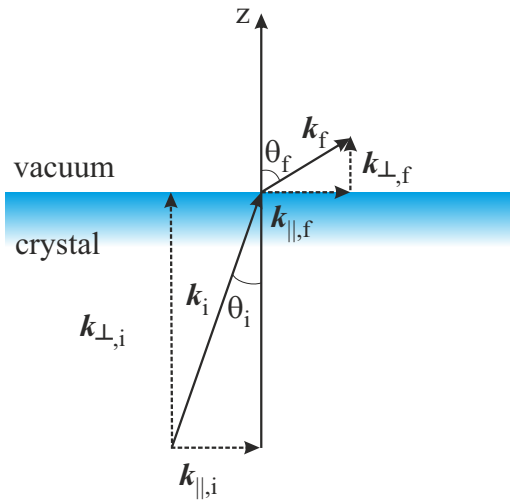

Figure 3.3: Schematic of photoelectron refraction at the surface of a crystal (after Ref. [Hüf95]). Only the parallel component of momentum is conserved during this process.

The final step – transmission through the surface – can be viewed as a refraction of the electron wave through the surface as in Fig. 3.3. The parallel component of momentum is conserved during this step: $k_{\parallel,i} = k_{\parallel,f}$. Thus it is possible to map the parallel component of the photoelectron momentum via the emission angle (θ_f) using the relation:

$$k_{\parallel,f} = \sin\,\theta_f \sqrt{\frac{2mE_{kin}}{\hbar^2}} \tag{3.4}$$

However, due to the energy barrier presented at the surface by the work function, translational symmetry is broken, resulting in the component of photoelectron momentum perpendicular to the surface ($k_\perp$) not being conserved during transmission. In the case of 1D and 2D systems this problem is avoided as the dispersion of electronic states along $k_\perp$ is small, this is not true for 3D materials. However, within the free electron final state assumption, it is possible to determine $k_\perp$ by:

$$k_{\perp,f} = \sqrt{\frac{2m}{\hbar^2}\,(E_{kin}\cos^2\theta_f + V_0)} \tag{3.5}$$

In this case V_0 is called the inner potential, and essentially gives the offset of the free electron final state to the vacuum level.

3.2.2 1-Step Model

The 3-step model is purely phenomenological, but has proved itself useful in describing photocurrents. However it has some conceptual issues. For example, how can the initially excited Bloch state (step 1) propagate to the surface of the sample after excitation (step 2), despite the fact that Bloch states are formally delocalised throughout the crystal? This was the reason for describing the states as wavepackets above, even though transitions occur between Bloch states. A more complete description is given by the 1-step model [Pen76] which considers photoemission as a single coherent process. In this case, the initial Bloch state in the crystal couples optically to a final state in vacuum. The final state is free-electron like with an amplitude that decays exponentially into the solid, shown schematically in Fig. 3.1b. Such a state is sometimes termed an inverse LEED state, due to similarities to the time-reversed LEED process in which an electron impinging on a surface may tunnel into the material with exponentially decreasing probability. The main drawback of the 1-step model is that it is more computationally complex, since all initial and final states as well as all scattering channels have to be explicitly included. The result has been that the 1-step model is typically been not used for photoemission calculations. However recent theoretical developments have shown that experimental spectra can be very accurately reproduced by this method [Gra11b, Gra12, Min13, Bra14].

3.2.3 Experimental Considerations

As already mentioned, the interactions in a material lead to scattering which limits the mean free path of electrons, and therefore the depth from which photoexcited electrons can escape from a solid. The universal curve shown in Fig. 3.2 shows the energy dependence of this quantity, and reveals that for the typical ARPES excitation energies of the order of a few tens of eV, the IMFP is extremely short: less than 10 Å. Therefore the cleanliness of the surface region is extremely important in ARPES measurements in order to maximise the transmission of electrons through the surface. In addition, the surface should be atomically well-ordered. To achieve this, photoemission measurements are carried out in Ultra High Vacuum (UHV). While the actual lifetime of a solid in UHV is strongly material dependent, at a base pressure of 10^{-11} mbar the time required to produce a monolayer of adsorbed residual gas is around two days, assuming a sticking coefficient of 1, compared with only 20 minutes at 10^{-9} mbar. In order to achieve typical UHV pressures in the mid- to low-10^{-11} mbar range, a number of pumping technologies have been utilised, including scroll backed turbo pumps, ion pumps and titanium sublimation pumps. UHV chambers are baked to around 180°C for a number of days in order to desorb water and other molecules from chamber walls and reach the low base pressures required.

To obtain photoelectrons, an excitation greater than a material's work function must be used, which is typically in the range of 3 to 5 eV. This requires excitation photons in the UV range, which can be generated by a number of sources. In the laboratory setting, the most popular excitation source for ARPES are gas discharge lamps, which employ plasma resonances of Noble gases (He is most common). Core level spectroscopy may be carried out with X-ray tubes. In recent years UV laser sources have become available, allowing for ~ 7 eV to be produced in non-linear crystals [Kor07, Liu08b, Tam13], or up to 11 eV in gas cells [Ber11, Bro15]. Such

continuous wave, or long pulse, sources allow for extremely high energy resolution, polarisation control and to some extent tunable excitation in the lab. Femtosecond laser sources have also allowed the development of trARPES, as will be discussed further below. Meanwhile synchrotron user facilities offer the advantage of photon energies tunable over a wide range, usually with high energy and momentum resolution at large photon flux.

Modern ARPES detectors allow for the simultaneous acquisition of energy and momentum information via 2D Multi-Channel-Plate (MCP) detectors, thus allowing for k-space cross-sections of the 3D band structure to be imaged directly. By scanning the emission angle of the sample with respect to the detector, the 3D band structure can be mapped out with high resolution. A schematic of the family of analyser used in all studies presented here is given in Fig. 4.4. This so-called hemispherical analyser consists of a drift tube of electronic lenses and a hemispherical capacitor which disperses electrons in energy. Angular information comes from the angle of emission from the sample, within the acceptance range of the analyser entrance slit. A number of factors govern the resolution of such a detector, which is given by Eq. 4.2. In principle the best achievable resolution is less than 1 meV. Time-of-Flight (ToF) detectors may also be used for ARPES, although as they require a pulsed photon source, this is only applicable to synchrotron or pulsed-laser based experiments.

3.3 Theory of ARPES

3.3.1 Photoexcitation

This section offers an introduction to the mathematical formalism used to describe the photoemission process, including the spectral function $A(k, \omega)$ already introduced in the previous chapter. Further details may be found in the extensive literature, as in Refs. [Hüf95, Dam03, Dam04, Rei05].

In order to derive an expression for the photoelectron spectrum, we start from Fermi's Golden Rule; a general expression derived from perturbation theory which expresses the rate of transition between initial Ψ_i and final states Ψ_f in a quantum system. Assuming a Hamiltonian $H = H_0 + H_1$ with the perturbing potential H_1 the transition probability between electron initial and final state is given by:

$$w = \frac{2\pi}{\hbar}|\langle\Psi_f|H_1|\Psi_i\rangle|^2\delta(E_f - E_i - \hbar\omega) \tag{3.6}$$

where the argument of the delta-function ensures energy conservation. The perturbation here is the light field, and the Hamiltonian for an electron (with mass m and charge $-e$) in this case is:

$$\begin{aligned} H &= \frac{1}{2m}(\boldsymbol{p} - \frac{e}{c}\boldsymbol{A})^2 - e\Phi + V \\ &= \underbrace{\frac{p^2}{2mc} + V}_{H_0} \underbrace{- \frac{e}{2mc}(\boldsymbol{p}\cdot\boldsymbol{A} + \boldsymbol{A}\cdot\boldsymbol{p}) + \frac{e^2}{2mc^2}\boldsymbol{A}\cdot\boldsymbol{A} - e\Phi}_{H_1} \end{aligned} \tag{3.7}$$

where $\boldsymbol{A}$ and Φ are the vector and scalar potentials of the light field, V is an external potential in which the electron moves, and $\boldsymbol{p} = i\hbar\boldsymbol{\nabla}$ is the momentum

operator. The $\boldsymbol{A}\cdot\boldsymbol{A}$ term corresponds to two-photon processes, and may be neglected for weak radiation fields, as used in the experiments in this thesis. Using the commutation relation $[\boldsymbol{p},\boldsymbol{A}] = -i\hbar\boldsymbol{\nabla}\cdot\boldsymbol{A}$, choosing the Coulomb gauge $\Phi = 0$ and setting $\boldsymbol{\nabla}\cdot\boldsymbol{A} = 0$ due to the translational invariance in solids, this gives the perturbation potential $\hat{H}_1 = -\frac{e}{mc}\boldsymbol{A}\cdot\boldsymbol{p}$. For photon energies in the range of a few tens of eV, the corresponding wavelength is much larger than the inter-atomic distance, therefore $\boldsymbol{A}$ can be assumed to be constant; this is known as the *dipole approximation*. Since $\boldsymbol{A} = A_0$ is assumed constant, the interaction term now only contains the momentum operator, which is related to the position operator $\hat{\boldsymbol{r}}$. Thus the interaction term is often written in terms of the dipole operator:

$$\hat{H}_1 \propto -\frac{A_0}{mc} e\cdot\boldsymbol{r} \tag{3.8}$$

We now consider a single electron excited from the initial state. To describe the initial and final states, the underlying assumption is that of the *sudden approximation*, which means that the creation of photoelectron and the remaining $(N-1)$ electron system occurs instantaneously such that the two do not interact. This allows us to factorise the initial and final state wavefunctions into one part containing only the photoelectron, and one containing only the $(N-1)$ electron remaining system. The total initial state is a product of the orbital ϕ_k that the photoelectron originates from with the initial wavefunction of the $(N-1)$ excited system

$$|\Psi_i\rangle = \hat{a}|\phi_{i,k}\Psi_i^k(N-1)\rangle \tag{3.9}$$

where the operator $\hat{a}$ anti-symmetrises the wavefunction, as required for fermionic states. The superscript k in the $(N-1)$ state denotes the momentum of the removed electron. Similarly the final state is the product of the photoelectron wavefunction ϕ_f, and the final state of the $(N-1)$-system.

$$|\Psi_f\rangle = \hat{a}|\phi_{f,k}\Psi_{f,s}^k(N-1)\rangle \tag{3.10}$$

assuming that there are s possible excited states that the system can be excited into. Combining these, we can write down the transition matrix element for the photoexcitation process:

$$\langle\Psi_f|\boldsymbol{r}|\Psi_i\rangle = \langle\phi_{f,k}|\boldsymbol{r}|\phi_{i,k}\rangle\sum_s\langle\Psi_{f,s}^k(N-1)|\Psi_i^k(N-1)\rangle \tag{3.11}$$

which is a product of a single electron matrix element, and a sum of overlap integrals of the $(N-1)$ system i.e. the extent to which the initial and final states overlap with one another. This overlap term $|c_s|^2 = |\langle\Psi_{f,s}^k(N-1)|\Psi_i^k(N-1)\rangle|^2$ gives the probability that the excitation of an electron from the initial orbital ϕ_k results in excited state s of the $(N-1)$ system. For a non-interacting system, only a single final state $s = k$ is involved, and a sharp photoemission line is observed in experiment. In the case of a strongly interacting system, the $(N-1)$ system is in general not in an eigenstate of the system; rather the photoelectron overlaps with a spectrum of final states. This gives rise to satellites from core level photoemission and a broadening of the photoemission line in valence band photoemission, as a number of final states now overlap with the initial state. This will be discussed further in the context of many-body interactions below (see also the discussion of Fermi Liquid theory in Chapter 2).

The sum over all possible final states, c_s, when momentum and energy resolved, is called the spectral function, $A(\boldsymbol{k}, E)$.

$$A(\boldsymbol{k}, E) = \sum_s |c_s|^2 = \sum_s \left| \left\langle \Psi^k_{f,s}(N-1) \middle| \Psi^k_i(N-1) \right\rangle \right|^2 \tag{3.12}$$

Since the overlap integral contained in this expression is given by the $(N-1)$ electron system, the spectral properties of the photoemission process are determined not by the photoelectron, but by the $(N-1)$ state i.e. the photohole, even though it is the photoelectron that ultimately reaches the detector.

The remaining part

$$\langle \phi_{f,k} | \boldsymbol{r} | \phi_{i,k} \rangle \tag{3.13}$$

is a matrix element describing the transition between one-electron initial and final states, which depends on the orbital characters of the two wavefunctions, and the polarisation of the light field encoded in the $\boldsymbol{r}$ vector [Wan12b, Mos16]. It is often simply referred to as the photoemission matrix element. Because of this term the experimental photoemission intensity can be reduced or even completely suppressed due to symmetry reasons, even when the spectral function is non-zero.

3.3.2 Many-Body Effects

Many-body effects can be described by the Green's function formalism. The spectral function is related to the imaginary part of the Green's function of the electron system by:

$$A(\boldsymbol{k}, E) = \frac{1}{\pi} \left| \mathrm{Im} G(\boldsymbol{k}, E) \right| \tag{3.14}$$

The Green's function describes the time evolution of electronic states: specifically the probability that an electron at position r_1 at t=0 will be found at position r_2 at some later time, $t > 0$. Alternatively in a momentum/energy picture it gives the probability that an electron in a Bloch state with momentum $\boldsymbol{k}_1$ at $t = 0$ will be scattered to $\boldsymbol{k}_2$ with an energy transfer of E.

For a non-interacting electron system, the Green's function is

$$G(\boldsymbol{k}, E) = \frac{1}{E - E^0(k) - i\delta} \tag{3.15}$$

where δ is an infinitesimal number and $E^0(k) = \hbar^2 \boldsymbol{k}^2 / 2m$ is the energy dispersion of a free electron with momentum $\hbar\boldsymbol{k}$. This results in a spectral function with the form:

$$A(\boldsymbol{k}, E) = \frac{1}{\pi} \delta(E - E^0(k)) \tag{3.16}$$

which is a delta function at $E^0(\boldsymbol{k})$. This is the case described above for a single final state s, giving a sharp photoemission line which follows the (free electron-like) energy dispersion. We now consider the effect that including multiple final states has on the spectral function, by turning on interactions in the system. This can be achieved by including a self-energy term, $\Sigma(\boldsymbol{k}, E) = \mathrm{Re}\Sigma + \mathrm{Im}\Sigma$ in the

Green's function, which contains contributions from all many-body processes e.g. electron-electron, electron-phonon and electron-impurity scattering:

$$G(\boldsymbol{k}, E) = \frac{1}{E - E^0(k) - \Sigma(\boldsymbol{k}, E)} \tag{3.17}$$

which corresponds to a spectral function:

$$A(\boldsymbol{k}, E) = \frac{1}{\pi} \frac{\mathrm{Im}\Sigma}{(E - E^0(k) - \mathrm{Re}\Sigma)^2 + (\mathrm{Im}\Sigma)^2} \tag{3.18}$$

The poles of this function give the spectroscopic energies of the system, as in the non-interacting case. This spectral function has the form of a Lorentz distribution:

$$f(x) = \frac{1}{\pi} \left[\frac{\frac{1}{2}\Gamma}{(x - x_0)^2 + \left(\frac{1}{2}\Gamma\right)^2} \right] \tag{3.19}$$

at position x_0 and with FWHM of Γ. From this comparison one can directly infer that the position and width of the peak of the interacting spectral function are related to $\mathrm{Re}\Sigma$ and $\mathrm{Im}\Sigma$ respectively. The re-normalisation of the peak position corresponds to an effective mass enhancement. In addition to a renormalisation compared with the bare non-interacting case, this can lead to kinks in the observed photoemission spectra due to the coupling of electrons to bosonic modes such as phonons [Ing05, Tam13] or magnons [Sch04a, Hof09] and plasmons [Bos06]. On the other hand the increased width due to $\mathrm{Im}\Sigma$ is related to the quasi-particle lifetime. The lifetime is reduced due to scattering interactions with other electrons, phonons, other quasi-particles and defects. This is the same as in the Fermi liquid picture of interacting systems in which electrons are "dressed" by virtual excitations with other electrons (see Chapter 2).

In general, the line width of the photoemission peak is related to both the lifetime of the photoelectron and of the photohole. The lifetime of the photohole is of particular interest since, as we have seen, it is this that determines the spectral function. The lifetime of the photoelectron is related to the exponential damping (imaginary part) of the wavefunction perpendicular to the surface, as described in the 1-step model outlined earlier. However, under the correct conditions, the line width of the photoemission peak is directly related to the lifetime of the photohole. At normal emission (zero polar angle between sample and detector) and assuming the dispersion of the initial hole state is small compared to the final electron state, we reach the relation:

$$\Gamma_{\theta=0} = \Gamma_h + \Gamma_e \left| \frac{v_{h\perp}}{v_{e\perp}} \right| \tag{3.20}$$

where $v_{h\perp}$ and $v_{e\perp}$ are the group velocities perpendicular to the surface ($v_{h\perp} = \hbar^{-1}(\partial E_h / \partial k_\perp)$). From this the advantage of 2D and 1D materials is clear: since the dispersion in the surface perpendicular direction vanishes, it becomes possible to relate the measured line width directly with the photohole width, and thus the imaginary part of the self-energy.

To make a final link to the Fermi Liquid discussion, the connection between the quasi-particle spectral weight Z and the self-energy is mentioned. Spectral weight is transferred from main peak to satellites which gives well separated photoemission

lines in gases [Sie69, Åsb70] and a broad background in solids, the form of the spectra being governed by the Franck-Condon principle. For this reason the Green's and spectral functions are sometimes separated into a coherent part with poles, and a non-coherent part without.

$$A(\boldsymbol{k}, E) = Z_{\boldsymbol{k}} \frac{\Gamma_{\boldsymbol{k}}/\pi}{(E - E^0 - \mathrm{Re}\Sigma)^2 + \Gamma_{\boldsymbol{k}}^2} + A_{inc} \tag{3.21}$$

where $\Gamma_{\boldsymbol{k}} = Z_{\boldsymbol{k}}|\mathrm{Im}\Sigma|$ and $Z_{\boldsymbol{k}} = (1 - \partial \mathrm{Re}\Sigma/\partial E)^{-1}$, evaluated at $E = E_k^0$, is the re-normalisation constant, or quasi-particle weight. In the Fermi liquid picture this corresponds to the overlap of the quasi-particle with the free-electron state from which it derives.

In the language of the Hubbard model, the increasing transfer of spectral weight (which is conserved) from the main peak to the background with increasing electronic interactions described by U is nothing other than the development of upper and lower Hubbard bands.

3.4 Time-Resolved ARPES

3.4.1 Overview

A relatively recent [Eff84, Fan92, Hai95], and still developing, addition to the tool kit of the photoelectron spectroscopist is time- and angle-resolved photoemission spectroscopy (trARPES). This extends the energy and momentum resolution of ARPES into the time domain, resulting in the extended spectral function $A(\boldsymbol{k}, \omega, \Delta t)$ which provides detailed access to the behaviour of electrons out of equilibrium. In trARPES experiments, two laser pulses are used: one with energy lower than Φ (the work function), which excites electrons from below to above the Fermi level and a second with energy greater than Φ which can photoexcite states both above and below E_F. This is shown schematically in Fig. 3.4a. By varying the relative delay Δt between these two pulses, termed pump and probe respectively, snapshots of the band structure may be obtained on time scales which closely match the intrinsic time scales of electronic processes: excitations on the order of hundreds of meV correspond to time scales of tens of femtoseconds (10^{-15} s).

A major difference compared with ARPES, is that the pump-probe capabilities of trARPES allow not only the mapping of occupied states but also of the unoccupied band structure [Sob13, Ber16]. Due to the possibility of exciting with relatively weak excitation densities that do not significantly perturb the system it is therefore possible to access the full spectral function. In this sense the weak field assumption ($\boldsymbol{A} \cdot \boldsymbol{A} = 0$) introduced in the previous section still applies for all excitation times, except possibly at pump-probe overlap. trARPES is a combination of two 1-photon processes in contrast to time-resolved 2-photon photoemission (2PPE), which is a 2-photon coherent process, see Ref. [Wol99] and references therein.

At higher excitation densities (but still in the $\boldsymbol{A} \cdot \boldsymbol{A} = 0$ limit, at least for the probe beam) significant changes to the band structure may be induced by the pump pulse. Ultimately, energy is added to the system, and this will increase its temperature, particularly of the electron distribution [Bov07, Gie13, Wan12b, Cre12], as shown schematically in Fig. 3.4b. For a Fermi-Dirac distribution initially at equilibrium at temperature T_0, the pump pulse will lead to an out-of-equilibrium situation in which

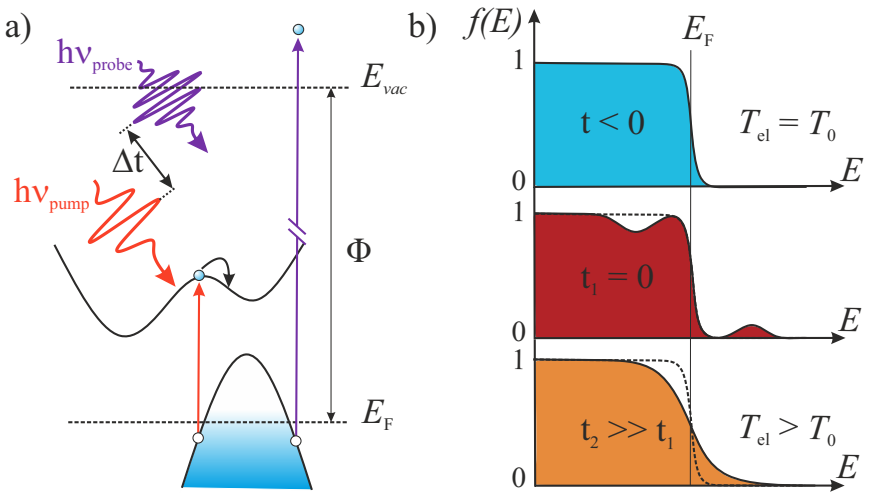

Figure 3.4: a) Schematic trARPES excitation. The pump pulse arrives first and excites electrons into unoccupied states. The later arriving probe pulse photoexcites electrons from both occupied and unoccupied states above the vacuum level. By varying the pump-probe delay, the electronic dynamics may be accessed. b) Schematic of the electronic thermalisation process.

electrons from below E_F are excited above it, resulting in a non-thermal distribution on short time-scales. These hot electrons will then thermalise, on short time scales predominantly through electron-electron scattering, and at later times the lattice, leading once again to a Fermi-Dirac distribution, but now with $T > T_0$. Typically, the initial thermalisation takes place on the scale of around 100 fs. However in reduced dimensions due to the reduced scattering phase space it can take several hundreds of femtoseconds (see chapter 7). Due to the small specific heat of electrons, transient electronic temperatures of thousands of Kelvin may be reached, whereas the lattice remains much cooler as a result of a typically much higher specific heat. Such high electronic temperatures also allow a detailed investigation of ultrafast phase transitions driven by photo-excitation [Per06, Sch08, Pet11, Roh11, Ret14, Mon16]. A number of these aspects will be addressed in Chapters 7 and 8 when investigating the photo-induced density wave transitions in In nanowires and Cr thin films respectively.

A further advantage is that the momentum resolution of trARPES allows scattering processes and the relaxation dynamics of excited states to be investigated in great detail [Bov12, Sob12, Roh13, Gie13, Ber16]. Compared with all-optical techniques, which integrate over momentum space, trARPES has the capability to resolve the response of individual bands on ultra short time scales, thus deconvolving ultrafast responses that occur simultaneously. This will be shown to be of particular use in Chapter 7 in understanding the ultrafast phase transition in metallic In nanowires, where the motion of individual atomic modes can be extracted from the momentum-resolved dynamics. In principle the lifetimes of states can be measured in order to investigate many-body interactions in a material, by accessing the self-energy of unoccupied states in a manner complementary to traditional ARPES [Sen13]. While this is complicated by population dynamics [Yan15], this may be an interesting future application for trARPES.

3.4.2 Experimental Considerations

Generation of Ultrashort Pulses

As described above, trARPES experiments require the generation of ultrashort pulses in the femtosecond regime. Such short pulses are only possible with a large bandwidth in frequency space as seen from the time-bandwidth product for a Gaussian pulse shape:

$$\Delta\nu\Delta t \geq \frac{2\ln 2}{\pi} = 0.4413 \tag{3.22}$$

where $\delta\nu$ and Δt are the FWHM values of the laser spectrum and time duration respectively. Femtosecond pulse generation therefore requires a medium that can emit radiation over a wide spectral range. This is often achieved by a Ti:Sapphire oscillator (as for example in Section 4.4) as a Ti:Sa crystal has a very broad emission band [Mou86] due to the presence of multiple vibronic levels. An alternative approach used in the trARPES setup developed at the FHI, Berlin (Section 4.1) is to seed an OPCPA with broadband white light generated in a YAG crystal due to filamentation processes [Cou07]. The other requirement for ultrashort pulses is that all the modes that make up the broad emission must be phase locked in order to combine to a short pulse; this is known as mode locking and occurs through non-linear effects such as Kerr lensing [Lam64, Har64, Kra92].

High-Harmonic Generation

As is evident from Eq. 3.4 access to larger regions of k-space requires higher photon energies. Being able to reach the Brillouin zone boundary, or even measure in higher Brillouin zones is a huge advantage in trARPES studies for two reasons. The first is that the dynamics of interest may simply occur away from the zone centre and therefore to access the states involved requires large energies. The second reason is that due to the photoemission matrix element as introduced in the previous section, it is possible that photoemission intensity is reduced or even completely suppressed due to symmetry reasons [Wan12b, Mos16]. Therefore it may be necessary to measure in higher Brillouin zones in order to maximise the signal of interest. As a result, the use of 6 eV laser systems has a clear drawback, as they allow access to a limited k-space region around the Γ-point. This is only around 0.4 Å^{-1} at 40°emission angle (depending on the sample work function) and limits the choice of materials that can be measured with these energies. By going to 20 eV this range is extended to 1.3 Å^{-1}. High Harmonic Generation (HHG) in gases is a mechanism which allows for the production of higher energy photons, which are still ultrashort. At the FHI in Berlin, a novel HHG-based trARPES experiment has been constructed (4.1) and utilised in the investigations presented in Chapter 7. A second HHG setup (4.4) has been employed in Chapter 8.

A semi-classical picture of the HHG process breaks the mechanism into 3 stages [Cor93, Cor07]: ionisation; motion; and re-collision which are shown schematically in Fig. 3.5. The ionisation step (1) can be thought of as the electrons tunnelling out of the ionic potential which is distorted by the intense driving laser pulse with electric field amplitude E_0. The tunnelling regime is achieved for a Keldysh parameter [Kel65] $\gamma \ll 1$ which means the tunnelling frequency (period) of the electron is much

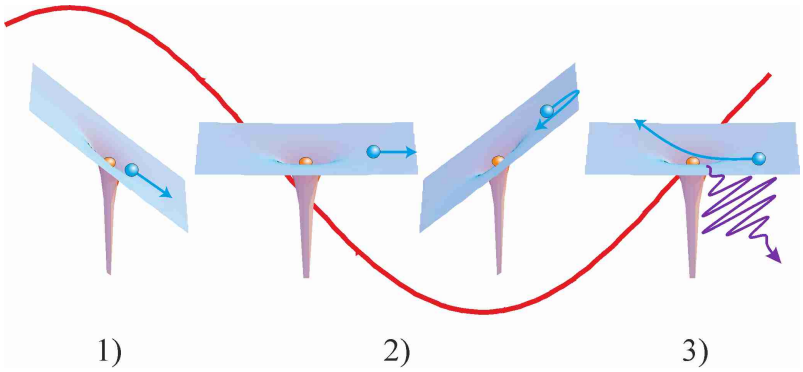

Figure 3.5: Schematic of the semi-classical 3-stage HHG mechanism after [Cor07]. The ionic core is shown as an orange ball while the electron is blue, moving in the potential of the ionic core. The oscillating waveform depicts the driving laser pulse.

higher than the frequency of the laser pulse, thus giving the electron enough time to tunnel within a single cycle of the pulse. This is necessary to produce coherent HHG output. The quasi-free electron is then accelerated in the new potential (2) gaining kinetic energy. The maximum energy available for the HHG process will depend on how far the electron travels during half the laser cycle, as once the field reverses the electron motion is reversed back towards the ionic core. The final step is the re-collision of the electron with the ion core and the emission of XUV light (3) in which the kinetic energy gained during the 2^{nd} phase can be emitted as photons. This naturally leads to a cut-off frequency of the HHG spectrum, which is at an energy:

$$E_{max} = 3.17U_p + I_0 \tag{3.23}$$

where $U_p = e^2E_0^2/4m_e\omega^2$ is known as the ponderomotive potential of the laser field and I_0 is the ionisation energy of the atom.

A fully quantum model [Gao98, Gao99, Lew94, Ede04] explains why the emitted light comes at harmonics of the driving frequency, rather than as a continuum. For electrons in the presence of a quantised electric field, the time-independent Schrödinger equation develops new stationary solutions, which are the high field equivalent of atomic bound states. These states are known as *Volkov states* and are evenly spaced by integer multiples of the driving frequency, $n\hbar\omega$. During the pulse cycle, the electron can exchange photons with the field and transition between Volkov states. In the case of HHG, the electron absorbs multiple photons and can then release the combined energy as a single, much higher energy, photon. Hence the spectrum of light emitted will be in multiples of the driving frequency. Thus HHG photons can then be seen as originating from Volkov-Volkov state transitions. The presence of the ionic core is clearly required to conserve momentum as a free electron cannot absorb or emit photons and conserve both energy and momentum. For HHG produced in a gas, the matrix element for even harmonics is zero, hence only odd harmonics are emitted; this restriction is lifted in solids. The Volkov mechanism also explains the phenomena of Laser Assisted Photo-Emission (LAPE) [MA06, Saa08]. In this case, during pump-probe overlap in a trARPES experiment, photoelectrons can absorb *and emit* photons with the pump wavelength. This leads to side bands in the ARPES spectrum spaced by exactly $\pm n\hbar\omega$, an example of which is shown in

Fig. 8.2. Since this only occurs in the presence of both pulses, this gives a reliable method for measuring the overall time resolution in trARPES experiments.

4 Experimental Details

A number of experimental setups have been used in the framework of this thesis, and each is presented in turn below, followed by details of the sample preparation. One of the tasks undertaken as part of this thesis was the develpment of a UHV ARPES system at the Fritz Haber Institute in Berlin with capabilities for epitaxial *in situ* growth of nanowire samples. From the sample preparation side this included assembly and maintenance of chambers and all related components; the design of sample holders and a heating stage for Si preparation, used as substrates for 1D nanowire growth; calibration of evaporation sources; and developing recipes for high quality sample growth. The connected ARPES system itself was also constructed and maintained as part of the thesis, including commissioning of the 2D electron spectrometer and 6-axis manipulator. As a result, this experimental setup will be described in most detail. Since all other experiments use very similar concepts to those that will be outlined in this first section, their descriptions are kept shorter.

4.1 trARPES setup at the Fritz Haber Institute

The trARPES experiment at the Fritz Haber Institute in Berlin joins two main components: a high-repetition rate XUV source, and a UHV ARPES experiment including *in situ* preparation capabilities for thin film sample growth. The development of the OPCPA [Pup15] for driving the production of XUV light via HHG has been the thesis work of Michele Puppin (FHI, Berlin) and is therefore presented here only briefly. Construction of the UHV ARPES chambers, design of components for thin film preparation and calibration tests of the electron analyser were carried out in the framework of this thesis, and are therefore presented in detail in what follows.

High-repetition rate laser sources for condensed matter experiments are highly advantageous, but combining this with XUV light produced by a HHG process is non-trivial. Previous approaches for trARPES have fallen broadly into one of two camps: high-repetition rate at low photon energies (~ 6 eV) [Gra11a, Fau12, Sob12] or low repetition rate XUV sources at around 1-10 kHz [Tur10, Roh11, Fri13, Wan15]. This is a result of the necessary conditions to produce HHG, which typically requires high pulse energies. Our idea is to combine these two approaches using OPCPA technology which has the advantage of being scalable to high pump powers as no energy is stored in a crystal medium. We produce an XUV output energy of 22 eV at a repetition rate of 500 kHz for use in trARPES experiments, which represents a significant technological step forward, as it allows both coverage of the full Brillouin zone and good counting statistics.

In this chapter an overview of both the laser system – including HHG generation – and the ARPES machine is given. The combined experiment was used to obtain the data on In/Si(111) nanowires presented in chapter 7.

4.1.1 Laser System

The description of the initial laser follows that given in [Pup15]. A schematic of the laser setup is presented in Fig. 4.1. The first section (Venteon GmbH) comprises of a Yb:YAG fibre oscillator at 1030 nm running at 25 MHz, and a fibre amplifier. Fibre-based lasers offer high beam quality and stable operation as thermal management is very efficient. The amplifier has three laser diode pumped stages, two fibre pre-amplifiers and an 80 cm long Yb:YAG rod-type photonic crystal fibre, which gives an average output of 9 W with a spectral bandwidth of 8 nm. An Acousto-Optic Modulator (AOM) is used to reduce the repetition rate to 500 kHz. The output from the fibre amplifier is split into two arms. Around 40 % is used to seed a Yb:YAG InnoSlab amplifier (Amphos) with an output power of over 200 W. This amplified output is compressed using a grating compressor to 1.2 ps and then frequency doubled in a BBO crystal. The output at 515 nm with an average power of 80 W is used to pump the OPCPA stage. The other arm of the fibre output is compressed to 360 fs and used to generate broad band white light via filamentation in a YAG crystal, which has a high damage threshold [Bra09]. The 1.3 μJ pulses focussed in the YAG crystal produces a continuum of light from 610-940 nm with pulse energies of 6 nJ, which acts as the seed of the OPCPA.

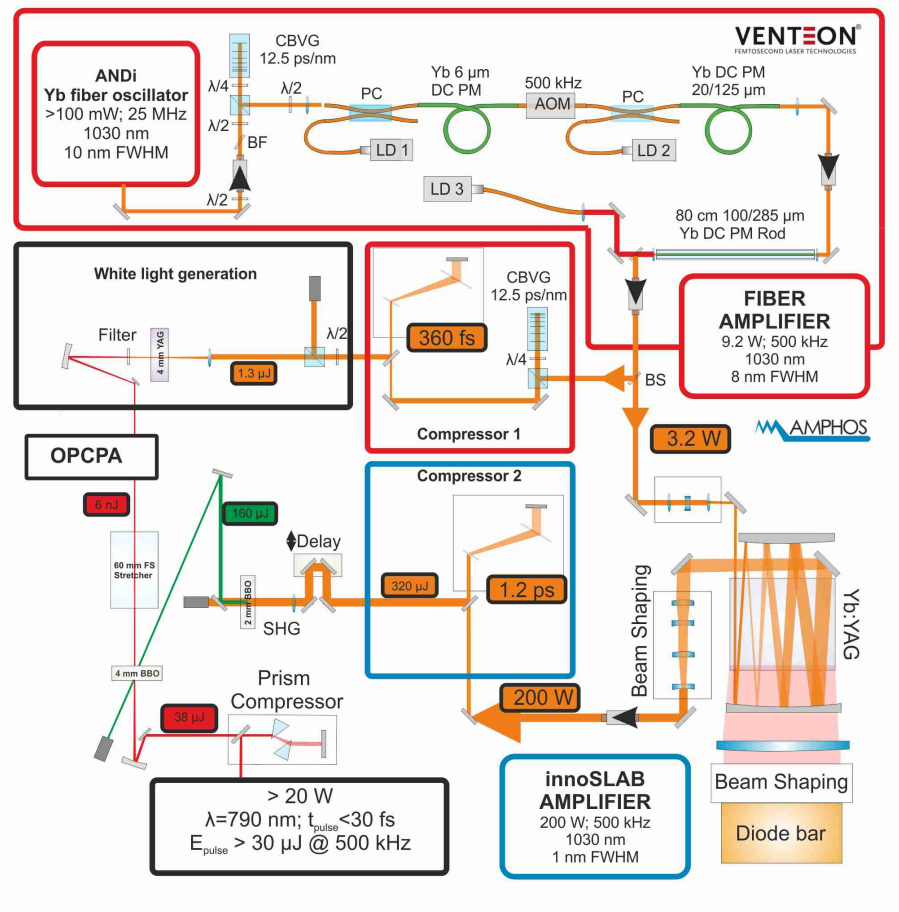

Figure 4.1: Schematic overview of the main components of the laser system used to produce 500 kHz output at 790 nm as the driver for the HHG process. Figure courtesy of M. Puppin.

Pump and seed pulses are spatially and temporally overlapped in a 4 mm BBO crystal using a non-collinear geometry. The seed pulses are stretched by dispersing them through fused silica glass (FS), resulting in a large amplified bandwidth at a central wavelength of 790 nm is obtained. The final power output of the OPCPA is around 21 W centred at 790 nm at 500 kHz repetition rate and pulse energies of 30 μJ after compression. Using a prism compressor the pulses are compressed to a FWHM of around 30 fs.

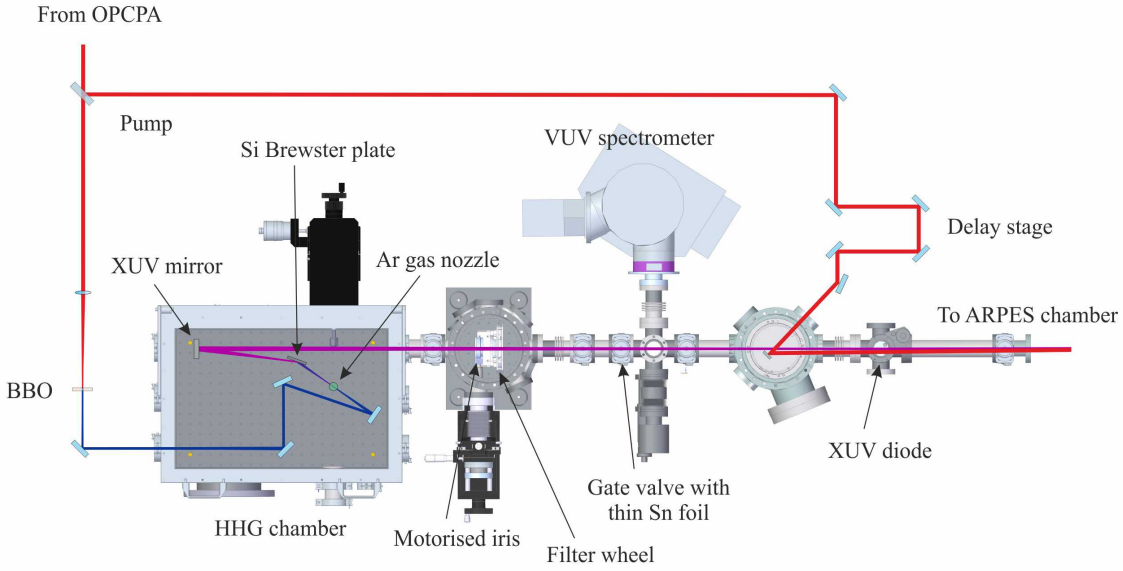

Figure 4.2: Schematic of the HHG generation chamber and beam line.

The majority output of the OPCPA is used to drive the HHG process, while around 1 W is made available for the pump beam of the trARPES experiment. A schematic of the pump beam path, HHG chamber and XUV beam line are shown in Fig. 4.2 and the beam line in relation to the UHV chambers in Fig. 4.3a. The pump arm leads to a delay stage which varies the temporal delay between pump and probe pulses in the trARPES experiments. The pump beam is coupled into the XUV beam line through a window in a chamber just before the ARPES analysis chamber. The 790 nm beam is frequency doubled by focussing into a BBO crystal in air before the HHG chamber. We have found that driving the HHG process with 395 nm (blue) to be more efficient than direct driving with the output of the OPCPA [Eic14]. The 395 nm beam has a power of around 5 W, corresponding to pulse energies of 10 μJ. It is transmitted into the HHG chamber through a 1 mm fused silica window which introduces minimal dispersion to the beam. It is then focussed into a gas jet of Ar, which produces the HHG spectrum. Due to the relatively low pulse energies in our setup as a result of the high repetition rate employed, it is necessary to use a tightly focussed beam in order to achieve the high peak electric fields required to drive the HHG process. The beam size in the focus is around 15 μm. The gas jet comes from a glass nozzle with a diameter of 40 μm which is mounted on a 3D manipulator allowing for fine control of the jet position with respect to the beam. Other nobble gases (Kr, Xe, Ne, He) have been tested, but Ar was found to give the highest photon flux. Directly opposite the nozzle is a gas skimmer which employs a large scroll pump to efficiently remove the gas without putting too large a strain on the turbo pumps in the chamber. Even with 2-4 bars of backing pressure – necessary

to achieve good phase matching – the background pressure in this chamber remains no higher than 5x10^{-3} mbar during operation.

HHG occurs in the interaction volume defined by the 395 nm beam and the Ar gas jet. After generation, the XUV and driver beams co-propagate until they reach a Si wafer mounted at the Brewster angle for the 395 nm beam, which suppresses a large part of the driver beam. The only remaining optical element is a multi-layered XUV mirror (quartz substrate overlaid with a thin Cr/Sc/Cr/Si multilayer structure) which reflects and focusses the beam down the beam line and onto the sample position. Spectral selection of a single harmonic (22.3 eV) is achieved through a combination of the XUV mirror, which has maximum reflection at our selected harmonic, and thin removable Sn filters in the beam line. Typically a single Sn filter of 100 nm thickness is used, which effectively blocks both unwanted harmonics and the residual driver beam. The residual signal from higher harmonics, which appears in the unoccupied part of the band structure and could in principle therefore mask weak pump-probe signal is typically 4 orders of magnitude weaker than the main signal. In the case that even higher spectral contrast is required, a second Sn filter may be placed in front of the beam in vacuum using a motorised filter wheel, at the expense of photon flux. A significant advantage of the present mirror plus filter monochromator design over a grating monochromator is that no temporal broadening is introduced into the pulse during monochromatisation, while also maintaining high photon throughput. On the other hand it is only possible to work with a single harmonic. A VUV spectrometer (Macpherson) can be used to measure the photon flux at different XUV energies, and an XUV diode gives a reading of the total photon flux after monochromatisation. The final available probe beam at the sample position is 2x10^{-11} photons/second at 22.3 eV and 500 kHz with a pulse duration of around 30 fs. The spot size is around 120x120 μm^2.

4.1.2 UHV Chambers

An overview of the ARPES end station, including the XUV beamline, is shown in Fig. 4.3a. The UHV end station is made up of three main chambers for sample preparation, sample storage, and photoelectron spectroscopy measurements respectively, each separated from the other by gate valves. All chambers are pumped with turbo molecular pumps (Pfeiffer) backed by scroll pumps (Edwards) and operate at or below 5x10^{-11} mbar. The analysis chamber is additionally equipped with a titanium sublimation pump (TSP) and ion pump for further improved vacuum. UHV conditions are essential for ARPES measurements due to the high surface sensitivity of ARPES. In particular for the long measurement times required for trARPES studies, a high quality, stable vacuum is particularly important. A more detailed view of the UHV chambers is given in Fig. 4.3b. Single crystals or substrates are introduced into the system via a load lock attached to the MBE growth chamber, which due to its small volume allows for rapid pumping and efficient transfer. The load lock contains a sample garage that can hold up to 6 sample holders at once. Sample preparation is carried out in the MBE growth chamber. Multiple evaporators can be attached to the underside of the chamber via CF40 ports. Typically there are two water-cooled Knudsen cell type evaporators attached at any one time, while a third port houses an Ar sputter source for metal single crystal preparation. A quartz-balance is used to monitor the deposition rate of the evaporators. Heat

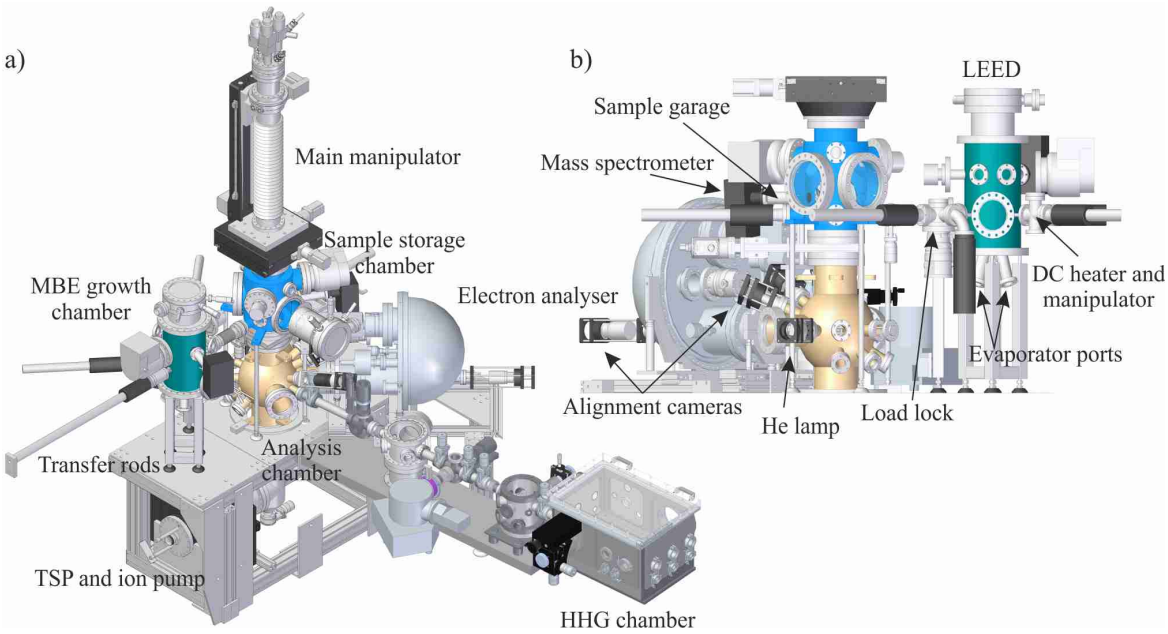

Figure 4.3: Schematic rendering overview of the UHV system and HHG beam line. MBE growth chamber (teal), sample storage and transfer (blue), and ARPES measurement chambers (gold) have been coloured to highlight them.

treatments are carried out in a direct current (DC) heating stage mounted on a 3D manipulator. A more detailed discussion of the heating stage and sample holder design is given in the section on Si preparation below. Si samples are heated by passing current directly through the crystal, while metal single crystals are heated via tungsten wires clamped around the edge of the sample. The temperature of the sample surface may be monitored remotely via an IR pyrometer installed on the underside of the chamber, between the evaporator ports. The sample surface quality can be checked by using the LEED optics mounted on the top of the chamber. A camera connected to a computer allows for the efficient acquisition of images.

From the growth chamber, samples are transferred into the sample storage chamber via magnetically coupled transfer rods. The storage chamber contains a mass spectrometer for analysis of the residual gas, a second sample garage, which again holds up to 6 samples and a second LEED optic. This chamber also houses the main manipulator (SPECS, Carving) which has six motor-controlled encoded axes and can be cryogenically cooled with either liquid nitrogen or liquid helium, allowing a base temperature of 10 K behind the sample to be reached. A heating coil behind the sample position, a Si diode for temperature sensing and a PID controller (Lakeshore) allows stable temperature dependent measurements to be carried out from room temperature. A wobble stick is used to transfer samples between the sample garage and the manipulator and additionally has a small Allen key attached to it that is used to clamp the sample holder in place in the manipulator via a screw. Once inserted into the manipulator, the sample is lowered into the analysis chamber. This chamber is made of μ-metal for increased magnetic shielding, which is required as the interaction with even a weak magnetic field (e.g. the Earth's magnetic field) can disturb the electron trajectories resulting in the loss of information. All ARPES and trAREPS measurements are carried out in this chamber, which contains the 2D hemispherical electron analyser (SPECS, Phoibos 150) and the in-coupling from the

XUV beam line. Pump and probe beams are overlapped on the sample at the focus of the electron analyser. Alignment of the beams is facilitated by optical cameras mounted on various flanges. A He discharge lamp is also installed in this chamber for static high energy resolution ARPES measurements, at the position marked in the figure. The lamp itself is not included in the image. This lamp was used for characterisation of the analyser as presented below.

4.1.3 Hemispherical Analyser

Angle and energy resolved electron spectroscopy measurements have been carried out using a 2D hemispherical analyser (SPECS, Phoibos 150) with internal μ-metal shielding, a rendering of which is shown in Fig. 4.4. The main components of such an analyser are the electron lenses, the energy dispersion element (the hemisphere) and the electron detector. Electrons emitted from a sample placed at the focus of the lens system (40 mm from the first lens element) are imaged onto the entrance slit of the hemisphere by the lenses. The size of this slit in part determines the energy resolution of the analyser, and may be varied without breaking the vacuum conditions. In addition, the energy of the electrons is reduced by a retardation potential such that the energetic distribution of electrons is centred around the nominal pass energy (E_{pass}), instead of the initial kinetic energy.

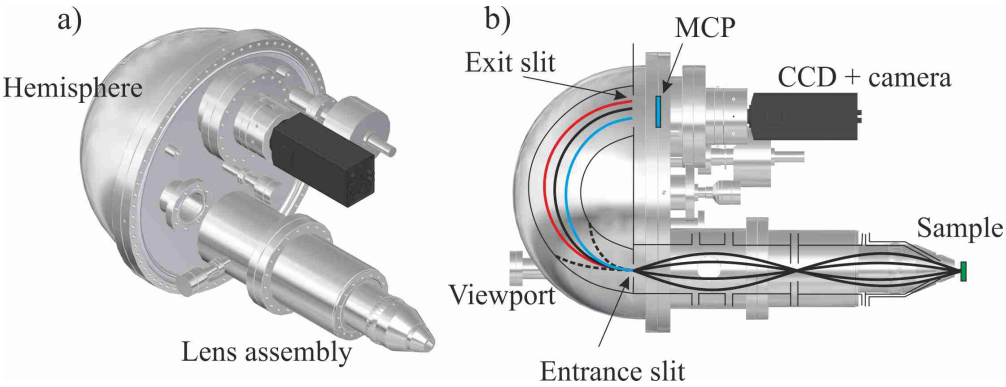

Figure 4.4: a) Rendering of the 2D hemispherical analyser. b) Side projection with schematic outline of lens system, slits and inner and outer hemispheres (thin black lines). Thick solid lines represent schematic electron trajectories which arrive the detector, while the dashed lines are trajectories that collide with the hemispheres.

Sample and analyser are in electrical contact and hence share a common Fermi level. However there will be a potential in the region between sample and analyser due to the difference in work functions. Since the measured value is $E_{\text{kin,analyser}}$ the result of this is that the binding energy (E_{B}) of the electrons may be determined without knowing the sample work function: only the analyser work function needs to be calibrated. This follows from:

$$\begin{aligned} E_{\text{B}} &= h\nu - E_{\text{kin,sample}} - \Phi_{\text{sample}}, \\ E_{\text{kin,sample}} + \Phi_{\text{sample}} &= E_{\text{kin,analyser}} + \Phi_{\text{analyser}} \end{aligned} \tag{4.1}$$

The energetic separation of electrons is achieved by dispersion through the hemisphere, entered via the entrance slit (Fig. 4.4b). The hemispherical analyser is

comprised of two concentric hemispheres (outer and inner) with a mean radius of 150 mm. The hemispheres are held at potentials symmetrically above and below the value of E_{pass}, such that electrons arriving at the entrance slit with the nominal E_{pass} are guided along a trajectory exactly between the two hemispheres. Electrons whose energies differ from E_{pass} will be deflected by the radial electrostatic field between the hemispheres, resulting in an energy dependent radial displacement of electrons on the exit slit. Only electrons within around 10% of E_{pass} arrive at the exit slit; those with two high or too low energies collide with the hemispheres. Hence electrons are focussed onto the exit slit plane, with a radial position dependent on their kinetic energy. An exit slit with a mesh is used in the experiments. Applying a negative bias voltage to the mesh reduces the background signal, particularly above the Fermi level, which is of importance when measuring the dynamics of excited states. Typically a retarding voltage of 80% of the pass energy is applied to maximally reduce background while leaving the signal unaffected. The mesh imprints itself on the data but may be removed by a Fourier filter as described below.

Momentum (angular) resolution is obtained from the spread of angles emitted from the sample that are accepted by the analyser. This initial spread of angles results in a spatial separation of electrons across the entrance slit in the horizontal plane, which is then imaged – including the energy spread induced by dispersion through the hemisphere – onto the exit slit and then to a 2D array of electron-multipliers: the microchannel plate (MCP). Electrons entering the MCP produce a cascade of secondary electrons when they collide with the walls of the MCP. The multiplied output impinges on a phosphor screen, and the final 2D image (energy vs. momentum) is captured by a CCD detector with a 12-bit digital camera (PCO, SensiCam) typically operated at around 20 Hz.

4.1.4 Calibration Measurements

The energy resolution of the analyser has been tested and compared with the theoretically achievable resolution. The results are summarised in Fig. 4.5. For testing purposes, a non-monochromatised He discharge lamp (Leybold) operated at a He pressure of $9\text{x}10^{-11}$ mbar was used to generate photons at 21.2 eV (He I). This offers a much higher intrinsic energy resolution than the XUV pulses which as a result of their ultrashort time structure have an intrinsically large energy bandwidth. The low He pressure is essential for obtaining the best possible resolution. The resolution of the analyser alone is given by [Pol76, Roy99, Spe08]:

$$\Delta E_{\text{analyser}} = E_{\text{pass}} \left(\frac{s}{2R} + \frac{\alpha^2}{4} \right) \tag{4.2}$$

where E_{pass} is the pass energy, s is the average size of entrance and exit slits, R is the mean radius of the hemispheres and α is the half acceptance angle of the analyser. Additional contributions to the total measured resolution come from thermal broadening ($4k_{\text{B}}T$) and the intrinsic width of the He I line (3 meV) [Spe]. The total resolution is given by the convolution of the individual widths (FWHM), which for Gaussian line widths results in:

$$\Delta E_{\text{total}} = \sqrt{\Delta E^2_{\text{analyser}} + \Delta E^2_{\text{thermal}} + \Delta E^2_{\text{He}}} \tag{4.3}$$

This total resolution value is computed for different combinations of slit size and pass energy, and plotted in Fig. 4.5a.

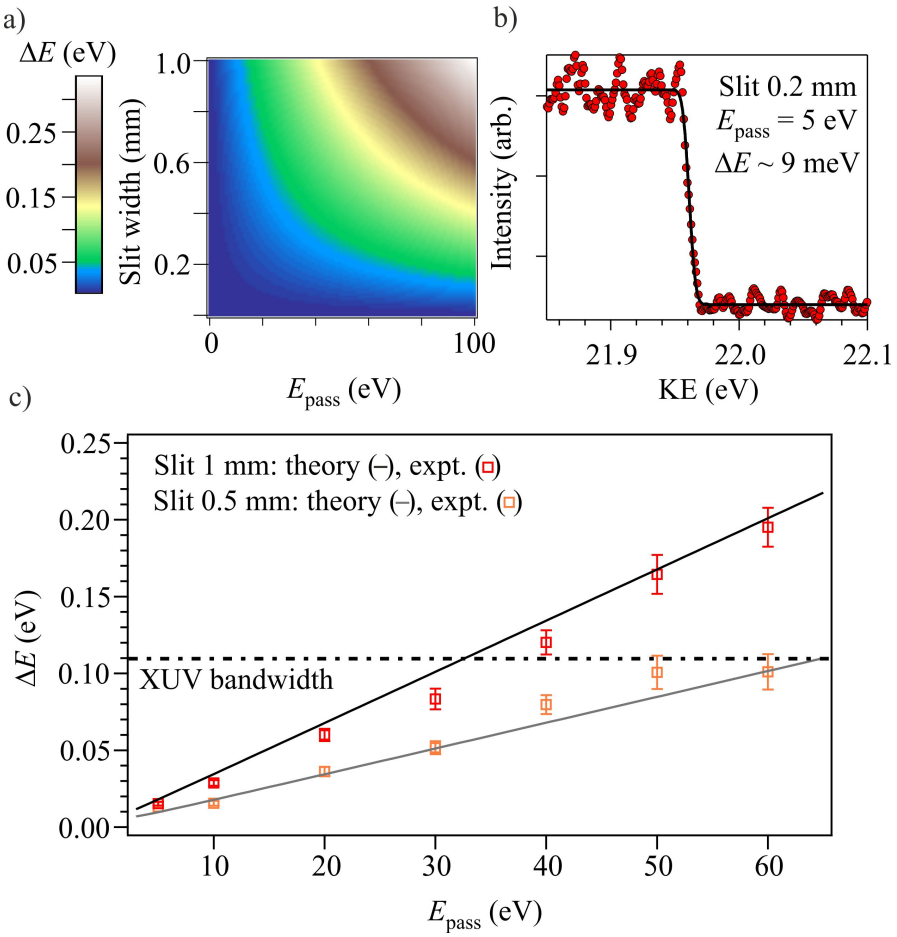

Figure 4.5: (a) Theoretical measurement resolution as a function of entrance slit size and pass energy. (b) Best resolution of 9 meV achieved using the the hemispherical analyser to measure a polycrystalline Ag sample. (c) Comparison of theoretical and experimental energy resolutions for two slit widths as a function of pass energy.

In order to compare with the experimental results, cuts through this 2D data set at fixed slit widths (1 mm and 0.5 mm) are extracted and plotted in Fig. 4.5c along with the experimentally determined widths. Experimental widths are obtained at 8 K from the Fermi edge of an Ag foil cleaned with an Ar sputter source in the MBE chamber shortly before measurements. An example Fermi edge and fit is given in Fig. 4.5b. It is clear that the experimentally obtained values agree well within errors with the prediction from theory across the full measured range. As a comparison, the bandwidth of the XUV pulses is drawn as a dashed-dotted line. From this graph it is therefore straightforward to determine at what settings of slit width and pass energy are appropriate for use with the laser: typically one wants to maximise electron flux by opening the entrance slit, but this reduces the resolution. A good balance is achieved with E_{pass} between 20 and 30 eV, and a slit size of 0.5 mm. The ultimate resolution of the analyser was obtained using a slit size of 0.2 mm and $E_{\text{pass}} = 5$ eV (Fig. 4.5b). However due to the low flux rate and correspondingly long acquisition time required with these parameters, such conditions are not typically used in our experiments.

Additional tests have been carried out by measuring the spin-split Shockley surface state of a Au(111) single crystal [LaS96, Rei01, Nic02]. The Au single crystal was cleaned *in situ* by sputtering and annealing cycles as described in the literature [Rei01]. In order to heat the Au crystal, we used a modified sample holder design based on that employed for Si heat treatments (see section on Si Preparation). The circular Au crystal has notches cut into the narrow cylindrical edge, into which W wires are inserted to clamp the crystal onto the sample holder. Instead of a current passing through the bulk of the crystal as in the case of Si, thick W wires additionally carry the current around the edge of the sample, hence allowing it to be heated. We found that multiple short sputtering followed by long annealing produced the best results.

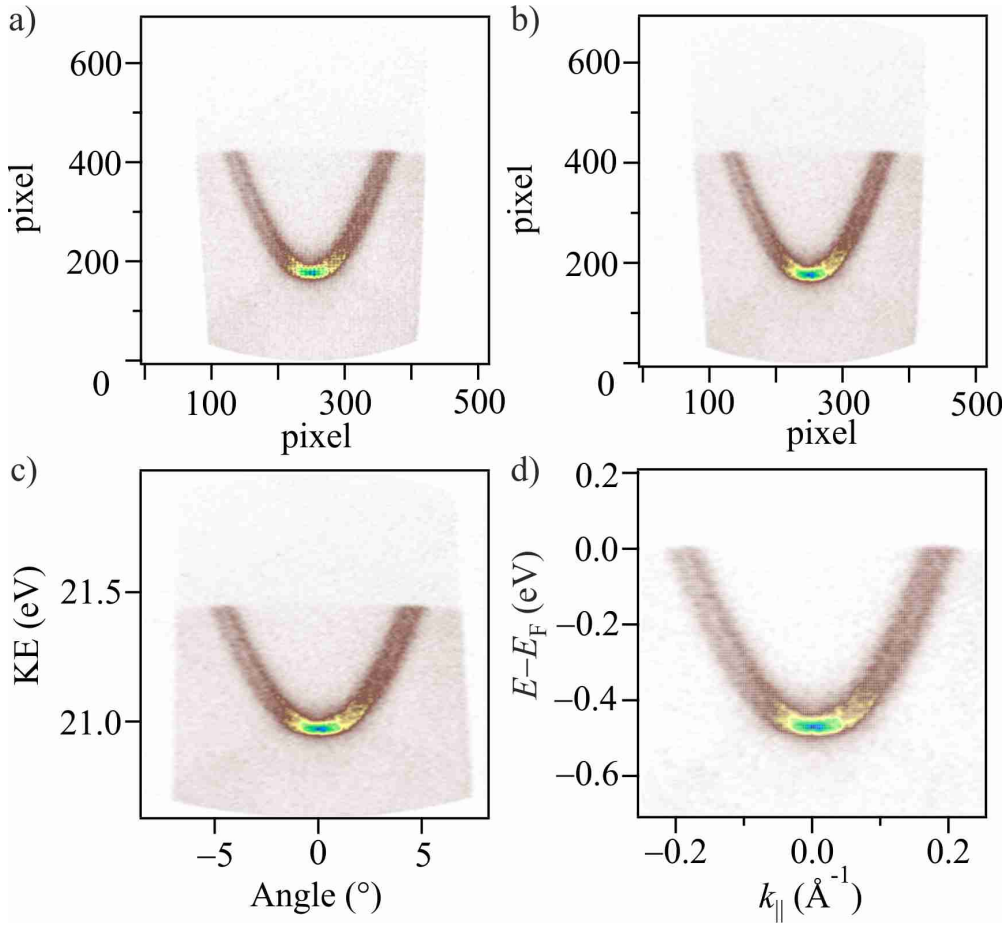

Figure 4.6: Au(111) Shockley surface state. (a) raw data and with (b) Fourier filter (c) angular correction and (d) k-space correction applied. The Rashba splitting is clearly visible.

The results obtained on the Au(111) surface state are presented in Fig. 4.6. The four panels additionally convey how the raw data obtained from the experiment are converted into the final energy and momentum plots; the same or very similar procedures are used in all results presented in this thesis. As described in the preceding section 2D images are obtained from the experiment. These are simply 2D arrays with no physical unit ascribed to either axis as in Fig. 4.6a. Additionally the influence of the exit slit mesh can be seen in the raw data. As a first step we use a low pass Fourier filter to remove the background mesh signal (Fig. 4.6b); this does

not influence the resolution of or the quality of the data. In order to retrieve energy and angular information, a calibrated image transformation (polynomial) provided by the analyser manufacturer is used with coefficients specific to the pass energy and lens modes used to acquire the data. In this case a pass energy of 10 eV and the Low Angular Dispersion (LAD) mode were used (with slit 0.2 mm). This produces an image with a kinetic energy and emission angle axis (Fig. 4.6c). The final steps are to convert the angular axis to momentum parallel to the surface, achieved by the relation given in Eq. 3.4 and convert the kinetic energy into a binding energy with respect to the Fermi level using Eq.4.1 and the position of the Fermi level extracted from the data. The final image showing the dispersion of the electrons as a function of energy and momentum is given in Fig. 4.6d for the Au(111) surface, in which one sees the classic parabolic dispersion of the free-electron like Shockley state with a minumum at −0.47(3) eV. The splitting of the surface state due to the Rashba effect is clearly resolved.

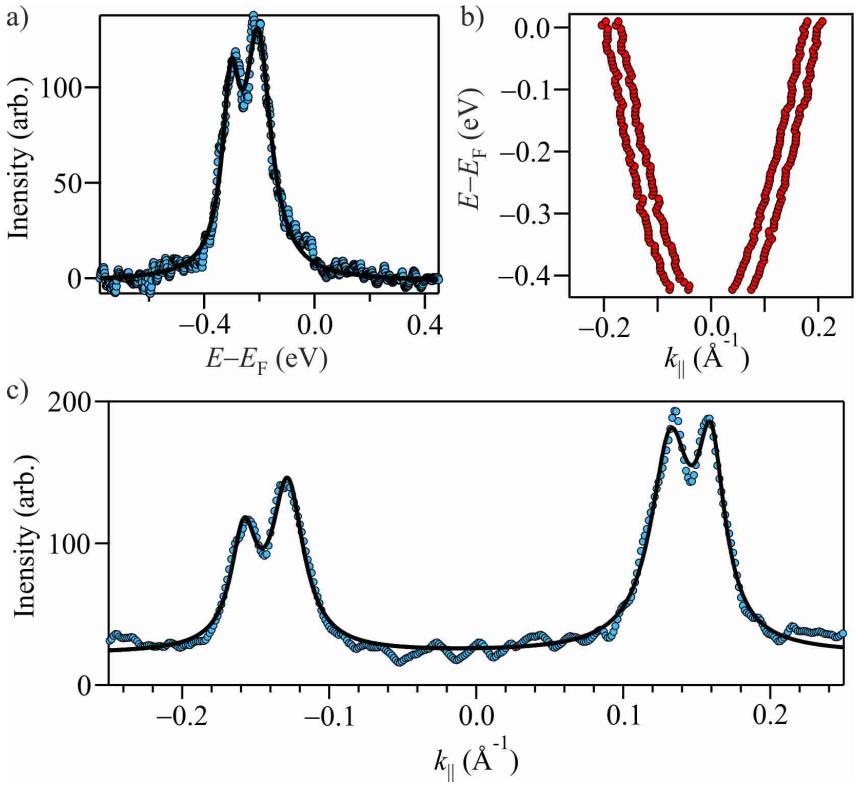

Figure 4.7: Analysis of Shockley state (a) EDC line cut at $k_{||} = -0.128$ Å^{-1} showing a splitting of 92 meV and (c) an MDC line cut at $E = -0.192$ eV revealing a momentum splitting of 0.02(6) Å^{-1}. In (b) the double dispersion extracted from a 4-peak Lorentzian fitting of the MDCs is shown.

Further analysis of the surface state is presented in Fig. 4.7. Line cuts through the data are used to highlight the two peaks arising from the non-degenerate bands. A vertical Energy Distribution Cut (EDC) at $k_{||} = -0.128$ Å^{-1} and a horizontal Momentum Distribution Cut (MCD) at $E = -0.192$ eV reveal a peak splitting of 92 meV and 0.02(6) Å^{-1} respectively. Using multiple MDCs, the dispersion of the surface state can be extracted by fitting 4 Lorentzians to the peaks, as in Fig. 4.7c. The resulting dispersion is shown in Fig. 4.7b, from which Fermi wavevectors with magnitude 0.19(5) Å^{-1} and 0.17(0) Å^{-1} are obtained. The values presented here are

in good agreement with the published literature [LaS96, Rei01, Nic02].

4.2 ARPES at Diamond Light Source, I05

The experiments on $NbSe_3$ presented in chapter 5 were obtained at the IO5 beamline at Diamond Light Source in the UK. In this section the beamline and end station used are briefly presented, following the description given in [Hoe17].

Beamline

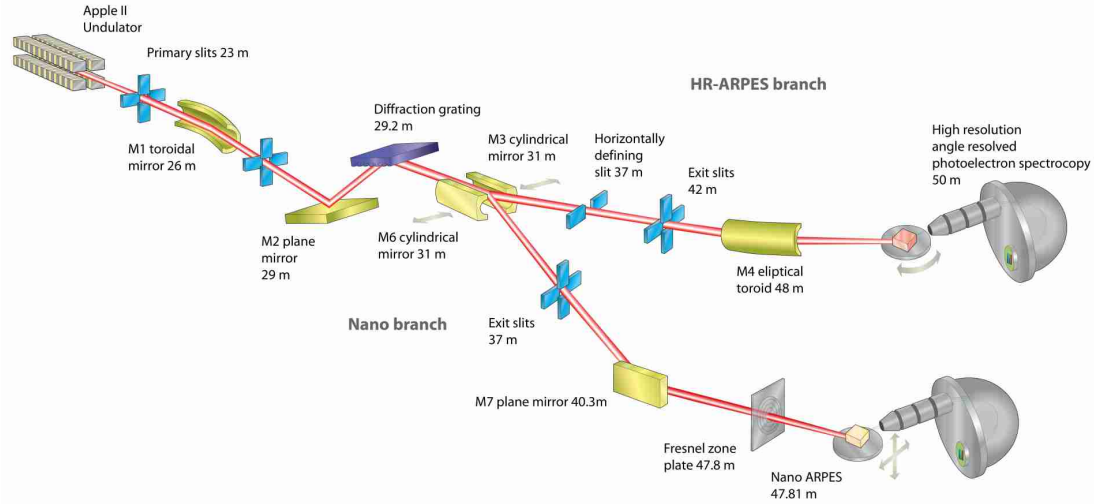

Figure 4.8: A schematic of the I05 beam line showing the optical elements between undulator and photoemission end station as described in the text. Reproduced with permission from [Hoe17].

The beamline offers two branches as shown in Fig. 4.8: a high resolution branch used for the $NbSe_3$ experiments and a nano-ARPES branch not discussed here. Photons are produced in the APPLE II-type undulator [Sas94] which consists of four linear arrays of magnets with periodically alternating polarity which may be translated with respect to one another. Such a design allows for the production of horizontal and vertical polarised, as well as circularly polarised, light. Particular photon energies are selected by a collimated plane grating monochromator [Saw97] diffraction grating. For typical high resolution measurements a grating of 800 lines/mm is used. The output of the monochromator is focussed by the cylindrical mirror M3 onto the exit slit, before being refocussed into the end station by an elliptical toroid mirror (M4). The slits in the beam line are used to block radiation, either unwanted radiation from the edges of the beam, or to reduce the overall flux of photons reaching the sample.

The core energy range of the beamline is in the vacuum ultraviolet (VUV), specifically 18 - 240 eV, for which the beamline is optimised in terms of energy resolution and photon flux. Operation is also possible up to just below 600 eV. Higher harmonic components are typically 100 times weaker than primary peaks, but can be further suppressed by the insertion of a 150 nm Al filter which absorbs above $\sim$70 eV. Over the core range an energy resolution of less than 2 meV at the

smallest slit sizes may be achieved by the beam line. With additional contributions to the energy resolution coming from the analyser and other contributions, the energy resolution measured by photoemission on a polycrystalline Au film at $T = 6$ K is 2.6 meV with an exit slit of 10μm. The available photon flux after the last mirror of the high-resolution branch is on the order 7x10^{12} photons/s. A typical spot size at the sample position of 50μm in both horizontal and vertical directions is available over the whole photon energy range.

End station

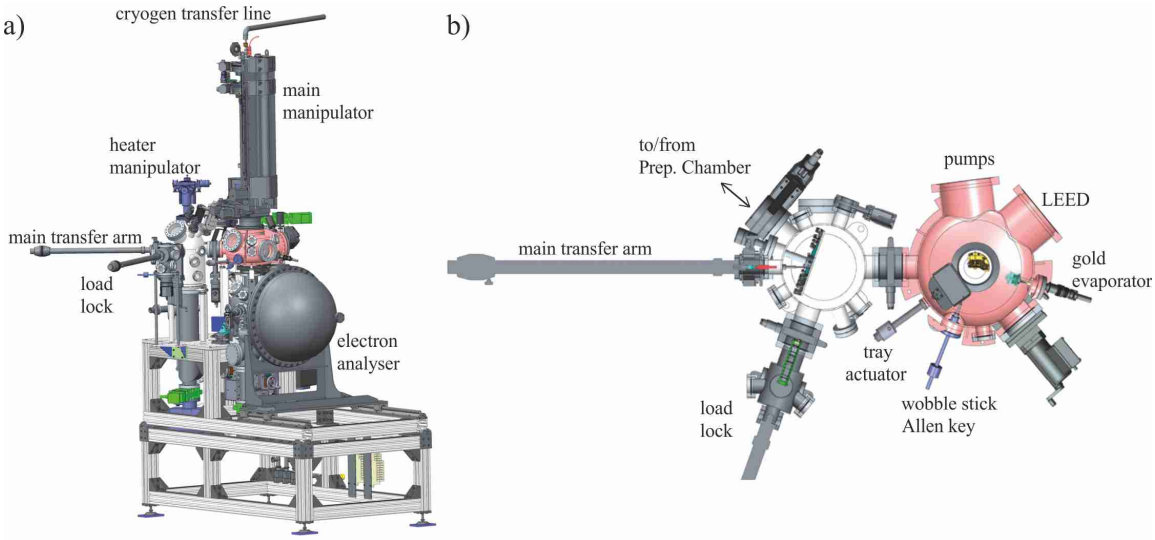

Figure 4.9: a) Side and b) top view of the I05 end station, the main components of which are the UHV chambers, cryo-manipulator and electron analyser. Samples are transferred around the system by magnetically coupled tranfer arms. Reproduced with permission from [Hoe17].

A rendering of the end station of the high-resolution branch is shown in Fig. 4.9. It comprises 3 UHV chambers into which samples may be introduced through a load lock. Multiple sample holders may be loaded into the load lock and then stored in the proceeding chamber, which is also connected to a preparation chamber for *in situ* MBE growth. The upper chamber (coloured pink in Fig. 4.9) houses LEED optics, an Au evaporator used for Fermi level referencing, and a wobble stick and tray utilised during the cleaving process: the wobble stick is used to remove the cleaving post from the sample surface, which is then caught in the tray. A discussion of the specifically designed sample holder and cleaving of $NbSe_3$ is given in later in this chapter. During cleaving the sample is already mounted on the 6-axis, cryo-cooled manipulator, with which temperatures below 10 K can be routinely achieved. An Allen key is attached to the wobble stick in order to tighten a screw which clamps the sample holder onto the manipulator, therefore ensuring good thermal contact. After cleaving the sample is moved via the manipulator to the lower chamber, where ARPES experiments are carried out. This chamber is made of μ-metal to improve magnetic shielding and houses the hemispherical electron analyser (Scienta R4000) and in-couples photons from the beam line. A camera microscope is also installed, focussed on the measurement position, and can be used for an initial alignment

with a resolution of 5 μm. A pressure in the range of 10^{-11} mbar is achieved during standard operation, which is important for maintaining a clean sample surface. The three rotational axes of the manipulator are reproducible within less than 0.05° with a sphere of confusion at the sample surface of ≈200 μm. At low temperatures the manipulator is known to contract by a maximum of ≈300 μm. For small samples such as $NbSe_3$, this change in vertical position may be automatically corrected by a software procedure.

4.3 ARPES at BESSY II, UE56/2-PGM-1

For the study in Chapter 6 of the metallic nanowire system Ag/Si(557) the UE56/2-PGM-1 beam line of the Max Planck Society at BESSY II in Berlin has been utilised. ARPES measurements we carried out on a dedicated sample preparation end station (AG Horn, FHI Berlin).

Beamline

The UE56/2-PGM-1 beamline is conceptually very similar to the IO5 beamline presented in the previous section. The insertion device is an APPLE-type undulator [Sas94] capable of producing both linear and circularly porlarised light which is focussed by a toroidal mirror onto a plane grating mirror [Saw97] to select a particular energy of radiation. Two gratings are available: 1200 lines/mm and 400 lines/mm. The beamline can operate over a wide photon energy range from 60 eV to 1200 eV, making it appropriate for both valence and core level spectroscopy. Maximum flux is obtained at 120 eV and falls off strongly at higher energies [Vit15].

End station

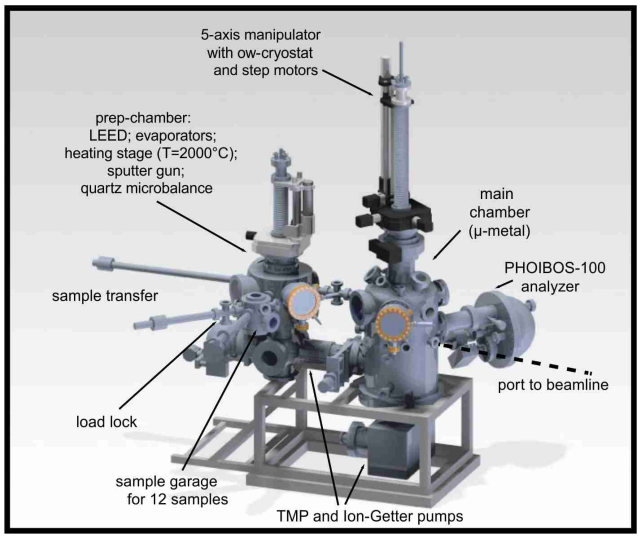

Figure 4.10: Schematic of the BESSY UHV end station, see text for details. Reproduced with permission from [Vit15].

A schematic overview of UHV end station is given in Fig. 4.10. It consists of a chamber for sample preparation and the main analysis chamber. Samples are

introduced via a load lock which includes a sample garage for up to 12 samples. The sample holder design comes from AG Horn [Vit15] and has been modified to allow the DC heating of Si samples as will be introduced in the section on Si preparation. The preparation chamber houses evaporators for MBE growth, a quartz microbalance, and LEED optics for determining the sample surface quality. Current is passed through the sample via a wobble stick that is electrically isolated from the chamber by a ceramic distance piece. The sample temperature during preparation may be monitored by a pyrometer mounted externally. The chamber also includes a sputter gun and e-beam heater for metallic single crystal preparation, which were not used in the studies presented here. Once prepared, the sample is transferred via magnetically coupled rods into the main chamber which is constructed from μ-metal for increased magnetic shielding. Photoemission measurements are carried out in this chamber using a 2D hemispherical analyser (Phoibos 100, SPECS GmbH). A 5-axis manipulator (AG Horn, FHI) with encoded stepper motors may be used for angle-resolved Fermi surface mapping. An additional manual axis allows for the azimuthal orientation of the sample to be adjusted. The sample may be cooled on this manipulator using either liquid nitrogen or liquid helium allowing a base temperature of 50 K to be reached when cooling with He. Typical operating pressures in the main chamber were in the mid to low 10^{-11} mbar range as measured by a filament ion guage.

4.4 trARPES at the Freie Universität, Berlin

The measurements of the spin density wave dynamics in Cr thin films presented in chapter 8 were carried out in collaboration with the group of Martin Weinelt, using a HHG-trARPES beam line, end station and *in situ* growth capabilities, at the time located at the Max Born Institute, Berlin. Here the HHG beam line and end station are briefly described, following the description given in [Fri13], while the growth of Cr thin films is presented later in this chapter.

Beamline

A Ti:Sapphire laser (Red Dragon, KM labs) operating at 80 MHz, and three helium cooled multi-pass amplifiers comprises the laser system. An output of 17 W at 10 kHz (1.7 mJ/pulse) is achieved, at a central wavelength of 785 nm ($\sim$1.6 eV). The pulse duration is 40 fs. This output is split into two arms: around 10 % is compressed and used to directly pump the sample in the time-resolved experiments; the rest is used to generate the XUV probe pulses by HHG. An overview of the beam line is shown in Fig 4.11.

XUV light is generated by focussing the IR pulses (around 1.5 mJ/pulse) into a closed Ar gas cell (stainless steel tube) with $50 - 100$ mbar backing pressure. The focussed beam burns through the walls of the cell, and the laser light interacts with the gas in the small volume, producing XUV photons. A single harmonic contains 10^{10}-10^{11} photons/s. After the gas cell, both IR driver and generated XUV pass through a 2 mm aperture. This acts as a differential pumping stage separating the HHG chamber from the rest of the beam line, and additionally blocks some of the transmitted IR light. The rest of the IR light is filtered by a 150 nm removable Al

foil, through which the XUV light is transmitted at around 50 %, depending on the XUV wavelength.

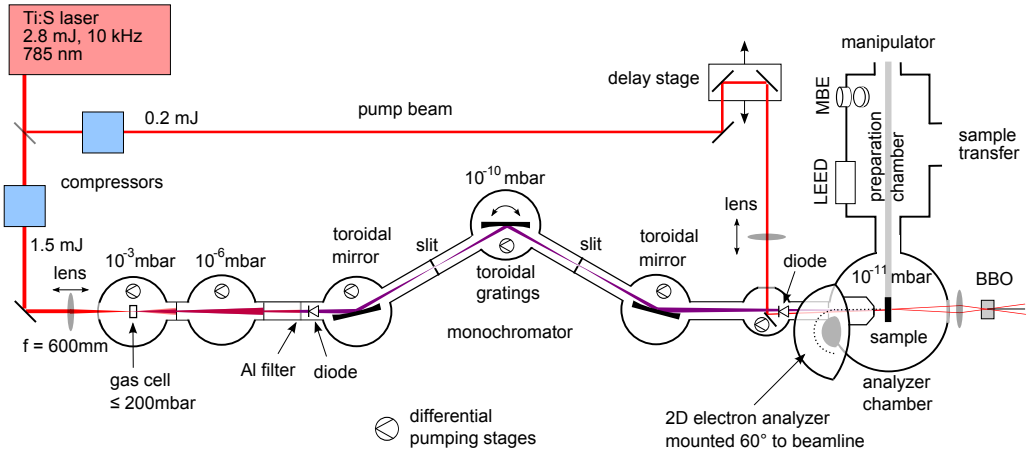

Figure 4.11: Schematic layout of the FU HHG laser system and coupling to the UHV chamber. Reproduced with permission from [Fri13].

A single grating monochromator is used to select individual harmonics from the full HHG spectrum produced in the gas cell. A single grating monochromator has the advantage of offering higher transmission over a double grating design, but introduces a temporal chirp due to the tilt of the wave front produced from diffraction from a single grating. The design is aimed at achieving a compromise between energy and time resolution, wavelength tunability and high optical throughput. In order to select single harmonics over the full available energy range (15−110 eV) two exchangable gratings are used, one with 200 lines/mm for low energies and one with 500 lines/mm for the higher energies. The overall energy resolution of the monochromator is in part given by a convolution of the input and output slits. Therefore the XUV beam is focussed on to the entrance slit of the monochromator by a grazing-incidence toroidal mirror. The mirror produces a 1:1 image of the HHG source on the entrance slit, while the grating itself images the entrance slit onto the exit slit. A second identical toroidal mirror after the monochromator images the exit slit onto the sample. Photodiodes sensitive to the XUV range are used for aligning the beam and to measure the flux before and after the monochromator.

Through the beam line there is a considerable range of pressures, from to 5 x 10^{-3} mbar in the HHG chamber to 10^{-11} mbar in the analysis chamber. This is achieved by multiple differential pumping stages along the beam line with turbo-molecular pumps and an ion getter pump in the last chamber.

End station

The end station consists of three UHV chambers: a preparation chamber; μ-metal analysis chamber and a sample garage. The sample preparation chamber contains MBE evaporators, a quartz balance, a sputter gun, gas inlets and LEED optics. A single manipulator is used to house the sample and transfer it between chambers, and can be cryogenically cooled. The W(110) crystal substrate used in the Cr/W(110) studies is fixed to the manipulator and can be heated via electron bombardment. The temperature is measured by a type C thermocouple placed in a hole drilled in the

side of the crystal. The μ-metal analysis chamber houses a 2D electron spectrometer (SPECS) for ARPES studies. The energy resolution of the experiment was measured by using the Schockley surface state on a Cu(111) surface. An energy resolution of 90 meV is achieved with the 23rd harmonic (35.6 eV) at a slit size of 10 μm. However this comes at the cost of photon flux. A more standard operation parameter set is an exit slit of 20 μm which gives 150 meV energy resolution at 3.6 x 10^7 photons/s reaching the sample, corresponding to around one electron detected per XUV pulse. The spatial overlap of pump and probe pulses is obtained by imaging both pulses on a phosphor screen at the sample position, while for temporal overlap a BBO crystal outside the UHV chamber is used to generate the second harmonic from the IR light in the pump arm and the IR light that passes through the beam line when the Al filter is removed. At the sample positions the pump spot size is around 130x130 μm^2 (FWHM). The overall time resolution of the experiment is around 125-130 fs, as measured by side band (laser assisted photoemission) signal produced in photoemission experiments [MA06, Saa08].

4.5 Sample Preparation

4.5.1 Metallic Nanowires on Si Substrates

Two of the nanowire systems presented in this thesis (chapters 6, 7) have been grown on Si substrates via metal deposition by *in situ* Molecular Beam Epitaxy (MBE). Due to the regular use of Si in the semiconductor industry, wafers of high quality are readily available and the preparation of well-ordered surfaces has been well documented in the literature [O'M93, Lin98, Hat00].

While different wafer orientations and dopings have been used in each of the projects, the general preparation of Si substrates share a number of common components, which will be outlined below. The preparation of both the specific Si substrates and the subsequent growth of metallic nanowires will also be described.

4.5.2 Preparation of Si Substrates

The preparation of clean Si(111) surfaces was achieved by direct current heating using a sample holder and heating stage specially designed at the Fritz Haber Institute, shown in Fig. 4.12. The basic sample holder is a modified version of the Swiss Puck (PSI, Switzerland) system design and is built from molybdenum, with ceramic plates used to electrically isolate the two sides. Care should be taken to avoid the inclusion of metals such as chromium, cobalt, and nickel, with which Si forms reconstructions. The Si sample is gently clamped by two Mo plates to the two electrically isolated sides of the sample holder. Si spacers have been used to give a more even distribution of force, and therefore heat, at the contacts. Current flows through the Si sample when a voltage is applied across the two isolated sides of the heating stage which are in contact with the edge of the sample holder. In this way the Si sample can be heated and cleaned.

The temperature during heating was monitored with a pyrometer mounted on the UHV chamber. Initially, the Si sample was outgassed for a number of hours, usually overnight, at 500°C. This allowed the pressure in the chamber to recover to the base level in the 10^{-11} mbar range, allowing for optimal conditions during the second phase

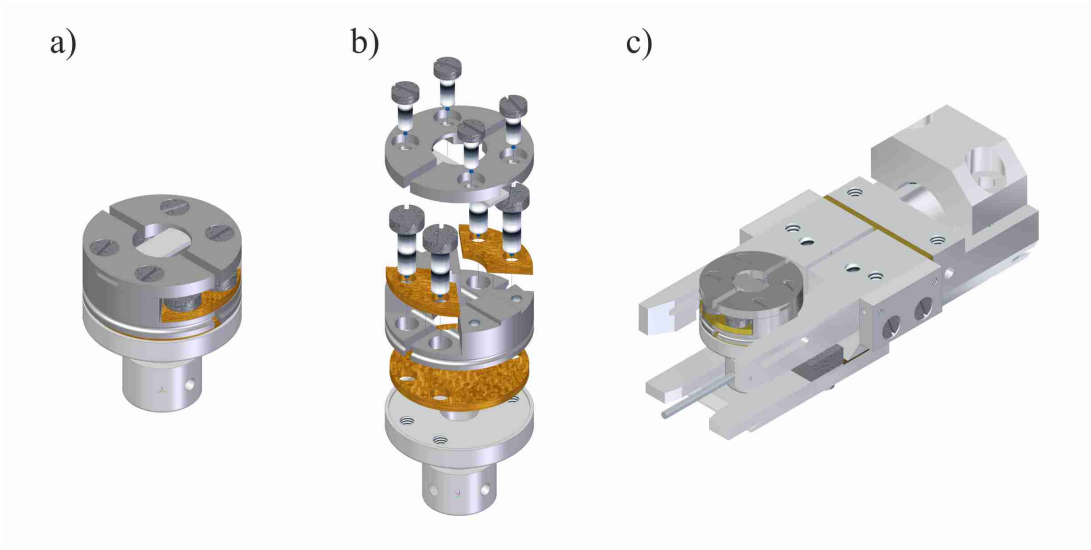

Figure 4.12: a) Rendering of the Si sample holder and in exploded view in b). c) Sample holder inserted into the heating stage. Ceramic parts are coloured gold.

of cleaning. The Si temperature is then gradually increased to around 1200°C for short periods of time (< 10 s) in order to desorb SiO_2 layers from the surface. Finally the sample is flashed to around 1400°C to sublime the topmost layers of Si and remove SiC. This procedure is repeated 3 to 4 times, which already produces the well-known Si(111)-7x7 reconstruction. For particular surface orientations, in particular Si(557), additional steps of slow annealing and rapid quenching are necessary to avoid the development of step bunches, as will be described in more detail below.

LEED is used to inspect the long-range order of the Si(111)-7x7 reconstruction. Typical LEED images are shown in Fig. 4.13 where the Si 1x1 reciprocal unit cell is marked by the red dotted line. The formation of the 7x7 reconstruction is revealed by the additional six spots that appear between each of the 1x1 spots. The characteristic shape of the 7x7 unit cell is also revealed in the image, highlighted by the green dotted line. A high sample surface quality are indicated by the sharp spots and low inelastically scattered background.

4.5.3 Preparation of Nanowires

Ag/Si(557)

As a basis for the preparation of the 1 ML Ag/Si(557) nanowire structure, a non-faceted Si(557) surface was used as a template. Si(557) n-type crystals were outgassed at 500°C for 12 hours. This was followed by flashing to 1150°C (< 5 s) followed by a rapid quench to 900°C. The sample was then slowly cooled to 800°C where it was subsequently annealed for between 5 and 10 mins. These last two steps are of particular importance for avoiding the migration of step edges due to thermal gradients, which results in large areas of non-faceted surface, and for inducing long range order. The base pressure in the chamber was $5\text{x}10^{-10}$ mbar, and was never higher than $1.2\text{x}10^{-9}$ mbar during flashing. The quality of the substrate preparation was confirmed by LEED, as in Fig. 4.14a. In particular the weak x2 intensity (marked by an arrow) produced by period doubling along the step edges is indicative of high

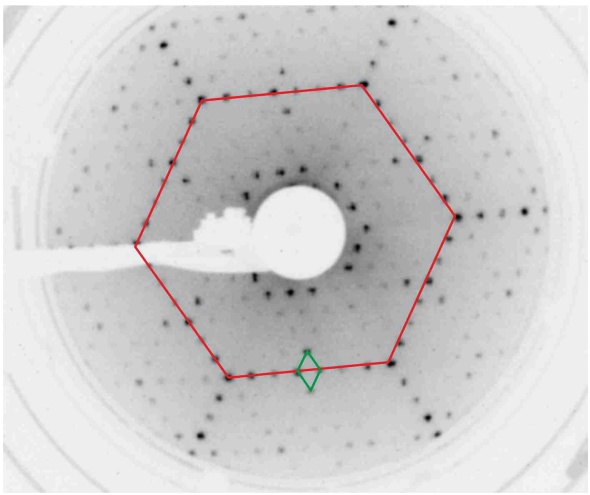

Figure 4.13: LEED image of the Si(111)-7x7 reconstruction taken at 60 eV incident electron energy. The 1x1 unit cell is marked in red, and the 7x7 in green.

quality surface preparation.

Ag was evaporated at a rate of around 0.05 ML/min from a home-built e-beam evaporation cell, with the Si substrate held at room temperature. The sample was then annealed at 500°C for 10 minutes to induce the $\sqrt{3}$ structure. Note that this procedure differs slightly from previous work [Kri13, Kri14], where Ag deposition was performed at 500°C. A LEED image of the $\sqrt{3}$ Ag nanowires is shown in Fig. 4.14b. The evaporator was calibrated using the LEED phase diagram of Ag/Si(111) and Ag/Si(557) [Wan93, Kri13].

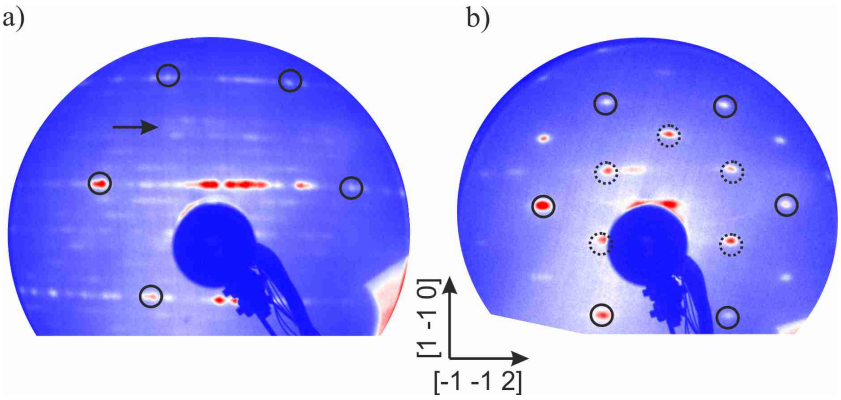

Figure 4.14: a) LEED image of the clean Si557; circles highlight the 1x1 structure and the arrow marks the (weak) x2 intensity produced by period doubling along the step edge, indicative of high quality surface preparation. b) 1 ML Ag on Si(557). Solid circles mark 1x1 structure as in a) and dotted circles mark the $\sqrt{3}$ spots. Both images were taken with 77 eV electron beam.

In/Si(111)

Atomic nanowires of In may be prepared on flat Si(111) surfaces [HB13]. However due to the presence of three equivalent rotational domains on the flat surface, a wafer with a miscut angle of 2° towards the [-1 -1 2] direction was utilised. This results in

steps in the sample surface, and breaks the three-fold symmetry, thus causing the nanowires to form only a single orientation along the [1 -1 0] direction. For ARPES studies such an off-cut angle is highly desirable, as without it the signal obtained would be averaged over all three domains, thus giving rise to multiple overlapping copies of the bands, making analysis of the band structure difficult.

The Si wafers used (MaTeck, Berlin) were p-doped with Boron and had a resistivity of 0.075-0.085 Ω cm. The preparation of the substrate followed the procedure outlined above for Si(111) surfaces. Following this, In was evaporated from a water-cooled Knudsen type evaporation source, built at the Fritz Haber Institute, employing a boron nitride crucible heated by wire coils. The sample was at room temperature during evaporation. Approximately 1.5 ML of In were evaporated at a rate of around 0.05 ML per minute. The sample was then turned 180° to face the LEED optics, and annealed at 500°C, which slowly removes the excess In. By monitoring the development of the surface structure with live LEED, it is possible to determine with ease when the optimum coverage (1 ML) has been reached, as the LEED pattern changes drastically in the nanowire phase. This was done with reference to the low coverage phase diagram [Kra97]. The coverage of the nanowires across the sample surface can also be checked, to ensure that a large homogeneous phase is formed. The LEED pattern obtained from a well ordered 1 ML nanowire phase is shown in Fig. 4.15.

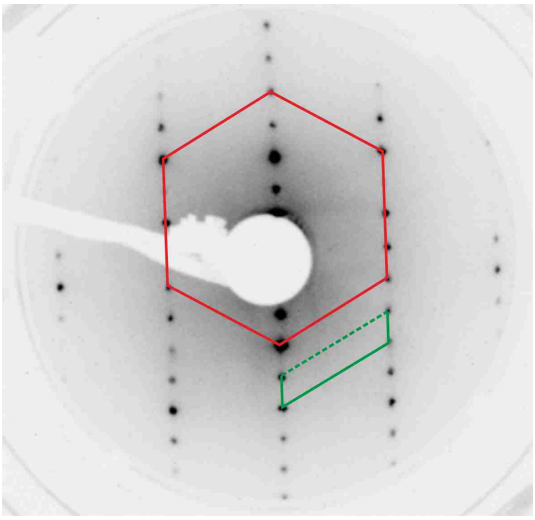

Figure 4.15: LEED image of In/Si(111) nanowires at 1 ML of In coverage on a 2° offcut substrate obtained at 80 eV electron energy. A single rotational domain with long range order is evidenced by the anisotropy of the spot orientations and their sharpness. The 1x1 unit cell is marked by the red hexagon, and the 4x1 surface reconstruction by the green rhomboid.

4.5.4 Preparation of $NbSe_3$

Crystals of $NbSe_3$ were grown and characterised by H. Berger (EPFL, Switzerland). This section briefly reviews the growth process and discusses the cleavage of $NbSe_3$ under UHV conditions.

Crystal Growth of $NbSe_3$

Single crystals of $NbSe_3$ are grown by a vapour transport method, as reviewed by Lévy and Berger [Lév83]. This method consists of sealing the component elements within a glass ampoule and heating them to produce a chemical reaction. In order to produce larger crystals, a chemical transport reaction via a transfer material is employed, in which the elemental components form an intermediate compound with the transport material. In many cases, including that of $NbSe_3$, iodine or chlorine are the most effective transport agents. By applying a heat gradient to the ampoule, the mixed phase of components plus transport can be spatially separated from the target solid. This can be understood by summarising the reaction in a simplified manner as:

$$NbSe_3 + I_2 \Longleftrightarrow \text{Transport compound} + \text{Heat}$$

When the reaction between the solid and the transport agent is exothermic, as in the example above, the target solid is transported from the cooler to the hotter end of the reactor ampoule, due to le Châtelier's principle. That is, by adding more heat, the reaction is driven towards the target solid phase. Repeated vapour transport cycles ensures high quality sample growth. The resulting crystals form a fibre-like mass. Typical dimensions of a single strand are 20 x 500 μm^2, with lengths of up to a few cm.

Cleavage of $NbSe_3$

In order to obtain clean, homogeneous surfaces for investigation with ARPES, $NbSe_3$ crystals were cleaved in UHV. Due to the small size and fragility of the fibres, a special sample holder was designed to maximise the chances of obtaining a good cleave; the key idea being to mimic the shape of the long, thin fibres. A schematic of the sample holder design is shown in Fig. 4.16 for different projections. $NbSe_3$ fibres were glued to the phosphor bronze sample holder using a silver-based epoxy (EPO-TEK E4110). The electrical and thermal conductivity are appropriate for avoiding charging of sample during ARPES experiments and for efficient cooling. Great care was taken when glueing crystals to the sample holder, as even small forces from tweezers could cause the crystal to split, or distort and break.

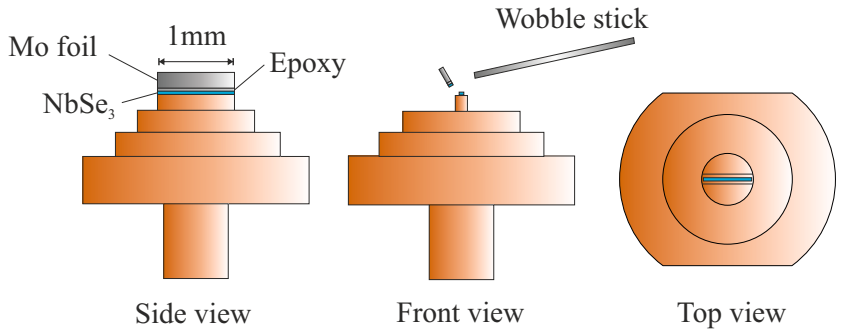

Figure 4.16: Phosphor bronze sample holder for $NbSe_3$ shown for side, front and top projections. The Mo top post is removed via wobble stick in the UHV chamber, exposing a clean surface.

To further enhance the chances of cleaving as large a portion of the sample as possible, a small piece of molybdenum foil was used as a cleaving post. This had the advantage of matching the sample dimensions better than a traditional cleaving post, and in addition applied a more homogeneous force across the sample surface. Alignment of the sample is straightforward, as the physical structure strongly reflects the chain-nature of the crystals. $NbSe_3$ cleaves in the (bc) plane with the b-axis along the wires being parallel to the long edge of the sample, and the c-axis perpendicular to it (see Fig. 4.17).

The cleave quality was inspected *in situ* with ARPES, and additionally with an optical microscope once the sample had been removed from UHV. Microscope images in Fig. 4.17 show examples of $NbSe_3$ crystals a) before cleaving b) with Mo top post and c)-f) post cleave and removal from UHV. While the majority of cleaves were successful, panel c) shows an example where the majority of the $NbSe_3$ was not cleaved, exposing only a tiny corner of clean surface. Conversely in panel f) the crystal has been almost entirely removed along with the top post, leaving only a few strands of material on the sample holder. Panels d) and e) show examples of well cleaved surfaces on which high quality data was obtained.

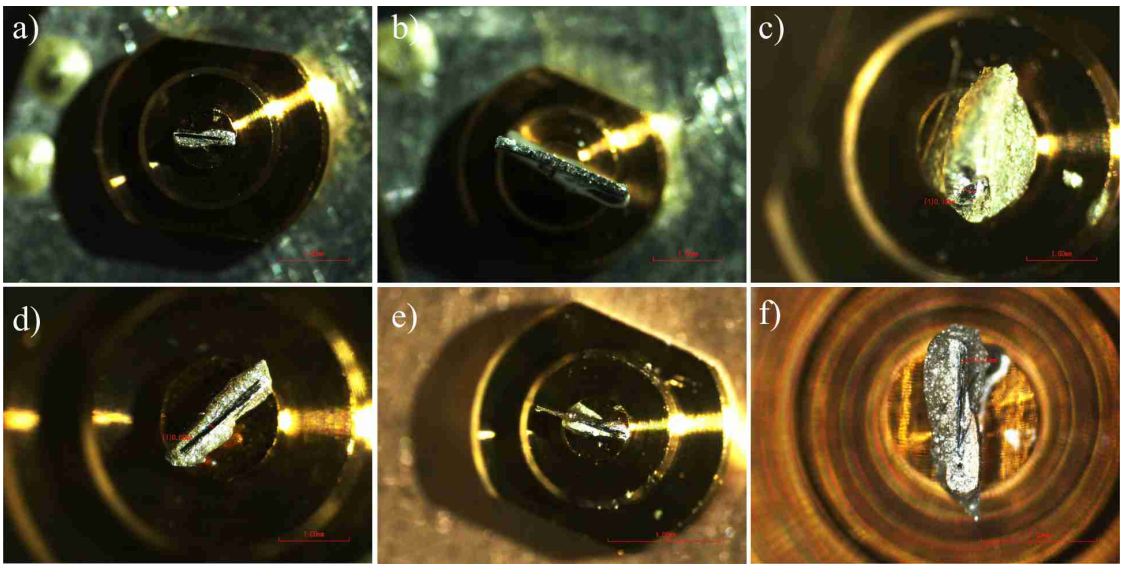

Figure 4.17: a) Optical microscope images of $NbSe_3$ crystals prior to cleaving and b) with Mo cleavage post mounted on top. c)-f) Exposed $NbSe_3$ surfaces after cleaving in UHV.

4.5.5 Preparation of Cr/W(110) Thin Films

In order to obtain clean Cr surfaces for trARPES studies, thin films were grown *in situ* on a W(110) substrate by Molecular Beam Epitaxy (MBE). Thin film growth offers the advantage that by an appropriate choice of substrate one can obtain the desired crystal orientation that may be difficult to obtain as a clean single crystal. In particular the (110) surface was chosen due to the fact that the SDW is not quantised in the surface normal direction, as on a (100)-orientated film [Rot05]. In addition the effects of the parasitic CDW (2nd harmonic of the SDW) is reduced on the (110) surface [Bra00]. The growth of Cr-films on W(110) and the SDW phase diagram thereof have previously been characterised with LEEM, LEED and ARPES [Rot05].

Preparation of W(110)

Single crystals of W(110) are cleaned by a cyclic procedure: first the crystal annealed at 1000 K in an oxygen atmosphere for 30 mins, following which a high temperature flash of (15 s) to above 2300 K is carried out [Bod07]. The annealing step removes carbon from the surface as CO or CO_2 but at the same time causes it to oxidise. The desorption of the resulting tungsten oxides is achieved by the flashing process. Repeated annealing and flashing cycles were carried out until a clean surface was obtained. A typical LEED pattern of a clean W(110) surface is presented in Fig. 4.18a.

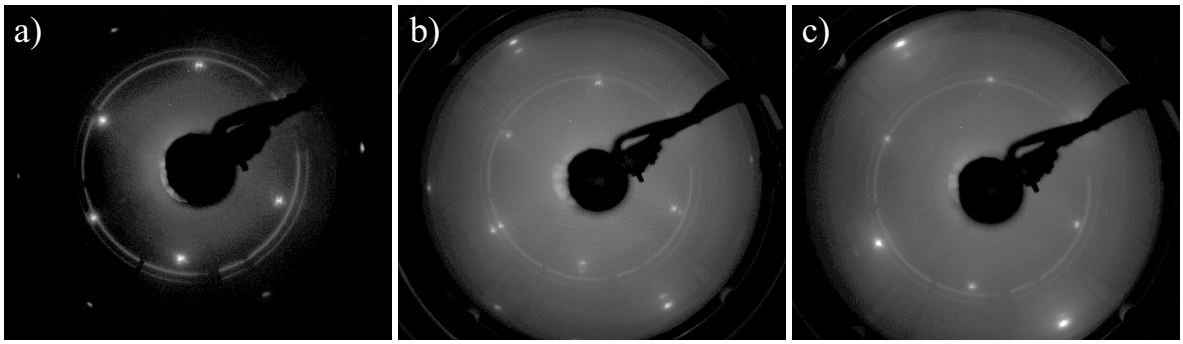

Figure 4.18: LEED images obtained at 165 eV during Cr/W(110) preparation. a) Clean W(110) substrate after flashing and annealing cycles b) Low coverage phase around 3 nm of Cr on W(110) where Bragg reflections from both Cr and W lattices are present and c) Cr film around 7nm. The rings in the images are due to the electron lens construction of the LEED. The electron gun can also be seen extending from the centre of the image to the upper right corner.

Growth and Characterisation of Cr Films

Once a clean substrate had been obtained, Cr was evaporated from an electron-beam evaporator calibrated with a quartz micro-balance. The substrate was held at room temperature during evaporation, following which the film was annealed to 850 K. According to previous LEEM data [Rot05], at low coverages Cr films form via a Stranksi-Krastinov growth mode i.e. initial growth develops in the form of islands which expand until a complete monolayer (ML) is formed. Layer growth continues until around 3 ML at which point 3D islands start to grow. At coverages between approximately 1 nm and 4 nm diffraction spots due to both Cr and W lattices are observed, as in Fig. 4.18b resulting from a mixted phase of (1x1)-Cr/W(110) plus higher coverage Cr islands [Rot05]. At higher coverages only the Cr spots remain, as shown in Fig. 4.18c.

5 Electronic Structure of quasi-1D $NbSe_3$

In 1D reduced screening and a restricted phase space for scattering heavily impact the electronic properties of materials due to the ensuing strong correlations. As a result, the well-known concept of Fermi liquid (FL) breaks down, and may be replaced by the Tomonaga-Luttinger liquid (TLL) [Tom50, Lut63], in which correlation functions display power-law behaviour. The fundamental excitations of a TLL are collective bosonic modes carrying only spin or charge, rather than electron-like fermionic quasi-particles [Voi93a, Voi94, Gia03]. Furthermore, long-range ordered phases are not stable in a purely 1D system as a result of quantum and thermal fluctuations [Mer66]; thus a dimensional crossover should be a prerequisite for a 1D system to enter an ordered phase, as occurs in a number of quasi-1D materials [Grü88, Grü94b]. This is distinguished by a crossover energy, E_C, or temperature above which excitations exhibit 1D character, while low-energy excitations behave as in a FL [Cas94, Arr99, Bie01]. In photoelectron spectroscopy experiments, spectral weight depletion near the Fermi energy has been interpreted as a characteristic of TLL behaviour in a variety of systems [Dar91, Gwe04], also at very low temperatures [Ish03, Oht15]. In contrast, in quasi-1D systems, power-law correlations are expected to be observed only above the dimensional crossover energy or temperature. To date, the properties of the low-temperature phase, in particular how strong one-dimensional correlations are imprinted on it, remain poorly understood [Gia04].

In this chapter we report a high-resolution ARPES study of $NbSe_3$ single crystals, including the evolution of the electronic structure over a wide temperature range and a mapping of the Fermi surface. We find evidence of a dimensional crossover from 1D to 3D as a function of decreasing energy and temperature. CDW gaps in the electronic structure are observed at low temperatures, occurring at momenta consistent with x-ray data and reproduced by theoretical simulations. Conversely at high temperatures a power-law suppression of the spectral function is observed, suggestive of 1D behaviour. From the warping of the Fermi surface measured at low temperature, a crossover energy scale of around $E_C \approx 110$ meV (1250 K) is extracted based on a tight-binding model. This is corroborated by an analysis of the density of states which reveals 1D behaviour only above E_C.

Electronic structure calculations have been carried out by C. Berthod (University of Geneva). The results have been published in Nicholson *et al.*, *Phys. Rev. Lett.*, 118, 206401 (2017) [Nic17].

5.1 Low Temperature Electronic Structure

Experimental Details

$NbSe_3$ is an archetypical linear-chain compound, which undergoes CDW transitions at $T_1 = 145$ K and $T_2 = 59$ K [Ong77] with incommensurate modulation wave vectors $\boldsymbol{q}_1 = (0, 0.243, 0)$ and $\boldsymbol{q}_2 = (0.5, 0.263, 0.5)$ respectively, in units of the reciprocal lattice parameters (a^*, b^*, c^*) [Fle78, Hod78]. The occurrence of the CDW has been ascribed to Fermi-surface nesting [Sch01, Sch03]. Despite intense research on $NbSe_3$ (for an overview see Refs. [Grü88, Mon12]), detailed information about the electronic dispersion is limited to only a few studies [Sch01, Sch03] by ARPES, in part due to the fragile nature of the micro-ribbon crystals. Recent work by scanning tunneling microscopy showed a surface CDW transition temperature higher than that in bulk, and confirmed the higher dimensional nature of this material at low temperatures [Bru09, Bru10] which had previously been observed in x-ray scattering data [Mou90]. In contrast, intriguing reduced dimensional behaviour at the surface has also been revealed as signatures of soliton behaviour [Bra12].

Single crystals of $NbSe_3$ of typical dimensions 20×500 μm^2 were cleaved in vacuum at a pressure lower than 5×10^{-11} mbar. ARPES measurements were carried out at the IO5 beam line of the Diamond Light Source [Hoe17] over a temperature range 6.5–260 K with photon energies 20–40 eV (linear horizontal polarization). The angular and energy resolution were 0.2° and 10 meV, respectively. All results presented here have been reproduced by measurements on multiple samples.

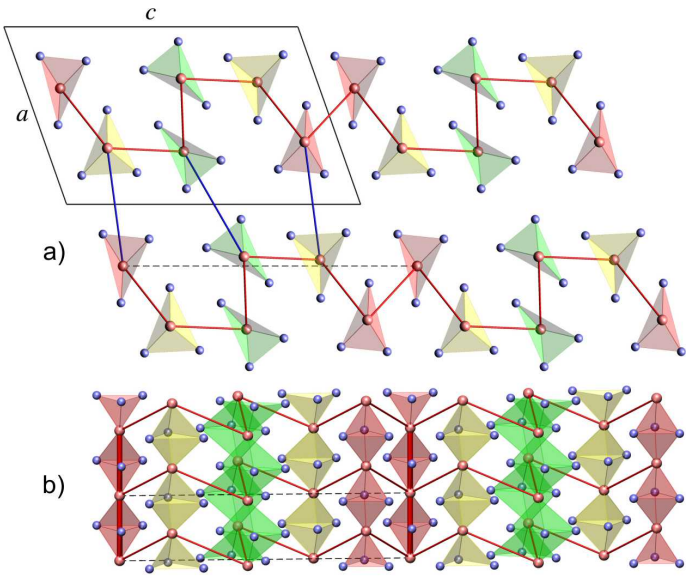

Figure 5.1: (a) Top view (ac plane) and (b) side view (bc plane) of the $NbSe_3$ crystal with Nb atoms in red and Se atoms in blue. The unit cell contains six chains running along the b axis, forming three pairs related by inversion symmetry and highlighted in red (denoted I in Fig. 1a of the main text), yellow (II), and green (III). Solid lines: unit cell in the ac plane; dashed lines: unit cell in the bc plane; thick red cylinders: strong bonds with t_b overlap integral along the chains; thin red cylinders: hopping path along the c axis leading to the effective t_c amplitude; thin blue cylinders: weak bonds along the a axis.

A schematic of the crystal structure of $NbSe_3$ is presented in Fig. 5.1a, and comprises three distinct triangular prism chains running parallel to the b axis. The three chain types are characterised by the relative size of the Se-Se bonds along the b axis [Mon12]; type III has the shortest bond length (2.37 Å) corresponding to strong Se-Se bonds while type II chains have a relatively large Se-Se distance (2.91 Å) and the weakest bonds. Type I chains are intermediate in bond length (2.49 Å) and strength. Transport along and across the chains is mediated by Nb orbitals, which have a much larger overlap parallel to the b axis (along the chains) compared with the perpendicular direction.

5.1.1 Fermi Surface

The Fermi surface obtained by ARPES in the bc-plane is shown in Fig. 5.2a and may be compared with that calculated by Density Functional Theory (DFT) in Fig. 5.2b (calculations as in Ref. [Sch01] using the WIEN2k code [Bla01]). While not all five sheets predicted by DFT are resolved at the Fermi level, Fig. 5.3b reveals five bands dispersing up to E_F in agreement with the DFT predictions (see also below). The dispersion is strongly anisotropic, revealing the quasi-1D nature of the electronic structure. Warping of the Fermi-surface sheets along the $k_{\|c}$ direction (along the c-axis in real space) reveals the presence of significant inter-chain coupling at these low temperatures.

The dispersion of the Fermi surface normal to the sample surface is presented in Fig. 5.2c. This is obtained by a scan of the photon energy between 20 and 40 eV, and using the relation

$$k_{\perp\text{surface}} = \frac{1}{\hbar}\sqrt{2m(E_{\text{kin}}\cos^2\theta + V_0)}, \tag{5.1}$$

where terms are defined as in Ref. [Dam04]. An inner potential $V_0 = 12$ eV was assumed. The warping of the Fermi surface reveals the quasi-1D nature of the states also in this plane. The warping in this direction is certainly not more than those presented in the bc-plane, confirming the quasi-1D nature of $NbSe_3$.

5.1.2 Electronic Dispersion in the bc-plane

The dispersion of the bands along $k_{\|b}$ at selected $k_{\|c}$ values is given in Figs. 5.3a–c. Second derivative plots are presented in Figs. 5.3d–f in order to highlight weak features. A number of features are visible which were not resolved in previous studies [Sch01, Sch03]. At $k_{\|c} = 0$ Å^{-1} we observe three bands dispersing symmetrically around the Γ point: the outer band with minimum at -550 meV and two inner bands with minima at -260 meV. All three bands appear to cross E_F, although the spectral weight strongly decreases at low binding energies. A very small pocket directly at E_F around Γ is also observed, corresponding to the blue intensity in Fig. 5.2a. At $k_{\|c} = 0.2$ Å^{-1} three inner bands can be distinguished. At $k_{\|c} = 0.35$ Å^{-1}, in the second Brillouin zone, strong effects of the varying photoemission matrix element lead to different relative intensities of the bands.

We note that the shape of the innermost band in Fig. 5.3e appears to bend away from the Fermi level at $k_{\|b} = 0.11$ Å^{-1}, consistent with previous observations which assigned this behaviour to the $\boldsymbol{q}_2$ CDW [Sch03]. We caution that such behaviour may

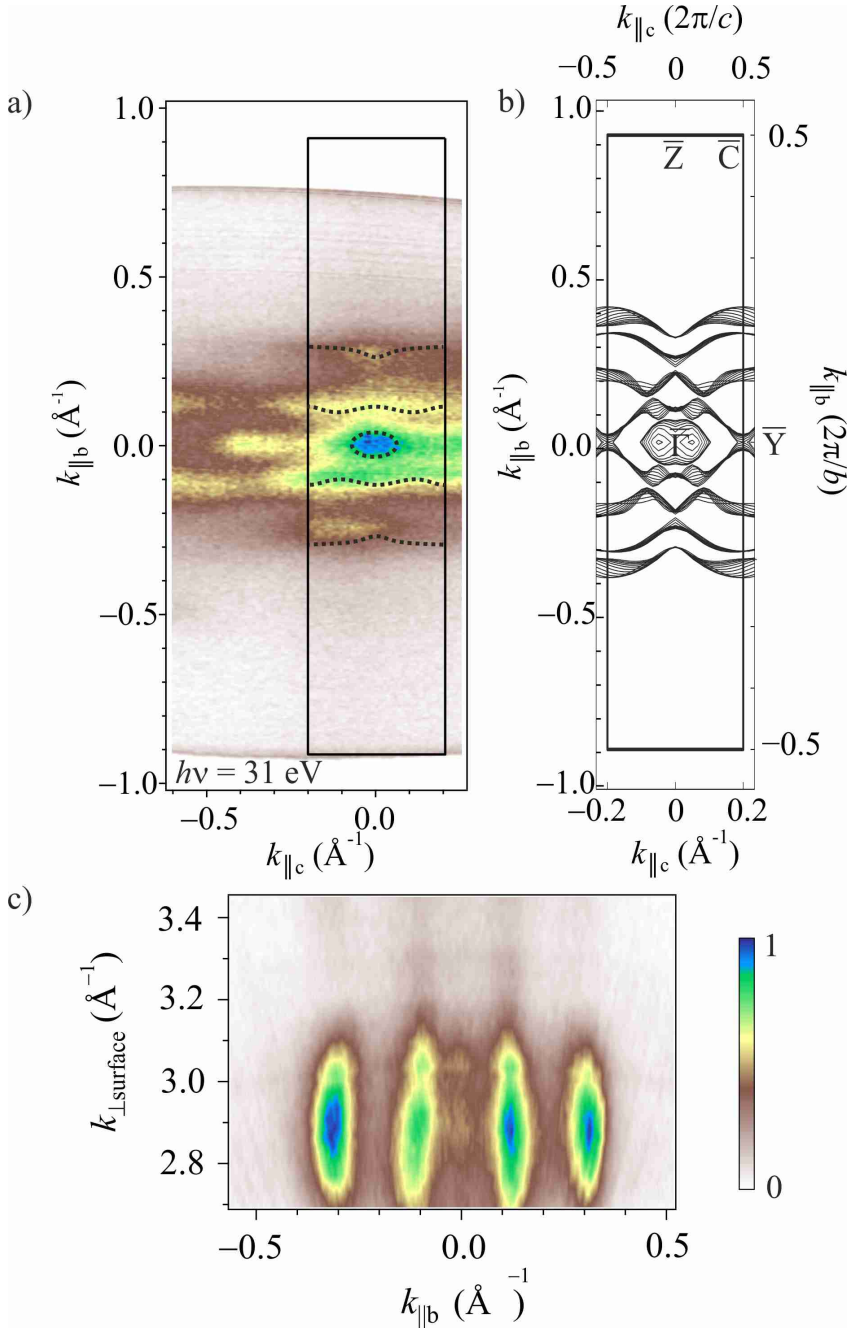

Figure 5.2: (a) Fermi surface obtained at 8 K with 31 eV photon energy in the b^*c^* plane. The rectangle shows the first Brillouin zone as in (b). Dotted lines are guides to the eye. (b) DFT Fermi-surface contours in the b^*c^* plane for various momenta covering the full Brillouin zone along a^*. (c) Dispersion of the Fermi surface in the plane perpendicular to the sample surface defined by the bc-plane.

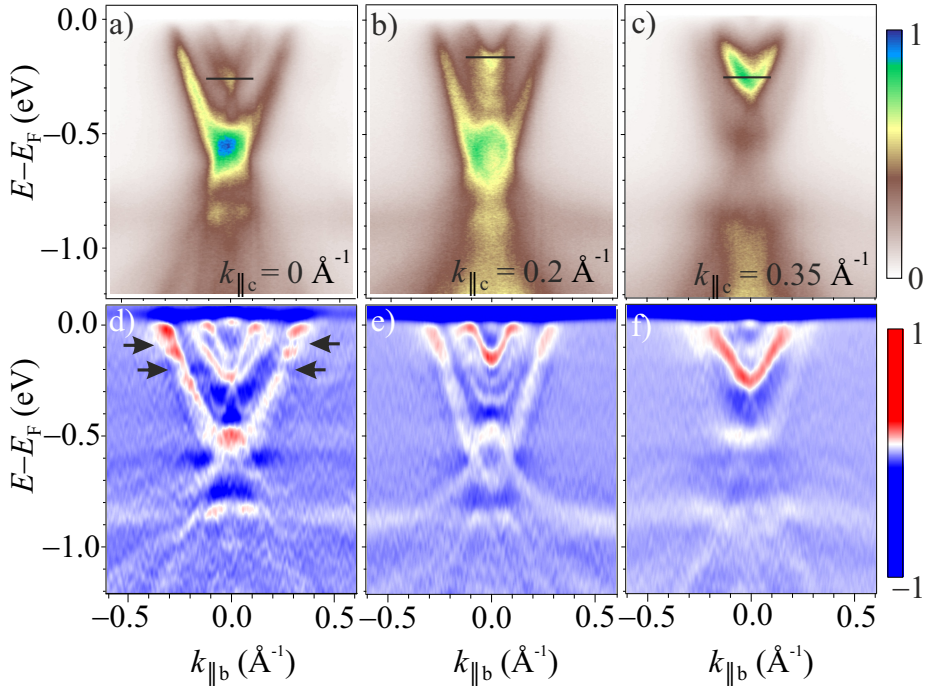

Figure 5.3: (a)–(c) Band dispersion along $k_{\|b}$ obtained at 6.5 K with 31 eV photon energy at the marked $k_{\|c}$ values. Black bars indicate the expected position of the band bottom based on a cosine dispersion along $k_{\|c}$ with bandwidth $4t_c = 108$ meV (see text). (d)–(f) Corresponding second-derivative plots. The position of the CDW gaps are marked in (d).

Table 5.1: Comparison of Fermi wave vectors (Å^{-1}) obtained from ARPES and DFT along two high-symmetry directions.

	Γ–Z		Y–C	
	Expt.	DFT	Expt.	DFT
$k^1_{F\|b}$	0.27(3)	0.3	0.27(5)	0.31
$k^4_{F\|b}$	0.10(6)	0.09	0.09(5)	0.12
$k^5_{F\|b}$	0.00(4)	0.07	0.00(6)	Above E_F

result from artefacts due to the second-derivative image processing in the presence of multiple bands and the Fermi edge. An analysis of energy and momentum distribution curves confirm the absence of a back-folded dispersion [Nic17]. While we cannot rule out gaps at E_F that are hidden by the depletion of spectral weight, our data and calculations reveal that the CDW wave vectors $\boldsymbol{q}_1$ and $\boldsymbol{q}_2$ open gaps only below E_F, which speaks against a Fermi-surface instability.

In Fig. 5.4, we present a comparison of the ARPES band structure with the band structure obtained from DFT calculations. Cuts are shown along the Γ–Z and Y–C directions. Both the positions and band widths of the experimental bands are in overall good agreement with the DFT, which points to minimal renormalization effects as a result of e.g. electron-electron interactions. The Fermi wave vectors of experiment and DFT are compared in Table 5.1 and confirm the good agreement. The 5 bands crossing the Fermi level in the DFT calculation are numbered 1–5 from outer to inner. Our calculations indicate that all bands close to the Fermi level have

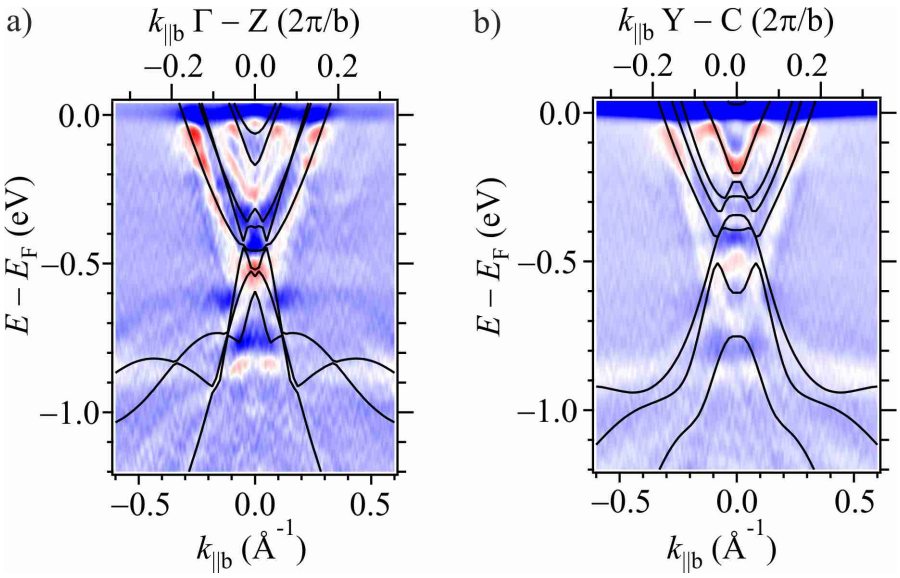

Figure 5.4: ARPES second derivative along Γ–Z (a) and Y–C (b) overlaid with DFT calculations along the respective high-symmetry lines.

predominantly Nb *d*-orbital character (data not shown).

5.1.3 Charge Density Waves

Fig. 5.3d further reveals a loss of intensity in the outer band at specific energies which appear symmetrically on both sides of Γ (arrows), further emphasised in Fig. 5.5a. To ensure these are not artefacts of the image processing, we present in Fig. 5.5c energy distribution curves (EDCs) of the raw data at the momenta corresponding to these features. Weak but distinct two-peak structures are observed, centered around $E_1 = 210$ meV and $E_2 = 120$ meV below E_F, which we identify with gaps caused by the $\boldsymbol{q}_1$ and $\boldsymbol{q}_2$ CDW super-periodicities, respectively. The scattering vectors deduced from our data, 0.43 Å^{-1} and 0.47 Å^{-1}, match within errors the b^* components of the $\boldsymbol{q}_1$ and $\boldsymbol{q}_2$ modulation obtained by x-ray diffraction [Fle78]. This is strong evidence that these gap features occur as a result of the CDWs. The formation of both gaps in the outer band and the observation of both modulations on all chains by STM [Bru09, Bru10] show that Nb orbitals on the three types of chains are coupled and feel both CDW potentials. In addition, as the temperature is increased, the gap features become weaker up to 50 K and then disappear, as shown for the $\boldsymbol{q}_1$ gap in Fig. 5.5d. The fact that the CDW gaps disappear before the bulk transition temperature should not be taken as evidence for a lower CDW transition temperature at the surface, but more likely due to phonon broadening washing out the signal as T increases. The occurrence of the gap at 210 meV agrees with that observed in Refs. [Sch01, Sch03]. It seems likely that the outer band and the two inner bands relate to the two bands observed in Ref. [Sch01], but the dispersion observed previously may include some artifacts, as our high resolution data does not reproduce it. In particular, the large backfolding close to E_F is not reproduced in our data at any temperature. Additionally it does not appear to be reproduced in Ref. [Sch03]. Most likely the differences arise from the higher resolution and spot size available in our study, which have become available with the improvements in

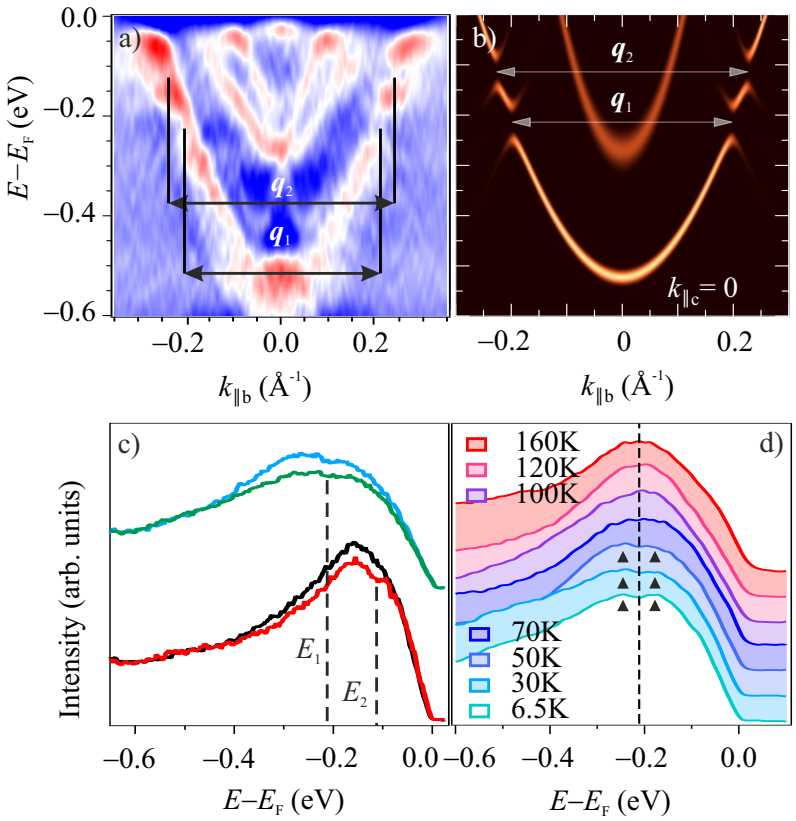

Figure 5.5: (a) Zoom of the data from Fig. 5.3d including the b^*-axis component of the $\boldsymbol{q}$ vectors for the two incommensurate CDWs: $q_{1,b^*} = 0.435$ Å^{-1}; $\boldsymbol{q}_{2,b^*} = 0.468$ Å^{-1} as measured by x-ray diffraction [Fle78, Hod78]. (b) Simulation of the spectral function in a CDW system with ordering vectors q_{1,b^*} and q_{2,b^*} (see text). (c) EDCs of the raw ARPES data at $k_{\|b} = 0.21$ Å^{-1} (blue), $k_{\|b} = -0.20$Å $^{-1}$ (green), $k_{\|b} = 0.25$ Å^{-1} (red) and $k_{\|b} = -0.24$ Å^{-1} (black). The center of the CDW gaps is marked by dashed lines. All data are taken at $k_{\|c} = 0$ and $T = 6.5$ K. (d) Temperature dependence of the $\boldsymbol{q}_1$ gap at $k_{\|b} = 0.21$ Å^{-1}.

ARPES hardware in the intervening almost two decades since the previous studies. Given the particularly delicate nature of $NbSe_3$ crystals, and their small size, these are not trivial considerations.

A calculation of the spectral function for a two-band tight-binding model with a two-component CDW is presented in Fig. 5.5b and described in more detail in Appendix D. The CDW potential opens gaps at momenta connected by the ordering vectors. The resulting spectral function shows a suppression of spectral weight at the energies that satisfy the scattering condition $E_{n\boldsymbol{k}} = E_{n\boldsymbol{k}+\boldsymbol{q}_{1,2}}$. For the second band this condition is only met at positive energy and no signature of the CDW is therefore seen in the occupied states. It is evident from this simulation that the influence of the CDW on the spectral function can be rather weak and the inner band is not affected at all.

5.2 Dimensional Crossover

5.2.1 Tight-Binding Model

We now analyse the Fermi-surface in more detail, in order to determine the relative hopping amplitudes along and across the Nb-chains and hence quantify the anisotropy in the system. It is clear that the dispersion in the $(k_{\|\mathrm{b}}, k_{\|\mathrm{c}})$ plane is strongly anisotropic (i.e. quasi-1D), with a finite warping along $k_{\|\mathrm{c}}$ resulting from interchain hopping (Fig. 5.2a and Fig. 5.7a). Such a quasi-1D dispersion is minimally described by the tight-binding model

$$E_{\boldsymbol{k}} = -2t_b \cos(k_{\|\mathrm{b}} b) - 2t_c \cos(k_{\|\mathrm{c}} c) - \mu, \tag{5.2}$$

in which t_b and $t_c \ll t_b$ are the effective hopping amplitudes along the chains and along the c axis, respectively, and μ is the chemical potential. $b = 3.48$ Å and $c = 15.56$ Å are the lattice constants along the corresponding directions. This is a minimal effective model which does not take full account of the $NbSe_3$ unit-cell structure. The latter involves six formula units per cell as depicted in Fig. 5.1. The dispersion along the c axis implies hopping through six Nb–Nb bonds running across the unit cell, leading to an effective hopping amplitude t_c from one unit cell to the next. The length of these bonds varies between 4.2 and 4.4 Å, slightly longer than the strong Nb–Nb bonds along b. The dispersion along the a axis is more strongly suppressed due to larger distances between the Nb atoms (6.5–6.6 Å).

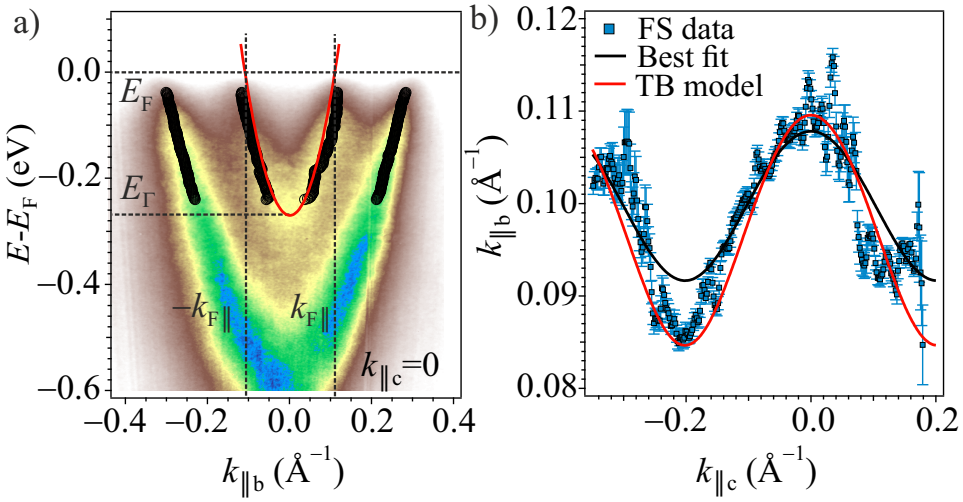

Figure 5.6: (a) ARPES intensity vs $E - E_F$ and $k_{\|\mathrm{b}}$ at $k_{\|\mathrm{c}} = 0$, with the position of the bands extracted from the MDCs overlaid in black. The minimum and Fermi points are shown for the inner band. The solid red line is the tight-binding model discussed in the text. (b) Position of the inner-band Fermi surface (upper branch) extracted from MDC fits overlaid with the tight-binding model (red) and a Fermi-surface fit (black).

The data that we have used in order to determine the tight-binding parameters of the model are presented in Fig. 5.6. We focus on the inner band, where the Fermi-surface warping is most clearly observed (Fig. 5.7a). Fig. 5.6a shows the dispersion at $k_{\|\mathrm{c}} = 0$ and Fig. 5.6b shows the extracted Fermi surface of the inner

band around $k_{\|\mathrm{b}} = 0.1$ Å^{-1}. The Fermi surface positions are extracted from the data of Fig. Fig. 5.7a by fitting vertical cuts through the 2D data set.

As an effective model, we expect (5.2) to reproduce the bandwidth along $k_{\|\mathrm{b}}$ and the warping of the Fermi surface. We determine the three tight-binding parameters (t_b, t_c and μ) from the conditions that (i) the energy at the band bottom for $k_{\|\mathrm{c}} = 0$ is $E_\Gamma = -0.262$ eV as shown in Fig. 5.6a; (ii) the Fermi wave vector at $k_{\|\mathrm{c}} = 0$ is $k_{\mathrm{F}\|\mathrm{b}} = 0.108$ Å^{-1} as observed in Fig. 5.6b; and (iii) the Fermi-surface warping is given by the peak-to-peak value observed in Fig. 5.6b, namely $\Delta k_{\|\mathrm{b}} = 0.0247$ Å^{-1}.

At $k_{\|\mathrm{c}} = k_{\|\mathrm{b}} = 0$, the expression (5.2) simplifies to

$$E_\Gamma = -2t_b - 2t_c - \mu. \tag{5.3}$$

The Fermi point at $k_{\|\mathrm{c}} = 0$ satisfies the equation

$$0 = -2t_b \cos(k_{\mathrm{F}\|\mathrm{b}} b) - 2t_c - \mu. \tag{5.4}$$

Inserting the values of E_Γ, $k_{\mathrm{F}\|\mathrm{b}}$, and b in Eqs. (5.3) and (5.4), we obtain $t_b = 1.88$ eV and $\mu = -3.49$ eV $- 2t_c$. Next we make use of the Fermi-surface warping. The extremal values of $k_{\|\mathrm{b}}$ occur for $\cos(k_{\|\mathrm{c}} c) = \pm 1$. Rearranging Eq. (5.2) for $E_{\boldsymbol{k}} = 0$, we therefore arrive at:

$$\Delta k_{\|\mathrm{b}} = \frac{1}{b}\left[\cos^{-1}\left(\frac{\mu - 2t_c}{2t_b}\right) - \cos^{-1}\left(\frac{\mu + 2t_c}{2t_b}\right)\right]. \tag{5.5}$$

Substituting the known values and the relation $\mu = -3.49$ eV $- 2t_c$ leads to the solution $t_c = 0.027$ eV. The resulting tight-binding dispersion is displayed in Figs. 5.6a, 5.6b and 5.7a as a solid red line. This set of tight-binding parameters gives a good account of the Fermi-surface warping.

The transverse bandwidth $4t_c \equiv E_\mathrm{C}$ defines the energy (temperature) scale at which the system crosses over from 1D to higher dimensional behaviour. Excitations with energies $E \gg E_\mathrm{C}$ are insensitive to the dispersion along c and exhibit 1D character, with the typical power laws expected for a TLL, while excitations with $E < E_\mathrm{C}$ behave as in a FL. From the analysis presented above we extract a value $t_c = 27$ meV. This implies a typical energy scale $E_\mathrm{C} = 108$ meV (1250 K) above which 1D signatures should be observed. A simple cross check of this value can be obtained by comparing the relative band bottoms throughout the Brillouin zone along the $k_{\|\mathrm{c}}$ direction with that expected from a bandwidth of $4t_c$. These are presented in Fig. 5.3a-c by black horizontal bands and show good agreement.

5.2.2 Analysis of the Spectral Function

We now compare the energy scale of the dimensional crossover extracted from the warping of the Fermi surface with the energy dependent behaviour of the Density of States (DOS), which should similarly reflect the dimensional crossover above the characteristic energy E_C.

In Fig. 5.7b we show the $k_{\|\mathrm{b}}$-integrated ARPES intensity at $k_{\|\mathrm{c}} = 0$ within 400 meV of E_F and for different temperatures. This quantity approximates the DOS multiplied by the Fermi function, apart from inessential corrections associated with the finite experimental resolution and weak $k_{\|\mathrm{c}}$ dispersion and assuming constant matrix elements as a function of temperature. We have checked that integrating

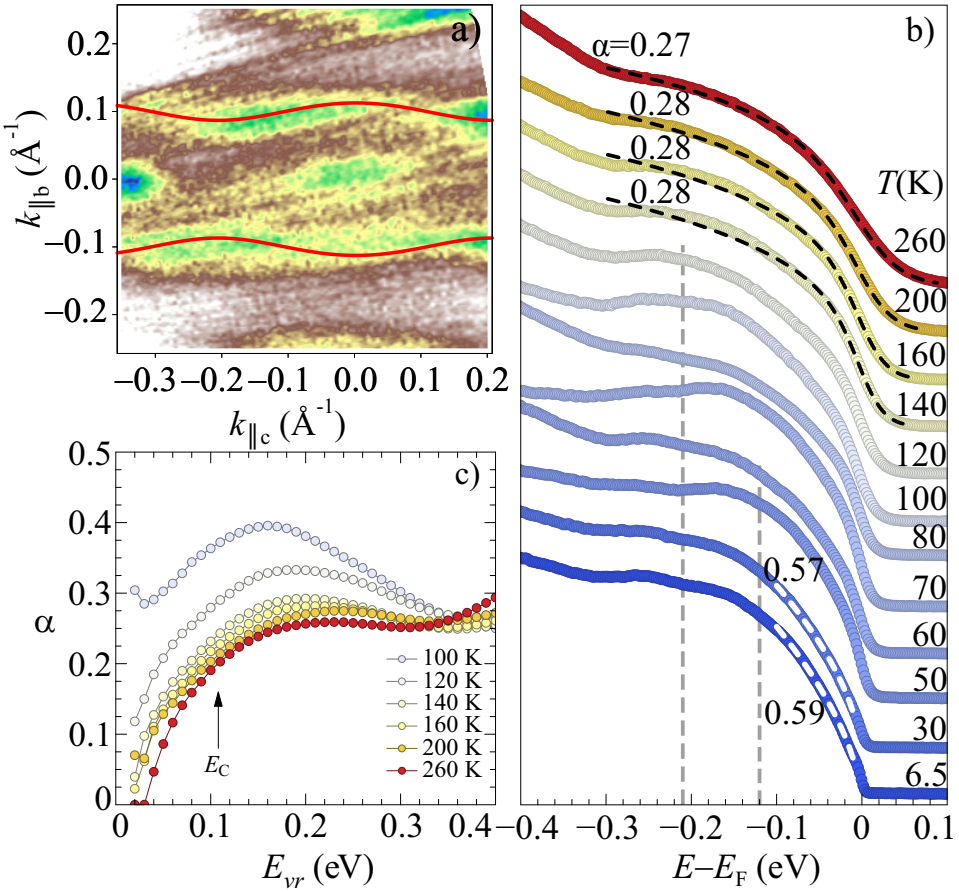

Figure 5.7: (a) Fermi surface obtained at $h\nu = 22$ eV, overlaid with the tight-binding model described in the text. (b) $k_{\parallel b}$-integrated ARPES intensity at $k_{\parallel c} = 0$ for various temperatures. White dashed lines indicate simple power laws with exponents close to 0.6; black dashed lines show best fits to a TLL model spectral function with $\alpha \approx 0.25$; vertical dashed lines indicate the energies of the CDW gaps seen in Fig. 5.3d. (c) Energy-dependent exponent showing dimensional crossover at E_C for $T > T_1$.

over smaller k-ranges or at other $k_{\parallel c}$ values does not change the form of the DOS [Nicholson 2017]. At the lowest temperatures, the DOS suppression near E_F is markedly different from the expected Fermi edge and resembles a power law. We rule out CDW gaps as a possible explanation for this anomalous suppression of spectral weight: the CDW gaps seen at finite energy in our data have a typical peak-to-peak size of 70 meV (Fig. 5.5c), while the DOS suppression occurs over a much wider energy range. Furthermore, the signatures of the CDW in the DOS are rather weak: they can be identified near −210 meV and −120 meV in the momentum-integrated ARPES data below the CDW temperatures T_1 and T_2, respectively (Fig.5.7b). A complete gapping of the Fermi surface would also be inconsistent with the fact that $NbSe_3$ remains metallic even at these low temperatures [Ong77].

The power-law depletion evokes a TLL where the DOS is suppressed like $|E-E_F|^\alpha$ at low energy due to the disappearance of single-particle excitations [Voi94]. The non-universal exponent $\alpha = (K_\rho + K_\rho^{-1} - 2)/4$ (see below) depends on the parameter K_ρ which measures the strength of interactions and varies between $0 < K_\rho \leqslant 1$. $K_\rho = 1$ ($\alpha = 0$) corresponds to a non-interacting electron system with flat DOS.

The microscopic description of a temperature-induced dimensional crossover requires minimally a quasi-1D Hamiltonian with a small transverse kinetic energy $t_\perp$. At $T \gg t_\perp$, we are in the 1D regime: the equivalent 1D Hamiltonian has only two parameters, an effective Fermi velocity and an effective Luttinger coefficient K_ρ which both depend on the parameters of the original quasi-1D Hamiltonian, including $t_\perp$. At $T \ll t_\perp$, we expect an anisotropic Fermi liquid (FL) with a featureless DOS (as the FL system is 2D). Therefore, the DOS evolves from a power law at high T to a constant at low T when going through a dimensional crossover. However, we are not aware of an analytical solution which would capture the evolution of the DOS in such a quasi-1D system as a function of the crossover parameter $T/t_\perp$. In a Tomonaga-Luttinger liquid (TLL), a similar evolution is achieved by varying K_ρ in the range $0 < K_\rho \leqslant 1$, and indeed an analytical expression is available for the temperature-dependent DOS of a TLL [Sch93]. Our analysis assumes that the dimensional crossover in the quasi-1D model as a function of $T/t_\perp$ and/or $E/t_\perp$ can be mapped onto a TLL to FL transition in a strictly 1D model with varying K_ρ. This is justified as when $T \ll t_\perp$ the system is effectively a 2D FL i.e. a renormalised free electron gas, which is the same as the TLL model in the limit $K_\rho = 1$. Thus α should decrease as a function of decreasing energy/temperature.

We therefore analyze the integrated ARPES intensity, as was already done in Refs. [Blu11, Oht15], using the expression

$$I(E,T) \propto T^\alpha \cosh\left(\frac{\varepsilon}{2}\right) \left|\Gamma\left(\frac{1+\alpha}{2} + i\frac{\varepsilon}{2\pi}\right)\right|^2 f(\varepsilon) * g(E). \tag{5.6}$$

$\varepsilon = E/k_\mathrm{B}T$, Γ is the Euler gamma function, and $f(x) = (e^x + 1)^{-1}$ is the Fermi distribution. The symbol $*$ stands for a convolution with the instrumental resolution, represented by a Gaussian $g(E)$ of width 10 meV (FWHM). The exponent α describes the asymptotic zero-temperature DOS of the TLL behaving as $|E|^\alpha$. It is related to the microscopic parameters K_ρ and K_σ controlling the algebraic decay of correlation functions in the charge and spin sectors, respectively, by [Gia03]

$$\alpha = \frac{K_\rho + K_\rho^{-1} + K_\sigma + K_\sigma^{-1}}{4} - 1. \tag{5.7}$$

For spin-rotation invariant systems like $NbSe_3$ we have $K_\sigma = 1$, such that $\alpha = (K_\rho + K_\rho^{-1} - 2)/4$ and we can deduce the value of K_ρ from the fitted exponent α:

$$K_\rho = 1 + 2\alpha - 2\sqrt{\alpha(\alpha+1)}. \tag{5.8}$$

In the pure 1D model (5.6), α relates to the strength of the microscopic interactions. Our interpretation is that the value of α obtained by fitting Eq. (5.6) to the DOS of a quasi-1D system like $NbSe_3$ can indicate the evolution from a 1D regime where $\alpha > 0$ to a 3D regime where $\alpha = 0$, as the temperature and/or the energy is lowered.

TLL signatures should be searched for at energies and/or temperatures larger than E_C. Our highest measured temperature (260 K) is well below the crossover scale ($E_\mathrm{C} \approx 110$ meV ≈ 1250 K), such that our whole data set can be regarded as being in a low-temperature regime with respect to the dimensional crossover. In the CDW state, the DOS at $E > E_\mathrm{C}$ is perturbed by the CDW gaps such that TLL signatures may be masked if present. We therefore look for the TLL power law at temperatures higher than $T_1 = 145$ K. The fits are performed in a variable energy

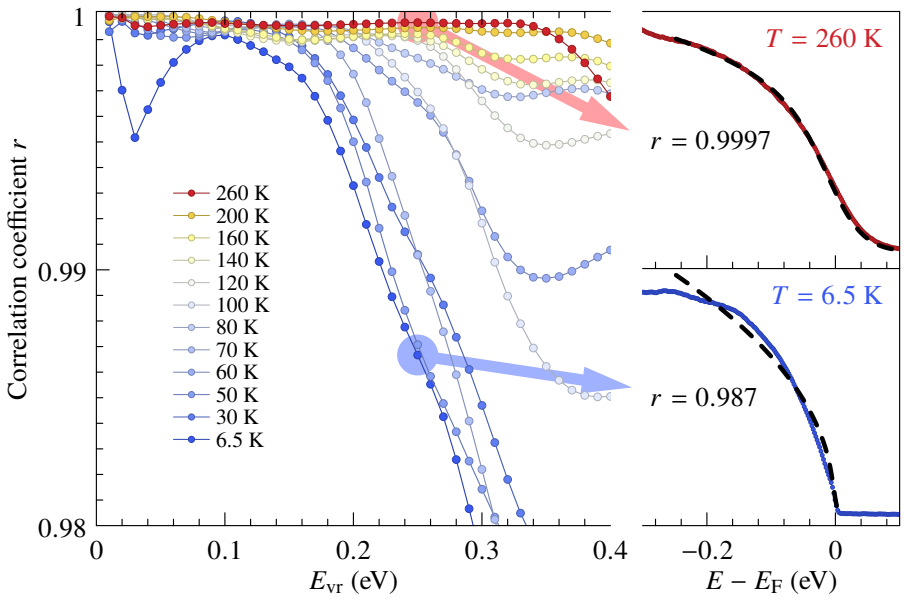

Figure 5.8: Correlation coefficient of the fit of Eq. (5.6) to the momentum-integrated ARPES intensity in the energy range $[-E_{\mathrm{vr}}, \min(E_{\mathrm{vr}}, 4k_{\mathrm{B}}T)]$. Two examples of fits with high and low correlation are displayed on the right.

range $[-E_{\mathrm{vr}}, \min(E_{\mathrm{vr}}, 4k_{\mathrm{B}}T)]$ around E_{F} and we extract the exponent α as a function of this range (Fig. 5.7c). At $E_{\mathrm{vr}} < E_{\mathrm{C}}$, the data approach a pure Fermi edge with $\alpha = 0$ (3D regime), while at $E_{\mathrm{vr}} > E_{\mathrm{C}}$, the fit yields a stable exponent $\alpha \approx 0.25$ ($K_\rho = 0.38$) over a broad energy range (1D regime). The fit includes all data at $E < E_{\mathrm{vr}}$ and therefore yields a continuous drop of α towards zero when reducing E_{vr} below E_{C}; this trend is observed at temperatures above 120 K. Such a decrease of α with decreasing energy is indeed expected based on our assumption of a mapping between the DOS crossover from 1D to 3D and the TLL model in the non-interacting limit.

An analysis of the fit quality (Fig. 5.8) shows that the best fits are obtained for an upper E_{vr}-bound between 0.2 and 0.3 eV. Beyond this the DOS upturn from -0.3 eV due to the band bottom at -0.6 eV means that the power-law analysis in this range is no longer appropriate. The Pearson correlation coefficient is plotted in Fig. 5.8 as a function of E_{vr} for all temperatures in our data set. We consider this fitting as meaningful only for temperatures higher than the highest CDW transition temperature (145 K) and energies higher than the dimensional crossover scale (110 meV) since below 100 K the data violates the assumption that α should tend to zero with reducing temperatures. In the higher temperature data the correlation coefficient is typically above 0.997. At low temperature, the fit worsens at large E_{vr} because of the CDW gaps in the DOS, while at low E_{vr}—where the fit quality improves due to reduced number of data points—the resulting exponent increases, revealing the inconsistency with the 1D model. As a result the curves of α vs E_{vr} in Fig.5.7c are not shown for $T < 100$ K.

Figure 5.7b shows the best fits with $E_{\mathrm{vr}} = 0.3$ eV and the corresponding TLL exponents for $T > 100$ K. For $T < T_1$, the fit deteriorates and the extracted exponent becomes strongly energy dependent due to the CDW gaps, while the exponent at low E_{vr} increases steadily with decreasing T due to the anomalous spectral-weight

suppression.

In the 1D Hubbard model, infinite U leads to $K_\rho = 0.5$, thus $K_\rho > 1/2$ for finite U, while $K_\rho > 1/8$ in the extended Hubbard model [Voi94]. The value 0.38 ($\alpha \approx 0.25$) therefore points to a moderate interaction and locates $NbSe_3$ far from an interaction-driven metal-insulator transition. In contrast, the apparent DOS exponent close to $\alpha = 0.6$ at low T (Fig. 5.7b) would indicate much stronger correlations with $K_\rho = 0.24$. Since our DFT Fermi surface and bands agree with the observed band structure it is unlikely that such a strong renormalization occurs. We conclude that the TLL spectral function is not an appropriate description of the system at these low temperatures where a FL phase is expected, since the large value of α deviates from the expectations of the FL phases. Our assumption that the TLL model can be mapped onto the DOS dimensional crossover therefore appears only to work at temperatures above 100 K. The origin of the spectral weight depletion at low temperatures remains unclear.

Our analysis suggests that $NbSe_3$ is never observed in a truly TLL regime up to room temperature. Instead below $E_C \approx 110$ meV (1250K) a gradual crossover from 1D to 3D occurs, as evidenced by the energy-dependence of the α exponent. This gradual crossover of dimensionality implies that the bosonic excitations expected for a purely 1D system can still partially survive while approaching the FL regime of 3D coherence. Such a dimensional crossover is expected in all quasi-1D materials at the energy of the renormalized interchain coupling. This invites to reconsider previous reports of TLL power-law DOS suppression and check whether the exponents were indeed measured in the 1D regime where the analysis is valid. We note that DOS exponents close to 0.6 have been reported for several systems, which may indicate longer-range interactions as in carbon nanotubes [Ish03] and atomic chains [Mey14, Blu11, Oht15] or multiband effects like in lithium purple bronze [Wan06, Dud13].

5.3 Summary

In summary, we have performed detailed ARPES measurements over a wide temperature range which reveal evidence of a dimensional crossover in $NbSe_3$. Such a dimensional crossover is consistent with the quasi-1D warping of the Fermi surface. A careful analysis of the density of states and comparison with expectations for 1D behaviour reveal a changing dimensionality of excitations above a characteristic energy E_C. At low temperatures we observe CDW gaps in the electronic structure at the momenta indicated by x-ray diffraction. With regard to $NbSe_3$ specifically, our study has clarified the band dispersions and deepened the understanding of the CDW on the electronic structure.

We expect the analysis presented here to be applicable to other quasi-1D systems due to the generality of finite inter-chain coupling in real materials, and hope this will stimulate further experimental and theoretical research on the dimensional crossover. Particularly from the theoretical side, the dimensional crossover represents a fundamental challenge that is actively under investigation [Gia08, Ima09, Lak13, De 16, Fur16].

6 Electronic Structure of Ag/Si(557) Nanowires

Metal wires on semiconducting substrates are important model systems for low dimensional materials. Not only do some of these systems exhibit well defined quasi-1D metallic band structures [Cra04, Sni10] but through variation of parameters such as the terrace width or by doping, a degree of control over electronic confinement and interactions may be achievable which is difficult to obtain with bulk 1D crystals such as $NbSe_3$ or the Bechgaard salts [Grü94a, Mon12]. Metallic states are of particular interest as 1D electrons have the potential to exhibit exotic electronic properties – as outlined in chapter 2 – but the number of available metallic systems is very limited. An examination of electronic states at the Fermi level is able to reveal the degree to which a system can be considered to be electronically 1D, and probes the effects that arise from electronic localization and coupling to the bulk environment of the substrate.

Ag on the Si(557) surface at coverages around 0.3 ML forms atomic nanowires, however ARPES, electron energy loss spectroscopy (EELS) and scanning tunnelling spectroscopy (STS) all show that these wires are semiconducting rather than metallic [Mor08, Kri13]. More recent work has focused on metallic Ag/Si(557) wires at a coverage of 1 ML of Ag [Kri13, Kri14]. Unlike the 0.3 ML wires, at these higher coverages Ag forms a $\sqrt{3}$x$\sqrt{3}$ structure, as on the Si(111) surface, but with a clear real space anisotropy induced by the stepped Si(557) surface. A strong anisotropy in the plasmon dispersion along and across these wires has been interpreted as evidence for quasi-1D behaviour [Kri13]. These collective excitations occur beyond coverages of 0.3 ML, where the $\sqrt{3}$ structure starts to form and has therefore been associated with this structure. The clean, stoichiometric 1ML Ag/Si(557) surface is thought to be semiconducting, only becoming metallic upon doping. The appearance of metallic states was assigned to electron doping by Ag atoms or residual gas [Kri14] which populates the Ag-induced bands and shifts them below the Fermi level in a similar way to that observed on the Ag/Si(111) surface [Cra05]. These observations call for an investigation of the momentum-resolved valence level structure; in particular near the Fermi level.

The 1 ML Ag/Si(557) system is studied with ARPES. Fermi surface mapping reveals two-dimensional (2D) Ag-induced electron pockets, which shift to higher binding energies by n-type doping due to residual gas absorption. Additional 2D metallic states near the Fermi level are also observed, which we argue originate from substrate induced super-periodicities. An analysis of the step potential suggests a regime in which terrace confined states could be expected to be observed, however the structural inhomogeneity of the step edges may mask their observation. By comparison to a number of other literature studies, it appears that the observation of confined plasmon states in EELS implies a more 2D environment as viewed by ARPES. The work presented in this chapter has been published in Nicholson *et al. New J. Phys.* 17, 093025 (2015) [Nic15].

Experimental

Measurements have been carried out at the BESSY II facility in Berlin, using the UE56-PGM1 beam line end station introduced in chapter 4. 1 ML Ag/Si(557) with respect to Si(111) surface atom density i.e. 1 ML = 7.83x10^{14} cm^{-2} is composed of a (111) terrace 3.6 nm wide and step edges with a (113) orientation as shown in Fig. 6.1. The size of one full unit is 5.7 nm. For details of the preparation please see section 4.5.3. After preparation the sample was transferred in vacuum to a liquid N_2 cooled manipulator in a chamber with a base pressure of 3x10^{-11} mbar when cold. Linear horizontally polarised radiation at a photon energy of 112 eV was used, as this maximised the ARPES signal of bands close to the Fermi level. Fermi surface mapping was carried out at 100 K.

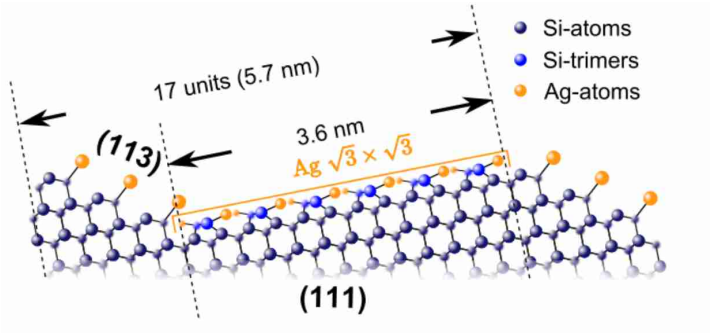

Figure 6.1: Schematic representation of the 1 ML Ag/Si(557) structure, reproduced with permission from [Kri15].

6.1 Electronic Structure

6.1.1 Doping Effects

The valence band features as measured by ARPES of a freshly prepared 1 ML Ag/Si(557) surface (which includes around 20 mins. exposure to residual gas during which time LEED and transfer to the measurement chamber are carried out) and one which has acquired a considerable n-type doping are shown in Fig. 6.2a and 6.2b. The data are normalised to the sum of the energy distribution curves (EDCs) in order to highlight features near the Fermi level. In the undoped case, emission from the Si-derived bands is observed at normal emission ($k_{||} = 0$) and at binding energies below 0.3 eV. A small electron pocket just below the Fermi level is observed at 1.15 Å^{-1}, which is shifted down towards higher binding energies over the course of a few hours until a parabolic band is seen as shown in Fig. 6.2b. An electron pocket at normal emission is now also evident. The intensity distribution of the pocket resulting in half of the band appearing much brighter than the other is caused by matrix element effects which are further revealed by the full Fermi surface presented below. During the time between the two data sets, no additional material was introduced to the system; hence we assign the changes to residual gas adsorption.

The appearance of a pocket already in the freshly prepared sample is likely a result of residual gas absorption during the time taken to check the preparation with LEED and transfer to the measurement chamber. Thus it is likely that the true

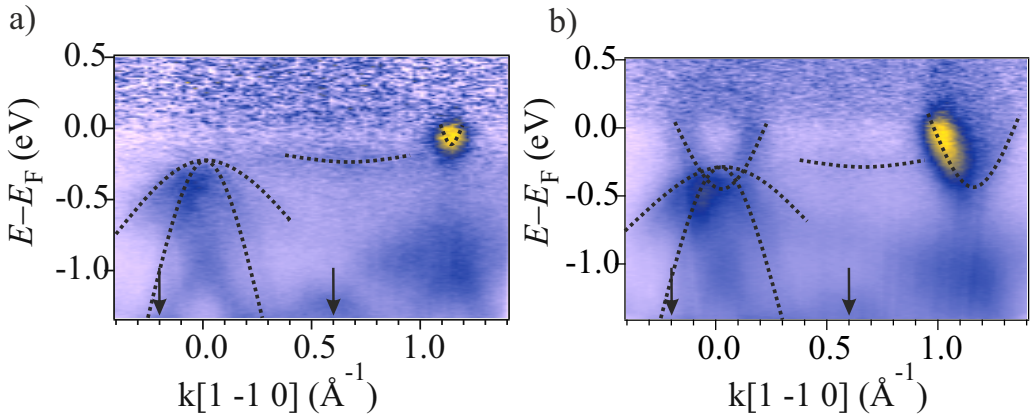

Figure 6.2: a) Photoemission image of valence band states recorded with a photon energy of 112 eV from a freshly prepared sample showing only a very small electron pocket below the Fermi level at $k_{||} = 1.15$ Å^{-1}. States from the Si substrate are also highlighted. b) Same sample after 2 hours in residual gas pressure of 5x10^{-11} mbar showing well developed bands. Dotted lines are a guide to the eye. Arrows in mark the fixed k positions at which the EDCs in Fig. 6.3b and c are obtained.

1 ML surface is semiconducting. Fig. 6.3a summarises the band position dynamics, obtained by extracting the minima of the band at 1.15 Å^{-1}. Band positions were extracted by fitting the momentum distribution curves with Lorentzian peaks and a constant background. A parabolic distribution was then fitted to the band position in order to obtain the energy minima. The band is shifted by 250 meV over a period of around 2 hours.

This time scale is consistent with the EELS study on this system [Kri14] which also reveals residual gas doping. In addition to the Ag surface state, the Si bands from the substrate are shifted during this time, but only by 80 meV (see Fig. 6.3b), most likely due to surface photo voltage induced band bending. No change was observed in the LEED pattern of the sample, other than a broadening of spots due to increased scattering at the surface adsorbed species, hence a surface reconstruction can be ruled out as the cause of this shift. Quantitatively similar residual gas induced shifts were also found on the Ag/Si(111) surface [Joh89]. Previous work has shown that Ag may also be used to dope the semiconducting 1 ML Ag/Si system into the metallic phase [Kri14, Cra05].

An additional electronic band is found at 220 meV below E_F with the minimum in energy centred at 0.6Å^{-1} in Fig. 6.2a and b. EDCs around this value are presented in Fig. 6.3c. Annealing the sample to 600°C for 15 s removes this state, while retaining around 90% of the surface Ag [Kri14]; we hence assign this feature to a surface state. We speculate that this state may be the signature of (residual gas) atoms weakly bonded to the (113) step edges which extrinsically dope the Ag states on the (111) terraces, as proposed in a recent study [Kri15]. This model additionally predicts a band bending induced by the charges absorbed at the step edges. As previously described, we observe a rigid band shift of 80 meV during the time in which the Ag pocket is doped into the metallic phase, which we attribute to a band bending effect. Our data appear consistent with the proposed extrinsic doping model.

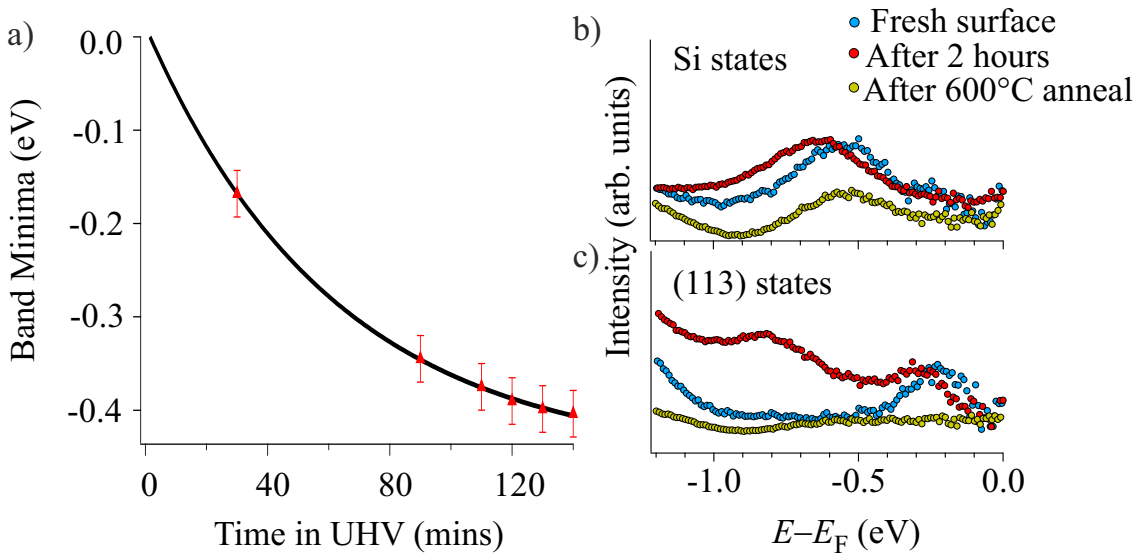

Figure 6.3: a) Shift of Ag-induced surface state band minima at 1.15 Å^{-1} as a function of time in residual gas. b) The position of the Si bands at k[1 -1 0]=−0.2 Å^{-1} is shown as a comparison. A shift of 80 meV in the time it takes to dope the Ag bands is observed. c) EDCs at 0.6 Å^{-1} (± 0.15 Å^{-1} integration window) revealing the additional surface state at 220 meV below E_F, which is assigned to atoms bonded to the (113) step edges. This state surface state may be removed by annealing to 600°C.

6.1.2 Fermi Surface

The Fermi surface for the 1 ML Ag/Si(557) surface in the fully doped case described in the previous section is shown in in Fig. 6.4a. To aid explanation, a schematic of the (111) and $\sqrt{3}$ Brillouin zones of the (111) are overlaid. The Ag/Si(111) Fermi surface has hexagonal symmetry, with an Ag-induced electron pocket appearing at each of the K-points of the (111) Brillouin zone, which are the Γ-points of the $\sqrt{3}$ reconstructed Brillouin zone [Cra02]. Thus only Ag states contribute to the Fermi surface. These pockets have parabolic dispersion below the Fermi level (E_F). The pockets are circular in the k_xk_y plane, but each has a notch of intensity removed, the exact position of which is dependent on the energy and polarisation of incident light. This is most likely due to the photoemission matrix element introduced in Chapter 3 but is also reminiscent of the "dark corridor" observed on graphene due to the Berry phase [Liu11].

As can be seen, a similar result is obtained on the Ag/Si(557) surface. The fully doped Fermi surface shows the same 2D electron pockets at the $\sqrt{3}$ Brillouin zone centres as on the Ag/Si(111) surface. In our measurements the position of normal emission is rotated by 9°compared with that of a flat (111) surface, corresponding to the miscut direction required to produce the vicinal Si(557) surface. The measurement presented here is from the second Brillouin zone and the scale is referenced to the centre of this zone.

In addition to the Ag-induced features from the $\sqrt{3}$ Ag/Si(111) surface in Fig. 6.4a, weak intensity at the Fermi level is observed between the main Ag pockets. These weak features have a circular intensity distribution and generally appear similar to the (111) Ag states. The energy vs. momentum behaviour of two of these additional

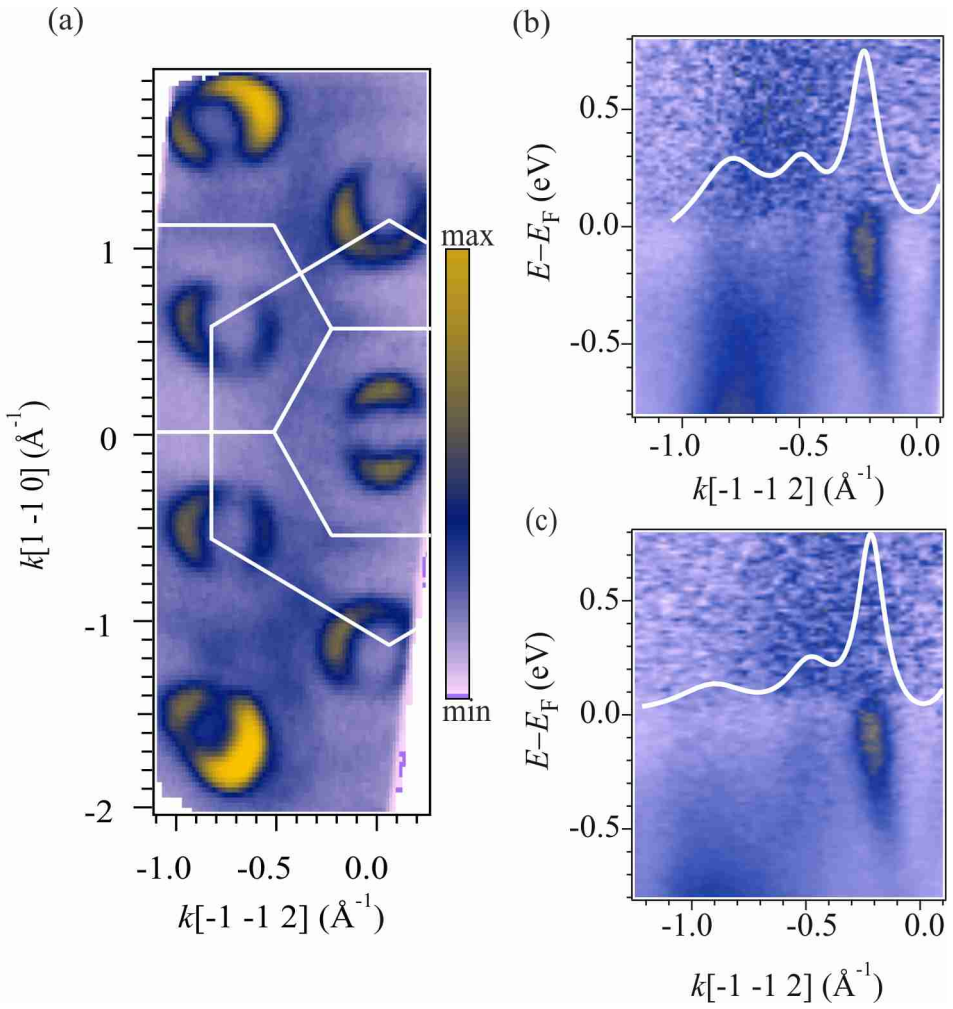

Figure 6.4: a) Fermi surface of Ag/Si(557) taken with 112 eV photon energy. The matrix element effect which produces regions of missing intensity is clearly visible. The Brillouin zones of the (111) (large hexagon) and $\sqrt{3}$ (smaller hexagons) surfaces are overlaid in white. A slight uncorrected distortion due to misalignment causes the pockets towards the edge of the image to appear non-circular. b) Cut in energy and momentum through the Fermi surface along [-1 -1 2] (perpendicular to the wire direction) at -1.3 Å^{-1} in a). Two dispersing states are observed, which are assigned as the Ag/Si(111) surface state at the $\sqrt{3}$ Brillouin zone centre and a replica of this. c) A similar cut along [-1 -1 2] at 1.3 Å^{-1}shows again main and replica bands. The white curves are fits to the MDC spectra in a 100 meV window around the Fermi level.

features are displayed in figure Fig. 6.4b and 6.4c. Electron-like states are seen to disperse towards E_F in a parabolic fashion. Despite being weaker in intensity and sitting on top of a larger background, the similarity to the (111) states is clear. These observations were reproduced on different substrates prepared on different days and are therefore thought to be intrinsic to the Ag/Si(557) surface.

In order to further highlight the shifted replica states, the data in Fig. 6.4a are presented with a different colour scheme and changed contrast in Fig. 6.5d. This image clearly reveals a number of circular replica pockets, additional to the pockets found on the Ag/Si(111) Fermi surface.

These replica states are shifted in momentum along both the [-1 -1 2] and the [1 -1 0] azimuths. The value of the shifts are extracted by analysis of line cuts through the Fermi surface along the two azimuths as presented in figures 6.5a and 6.5b. Along the [-1 -1 2] direction we observe a shift vector of 0.15 Å^{-1} while parallel to the wires along [1 -1 0] it is 0.38 Å^{-1}. A schematic of the Ag/Si(557) Fermi surface is presented in Fig. 6.5e.

The Umklapp vector of 0.15 Å^{-1} perpendicular to the nanowires corresponds closely to the value expected for the interwire distance resulting from the 5.7 nm periodicity, which suggests the replicas are a direct result of the super-periodicity in the system. If this is indeed the case then electrons cannot be purely confined to the quasi-1D terraces, but can propagate across multiple terraces, meaning some amount of inter-wire coupling exists in this system. As will be discussed further below, the short electronic coherence length in this sample suggests that inter-wire coupling is rather small. Considering the very weak intensity of these replicas compared with the main electronic states, we would interpret this to mean that the potential induced by the step edges does not introduce strong scattering. A similar scenario is observed in Pb/Si(557) nanowires [Kim07], and on Cu and Au vicinal surfaces [Bau04b, Ort05].

The value of 0.38 Å^{-1} is very close to 1/3 of the $\sqrt{3}$ Brillouin zone size of 1.1 Å^{-1}. If such a periodicity exists, it should also appear also in the structural measurements obtained by LEED. Our LEED data indeed reveal a 1/3 periodicity as presented in the line cut Fig. 6.5c. This is suggestive of a real space super-periodicity along the [1 -1 0] direction i.e. along the wires. STM work on this system has shown the step edges display a characteristic triangular roughness [Kri13] which results in a "zig-zag" structure due to the $\sqrt{3}$x$\sqrt{3}$ structure formed by Ag on the Si(111) terraces. Such a periodic modulation may be responsible for the shift of the Ag replica along the [1 -1 0] azimuth via the transfer of a reciprocal lattice vector. However, it can be difficult to directly match this periodicity with that observed in the STM, as the exact nature of the step edges depends on the preparation and varies from sample to sample.

A sharp feature in ARPES additionally requires structural homogeneity on the length scale of the probing light beam, because of the incoherent superposition of spectral features from the sampled region. However, due to the roughness of the step edges as imaged by STM [Kri13], replica features are strongly smeared out as clearly observed in our data.

6.2 Dimensionality

We now try to reconcile the strong anisotropy in the plasmon dispersion along and across the wires seen by EELS [Kri13], suggesting a 1D confined behaviour of

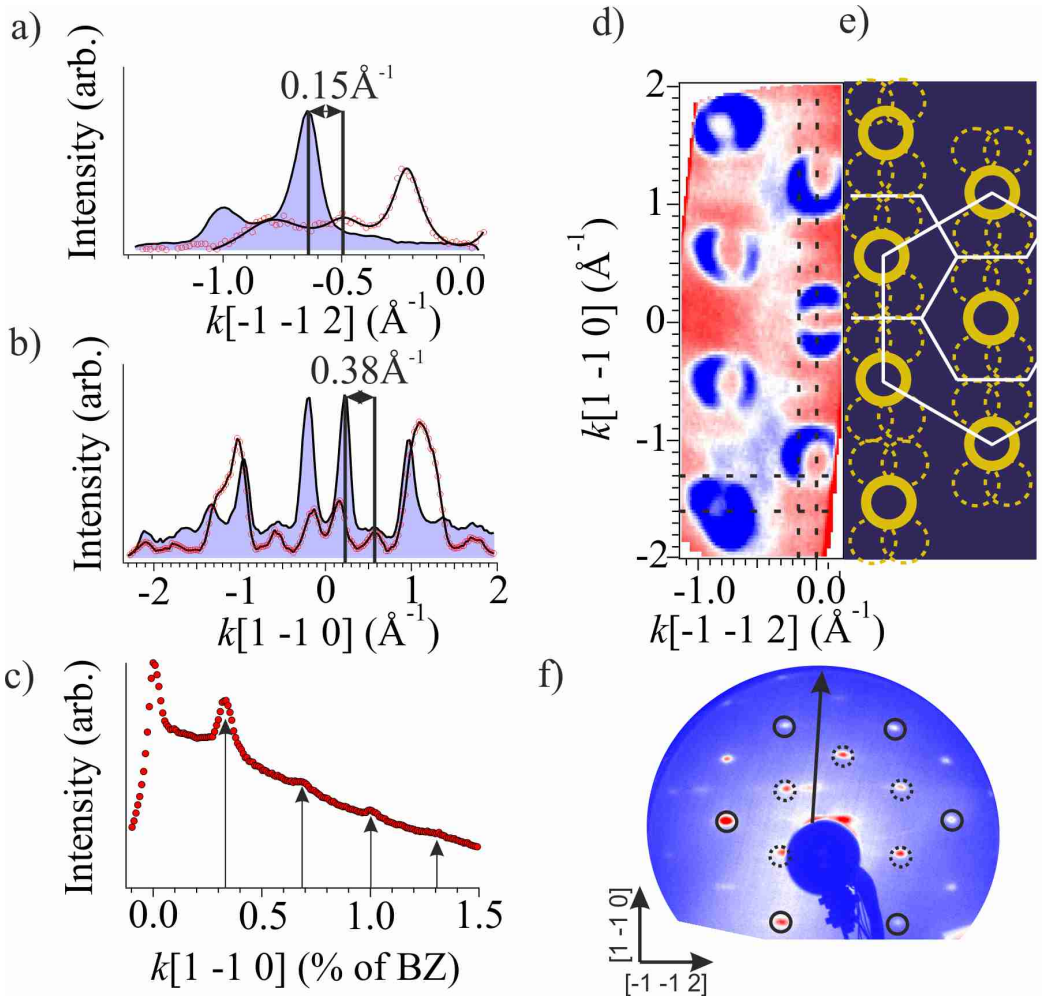

Figure 6.5: a) Cuts through the Fermi surface shown in figure 3 along the [-1 -1 2] direction at -1.6 Å^{-1} through the Ag pockets (solid blue curve) and at at -1.3 Å^{-1} through the replica state (x10) (red dots and black fit curve) revealing an offset in momentum. b) Cuts along the [1 -1 0] direction. Blue filled curve taken at 0 Å^{-1} through the Ag pockets, red dots and black fit at -0.15 Å^{-1} centred on the replica states. Positions of cuts are shown in d. c) Cut through the LEED image shown in f) revealing a $\frac{1}{3}$ (0.4 Å^{-1}) periodicity along the wire direction. d) Fermi surface as in Fig. 6.4a, with a colour scale chosen to highlight the replica pockets and a schematic Fermi surface showing the replicas (dotted circles) and the pockets that are the same as the Ag/Si(111) Fermi surface (full circles). Dotted lines show the position of line cuts made in Fig. 6.4a and 6.4b. e) Schematic Fermi surface for Ag/Si(557). States which are the same as on the Ag/Si(111) Fermi surface are shown as solid yellow circles, while replica states are presented as dotted circles. f) LEED image of the Ag/Si(557) showing the cut in c). Si spots are marked by full and Ag spots by dashed circles.

collective electronic excitations, and the electronic band structure of the $\sqrt{3}$x$\sqrt{3}$ terrace structures as revealed by ARPES, which appears to be dominated by features stemming from a 2D electronic structure. A salient point is that there is a difference between 1D behaviour of *collective* excitations, and the dimensionality of metal-induced electronic surface states i.e. the 1D behaviour of collective excitations as observed by EELS does not necessarily imply that the electron quasi-particles on the terraces themselves experience a 1D potential. As presented above, we find no evidence for either 1D dispersion, or quantum confined states in our ARPES data. It seems very unlikely that this is due to limitations of the ARPES technique. Confined states perpendicular to the step edges in terraces as large as 5.6 nm in Au(23 23 21) are observed with ARPES [Mug01]. This is despite the fact that at the surface of a metal single crystal electrons may also be scattered perpendicular to the surface, potentially reducing the interaction with the super-periodicity step potential. In contrast, in hetero-systems of metals on a semiconducting substrate the electrons may be more effectively confined to 2D as surface states typically exist in the bulk band gap. This implies that the reason we do not observe a 1D dispersion or quantised states in the above data is the intrinsic to the Ag/Si(557) system. Below we present an analysis that attempts to quantify this.

6.2.1 Confining Potential

By fitting the extracted dispersion of the replica band with a parabola, shown in Fig. 6.6a, and extracting the effective mass ($0.21\mathrm{m}_e$) the step potential may be estimated using the Kronig-Penney model introduced in Chapter 2. The dispersion of the band was extracted by fitting Lorentzians to MDCs of the surface band. A representative fit is shown in Fig. 6.6b, where four Lorentzians have been used to fit the band plus its replica. The band position was taken to be the maximum of the peak. Due to the overlap with the bulk Si bands at higher binding energies, the fit range is restricted and does not extend to the bottom of the band.

Using this method a value of $V_0 b = 5$ eV Å is calculated for the step potential. This is similar to the potential barriers of the order $V_0 b = 2$ - 3 eV Å, observed in Au(887) and Cu(10 10 11) or even 10eV Å, as in Au(23 23 21) [Ort05]. We note that the lack of clear band gaps due to quantum confined states prevents us from extracting the absolute step potential in our data. As a comparison, micro-conductivity measurements at the Ag/Si(111) surface found a potential of $V_0 b = 10$ eV Å at a single atomic step [Mat04].

6.2.2 Discussion

The value of the step edge potential estimated from the data is consistent with a system which supports both super-lattice replicas and quantum confined states [Ort05]. For weak confining potentials electrons may propagate across many steps, resulting in super-lattice replicas spaced by the step periodicity, while a strong potential confines electrons to a single terrace resulting in quantum well states appearing perpendicular to the step potential. At intermediate values of the step potential as in Au(887) it is possible to observe both effects simultaneously such that one observes a super-lattice replica with band gaps due to 1D confined quantum well levels [Ort05]. In Ag/Si(557) we observe replicas, but no signatures of quantum

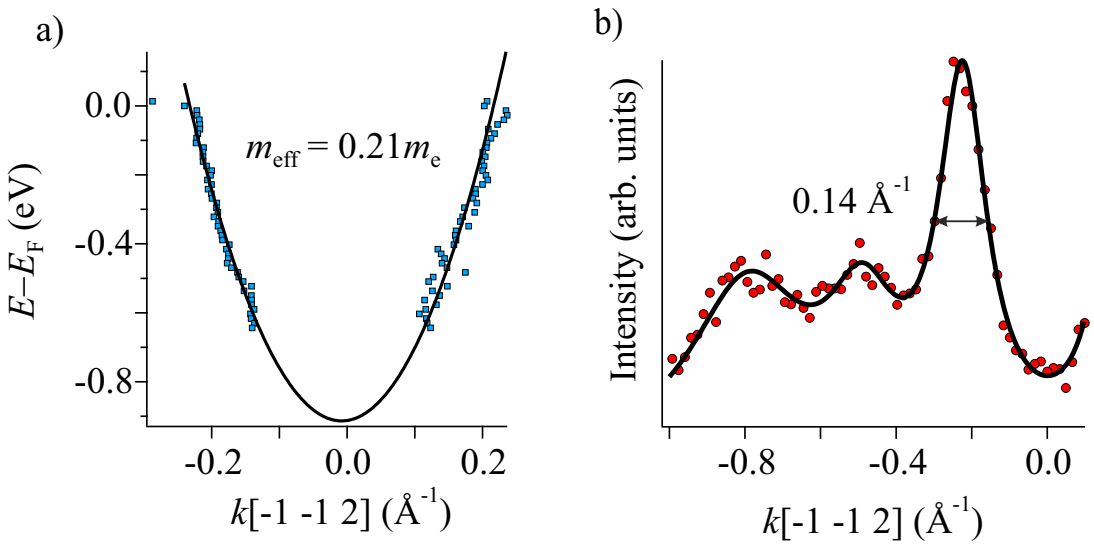

Figure 6.6: a) The extracted dispersion obtained by fitting the MDCs as a function of energy. From this an effective mass of 0.21 e_e is obtained. b) Typical MDC of the surface state including fit curve in black, from which an overall width of 0.14 Å^{-1} is extracted.

confined states. This implies the strength of the edge potentials is rather low, in contrast to our estimate using the Kronig-Penney model. It is possible, however, that any confined state behaviour is obscured by the structural inhomogeneity of the nanowires. Inhomogeneities lead to an enhancement of scattering centres for electrons, with the result that electronic states have shorter lifetimes (ReΣ) and hence broader line widths than well ordered surfaces. Thus the edge potential should be homogeneous in order to produce a coherent signal. Indeed a variation in terrace width has been seen to contribute to the apparent 2D dispersion in photoemission from Cu(443) and Cu(665) [Bau04a]. From a structural point of view the Ag/Si(557) nanowires exhibit a considerable edge roughening, as imaged by the STM data in Fig. 3 of reference [Kri13], which may broaden spectral features in ARPES and hide evidence of a gap opening. Indeed the width of the MDCs extracted and shown in Fig. 6.6b bears this picture out. The extracted FWHM is 0.14 Å^{-1} which clearly dominates over the width introduced by the experimental apparatus, estimated at 0.03 Å^{-1}. The influence of the surface roughness is clear. Thus it is entirely possible that confined states exist, but that they are washed out and not resolved in our measurements. In a closely related system, Pb/Si(557), which has shorter terrace widths and atomically ordered step edges, multiple replicas at the Fermi level are observed with a step potential estimated at 60 meV [Kim07]. The stronger signal compared with that observed in our data suggests that in the Pb system electrons are able to propagate over multiple steps while maintaining coherence and thus result in a stronger photoemission signal. Even in the case of Pb/Si(557), the ARPES signal is already essentially 2D, with a quasi-1D band gap of only 50 meV observed to open at E_F [Teg08].

It is appears from the previous EELS studies that the step edges in Ag/Si(557) act as strong reflectors for plasmons so that standing waves on individual terraces are observed. In contrast to the single particle excitations measured by ARPES, a plasmon is a collective property of the electron gas resulting from the generation

of electron-hole pairs. By virtue of being collective, such an excitation causes displacement of all electrons within the coherence length of this excitation. Therefore confining the excitation to a region on the order or smaller than its own wavelength e.g. in a nanoparticle or perpendicular to the nanowires, all electrons in the structure will participate in the excitation. From the previously published EELS data it is known that plasmons disperse up to 0.19 $Å^{-1}$ along the [1 -1 0] direction. This corresponds to a real space value of 3.3 nm; very comparable to the 3.6 nm terrace width. Thus it is possible that the collective mode extends throughout the entire terrace and does not propagate, but gives rise rather to standing waves as observed in [Kri13]. This has been supported by time-dependent density functional theory calculations [Ina04, Yan08]. Assuming a single dipole field confined to a terrace leads to quantised energy states of the plasmon oscillations across the wire direction. This gives rise to discrete energy losses perpendicular to the wires found in a number of systems, including Ag/Si(557) [Rug10, Blo11, Kri13].

Notably no confined EELS states are found on the (4x1)-In/Si(111) or Au/Si(557) systems [Liu08a, Lic16]. These atomically narrow chains are much narrower than the terraces of the systems on which discrete plasmon loses are observed. It appears they are in fact too narrow to support collective oscillations perpendicular to the chain, whereas along the chain a clear metallic dispersion is observed. By comparison, ARPES clearly reveals strong quasi-1D features in the well separated single atomic chains as in the (4x1) reconstruction of In/Si(111), Au/Si(557), or by double chains in Au/Si(553) and Au/Si(775) [Yeo99, Cra04]. Another similar surface, the 5x2-Au/Si(111), reveals a continuous 1D to 2D transition in a surface electron band, with a Peierls gap at the Fermi level [Los00]. However, as already described, a very different situation arises for Pb/Si(557) close to 1 ML coverage. Due to uncovered step edges, this structure still consists of well separated mini-terraces, but the ARPES signal is already essentially 2D, with a substrate mediated interaction producing replica states at the Fermi level [Kim07, Teg05]. It appears that the observation of confined plasmon states on single terraces is already in the limit of 2D excitations for ARPES. On the other hand single atomic chains support both quasi-1D plasmons and quasi-1D dispersions in ARPES.

6.3 Summary

The Fermi surface of the 1 ML Ag/Si(557) nanowire structure exhibits 2D metallic pocket at the Brillouin zone boundary as observed by ARPES. Filling this band by electron doping moves it to higher binding energies by several hundred meV. Evidence for a surface state is found which supports the existence of step-edge bound residual gas atoms which dope the Ag states on the (111) terraces, supporting a previously suggested extrinsic doping mechanism. In the fully doped phase replicas of 2D Ag pockets are observed as a result of the interaction with the anisotropic substrate underlying the Ag surface. The analysis of the confining step potential suggests a regime in which confined states could be expected to be observed, however the structural inhomogeneity of the step edges may mask their observation. On the other hand, by comparison to a number of other literature studies, it appears that the observation of confined plasmon states in EELS implies a more 2D environment as viewed by ARPES. Such considerations will be important when considering the application of low dimensional systems to device design.

7 Ultrafast Phase Transition in quasi-1D In/Si(111) Nanowires

A key concept in structural and chemical reactions is that the system evolves along a Born-Oppenheimer (BO) potential energy surface from reactants to products; or in the case of phase transitions, from phase 1 to phase 2. The BO surface is determined by the electrons: in particular the transient electronic band structure and its occupation. This naturally suggests trARPES as a tool for elucidating microscopic insights of the dynamics of phase transitions, and for better informing theory about realistic conditions during such reactions. Here trARPES is used to obtain detailed insights into the evolution of individual electronic states in a quasi-one dimensional (1D) atomic-chain metallic nanowire (MNW) system. One of the most interesting and intensively studied of the MNW systems is In/Si(111), which undergoes a transition from a (4x1) to an (8x2) structure at low temperatures [Yeo99] concomitant with an metal-to-insulator transition [Tan04]. It has been suggested that the phase transition occurs through a multi-band Peierls instability [Yeo99, Ahn04] via the displacement of two particular atomic modes – a rotary and a shear distortion [Wip10, Jec16] – stabilised by electronic entropy [Wip10]. The motion of these modes is expected to set the time scale of the structural phase transition, as recently confirmed by time-resolved diffraction [Fri17]. However key information that has been missing is a momentum resolved view of the band structure during the phase transition, on time scales of a few tens of femtoseconds granting access to the response of individual electronic states. This should allow a rigorous test of the predictions from theory, as well as giving detailed microscopic insights into the reaction mechanism, and going towards real space electronic density dynamics.

Following photoexcitation we track the temporal evolution of individual electronic bands as they evolve through the phase transition revealing three distinct time scales for the phase transition including a separation in time between the metal-to-insulator and structural transitions. In addition we map the distribution of electrons throughout k-space and time, and use this information to perform molecular dynamics (MD) simulations with realistic electronic distributions and relaxation. The simulations reproduce the multiple time scales we observe in experiments and expose the microscopic role played by holes in driving the phase transition. As link is made from the transient electronic structure to the electronic density in real space, which may allow ultrafast bond dynamics to be extracted. These results provide unprecedented insights into the microscopic mechanism of a surface phase transition reaction involving electronic and structural interplay and have relevance for catalysis and surface chemistry as well as for optically driven phase transitions.

This work has been carried out in conjunction with the group of W. G. Schmidt at the University of Paderborn where the theoretical calculations presented here have been performed by A. Lücke. Samples growth and measurements have been carried out at the FHI, Berlin, in the framework of this thesis.

7.1 Background and Previous Work

Of the numerous surface reconstructions that occur on the In/Si(111) surface [Kra97] the most intriguing and intensively studied is the (4x1) reconstruction that occurs at around 1 ML of In coverage. Early studies found that the (4x1) phase was formed of quasi-1D metallic In chains on the Si surface [Abu95, Hil97]. However it was once Yeom *et al.* [Yeo99] both mapped the full quasi-1D Fermi surface and observed the opening of a gap at the Fermi level at $T_C = 120$ K that detailed investigations of the system began in earnest. The electronic structure of the metallic (4x1) phase and the low temperature gapped phase are presented in Fig. 7.1c and b respectively to give an overview of the relevant bands in the system.

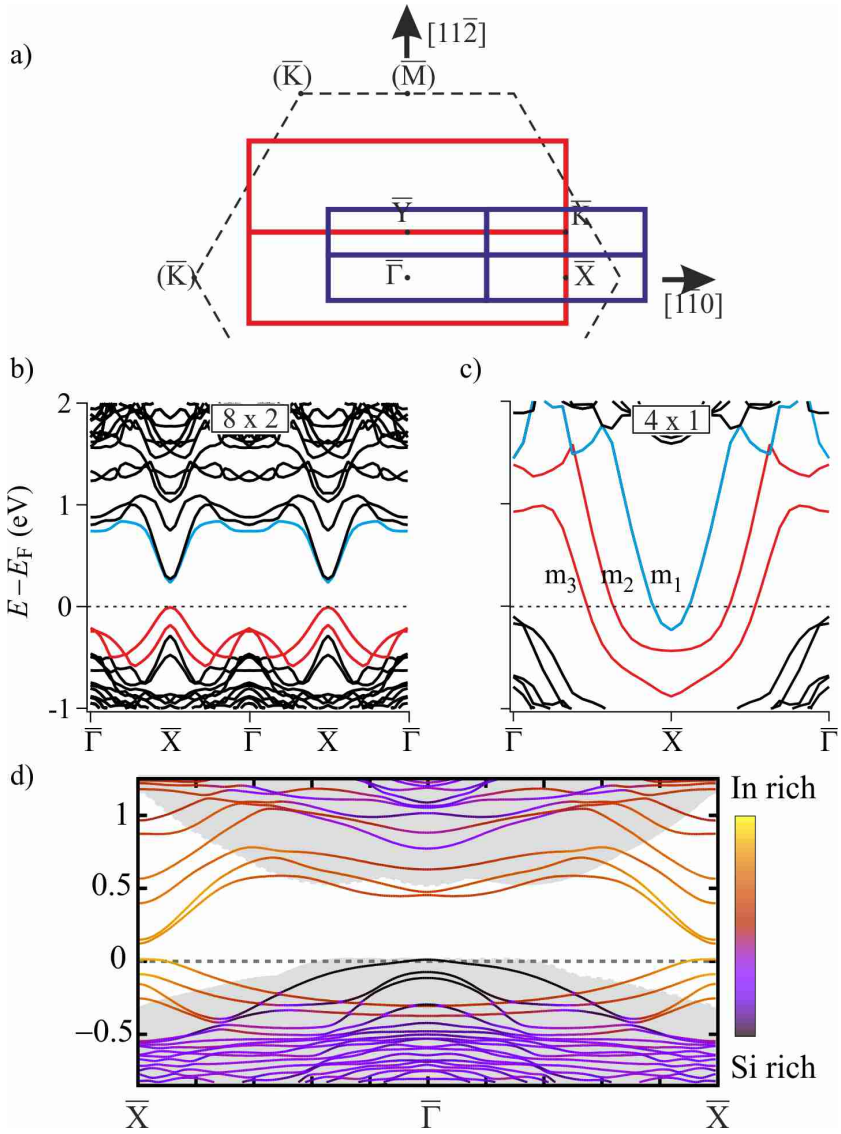

Figure 7.1: a) Schematic surface Brillouin zone of In/Si(111) 4x1 (red) and 8x2 phases (blue). High symmetry points of the 4x1 zone are marked. As a comparison the Si(111) surface BZ is included (dashed line) and high symmetry points in brackets. b) Calculation of the 8x2 and c) the 4x1 phase along the $\bar{\Gamma} - \bar{X}$ line. The 3 bands involved in the phase transition are marked (see text). d) DFT calculation showing the elemental character of states and Si bulk bands (grey shaded).

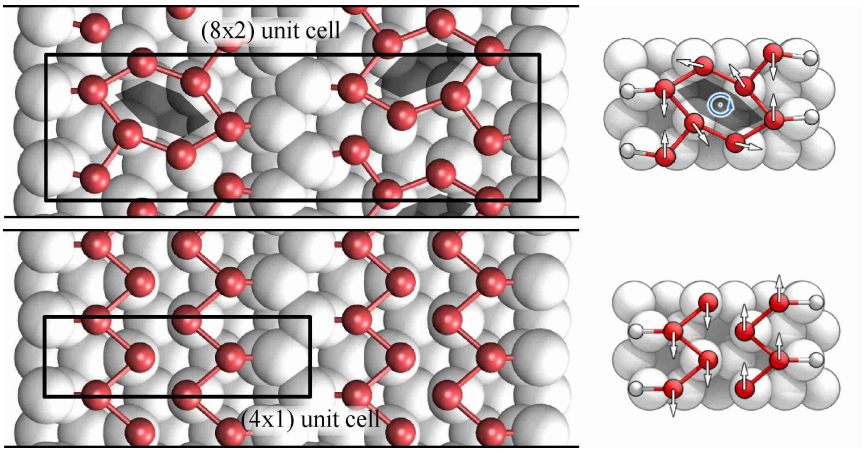

Figure 7.2: DFT calculated In/Si(111) structures for the low temperature (8x2) phase (top panel) and (4x1) phase (lower panel) from Ref. [Lüc17]. The structural transition is thought to occur through two particular atomic displacements, shown to the right of the main image from Ref. [Wip10]: a rotary (top) and shear (bottom) motion of the chains.

The metallic (4x1) phase is characterised by three In bands crossing the Fermi level that disperse symmetrically about the $\overline{\mathrm{X}}$-point along the $\overline{\Gamma} - \overline{\mathrm{X}}$ direction. These are termed m_1, m_2 and m_3. The low temperature phase exhibits a real space unit cell doubling both along and across the wires, resulting in a doubled (8x2) unit cell. The corresponding k-space unit cell is therefore one quarter the size of that in the metallic phase, with the result that four full Brillouin zones fit into a single (4x1) zone; thus the $\overline{\mathrm{X}}$-point of the (4x1) zone becomes the second $\overline{\Gamma}$-point in the (8x2) phase. To highlight the relation between high symmetry points, surface Brillouin zones of the (4x1) and (8x2) phase are given in schematically in Fig. 7.1a and are compared with the hexagonal Si (1x1) surface Brillouin zone.

The (4x1) to (8x2) transition was found to be fully reversible and of first order [Kla14], and concomitant with a metal-to-insulator transition [Yeo99, Tan04] due to the gapping of the electronic structure. The observed doubling of the unit cell along two directions in real space, as well as the parallel Fermi surface sheets resulting from the quasi-1D nature of the system naturally led to the suggestion that the transition to the low temperature phase was driven by a Peierls-type instability [Yeo99].

Further investigations [Kum00, Yeo02, Ahn04, Par04, Sun08] resulted in a more detailed model of the phase transition in this multi-band system, in which the m_1 band is depopulated by moving above the Fermi level and transfers its charge to the m_2 and m_3 bands which then combine to a half filled situation, and hence are unstable towards the formation of a Peierls gap. Frozen phonon calculations revealed that such a "triple-band Peierls" model may take place through the distortion of the lattice via two distinctive displacements [Gon05, Rii06, Wip10, Jec16]. In this picture the m_1 band (blue in Fig. 7.1b and c) is lifted above the Fermi level by the shear motion of the In atom chains against each other, while a period doubling rotation mode opens the Peierls gap at the (4x1) zone boundary (red bands in Fig. 7.1b and c). The resulting structural changes from a double "zig-zag" chain in the (4x1) phase to a distorted hexagon in the low temperature (8x2) phase are shown in Fig. 7.2. Also shown are the two displacement modes that transform the phases into each other.

The role of electronic entropy in stabilising the phase transition has been noted by Wippermann and Schmidt [Wip10]. This work also calculated the eigenvectors and frequencies of the expected Peierls modes, while a recent Raman study found evidence to support the Peierls scenario by observing the softening of the two modes when approaching the phase transition temperature [Jec16]. On the other hand, the importance of dynamical bond changes have also been found to be important in driving the phase transition, which could be thought of as an exothermic surface reaction [Kim13, Kim16, Lüc17], more in line with the first-order nature of the transition. The role of defects and dopants, in particular oxygen, in pinning and even stabilising the phase transition has also been extensively investigated, see Refs. [Lee02, Mor10, Wal12a, Uhm13, Oh14, Jec16] and references therein.

Regarding the photo-induced phase transition, efforts have predominantly focussed on time-resolved reflection high energy electron diffraction (trRHEED) [Wal12a, Fri17]. Key conclusions from these studies are that the photo-induced (4x1) phase is metastable, with a lifetime of hundreds of picoseconds [Wal12a] dependent on the number of surface defects, and that the initial "melting" of the (8x2) phase occurs on a time scale of $\sim$1 ps [Fri17]. The time scale of the structural phase transition is expected to be set by the two atomic displacement modes discussed above. In fact the evolution from low to high temperature phase as obtained by density functional theory based molecular dynamics (DFT-MD) simulations is in surprisingly good overall agreement with the experimental results as jointly presented in Ref. [Fri17]. However, a combined energy and momentum view of states during the ultrafast phase transition (on a sub-100 fs time scale) has not been possible owing to the necessity of accessing states at high parallel momenta with high counting statistics. This requires ultrashort pulses with high photon energy and high repetition rate, as has been presented in section 4.1. Access to the transient band structure during the phase transition should allow a rigorous test of the predictions from theory as well as allowing insights into the microscopic mechanism of the photoinduced transition.

Experimental

The *in situ* growth and charactersisation of In/Si(111) MNWs has been presented in chapter 4. Samples were characterised by LEED in the (4x1) phase at room temperature, as shown in Fig. 4.15. In this way it was possible to confirm the production of a homogeneous phase across the full sample surface before transfer to the cryo-cooled manipulator and ARPES chamber. Measurements of the electronic structure were carried out in the trARPES setup at the FHI, Berlin, presented in section 4.1, in which both a He gas discharge lamp and HHG source were available; for high energy ARPES and trARPES measurements respectively. The high quality UHV conditions of around $3\text{x}10^{-11}$ mbar during HHG operation meant that a sample could be measured for around 12 hours without any noticeable loss of quality. In order to ensure good reproducibility, a fresh sample was prepared each day, and when necessary on a fresh Si(111) substrate. Time resolved ARPES measurements were carried out with typical time resolution of around 40 fs, and energy resolution of 150 meV.

7.2 Electronic Structure

7.2.1 Occupied states and thermal phase transition

The Fermi surface of In/Si(111) in the metallic (4x1) phase is presented in Fig. 7.3 over multiple Brillouin zones. The data is obtained at 150 K with a photon energy of 22 eV from the HHG beam line and is symmetrised about $k_x = 0$. Surface Brillouin zones of the (4x1) (dashed lines) and (8x2) (solid lines) are overlaid while the $\overline{\Gamma}$ and $\overline{\mathrm{X}}$ points are marked for the (4x1) phase on the right and the (8x2) phase on the left half of the image respectively. The quasi-1D nature of the system is evident from the warped Fermi surface sheets that show a strong anisotropy compared with a 2D Fermi surface c.f. Fig. 2.3. We note that we are unable to measure the dispersion perpendicular to the surface as the HHG photon energy is not tunable. However due to the strong surface character of the In bands which exist in the bulk band gap of Si, no significant dispersion is expected in this direction. The three metallic bands are well resolved at the Fermi level, in agreement with previous ARPES work [Yeo99, Ahn04, Sun08].

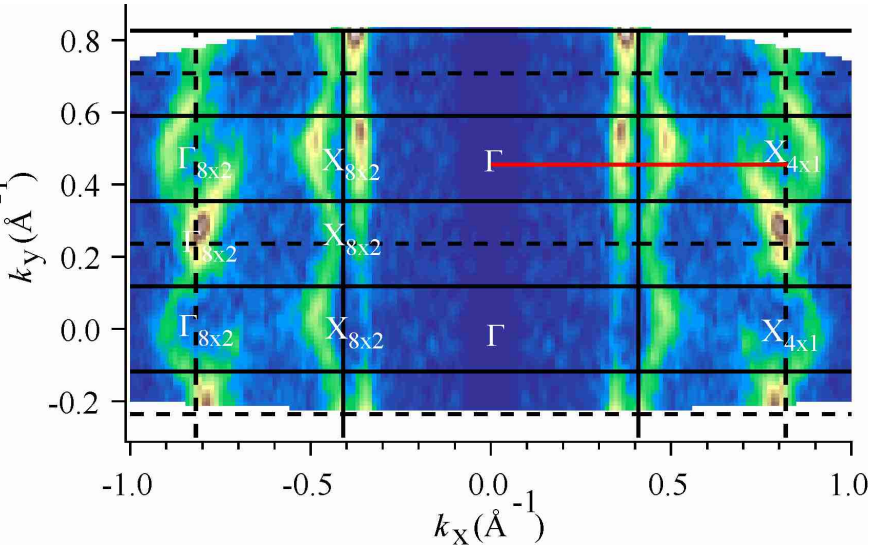

Figure 7.3: Fermi surface of In/Si(111) in the (4x1) phase measured at 150 K with HHG photons at 22.2 eV. Brilloiun zones of the (4x1) phase are shown with dashed lines, and the (8x2) phase with solid lines. High symmetry points of the two phases are marked. The solid red line shows the cut along which the majority of trARPES data regarding the phase transiton have been obtained.

The 2D plot of E vs. k at $k_y = 0.4\text{Å}^{-1}$ shown in Fig. 7.4a and b reveal the dispersion of the three bands, and may be compared to the GW-calculation in Fig. 7.1 along $\overline{\Gamma} - \overline{\mathrm{X}}$. This data is obtained with a He discharge lamp at 21.2 eVwith energy resolution set to 20 meV: much better than that available with the 22 eV laser. The asymmetry in the intensity distribution of the m_1 band comes from the position in the BZ and is the result of the photoemission matrix element. Data taken at 25 K, well below the transition temperature ($T_C = 120\ K$), shows changes in the band structure in line with previous work: a gap of around 120 meV opens in the m_2 and m_3 bands and the dispersion is seen to bend away from the Fermi level with weak spectral weight transferred into the new dispersion. The asymmetric transfer

of spectral weight into the renormalised dispersion is a common feature to CDW systems, as discussed in section 2.5.3; for the specific case of In/Si(111), this is calculated and shown in Fig. 7.7. Additionally the m_1 band is seen to disappear, although we note that some residual intensity is always present at this value of k_y. These spectroscopic markers of the phase transition do not appear homogeneously throughout the Brillouin zone, as characterised in a previous study [Ahn04].

Zoomed regions of the Fermi surface presented above are shown in Fig. 7.4c and d for the two phases. This reveals that some intensity at the Fermi level persists also in the low temperature phase, although at a much lower level than in the metallic phase, and only in particular regions. However the sharp three band crossing is replaced by a broad m_2, m_3 feature and a weak remnant of the m_1 band. In certain regions of k-space the intensity at the Fermi level is seen to disappear for all three bands.

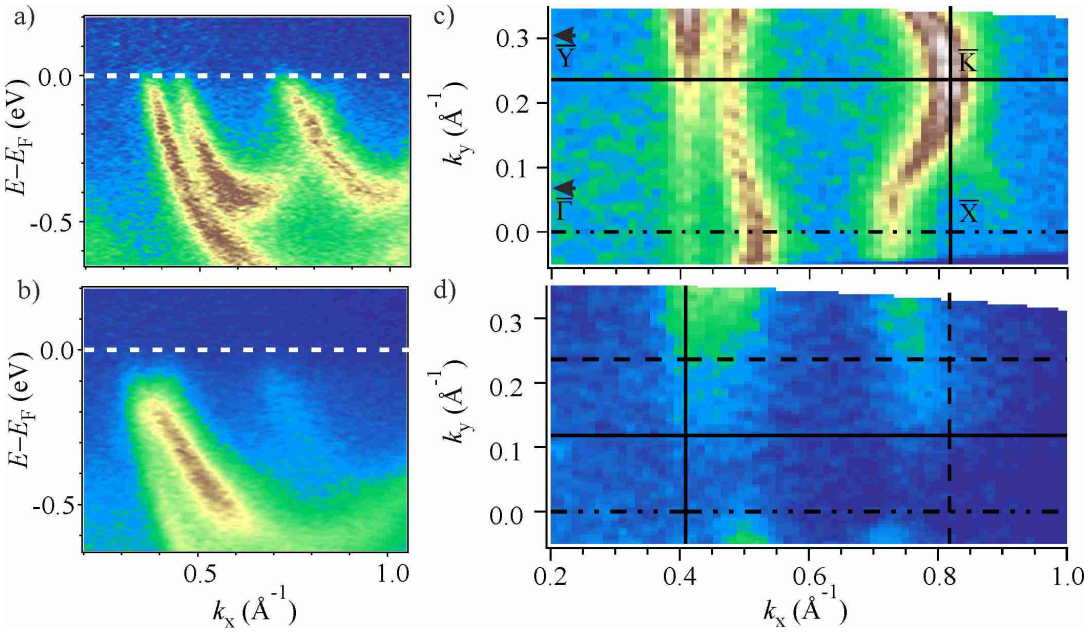

Figure 7.4: Thermally driven phase transition in In/Si(111). a) Cut close to $\overline{\Gamma}-\overline{X}$ in the second Brillouin zone along 0.4 Å^{-1} in the (4x1) phase at 150 K and b) in the (8x2) phase at 25 K. A clear gap at the Fermi level is evident in the region of the m_2 and m_3 bands. The m_1 band is seen to disappear. c) Zoom of the Fermi surface in the (4x1) phase and d) comparison to the (8x2) phase. Spectral features vary across Brillouin zones.

7.2.2 Unoccupied states

With trARPES it is possible to extend the characterisation of electronic states into the region above the Fermi level. Access to the energetic position of the unoccupied band structure allows for energy and momentum-resolved tests of calculated band structures, and therefore of the accuracy and limitations of such calculations. Data is obtained by fixing the delay between pump and probe beams to the maximum temporal overlap of the two beams. 2D momentum maps are then obtained as for occupied states: by varying the angle of the sample with respect to the hemispherical

analyser. The high repetition rate and photon flux available at the FHI setup is a huge advantage for such measurements which are still, however, time consuming.

4x1 phase

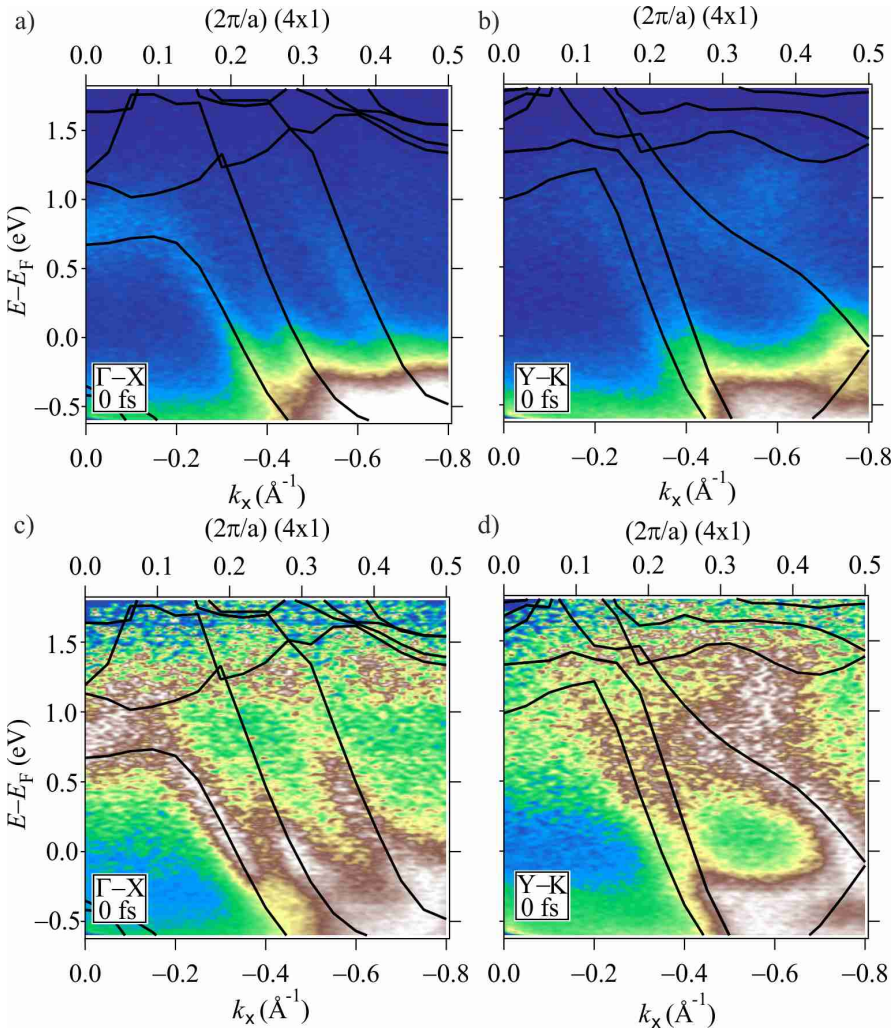

Figure 7.5: Unoccupied state dispersion in the (4x1) phase and comparison to GW calculations along $\overline{\Gamma}-\overline{\mathrm{X}}$ (a,c) and $\overline{\mathrm{Y}}-\overline{\mathrm{K}}$ (b,d). The images in c and d have had each MDC normalised in order to highlight the dispersion of states above E_{F}. Data are obtained at 150 K with HHG photons at 22.2 eV and 1.5 eV excitation.

Energy *vs.* momentum cuts along the $\overline{\Gamma}-\overline{\mathrm{X}}$ and $\overline{\mathrm{Y}}-\overline{\mathrm{K}}$ lines are shown in Fig. 7.5a and b respectively. The data are obtained at maximum temporal overlap (0 fs delay between pump and probe pulses) to maximise signal above the Fermi level. A pump fluence of $\sim$2 mJ cm^{-1} was used. It is immediately clear that states above E_{F} are much weaker than those below. In order to highlight the dispersion of electronic states above E_{F}, normalised plots are given in Fig. 7.5c and d. Each momentum distribution cut (MDC) is normalised to the maximum intensity within the cut which highlights weak intensity of excited states. This has the disadvantage that if features of unequal intensity appear in the same MDC the weaker one is suppressed, which leads to some un-physical intensity variations along individual bands; however the

main features of the dispersion are more clearly resolved. The data are overlaid with GW calculations for the respective BZ points. GW calculations include many-body self-energy effects, as captured by the Green's function (G), interacting via the screened Coulomb interaction (W). Good global agreement is found between experimental and GW band structures, also in the excited states. This is perhaps not surprising as, in the case of a metal, the unoccupied states are simply a continuation of the occupied states normally cut by the Fermi function.

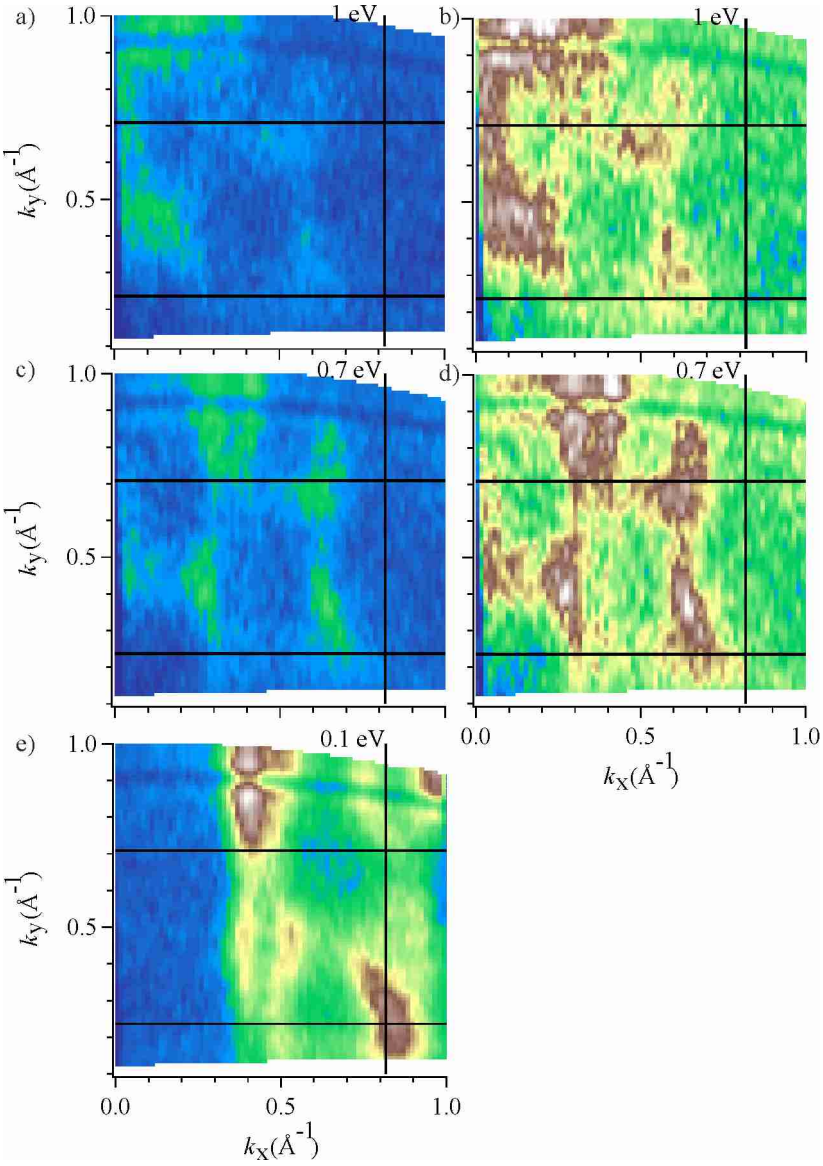

Figure 7.6: Excited state mapping of the (4x1) phase at a) 1 eV c) 0.7 eV and e) 0.1 eV above the Fermi level. Higher energy distributions are highlighted in b) and d). Data obtained at 150 K with HHG photons at 22.2 eV and 1.5 eV excitation.

The excited states can be mapped across 2D momentum space as shown in Fig. 7.6a, c and e at constant energies, similar to Fermi surface plots shown previously. The mapping region is chosen to be centred around 0.4 Å^{-1} in the 2^{nd} BZ, where spectroscopic signatures of the phase transition from the (8x2) phase have been found to be clearest. The scan covers the full 2^{nd} BZ and extends into both the 1^{st} and 3^{rd} BZs. The (4x1) BZ borders are marked by solid black lines. By comparison

with the cuts shown in Fig. 7.5 one can recognise the dispersion of all three metallic bands as a function of energy in the direction of the Γ-point. Since the intensity of states decreases at higher energies Fig. 7.6b and d show the higher energy maps with a different colour scale to highlight the distribution of electrons at these energies. It appears that at higher energies the states lose their clear quasi-1D linear form and instead tend toward 2D closed surfaces. With reference to Fig. 7.1d this may be a result of the mixing of In and Si characters, and therefore an increased bulk-like character of these higher energy states.

8x2 phase

Similarly, excited states in the (8x2) phase have been examined as presented in Fig. 7.7.

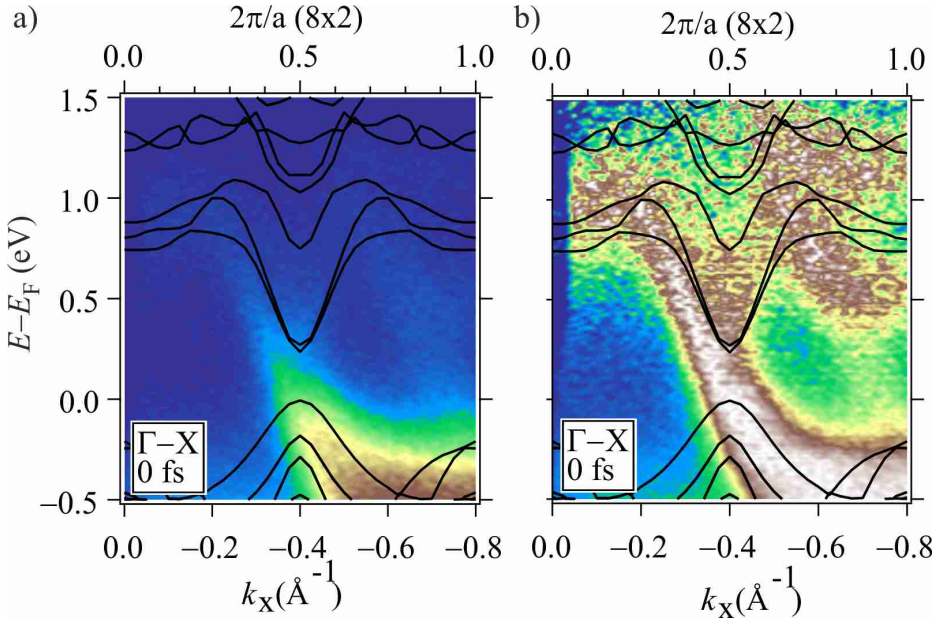

Figure 7.7: a) E vs. k raw data in the (8x2) phase and b) MDC normalised to highlight dispersions. Data obtained at 25 K. The GW calculated band structure is overlaid for comparison. c) DFT calculated (8x2) band structure unfolded onto the (4x1) states to reveal the expected distribution of spectral weight in the low temperature phase. d) Simple comparison to the unfolded bands whereby the overlap between (8x2) and (4x1) states is shown.

A comparison of the experimental and GW calculated band structures are shown in Fig. 7.7a, and MDC normalised data in b for data obtained at 25 K at a pump fluence of ∼2 mJ cm^{-1}. The comparison is more complicated than for the metallic (4x1) phase, but still shows good overall agreement. In particular, states at the $\overline{\Gamma}$-point are well reproduced, as are the dispersions of the m_2 and m_3 bands. A significant difference to the (4x1) structure is the state at around 0.5 eV above the Fermi level in the region of $k_x = 0.7$Å^{-1}. This state is not present in the (4x1) phase and this is therefore further evidence that the system has been transformed into the (8x2) structural phase at low temperatures. One notices however that the energetic position of the m_1 band at this position is poorly described by the GW calculation. This is somewhat surprising as the momentum points $k_x = 0$ and $k_x = 0.8$Å^{-1} are

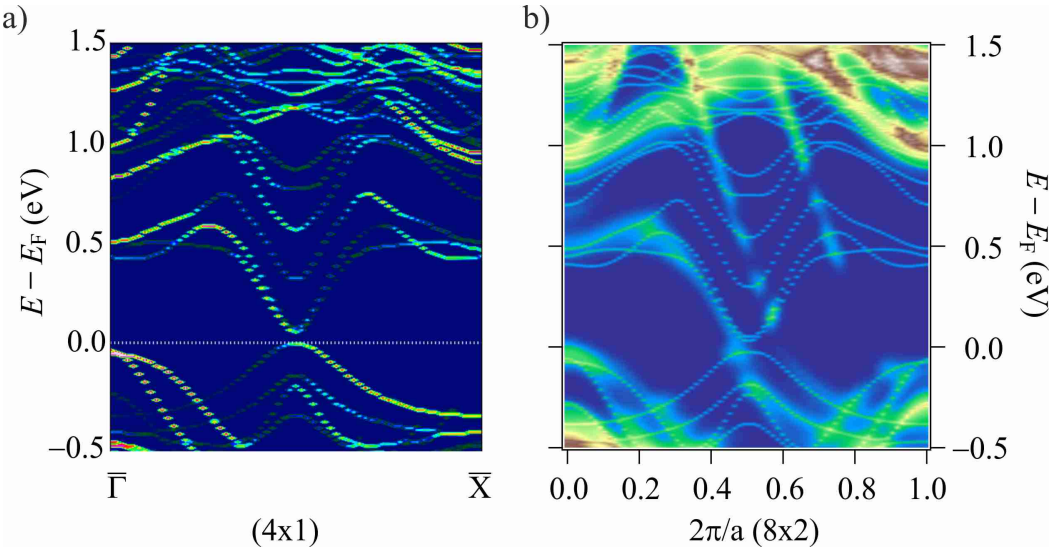

Figure 7.8: a) DFT calculated (8x2) band structure unfolded onto the (4x1) states to reveal the expected distribution of spectral weight in the low temperature phase. b) A simple comparison to the unfolded bands whereby the overlap between (8x2) and (4x1) states is shown.

in principle equivalent: both are $\overline{\Gamma}$-points of the (8x2) phase. The reason for this discrepancy is at this stage unclear, and may be the subject of future studies; one possibility is that enhanced excitonic coupling due to the reduced dimensionality of the system plays a role and is a direction for future work.

Regarding the expected gap at the (8x2) zone boundary ($k_x = 0.4$Å^{-1}) the overview data presented here do not clearly show such a feature. It is likely due to the intrinsic energy resolution of the trARPES experiment ($\sim$ 150 meV) that such a feature is not clearly seen in this 2D image. However a finer analysis reveals that this gap is indeed observable with the current experimental setup and will be presented in detail below.

One notices that the spectral weight distribution in the (8x2) phase strongly follows that of the (4x1) phase, with some modifications. This is often observed in CDW systems with the resulting renormalised dispersion (so called "shadow bands") in the CDW phase much weaker compared with the original dispersion (see also the discussion in section 2.5.3). To address this more precisely in the In/Si(111) system, an "unfolding" of the bands has been performed as in Ref.[XX] to map the spectral weight in the (8x2) phase onto a (4x1) basis in order to compare directly with the spectral weight distribution in the experiment, shown in Fig. 7.7c. This clearly reveals a strong tendency of spectral weight to follow the (4x1) dispersion and can also be compared with Fig. 7.4b in the unexcited low temperature phase where the back-folded band is clearly seen. A quick cross check is made by overlapping a broadened (4x1) structure with the (8x2) bands, shown in Fig. 7.7d. This reproduces the main results of the unfolded calculation, although such a simple approach does not capture all features. Note that these comparisons have been performed on a DFT-calculated band structure which severely underestimates the band gap at both $\overline{\Gamma}$ and $\overline{X}$ points.

The 2D momentum mapping of the (8x2) phase is shown in Fig. 7.9a, c and e for energies 1 eV, 0.7 eV and 0.1 eV above the Fermi level over the same momentum

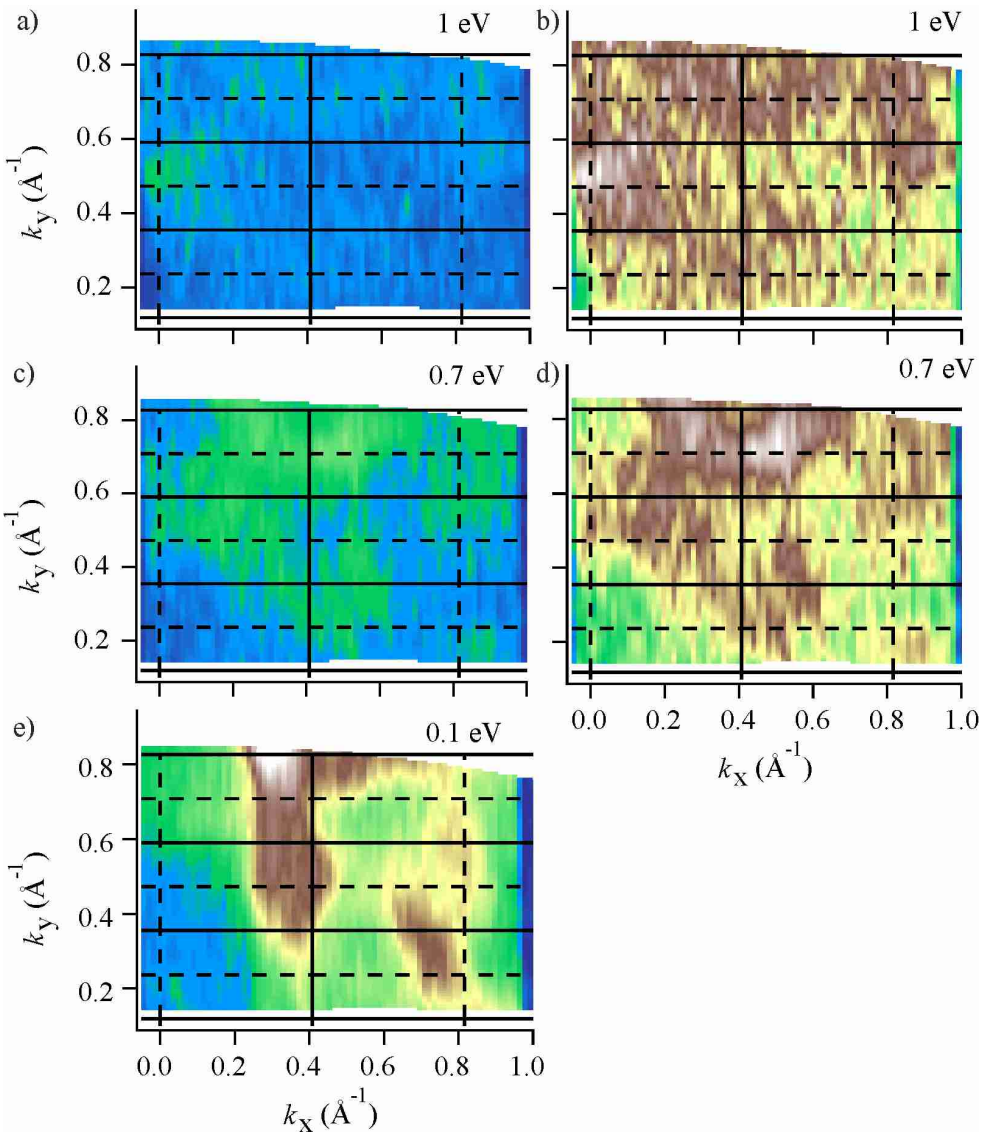

Figure 7.9: Excited state mapping of the (8x2) phase at a) 1 eV c) 0.7 eV and e) 0.1 eV above the Fermi level. Higher energy distributions are highlighted in b) and d). Data obtained at 25 K with HHG photons at 22.2 eV and 1.5 eV excitation.

range as presented before in the (4x1) phase. This data has been obtained at 25 K with a pump fluence of ∼0.8 mJ cm^{-1}. As in the case of the (4x1) phase, higher lying states are found to have weaker intensity, and are therefore presented also with a second colour scale in b and d. Again the influence of the underlying (4x1) phase is evident in the distribution of electrons throughout the BZ.

Such a mapping of the transient population is of particular interest for the dynamics of the phase transition, as the transient occupation of the electronic structure produces forces on the atoms in the system, and defines the potential energy landscape. As a result the excited states distributions presented here, and their relevance to the photoinduced phase transition will be discussed in greater detail in the following sections.

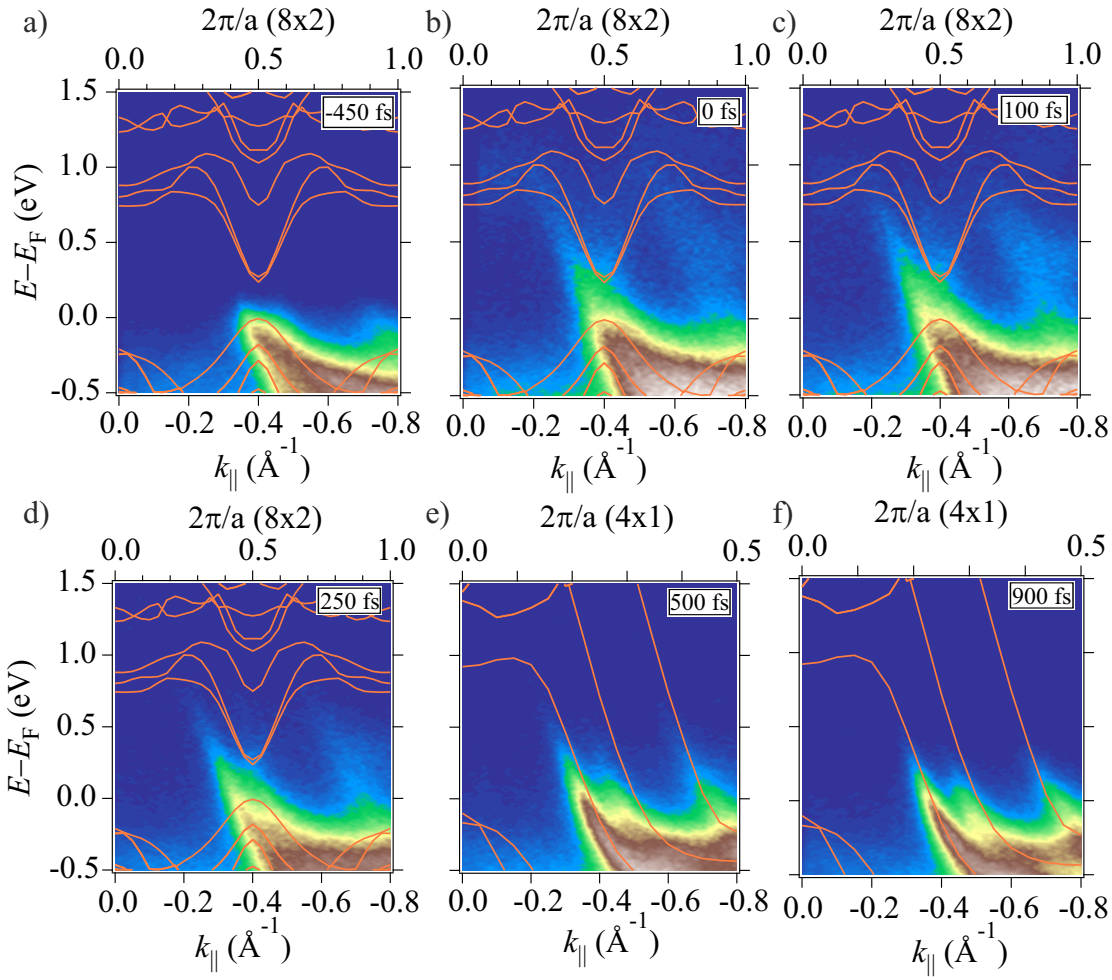

Figure 7.10: Snapshots of the In/Si(111) bands at selected time delays, given in the panels. The GW band structure of the (8x2) and (4x1) are overlaid, highlighting the photoinduced phase transition.

7.3 Photoinduced Phase Transition

Until now only a static view of the (8x2) structure has been presented, as an extension of the band mapping of occupied states typically accessible with ARPES. Going beyond this to access the dynamic, time-resolved band structure allows for a energy and momentum-resolved investigation of the phase transition between (8x2) and (4x1) phases, as will now be shown. The In/Si(111) nanowires are cooled to 25 K – well below the phase transition temperature – and then measured with the pump-probe scheme outlined in chapter 2. Snapshots of the electronic structure at six pump-probe delays obtained at a pump fluence of 2.1 mJ cm^{-2} are shown in Fig.7.10. Before the arrival of the pump (panel a, negative delays) the (8x2) phase band structure is evident with the gapped m_2 and m_3 bands at the (8x2) zone boundary, and only weak residual intensity in the m_1 band (c.f. Fig. 7.4b). GW calculations are overlaid as a reference. At pump-probe overlap (panel b, 0 fs) states are excited by 1.5 eV pump photons above the Fermi level, as discussed in the previous section. Following excitation, not only do electrons redistribute in energy and momentum as a result of scattering throughout the Brillouin zone, but the band structure itself is also

observed to change.

The evolution of the band structure following excitation is shown in panels c-f for time delays up to 900 fs as shown in the individual panels. Particularly striking is the comparison between panels a and f: while the band structure before excitation is that of the (8x2) phase, at 900 fs the three bands characteristic of the (4x1) phase are clearly discernible. This strongly suggests that the system has been driven into the high temperature phase in less than 1 ps. The transient evolution of individual regions of k-space will be addressed in more detail in the next section, but from this overview it is already clear that a number of changes occur. Firstly, the gap at the (8x2) boundary has to close in order to transition to the (4x1) metallic bands. Secondly there is a large transfer of spectral weight from the excited m_1 band (above E_F in the (8x2) phase) to lower energies, which ultimately becomes the occupied m_1 band of the (4x1) phase. The changes in these two regions of the Brillouin zone have been found to correspond to the two structural distortions calculated by DFT, that transforms the (8x2) into the (4x1) phase [Gon05, Jec16, Fri17]; each mode induces changes in a particular region of k-space. Additionally it is noted that even after 1 ps there are hot electrons still at energies up to 500 meV, implying a persistently elevated electron temperature.

7.3.1 Momentum Resolved Dynamics

The time resolved data from above are now analysed in greater detail, with the dynamics at the (8x2) zone boundary presented first. Raw EDCs centred at $k_x = 0.4\text{Å}^{-1}$ ($\pm$ 0.02Å^{-1}) are presented for multiple pump-probe delays in Fig. 7.11a. Before excitation, a single peak corresponding to the broad overlapping m_2 and m_3 bands is observed. Once excited, a number of hot carriers are produced as seen by the increase of intensity above E_F. Of particular interest is the development of a second peak above E_F observed as a shoulder on the peak present before excitation; the two peaks are marked in the figure. This feature in the excited states is assigned as the conduction band (CB) of the (8x2) phase above the m_2, m_3 gap. It now becomes clear why the band gap could not be seen directly by eye in Fig. 7.10: the spectral feature of the CB is weak due to the high background of excited carriers, and can only clearly be resolved on a log scale plot. In order to extract quantitative dynamics of the bands, the EDCs are fitted to obtain the position of the states as a function of pump-probe delay, a representative fit at 100 fs is given in Fig. 7.11b. The spectra are fitted with two Gaussians on top of a linearly decreasing background. The position of both peaks as a function of pulse delay is then presented in Fig. 7.11c. A maximum gap size of 0.39 eV is observed which is seen to gradually close over time as the two peaks merge together. After 200 fs the two peaks are no longer separable, which is taken to mean that the electronic gap in the system has closed. This fast gap closing at the (8x2) zone boundary therefore corresponds to the insulator-to-metal transition in the system, which as will be seen shortly is faster than the structural phase transition which takes hundreds of femtoseconds longer.

The second time scale in the system – the shift of the band at the zone centre – is now presented. Please note that it is states at the *second* BZ centre ($k_x \sim 0.8\text{Å}^{-1}$) that are observed to shift, while those at k_x=0 do not shift but only depopulate after the initial excitation. EDCs at $k_x = 0.75\text{Å}^{-1}$ ($\pm$ 0.02Å^{-1}) are presented in Fig. 7.12a. The spectra before excitation shows a broad intensity distribution corresponding to

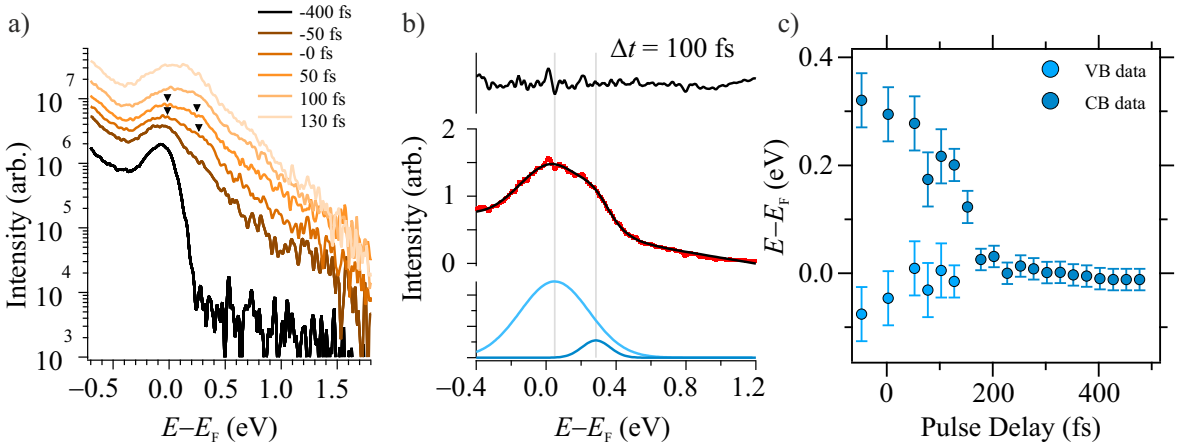

Figure 7.11: Zone boundary dynamics during the (8x2) to (4x1) phase transition. a) EDCs around $k_x = 0.4\text{Å}^{-1}$ starting from the (8x2) phase and after excitation. After excitation both valence and conduction bands are visible. The EDCs are offset for clarity. b) Fit of the EDC at a pulse delay of 100 fs; data is shown as red markers and the fit is overlaid as a black line. Underneath are shown the fitted Gaussians (blue curves); above is the fit residual (black curve). c) Extracted valence (VB) and conduction band (CB) positions as a function of pump-probe delay showing the closing of the electronic gap.

the residual (4x1) spectral weight of the m_1 band. Shortly after excitation peaks at 0.46 eV and 1.12 eV above the Fermi level are clearly observed. This is clearly different from the excited states of the (4x1) structure along the same cut in k-space as shown already in Fig. 7.5a and c, where only the higher excited band is observed. The band at 0.46 eV is understood to be the m_1 band of the (8x2) phase i.e. unpopulated at equilibrium. Already by eye in Fig. 7.10 one sees that this band is shifting downwards on a time scale of <1 ps. This is again addressed more exactly by a fitting analysis of the bands. Fig. 7.12b shows the results of fitted EDCs over the k-space range covered by this unoccupied m_1 band. In such a way it is possible to extract the dispersion of the band as a function of time delay and reveal clearly the downwards shift of this band by hundreds of meV. The position of the band minimum is also tracked and given in Fig. 7.12c. One sees the shift of the band from well above the Fermi level to just below is completed after 500 fs. At this point the band has formed the metallic m_1 band of the (4x1) phase (see also Fig. 7.10f). In contrast, the energetic position of the band intially at 1.12 eV is observed to be constant.

Thus after 500 fs the two electronic gaps of the system are closed, which leads naturally to the question of whether the phase transition is complete at this time or not? To answer such a question it is required to probe a feature that is sensitive to the change of structural symmetry in the system as the transition develops. We address two features that may indeed give the required sensitivity in Fig. 7.13. The first is the splitting of the m_2 and m_3 bands which is clearly observed to change between the two states in Fig. 7.10. In the (8x2) phase the two bands strongly overlap at the Fermi level, as already described, whereas in the (4x1) phase the states are clearly separated. Hence the splitting of the bands is likely to reflect the overall phase transition. The position of the two bands is analysed by taking an MDC

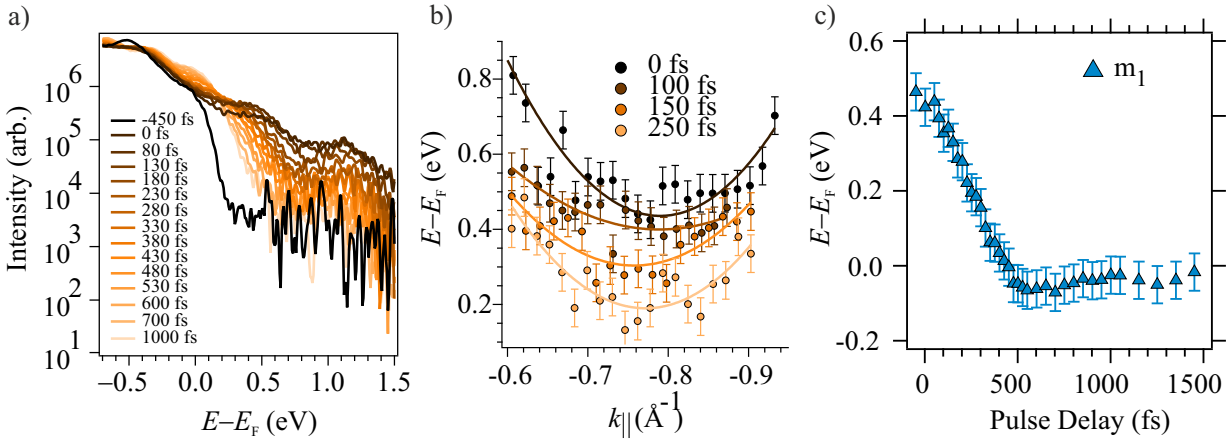

Figure 7.12: Zone centre dynamics during the (8x2) to (4x1) phase transition. a) EDCs around $k_x = 0.75$Å^{-1} for various time delays before and after excitation. Two states above E_F are clearly visible; the lower one evolves over time. b) Band dispersion in the excited states extracted from EDC fitting over the shown momentum range. The band is clearly shown to shift down towards the Fermi level over time. c) The extracted band minimum as a function of pump-probe delay, revealing the band evolves into the metallic (4x1) m_1 band after 500 fs.

(momentum distribution curve) at the Fermi level for each time point, as shown in Fig. 7.13a. The MDC is then fitted with two Gaussians on a constant background to extract the position of the peaks, which is overlaid on the image. In this way the evolution of the splitting becomes very clear: the m_2 moves significantly while the m_1 band is much less affected in terms of momentum position. By taking the difference between the two band positions, shown in Fig. 7.13b, the overall dynamics of the peaks is revealed. From this it is clear that at 500 fs the system is still evolving, as a stable value is only reached after 700 fs.

The second feature of interest is the spectral weight in the two arms of the parabolic m_1 band in the (8x2) phase. At this point in k-space the electron parabola in the (8x2) phase (Fig. 7.12b) transforms into the m_1 band of the (4x1) phase by transferring spectral weight out of the right arm of the dispersion. The left arm on the other hand is observed to smoothly transform into the dispersion of the (4x1) phase. This should lead to an uneven evolution of the spectral weight in the two arms. The development of spectral weight for the two arms is shown in Fig. 7.13c, where "left" and "right", corresponds to the dispersion in b. Spectral weight is integrated over a square region centred at 0.5 eV ($\pm$ 0.025 eV) above E_F for two momentum regions symmetric about the band minimum. A clear difference in the two regions is observed. The left arm (which becomes the metallic band) increases due to excitation and then stays at a roughly constant level for a few hundred femtoseconds as electrons scattering into the integrated region from higher lying energy states are balanced by electrons scattering out to lower energy states. Then, gradually, the intensity decreases as electrons scatter out of the window and are no longer replaced by higher lying states. In contrast the right arm is more or less constant up to 450 fs, after which it rapidly loses intensity. The rapid decrease cannot be explained by electrons scattering out of the integrated window region however, as both arms should behave in the same way. This points in the direction of a spectral weight transfer driven by the removal of the states themselves, due to the changing symmetry of the system.

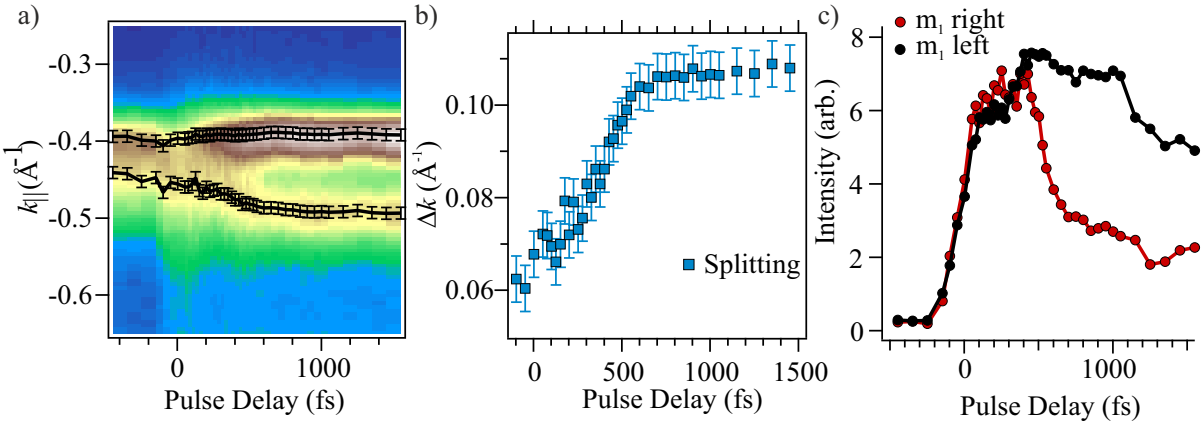

Figure 7.13: Structural dynamics of the (8x2) to (4x1) phase transition. a) MDC cuts at the Fermi level showing the m_2 and m_3 bands as a function of time. The fitted positions are overlaid. b) Difference between the extracted positions revealing dynamics longer than 500 fs. c) Spectral weight dynamics in the two branches of the unoccupied m_1 band. The unequal dynamics reveal a transfer away from (8x2) states only after 450 fs, and lasting until around 1 ps.

In this case the spectral weight is removed from the right arm because the states do not exist in the (4x1) phase, rather than simply that electrons scatter out of the bands. Such a case has also been described in the section 2.5.3 on spectral weight in CDW systems in ARPES measurements. This measurement also implies that the phase transition is indeed not complete after 500 fs since at this time these states start to disappear, but still persist until 700 fs.

These three time scales allow us to chart the progress of the optically induced (8x2) to (4x1) phase transition. The first gap closing occurs already after 200 fs at the (8x2) zone boundary, and gives the time scale of the insulator-to-metal transition in the system. According to calculations, the dynamics in this momentum region can also be related to the motion of the hexagonal rotation mode shown in Fig. 7.2. Next, the m_1 band at the (8x2) centre is observed to shift below the Fermi level and transform into the metallic (occupied) m_1 after 500 fs. This relates to the dynamics of the shear mode (Fig. 7.2). A more detailed discussion of the driving mechanism of the phase transition obtained by comparing to theory will be discussed further in a subsequent section. The final time scale – that of the structural transition – occurs only after both electronic gaps have closed. According to our data it takes between 700 fs and 1 ps for the transition to fully occur, from the point of view of the symmetry of the system. This is very different to standard Peierls materials such as the RTe$_3$ family [Sch08, Ret14, Ret16] in which the closing of electronic gaps and the transfer of spectral weight from renormalised bands of the broken symmetry phase occur simultaneously. It is also worth noting that the time scale of the structural transition obtained from the ARPES data presented here is in good agreement with the observations from trRHEED measurements that the phase transition is completed after around 1 ps [Fri17].

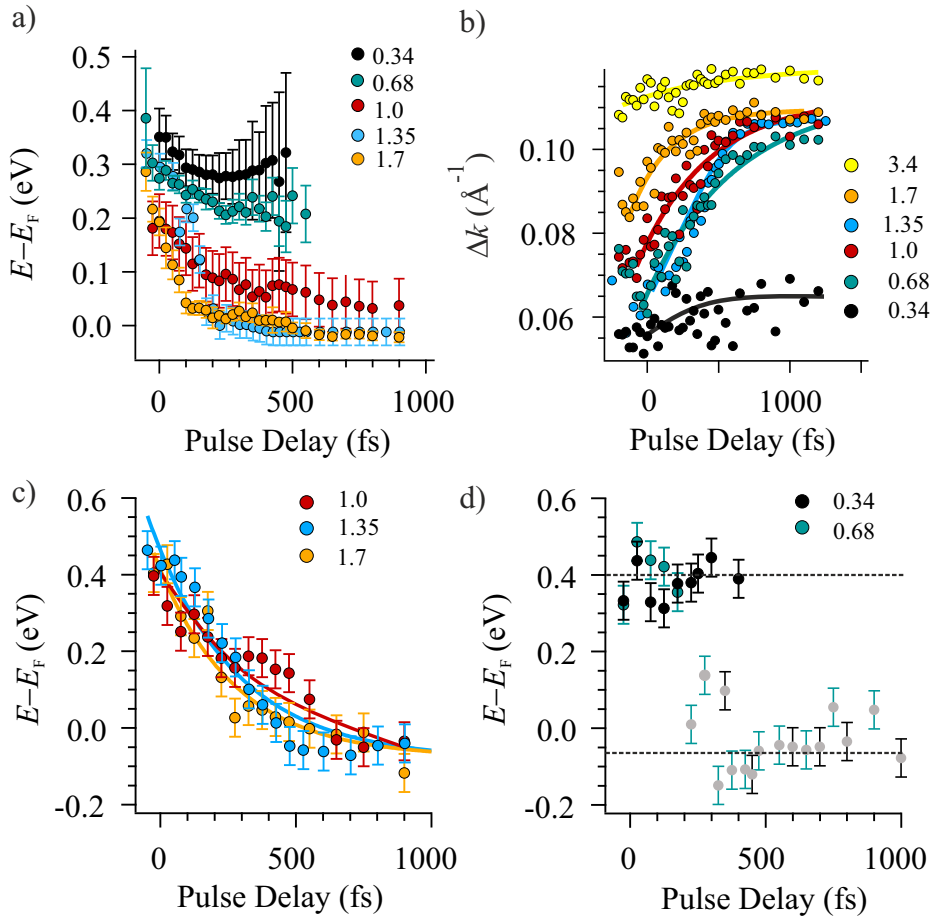

Figure 7.14: Fluence dependent phase transition dynamics at a) the (8x2) zone boundary and c), d) the (8x2) zone centre. b) Structural dynamics given by the splitting between peaks m_2 and m_3. The fluence values in the legends are given in mJ cm^{-1}.

7.3.2 Fluence Dependence

The phase transition data presented in the previous section was all obtained at a single fluence of 1.35 mJ cm^{-2}, and an obvious question is: how do the dynamics of the phase transition change if the fluence is varied? Fig. 7.14 summarises the fluence dependent results for the three regions already presented i.e. zone boundary gap (a), structural transition (b) and zone centre gap (c and d).

The zone boundary gap shows very similar dynamics for the highest three of the presented fluences, closing after around 200 fs. In contrast the two lowest fluences clearly show different dynamics. The excited CB is still observed, and shifts down over time, but it always remains above the Fermi level; as a result the gap never fully closes and an insulator-to-metal transition never occurs. However the gap is still reduced, meaning the phase transition is only partially driven. Very similar behaviour is observed for the zone centre dynamics (shown in c and d). The three highest fluences (c) show the m_1 band shifting gradually down below the Fermi level, again within errors on the same 500 fs time scale. The lowest fluence (0.34 mJ cm^{-2}), shown in panel (d) does not follow such a trend but instead is seen to remain constant at the initial excited state position. After around 400 fs there is no longer enough intensity in the excited states to produce a reliable fit and the peak

jumps to the lower energy position of the valence band. The reason the fit finds a maximum at this position is that a small amount of intensity in the metallic m_1 band is found at this position in the Brillouin zone, even far below the transition temperature (see e.g. the high resolution He data in Fig. 7.4). The reason for this residual intensity is unclear, but it is likely to result from the coexistence of (8x2) and (4x1) phases in domains [Guo05] which may be stabilised by defects or adsorbates [Lee02, Mor10]. These positions are marked in grey as they reflect different states to those at smaller time delays. The two levels are highlighted by the dashed lines. Data at 0.68 mJ cm^{-2} shows similar two level behaviour, although less clearly which may reflect a partial closing of the m_1 gap at this higher excitation density. The combination of these data sets implies a threshold excitation density between 0.68 and 1.0 mJ cm^{-2} above which the phase transition is fully driven, and below which it is only driven partially. This appears to be in agreement with the threshold value obtained from trRHEED measurements [Fri17].

The behaviour of the structural dynamics (panel b) is a little more complicated to interpret. For the lowest fluence data, 0.34 mJ cm^{-2}, the peak splitting increases slightly after excitation and then appears to reach a constant value – although note that the low fluence results in noisy data – implying that the (8x2) structure is only perturbed at this fluence, consistent with the dynamics at the zone centre and boundary. In contrast at the very highest fluence of 3.4 mJ cm^{-2}, the size of variation is again small, but the value is shifted to a higher value. In this case it appears that the transition is almost completed even at negative time delays, which may be due to an average heating of the sample due to the high repetition rate used during these experiments, combined with the high incident power in this particular measurement. The result is that the energy deposited into the system is too much for it to fully relax between laser shots and hence the phase transition dynamics are not observed. The influence of sample degradation can be ruled out as the cause of this effect due to the order in which the data was acquired: 1.35 and 3.4 mJ cm^{-2} being the first two to be measured, followed by those at lower fluences. Intermediate fluences e.g. 1.7 mJ cm^{-2} start to show some influence of this average heating effect, seen by gradual increase of the starting position of the dynamic curve. If the initial offset due to heating is removed by scaling the curves on to each other, all fluences show dynamics with the same time constant, implying the structural transition proceeds at the same regardless of excitation density. This is in contrast to what has been observed in trRHEED, where an increase of the time constant for the structural transition is observed for low fluences [Fri17]. In order to check whether residual intensity at E_F caused by domains could play a role in this, the analysis was repeated at lower binding energies. Although the absolute value of the splitting is slightly different, the same dynamic behaviour is found. However it could still be that in the trARPES experiments, which are spatially averaged, the dynamics observed are always those of a mixed phase sample, as suggested by the residual intensity of the m_1 band. The result being that when enough energy is given to the regions of (8x2) they are driven into the (4x1) phase on the same time scale. Furthermore the 0.68 mJ cm^{-2} fluence data shows a structural transition change that appears consistent with a full transition, in contrast to the electronic gap analysis. This is somewhat puzzling. In the case of the previous simulations, when a low fluence is applied – one that does not fully drive the transition – the time scale is extracted from a trajectory that has a shallower curve, but the system does not end up in the (4x1) phase (Fig. 3

Ref. [Fri17]). As a result a longer time constant is extracted, even though the phase transition does not occur. For the trRHEED, it has previously been shown that adsorbates on the surface strongly affect the dynamics of the (4x1) to (8x2) transition [Wal12a]. This should also affect the (8x2) to (4x1) transition, as (8x2) domains are known to be stabilised by adsorbates [Lee02, Mor10, Uhm13, Oh14]. Considering that the trRHEED measurements have been conducted in UHV pressures around one order of magnitude higher ($2x10^{-10}$ mbar) than in our trARPES chambers ($3x10^{-11}$ mbar), it is perhaps to be expected that the exact form of the fluence dependence of the structural transition would therefore differ. This does however suggest the intriguing possibility of controlling the structural dynamics via doping.

Overall however, the fluence dependent data are consistent with a phase transition which occurs only above a threshold excitation level. In the transition regime, no clear evidence for a difference in time scales is observed, instead the dynamics data curves fall very closely on top of one another. Below the threshold value the electronic structure is changed only slightly, depending on the level of excitation. Overall this behaviour is very similar to that observed by trRHEED [Fri17] (Fig. 2c), although the exact dependence on fluence differs.

7.3.3 Recovery Dynamics

A further aspect related to the phase transition is the recovery of the (8x2) phase from the photoexcited (4x1) phase. The ultrafast dynamics of the structural transition have already been studied with trRHEED [Wal12a] where it has been shown that the recovery time depends on the time the sample has spent in UHV. The rate of recovery was found to increase with time in UHV i.e. with the number of absorbates (and presumably also defects). It was suggested from this study that defects act as nucleation centres around which the (8x2) phase can form, and then propagate along the atomic chains. All data presented in this previous study were obtained at a fluence of 2.1 mJ cm^{-2}. Note that the experiments were performed at a base pressure of $2x10^{-10}$ mbar: almost an order of magnitude higher than in our trARPES experiments. As a result, residual gas absorption can be expected to play a less critical role in our data. The recovery itself has been found to take hundreds of picoseconds ($\tau = 440$ ps), suggesting the photoinduced (4x1) phase is metastable, requiring an energy barrier to be overcome before transforming back to the (8x2) [Wal12a]. The metastable potential is, however, obtained from a ground state calculation, and it is not obvious that the form of the double well potential should persist after photoexcitation, or indeed that the 40 meV barrier extracted should hinder the recovery in such a highly excited system. It is noted that the nucleation of the low temperature phase at adsorbates does not in itself explain the observed long recovery times of the (8x2) phase, but does explain the relative decrease of recovery time with increased adsorbate concentration.

Here we show the results obtained with trARPES for the recovery dynamics. Since electronic states are rapidly depopulated within a few picoseconds after excitation, it is not possible to follow the three signatures of the phase transition presented in the previous sections with our current setup: to do so would require a three pulse experiment e.g. Ref. [Ret14]; this may be interesting for future measurements. Instead we focus on what can be measured in the occupied states: the splitting of m_2 and m_3 bands representing the structural transition, and the broadening of

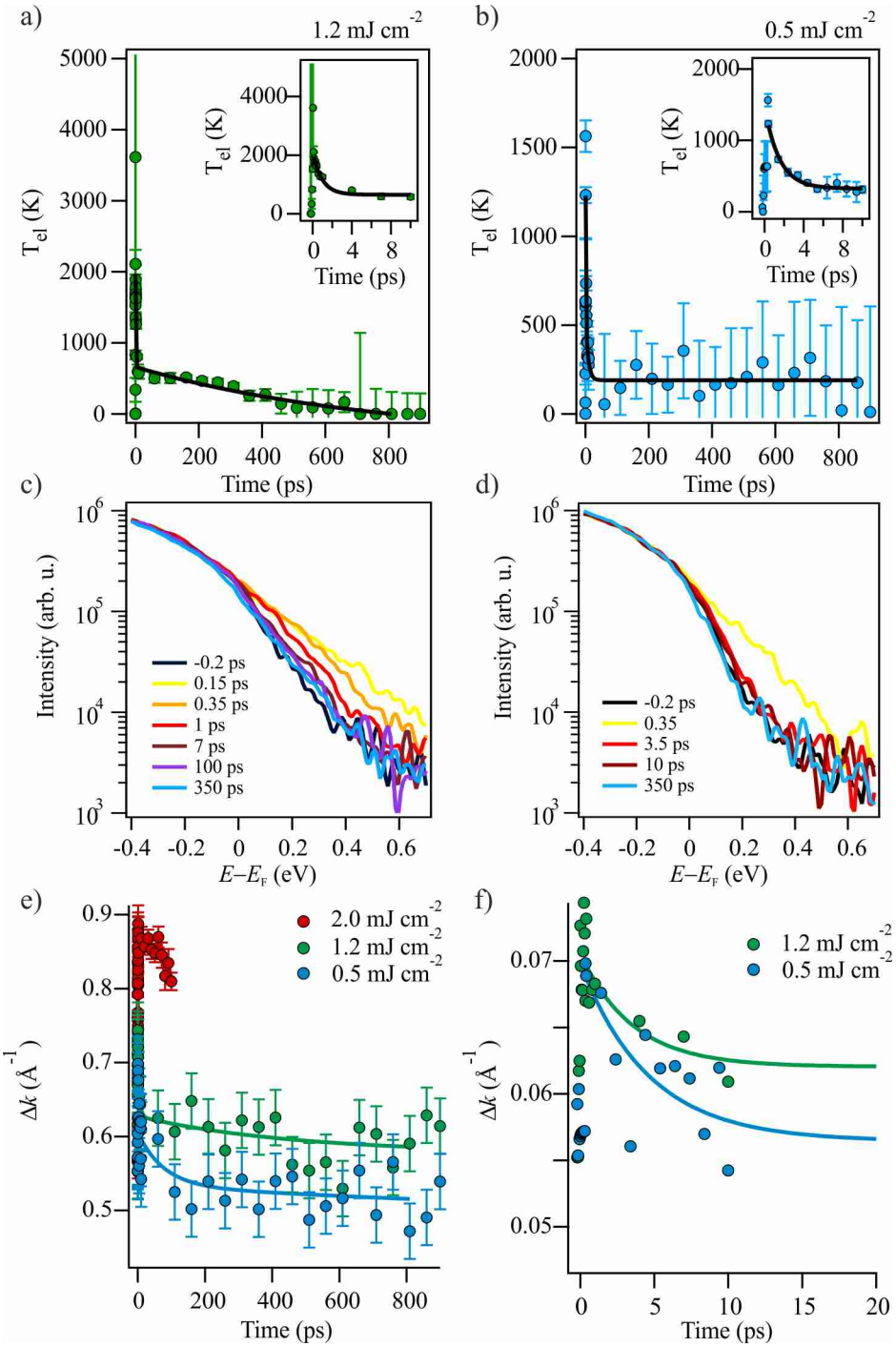

Figure 7.15: Recovery of (8x2) phase. Electronic temperature at long time delays for a) 1.2 mJ cm^{-2} and b) 0.5 mJ cm^{-2}. The inset in each case is an expanded region at delays up to 10 ps. EDCs from which the electronic temperature are extracted are shown in c) and d) for 1.2 mJ cm^{-2} and 0.5 mJ cm^{-2} respectively. e) Recovery of the structural transition (peak splitting) and f) expanded axis up to 20 ps.

the Fermi level (electronic temperature), both of which are presented in Fig. 7.15. The electronic temperature (panels a and b) is extracted from EDCs averaged over the measured k-space region. The EDCs are fitted with Gaussian peaks convolved with a Fermi-Dirac distribution and the experimental resolution. A more detailed analysis on short time scales is presented in a subsequent section and used as an input to theoretical simulations. It is found that the system is already electronically thermalised after a few tens of femtoseconds (Fig. 7.21); thus on the time scale of a few picoseconds such a thermal description is entirely appropriate. After an initial rapid increase following excitation, two time scales are observed in the 1.2 mJ cm^{-2} data (Fig. 7.15a): a rapid decrease to around 1000 K with $\tau = 0.95 \pm 0.1$ ps followed by a much longer, gradual decrease towards the base temperature which takes around 350 $\pm$100 ps, as judged from the time-resolved EDCs ((Fig. 7.15c)). The peak splitting data at this fluence (*panel e*) show a long time recovery with $\tau = 460 \pm 100$ ps. This latter time scale matches the electron diffraction result of $\tau = 440$ ps within experimental margins. We note that in addition to the long time recovery of the peak splitting, a second shorter time scale of $\tau = 5.5 \pm 2$ ps is observed.

At the lower fluence of 0.5 mJ cm^{-2} somewhat different dynamics are observed. In this case both the electronic temperature and the structure relax to their base levels much faster than at the higher fluence. The electronic temperature recovers with a fast component of $\tau = 1.5 \pm 0.2$ ps, similar to the high fluence data. Recovery to the base temperature is completed after around 10 $\pm$5 ps, much faster than at the higher fluence. Note that the reduced statistics available for low fluence pumping introduce significant error margins. Again, the peak splitting shows a short time scale similar to the high fluence data of $\tau = 6$ ps, but the second relaxation to the base level is now only $\tau = 80 \pm 90$ ps. As a final point it is noted that at a fluence of 2.0 mJ cm^{-2} a more sustained level of peak splitting is observed (red trace in panel c). Unfortunately the data does not extend to the long times available at the two lower fluences, but it hints that the recovery dynamics at higher fluences may be even slower; further measurements are required to confirm this. It would also be interesting to compare to diffraction results at different fluences, once the role of the residual gas has been minimised.

Regarding the metastable (4x1) phase, a possible explanation is that the energy injected into the system by the laser pulse is inefficiently removed from the In layer, as evidenced by the electronic temperature. The short time scale of $\sim$1 ps is remarkably rapid for such a quasi-1D surface system, but most likely occurs from the transfer of energy to the manifold of surface optical phonons present in the system [Fri17]. However it is clear that after a few ps (Fig. 7.21), and even up to a couple of hundred ps (Fig. 7.15), highly excited states persist. It seems clear that the coupling of these surface modes, to the substrate is not an efficient heat sink; the same goes for the electronic wavefunctions, which are localised in the Si bulk band gap. As a result the electronic temperature remains high even for long delays. This suggests that it is this failure to remove excess energy from the In wires that allows for the metastable behaviour of the photoexcited (4x1) phase. At longer times the energy stored in the electronic system will be transferred to the lattice via the excitation of incoherently excited acoustic phonons, presumably proceeding through the In layer and into the Si bulk. The strength of coupling between the In and Si layers therefore appears to be small, considering the long time that the system required to lose its heat. It

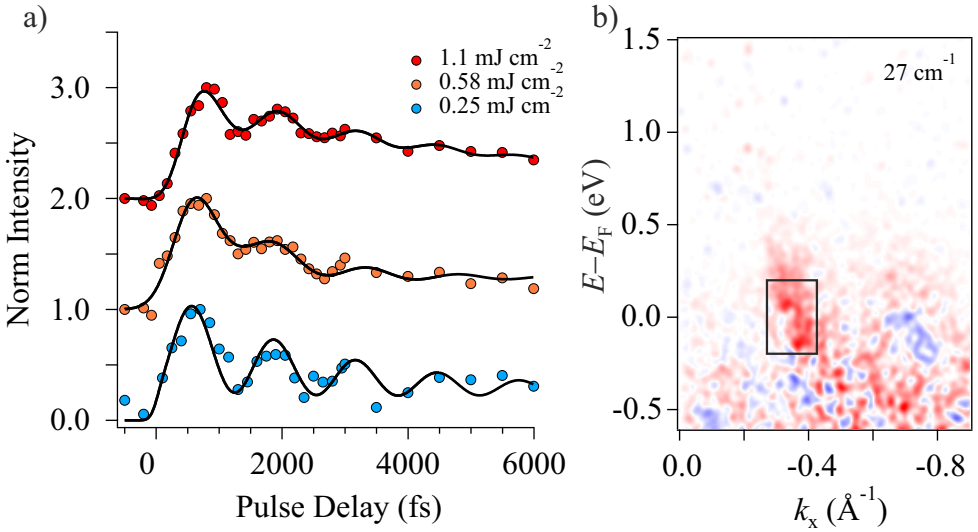

Figure 7.16: a) Coherent oscillations of the amplitude mode at 27 cm^{-1} at three fluences from the region of the band structure corresponding to the m_3 band, as marked in b. Oscillations at this frequency are not observed in the other bands. b) 2D difference image at the maximum and minimum of the oscillation, revealing the 27 cm^{-1} mode most strongly affects the m_3 band.

would be interesting to quantify this coupling by measuring the dispersion in the direction perpendicular to the surface, which could be achieved by a photon energy dependent study.

7.3.4 Coherent Oscillations

As the phase transition is thought to be a multi-band Peierls-like type transition, it is reasonable to ask whether coherent excitation of the amplitude mode (see chapter 2) is possible, as has been observed in other CDW systems e.g. Refs. [Sch08, Ret14, Ret16]. The possible amplitude modes as determined by DFT calculations [Wip10] are the rotary and shear distortions already described in previous sections and shown in Fig. 7.2. Most convincingly these modes have been observed to soften upon approaching the transition temperature [Jec16], as is expected due to the "frozen-in" distortion being gradually removed. These modes have nominal frequencies of 20 cm^{-1} (shear) and 28 cm^{-1} (rotary) respectively and are observed to soften by around 10% at 120 K.

Amplitude Mode

Low temperature data does indeed show a coherent response, as presented in Fig. 7.16a for three fluences, which appears at 27 $\pm$ 3 cm^{-1}. The observed frequency is already suggestive that this could relate to the oscillation of the rotary mode (28 cm^{-1}). Data have also been taken above the transition temperature, at 180 K, where the mode is no longer observed, as expected for a mode that exists only in the (8x2) phase. An additional piece of evidence is that the rotary mode is expected to most strongly affect the bands at the (8x2) zone boundary, causing the band gap opening in the m_2 and m_3 bands. In order to confirm this, a difference image between data obtained in the peak and the trough of the oscillation is extracted and shown in

Fig. 7.16b. The strong red (positive) signal does indeed most strongly show up in the expected m_2, m_3 region of k-space, lending further weight to this being the amplitude mode.

Intriguingly the oscillations are still observed for fluences above which the phase transition is driven, according to the previously presented analysis. As has been observed both in Raman studies [Jec16, Spe16], and also in the present data, in the case of the thermally driven transition, the oscillation completely disappears above the transition temperature. Thus it appears that the amplitude mode can exist even once the photoexcited (4x1) phase has been fully reached. The current situation contrasts to the $R\mathrm{Te}_3$ family of CDW compounds [Sch08, Ret14, Ret16]. The phase transition in $R\mathrm{Te}_3$ is never fully completed, as seen from the fact that the CDW gap never completely closes, even at high excitation densities [Ret16]; therefore the oscillation of the amplitude mode persists always in a broken symmetry phase, albeit an excited one. In the present case of In/Si(111) the indications from the electronic structure are that the electronic gaps *fully* close and that the structure becomes that of the (4x1) phase. In this case the excitation of the amplitude mode is not expected, as it exists only in the ground state. However since the amplitude mode is always excited in the (8x2) phase it may still possible for the mode to continue to ring after the transition, despite the change of symmetry in the system. In contrast, studies on VO_2 – which also exhibits an complete insulator-to-metal transition above a threshold fluence – have shown that at high fluences the phonon modes of the insulating phase are lost within the time scale of the excitation pulse, while close to this threshold the phonon modes are excited but rapidly disappear [Wal12b, Wal13]. It would be interesting to perform further investigations to compare the amplitude mode in both the ground state and photoexcited state in In/Si(111). Determining whether the photoexcited (4x1) phase is equivalent or not to the thermal would be of particular intriguing: in the case that they are inequivalent this would be evidence for a "hidden-state" [Ich11, Sto14]. This could be achieved via a three pulse experiment [Wal13, Ret14], in order to attempt to re-excite the amplitude mode at a time when the transition is already complete.

Spectator Phonon

In addition to the amplitude mode, a second coherent oscillation is observed as shown in Fig. 7.17a. This mode occurs at 80 cm^{-1}, which is a much higher energy than either of the expected amplitude modes and is therefore unlikely to be involved in the phase transition. In fact this mode is also observed well above the transition temperature (180 K), which is strong evidence that this phonon plays no direct role in the phase transition, and is therefore a spectator mode. The same difference plot analysis as presented for the amplitude mode is presented for the 80 cm^{-1} mode in Fig. 7.17b. In this case the effect of the oscillation is seen in all three bands, in contrast to the more localised effect of the amplitude mode. Given the wavenumber, this oscillation may correspond to a lateral displacement of parallel In wires perpendicular to the shear motion [Spe16]. It has been shown theoretically that after excitation the energy in the system is rapidly transferred into a large number of phonon modes, but it is not clear why this particular mode should show up so strongly.

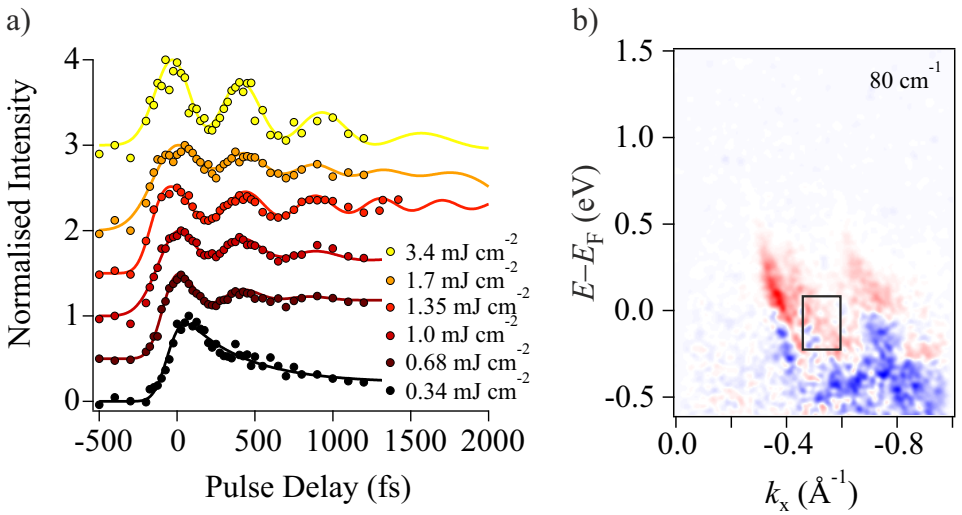

Figure 7.17: a) Coherent oscillations of the spectator mode at 80 cm^{-1} at various fluences from the region of the band structure corresponding to the m_2 band, as marked in b. b) The 2D difference image at the maximum and minimum of the oscillation is shown, revealing this mode is present in all three bands in contrast to the amplitude mode.

7.4 Simulations and Phase Transition Mechanism

In chemical and structural reactions the system evolves along a Born-Oppenheimer (BO) potential energy surface from reactants to products; or in the case of phase transitions, from phase 1 to phase 2. The BO surface is determined by the electrons: in particular the transient electronic band structure and its occupation. This means that the forces moving atoms around depend on the distribution of electrons in excited states, which naturally suggests trARPES as an important probe for understanding the origin of the microscopic forces that drive the phase transition.

The previous combined study of the In/Si(111) system with trRHEED and DFT-based molecular dynamics (MD) simulations by Frigge *et al.* [Fri17] has shown that the time scale of the photoinduced ultrafast (8x2) to (4x1) transition can be well reproduced by simulations. However one should be cautious in claiming the phase transition can be understood microscopically from this. It is found that a very particular distribution of electrons and holes is required to drive the phase transition; namely that the electrons should be localised at the centre of the Brillouin zone, and at the same time holes must be localised at the Brillouin zone boundary as shown in Fig.7.18. Alternative distributions are found not to drive the phase transition. There are two significant weaknesses with these simulations: 1) the assumed electronic distribution has not been justified experimentally, as this requires a momentum and energy mapping of the full Brillouin zone not accessible during the trRHEED study and 2) the excited electrons are assumed to stay in the excited states at the initial excitation density for the entire simulation without relaxing. This is clearly not a physically realistic situation for an optically induced phase transition, as after excitation electrons will scatter from higher to lower lying energy levels. In particular since electrons will scatter to the lowest energy point i.e. that closest to the Fermi level, the assumption that the electrons sit at the $\overline{\Gamma}$-point is therefore particularly suspect, as the m_2 and m_3 bands join these states to the Fermi level meaning they

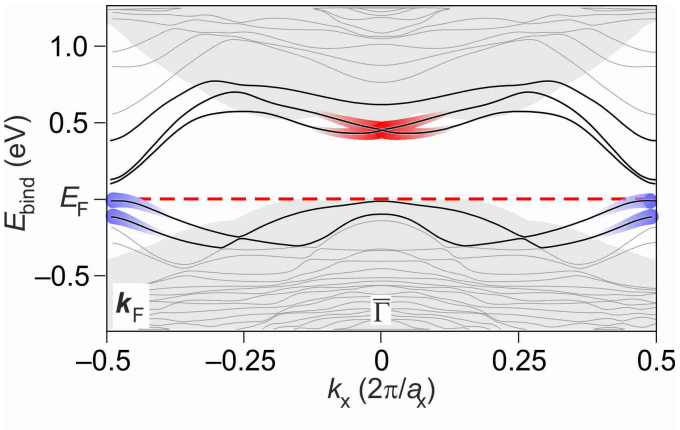

Figure 7.18: Band structure of the (8x2) phase, highlighting the regions of excited states assumed in the simulations of the study by Frigge *et al.*. Red marks the position of excited electrons, and blue the excited holes. Reproduced from [Fri17].

would be expected to depopulate these states. This is observed in our data as shown in Fig. 7.10.

Indeed trARPES is in a unique position to test the assumptions of these simulations by measuring the electron distributions in k-space and their transient redistribution. Using this information gives an experimentally justifiable and physically realistic input to MD simulations, which then affords important insights into the microscopic phase transition mechanism. In the following sections the electronic, and hole, distributions will be presented, along with the transient electronic temperature. These are used as inputs for new MD simulations, the results of which are also shown.

7.4.1 Excited State Distributions

The excited electron distributions for the (8x2) phase has already been presented in Fig. 7.9. Here, the distributions are presented as difference images between data before ($\Delta t = -450$ fs) and at time zero, to better highlight the regions where signal is seen. Thus what is shown for the electrons in Fig. 7.19 is $I_{\text{map}} = I_{t=0} - I_{t=-450}$. This difference presentation also has the advantage that the excited *hole* distributions may be accessed. For the electrons it is clear that such a difference map gives the total signal in the excited state region, since at $t = -450$ fs there is no signal. However the holes appear in the occupied part of the band structure where the signal at $t = -450$ fs is strong, and thus any changes will appear large in a simple difference plot, even if the absolute intensity change is small. The hole map is therefore normalised to the intensity at $t = -450$ fs i.e. $I_{\text{map}} = (I_{t=0} - I_{t=-450})/I_{t=-450}$. This also removes the variation of intensity across Brillouin zones due to matrix element effects.

The electrons are observed to be widely spread over k-space, in contrast to the distribution used in the previous simulations, which placed them at the centre of the Brillouin zone. Even more striking is that at this position the signal is actually very small compared to that in other momentum regions. The energy cut at $E = 0.85$ eV ($\pm$ 0.025 eV) does indeed show electrons at the zone centre, but as seen from the colour scale this is much weaker than that towards the zone boundary at slightly lower energies, for example. It therefore seems clear that the assumed distribution of

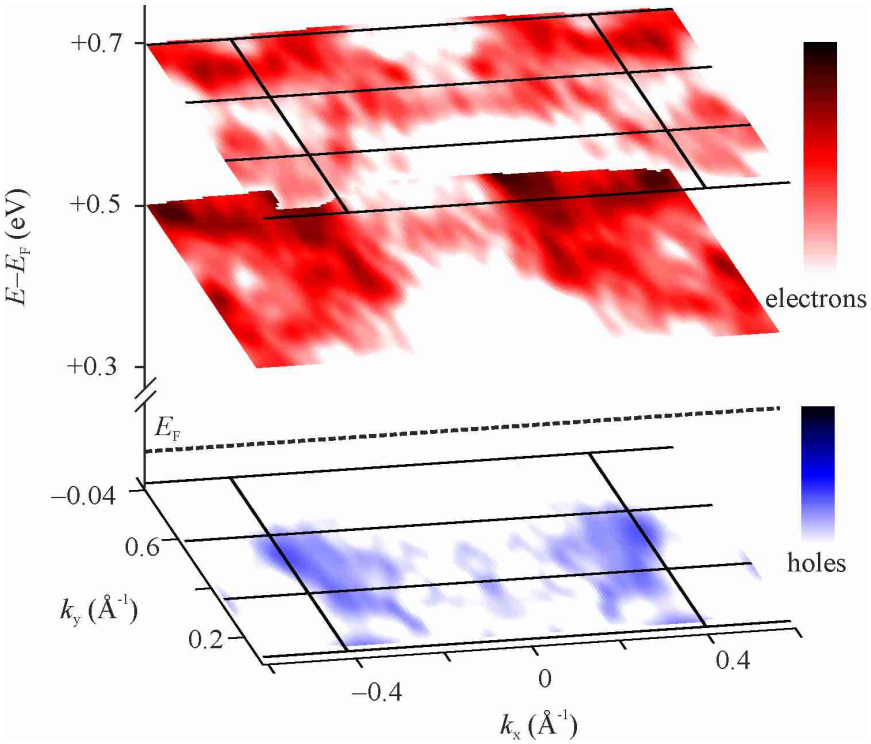

Figure 7.19: Excited states mapping in the (8x2) phase. Constant energy cuts for electrons (red scale) and holes (blue scale) reveal the distributions of excitations throughout multiple BZs. The data is symmetrised about $k_x = 0$ and smoothed to remove unphysical features produced by the symmetrisation procedure.

electrons at the zone centre is not justifiable.

The distribution of excited holes is presented in the lowest panel at an energy cut of $E = -0.04$ eV ($\pm$ 0.025 eV). In this case the signal is much more localised to the region around the zone boundaries. Surprisingly this is what was assumed previously in order to drive the phase transition in the MD simulations. But why should the holes be so localised? The DFT calculated band structure (Fig. 7.20) shows that the occupied states below E_F at the $\overline{\Gamma}$ and $\overline{X}$ points are at the same energy. Thus the potential for the holes is equivalent at these points, which should result in holes being found at zone centre and boundary in equal amounts, in contrast to what is observed. A reason for localisation is suggested by comparing the DFT and GW calculated band structures also in Fig 7.20. The GW band structure has already been found to better describe the observed band structure, for example the gap at the zone boundary is strongly underestimated in the DFT calculation. Most likely this is related to enhanced many-body interactions in this reduced dimensional system. The GW calculation show a clear qualitative difference to the DFT band structure in terms of the hole potential minimum: the bands at $\overline{\Gamma}$ are now around 0.2 eV lower than states at the zone boundary. The difference in state energy positions should lead to a localisation of hot holes around the $\overline{X}$-point.

The above electron distribution maps suggest how the MD simulations of the (8x2) to (4x1) transition may be improved to better reflect the experimental situation. First, instead of a fixed electron population at the zone centre, electrons should be distributed throughout the Brillouin zone. These electrons should also be allowed to relax to lower lying energy states over time, instead of remaining in states far above

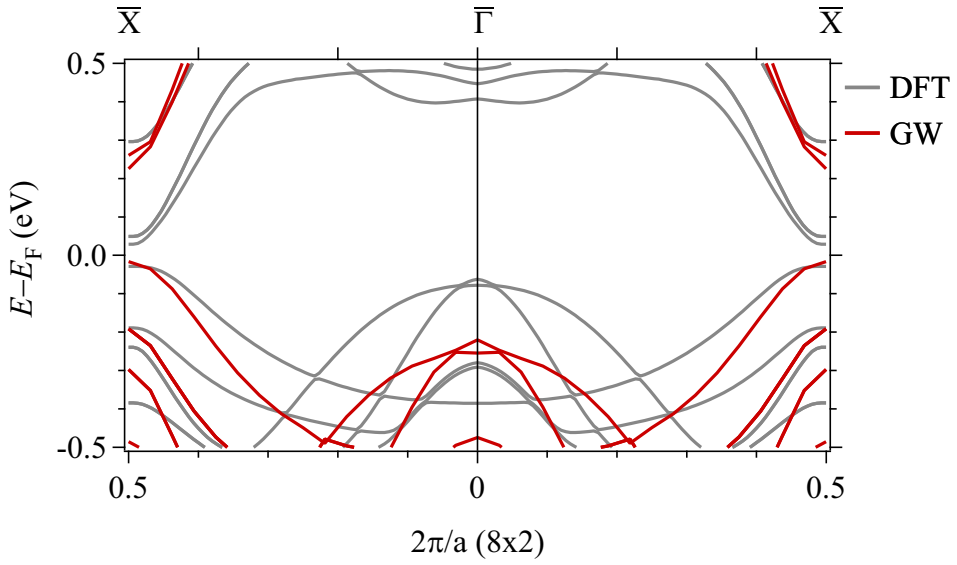

Figure 7.20: Comparison of DFT (grey) and GW (maroon) calculated band structures around the Fermi level. In the GW calculation the Si states at the $\overline{\Gamma}$-point are around 200 meV lower than those at the zone boundary, leading to a localisation of hole excitations at the boundary, in contrast to DFT. The electronic gap at the $\overline{\text{X}}$-point is also much better reproduced with GW.

the potential minimum. This will be parametrised by a thermal electron distribution, taking as input the experimentally determined electronic temperature, which will be presented in the next section. A final point will be to restrict the holes to the zone boundary. Since MD simulations with a GW or even hybrid band structure are too computationally expensive, it will therefore be necessary to use the DFT derived band structure and impose hole occupation at the zone boundary. This can be achieved in the DFT calculation by forcing the Si states at the $\overline{\Gamma}$-point to be fully occupied. As a cross-check, this can of course also be compared to the case where a thermal distribution is assumed, but the holes are not localised, as will be presented below.

7.4.2 Electronic Temperature

Before using a thermal approach to describing the electronic distributions, it is necessary to confirm that such a description is appropriate. The EDCs presented in Fig. 7.11a already suggest that such a description may be valid, at least in some regions of k-space. Although a gap in the band structure is observed at this position, the signature is relatively weak and sitting on top of a quasi-thermal electron distribution. A second more quantitative check is to address the energy content in the system at each time delay and to compare this to the temporal electronic temperature. A thermal system should show an electronic temperature proportional to the square root of the energy density, ϵ, since [Bov07, Per07]: $\epsilon(t) = C_{el}T_{el}(t)/2 = \gamma T_{el}(t)^2/2$, where $C_{el} = \gamma T_{el}$ is the electronic heat capacity. The factor γ is related to the density of states at the Fermi level: $\gamma = \frac{\pi^2}{2}k_B^2 D(E_\text{F})$.

The energy density was evaluated at two regions in k-space: at the (8x2) zone boundary integrated over the m_2/m_3 bands, and at the zone centre at the position of the m_1 band. The electron signal in these two momentum regions was extracted for

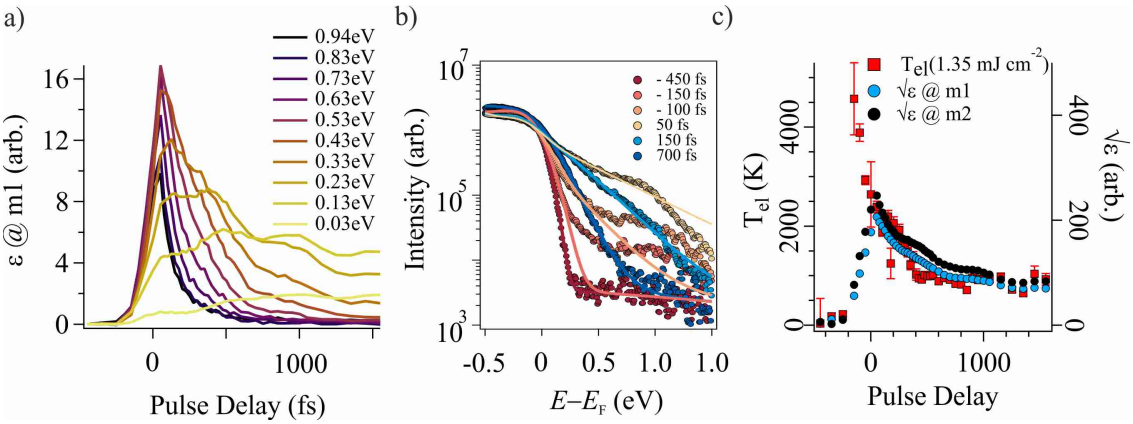

Figure 7.21: a) Integrated time traces over the m_2 and m_3 bands at the marked energy positions, weighted by the energy above the Fermi level. This is used to calculate the energy content as a function of time (see text), presented in c). b) EDCs around the Fermi level at selected pump-probe delays which were fitted (also shown) to extract the electronic temperature. Note the logarithmic scale. For times < 150 fs a non-thermal distribution is observed and the fit function does not match the data well. c) Extracted electronic temperature and comparison with the energy content obtained from a). This analysis reveals that the system can be described as electronically thermal after around 50 fs.

each time delay using an energy window of 0.1 meV. This was then multiplied by the average energy of the integrated region, in order to weight the states according to their energy position above E_F i.e. higher lying states are more energetic, but less occupied than those close to the E_F. The traces at different energies are shown in Fig. 7.21a, and the time dependent energy density in 7.21c. The analysis in both regions of k-space produce almost identical results. This is then compared to the extracted electron temperature also in Fig.7.21c. The electron temperature is extracted by fitting EDCs with a Gaussian peak multiplied by the Fermi-Dirac distribution and convolved with the energy resolution of the experiment. A background term is also included. The evolution of the EDCs, and their respective fits, are presented in Fig. 7.21b. Shortly before and after excitation it is clear from the EDCs that a thermal model is unable to reproduce the data. It is only by around 150 fs that a thermal distribution is reached. This is perhaps unsurprising, as the initial excitation of states via a pump pulse is well known to induce non-thermal populations on short time scales, and to reach a thermalised distribution within a couple of hundred femtoseconds [Bov07] or shorter due to electron-electron scattering. Pre-time zero, the fit function finds most of the spectral weight close to E_F with a form similar to the unexcited EDC; as a result the temperature extracted is rather low. Note that the logarithmic scale used highlights weak states above E_F, which are 3-4 orders of magnitude weaker than the signal in the occupied states. During excitation, spectral weight is distributed into states up to 1.5 eV above $E_F$non-thermally, revealed by the peak around 1 eV in the EDC at 50 fs. This distorts the distribution as seen by the fit function, which now extracts an inflated value for the electronic temperature due to these high lying, and significantly populated states. The values extracted before 150 fs suffer from this systematic error. Once a thermal population has been achieved (100-150 fs) the system remains thermalised and cools over time; an EDC

at 700 fs is shown to highlight this. On the other hand, according to the energy density analysis, the system can be considered as thermal already around 50 fs after excitation, at which time the EDCs clearly do not show thermal behaviour. It may be that although by eye the fit of the EDC at this time is rather poor, the actual deviation of the model from the data is not so large. Essentially the general trend is correctly described until around 1 eV where the slope (and hence the electronic temperature) are too large due to the presence of the non-thermal population at this energy. Since the intensity in these high lying states is still an order of magnitude less, even directly at maximum excitation, than occupied states, the energy density analysis is perhaps insensitive to these subtleties. Thus it is useful to make a comparison of the EDCs/thermal model with the energy density analysis in order to corroborate the thermalising dynamics.

The initial rapid loss of energy from the electronic sub-system is surprising for such a quasi-1D surface state, for which both the coupling between wires in-plane and coupling to the bulk out-of plane is small. However as already mentioned, a large number of surface phonons exist in the system, which simulations have shown are efficiently excited following an excitation, on a time scale of around 500 fs [Fri17] which closely matches the rapid decrease in electronic temperature in Fig 7.21c. The coupling to bulk phonon modes is apparently restricted, as the electronic temperature remains elevated to as much as 1000 K after 1.5 ps, which suggests a strong confinement of energy within the surface system. In fact, as was already discussed in the previous section, depending on the fluence of the excitation the electronic temperature can take hundreds of picoseconds to recover to the base value. The slow cooling will proceed by the incoherent excitation of bulk phonon modes, allowing the gradual transfer of energy out of the surface layer, which typically occurs on a time scale from tens to hundreds of picoseconds.

7.4.3 Molecular Dynamics Simulations

The above data and analysis now allows for MD simulations that reflect the experimental results i.e. electrons spread throughout the Brillouin zone that decay over time. In Fig. 7.22 the results of various simulations are presented. The black curve is the simulation as in Fig. 3c of Frigge *et al.* [Fri17] (data courtesy of A. Lücke) using the electronic distribution already discussed with electrons at the zone centre and holes at the zone boundary. What is plotted is the squared difference between the atomic positions in the (8x2) system compared with the (4x1) positions as a function of time in picoseconds after the excitation. Thus a value of "0" would be exactly the (4x1) phase. However since the system is electronically excited, the equilibrium position of the ions in the excited state is not exactly the same as the one of the 4x1 phase with no excited electrons; as a result the true zero is never reached in the simulation. One sees that in the case of the specific electron population already described, a value close to zero is obtained in the simulation after around 0.5 ps i.e. the phase transition occurs.

As a next step, the experimentally determined electronic temperature (shown again in the lower panel) is used as an input to define the occupation of electrons across the full Brillouin zone. However as the red trace in Fig. 7.22a shows, the transition is not driven under these conditions; instead the system returns to the (8x2) phase. In contrast, if the temperature is artificially kept at the maximum value

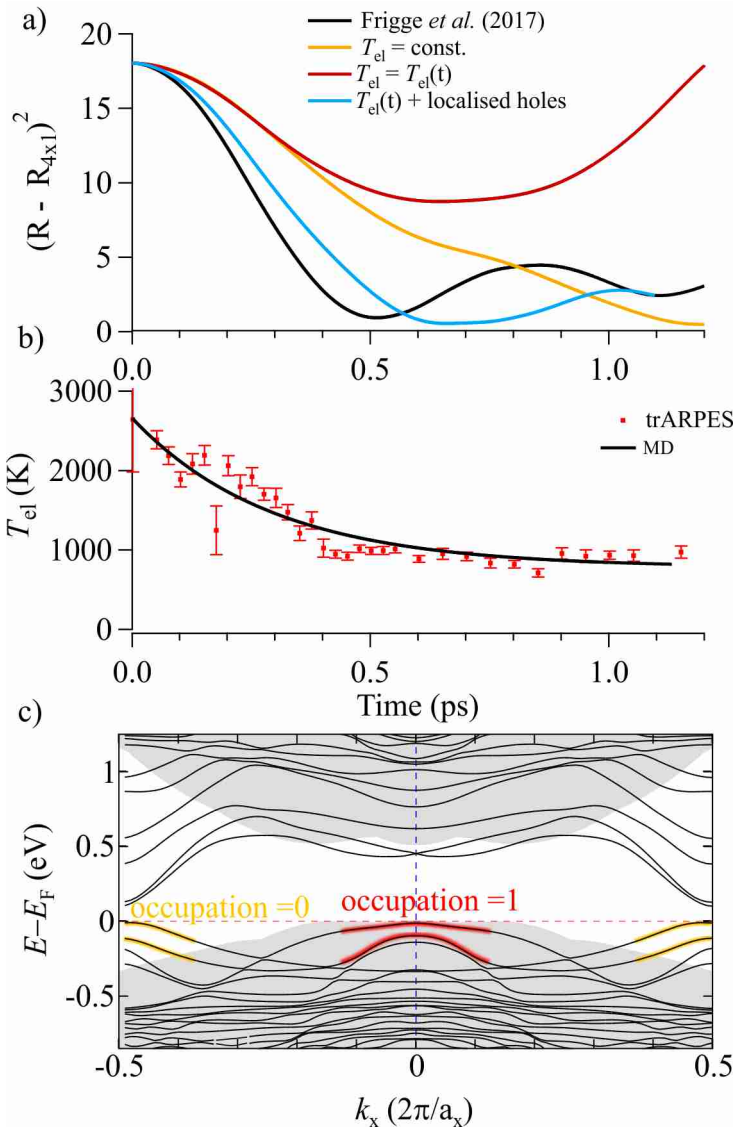

Figure 7.22: a) The evolution of the In/Si(111) system in MD simulations for various excitation conditions explained in the main text. The most realistic ($T_{el}(t)$ + localised holes) uses the electronic temperature extracted from measurements, shown in b). c) DFT calculated band structure in the (8x2) phase showing the forced distribution of holes which simulates the occupation of Si states in the GW band structure.

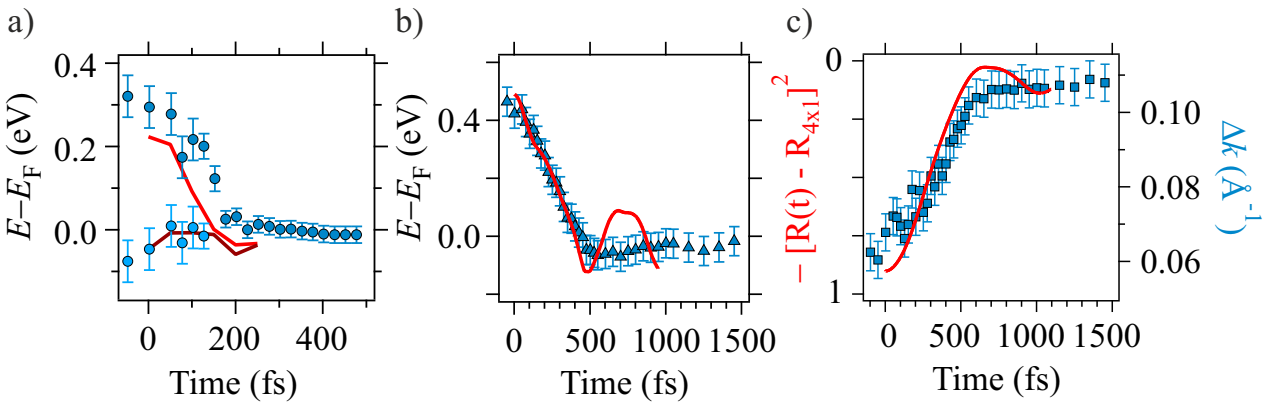

Figure 7.23: Time scales of the three phase transition markers from the experiment compared with the simulated time scale: a) zone boundary b) zone centre and c) structural transition.

of around 2500 K (orange curve), similar to the previous calculations of Ref. [Fri17] that assumed a constant excited population, the transition is indeed driven. This suggests that by keeping electrons in excited states throughout the phase transition time range produces un-physical forces on the atoms. The lack of a transition in the case of a transient thermal distribution implies that something is missing from the description of the experiment given by the DFT-based simulations. As was mentioned already in the section on the electron and hole distributions, there is a clear difference between DFT and GW calculations of the energy levels in which the holes sit i.e. states below E_F. Thus to further approach the experimental conditions, while still using DFT to avoid making the calculations too computationally expensive, the DFT band structure is used but the holes are forced to sit at the zone boundary by applying the condition that the Si states at the boundary should have an occupation number of "0" while those at the zone centre should be filled and therefore have an occupation number of "1". This is shown in Fig. 7.22c. Each of these conditions is applied to a momentum range of around 2/5 of the full (8x2) Brillouin zone size. In this case (blue curve in Fig. 7.22a) the phase transition once again occurs, clearly highlighting the important role of the forces induced by the photoexcited holes during the transition. An analysis on the bonding strength based on the occupancy of particular bands will be presented in the next section.

Based on the outcome of the simulations presented above, it appears that the (8x2) to (4x1) transition can be reproduced theoretically even on a femtosecond time scale. One thing that still remains to check is whether the time scales that the theory produces agree with the trARPES data or not. From the comparison between the blue and black curves in Fig. 7.22a, it appears that our simulations predict a similar time scale for the structural phase transition as was found in the previous work and is therefore also consistent with the time-resolved electron diffraction results [Fri17].

A detailed comparison of the three time scales extracted from the trARPES data presented in the section on the momentum resolved dynamics of the phase transition are presented again in Fig. 7.23. In each case the curve is overlaid with the dynamics from the DFT simulations discussed in the previous section, in which a thermal distribution of electrons is used, in addition to a hole population centred at the zone boundary. Note that the gap at the zone boundary (panel a) is severely underestimated in DFT calculations, as has already been shown. Therefore the

dynamics at this point are obtained by scaling the DFT band gap before excitation to the more realistic GW calculation in the low temperature (8x2) phase, and assuming that the variation of the band gap value scales in the same way. As can be seen, the experimentally observed and simulated time scales are in very good agreement. This is a remarkable success for the MD simulations. The implications of such an agreement between experiment and theory, where the simulations are obtained with realistic conditions based on experiments, suggests that the the microscopic forces and potential energy surface during the transition can be extracted with a high degree of accuracy, which suggests the exciting prospect of controlling phase transitions or even chemical reactions.

7.4.4 From bands to bonds

The data and analysis presented above reveal the detailed pathway of the phase transition occurring on three distinct time scales. These time scales are reproduced by DFT simulations, which therefore give powerful insights into the driving forces responsible for the phase transition. The excellent agreement between data and theroy is further highlighted in Fig. 7.24a-c. The data points mark the position of the m_1 state at the Brillouin zone centre, and are shown for three delay points, revealing both the gradual shift of the band towards the Fermi level and a change in the slope of the dispersion as the state evolves from gapped to metallic. Also plotted are selected DFT calculated bands: those corresponding to the m_1 state and (below E_F) Si states as a reference. In the calculations, two almost degenerate bands are found at to correspond to the m_1 states, which are not resolved within our experimental resolution; therefore these are both plotted and the area between them shaded, in order to give a fairer comparison between data and theory. As can be seen, both the position and slope of the band is well described at each time point. Based on the excellent agreement between experiment and theory in k-space, we conclude that the simulations may be used to extract information that the experiment itself does not directly provide. In the following, a link is made from momentum space, where all measurements have been carried out, to real space dynamics; specifically the possibility of accessing the ultrafast dynamics of bonds during the phase transition from trARPES data.

It is clear that a relation between bands in momentum space and bonds in real space exists, since one can move between the two via the Fourier transform. However it is not so clear to what extent features in one space e.g. gaps closing in k-space can be directly associated to features in the other i.e. bond formation in real space. An obvious question is how to reliably define a bond, particularly in extended metallic systems. In molecular systems, an intuitive way of relating the two has been presented by Hoffmann, see e.g. Refs. [Hof87, Hof88]. A powerful method for relating bands occupation to relative bond strengths is the well-known crystal orbital overlap population (COOP) [Hof87], which is based on the overlap of wave functions between atoms. The COOP resolves each individual band into bonding and anti-bonding contributions as a function of energy; essentially a bonding character density of states for each electronic band. This reveals whether the addition or removal of electrons at any particular energy from a particular band will result in a strengthening (increased bonding) or weakening (increased anti-bonding) of the bond. This allows relative bond strengths to be easily described, but what about a quantitative description

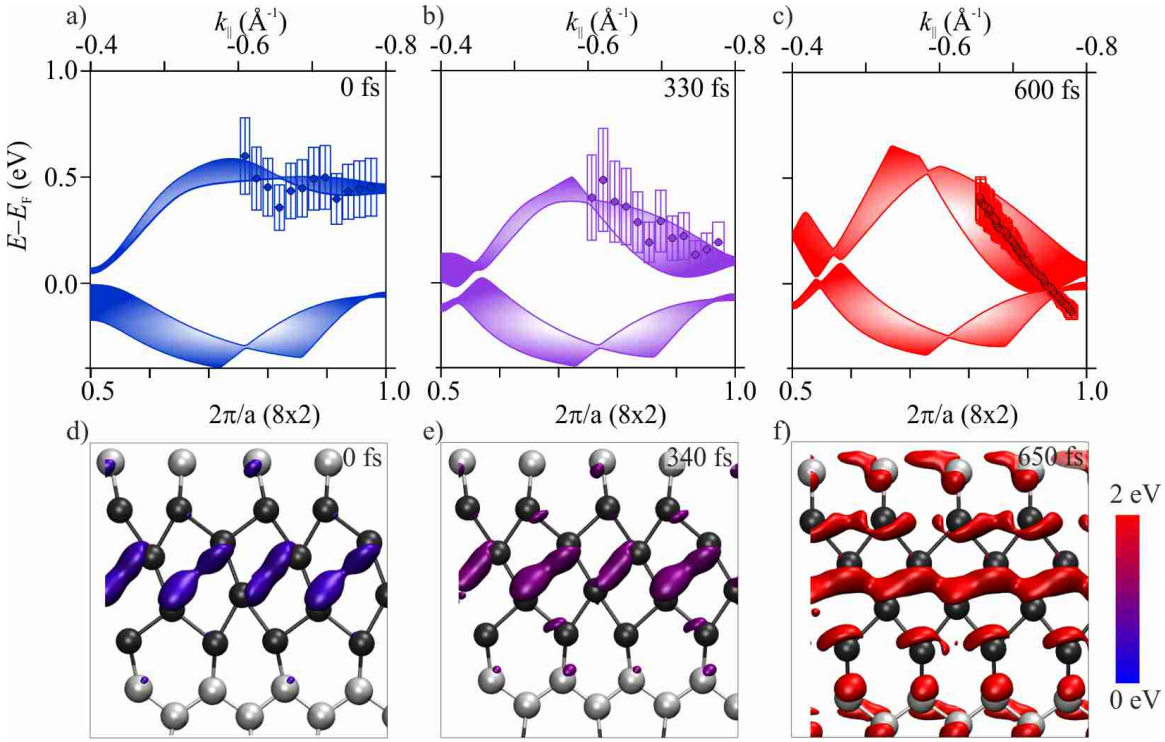

Figure 7.24: a)-c) Extracted position of the m_1 states at selected times during the phase transition and the corresponding DFT calculations. Two nearly degenerate bands, which are not resolved individually in our measurements are plotted. Lower lying states are from the Si substrate. d)-f) Real space images of the atomic orbitals related to the m_1 states at selected times. The orbital stretches between In atoms across the (8x2) phase hexagon and becomes strongly delocalised at later times. The colour of the orbital represents the bond strength from the COHP analysis.

of the bond itself? This can be obtained from the crystal overlap Hamiltonian population (COHP) [Dro93, Mai13], which gives a numerical evaluation of the bond strength by integrating all bonding and anti-bonding eigenvalues and weighting them by their occupation i.e. states that are not occupied do not contribute. A COHP analysis has previously been applied to the equilibrium case of In/Si(111) to reveal the bonding network in the two phases [Lüc17] but not to the ultrafast phase transition. This study has shown that the m_1 states in the (8x2) phase have a strong bonding character in the unoccupied states, therefore an excitation that populates these states produces a strengthened bond, producing a force on the corresponding atoms and even launching the characteristic sheer mode [Fri17]. Since clear measurements of the dynamic occupation of individual bands are available, as shown in previous sections, it should therefore be possible to extract specific bond dynamics during the phase transition.

The states at the Brillouin zone centre ($\overline{\Gamma}$) are focussed on since they are well separated from other bands and have very clear k-space dynamics, making them an ideal test case. In the simulation, the band is populated by the thermal distribution presented in Fig. 7.22b. The real space Bloch orbital associated with the m_1 states are presented in Fig. 7.24d-f. One notices immediately that the orbital changes from localized to strongly delocalized during the transition, reflecting the insulator-to-metal change in the orbital character. Note that the orbital itself is always present,

even before excitation, in the same way that the related band is always present, although both are unoccupied before excitation.

By performing a COHP analysis for each time point in the simulation the dynamic bond strength for the m_1 orbital can be calculated during the phase transition. The absolute value of the bond strength is encoded in the blue to red colour scale in the lower right part of Fig. 7.24. A gradual evolution of the bond strength from 0 to 2 eV is observed, as the m_1 states shift from above to below E_F. During this time the atomic nuclei shift their positions driven by the forces resulting from the transient occupation of the m_1 orbital above E_F. From this picture it is possible therefore not only to see the extent and change of the orbital shape, but also the bond strength varies through the phase transition due to the population dynamics that favour a bonding scenario for this orbital. While this analysis does not give an exact "moment" of bond formation, such a procedure is not particularly meaningful as it would require an arbitrary value for bond strength to be defined. Rather the nature of the electronic rearrangement in the system, highlights the gradual way in which the bond is formed, which is likely to be a common feature in ultrafast reaction processes in which bond dynamics play a role.

7.5 Summary

The combination of time, energy and momentum resolution has been used to investigate the photo-induced (8x2) to (4x1) phase transition in In/Si(111) nanowires, and has yielded a detailed picture of both the reaction pathway and microscopic driving forces with the help of MD simulations. By following the temporal evolution of individual electronic bands as they evolve through the phase transition, multiple distinct time scales for the phase transition have been identified, including those of the metal-to-insulator ($\sim$ 200 fs) and structural transitions ($\sim$ 700 fs). In addition the distribution of excited states throughout multiple Brillouin zones (BZ) has been mapped, revealing that hot electrons are found throughout the BZ, while in contrast holes are found to be much more localised. Based on these experiments, molecular dynamics (MD) simulations with realistic electronic distributions and relaxation dynamics have been performed, which not only reproduce the multiple time scales observed in experiments, but also expose the microscopic role played by holes in driving the phase transition. A link is made from the transient electronic structure to the ultrafast formation of bonds in real space. These results provide unprecedented insights into the microscopic mechanism of a surface phase transition reaction involving electronic and structural interplay and have relevance for catalysis and surface chemistry as well as for optically driven phase transitions. The exceptional agreement between experiment and theory in this model system is a step towards understanding and even controlling the energy landscape during ultrafast reactions.

8 Ultrafast SDW transition in Cr/W(110) Thin Films

In ultrafast pump-probe measurements, the transfer of energy from the laser pulse can lead to the population of excited states [Sob12, Gie13, Gru15, Ber16], changes in magnetic ordering [Rad11, Fri15] and even electronic [Sch08, Roh11, Mon16] or structural [Bea14, Wal15, Ish15, Fri17] phase transitions. In many cases a transient increase of the electronic temperature occurs which may be tracked, for example, by angle-resolved photoemission spectroscopy (ARPES) [Gie13, Wan12b, Cre12]. An open question is to what extent the electronic temperature alone can be said to govern ultrafast changes, particularly for phase transitions, due to the strongly non-adiabatic nature of pump-probe experiments and the possibility of exciting non-thermal electron distributions on short time scales. Such a description is further complicated in many correlated materials such as high-T_c superconductors, charge density waves (CDWs) and ferromagnets, in which lattice degrees of freedom play an important role. In CDW systems, the coherent excitation of the atomic cores (phonons) can lead to a periodic opening and closing of the spectral gap [Sch08, Ret14, Ret16] independent of the temperature of the electronic system. In the case of the ultrafast demagnetisation of ferromagnets, a bottle neck for the transition is the transfer of angular momentum, which proceeds through the lattice [Stö06] meaning that a hot electron system may be necessary, but is not sufficient to drive the system from one magnetic phase to another. In contrast, antiferromagetic materials which have overall zero angular momentum may exhibit faster dynamics. This is further expected in spin density waves (SDW) materials where the ordering stems directly from electronic correlations [Ove62] and thus offers an opportunity to study the dynamics of a phase transition in which the role of the lattice is minimised. The idea is to investigate the role played by the electronic temperature in driving materials from one phase to another under non-equilibrium conditions.

In this chapter a time-resolved ARPES investigation of the well known antiferromagnetic-SDW transition in Cr [Faw88] is presented. Although the SDW in Cr has been widely studied [Faw88, Sch99a, Faw94, Sch04b, Rot05, Rot08], very few studies of the time-domain dynamics exist [Hir03, Sin15, Sin16], none of which directly address the electronic structure. Despite the fact the Cr is a bulk metal, the specific shape of the Fermi surface [Faw88, Rot05] with large parallel sections results in a single Q nesting wavevector that drives the SDW; similar to the case of quasi-1D materials as outlined in chapter 2. The ultrafast disappearance and recovery of the SDW-derived electronic structure following pulsed infra-red excitation is observed. The ultrafast dynamics of the electronic structure are simulated with a mean field model in order to disentangle intrinsic SDW dynamics from other non-equilibrium effects. It is found that the order parameter of the SDW is governed by the transient electronic temperature, implying an intimate link between electronic temperature and spin ordering as the driving mechanism of the SDW in Cr, thus demonstrating that equilibrium thermodynamic concepts can still survive on ultra-short time scales, in cases where the temperature of a single sub-system governs the behaviour of an

ordered phase. Thus the case of the SDW in Cr contrasts to the dynamics of CDW materials, including quasi-1D In/Si(111) which shows a strong lattice component as already presented in chapter 7.

This work has been carried out in collaboration with the group of M. Weinelt, then at the Max Born Institute in Berlin. The laser was prepared and maintained for these experiments by R. Carley and B. Frietsch. Initial sample preparation work was carried out by C. Monney, R. Carley and J. Bowlan. The acquisition of trARPES data and its subsequent analysis have been carried out as part of this thesis. The results presented in this chapter have been published in Nicholson *et al. Phys. Rev. Lett.* **117**, 136801 (2016) [Nic16].

Experimental Details

Sample preparation and the tr-ARPES system have been described in chapter 4. In brief, Cr(110) films were grown epitaxially on a clean W(110) crystal at room temperature at a pressure of 1x10^{-10} mbar, and then annealed to 600°C. A film thickness of 7 nm was produced by reference to the LEED and ARPES phase diagram [Rot05]. For the pump-probe measurements a linear polarised 1.5 eV pump and 40 eV XUV (extreme ultraviolet) probe were utilised to collect snapshots of the electronic structure. Due to the optical-absorption depth of 30 nm at the pump wavelength [Rak98], the entire thin film will be excited nearly homogeneously. The combined time resolution of the experiment was measured to be 130 fs. ARPES measurements were carried out with a hemispherical electron analyser (SPECS) at 100 K, well below the surface SDW transition temperature of 440 K [Sch99a]. The quality of the films after preparation was confirmed with ARPES using a He lamp. Typically a successfully prepared film was measured for around 12 hours. On these time scales some degradation was observed (broadening of features in ARPES and LEED). The substrate was flashed to removed all Cr, and a fresh film was deposited.

8.1 Characterisation of the Band Structure

The Cr/W(110) thin films were characterised with ARPES as presented in Fig. 8.1a at 100 K, well into the SDW phase. The data are obtained with He I radiation along the $\overline{\Gamma}-\overline{\mathrm{S}}$ direction marked in Fig. 8.1b, and are plotted here in a false colour log scale to highlight weak features. An electron band is seen to disperse towards the Fermi level (E_F) from $\overline{\Gamma}$ towards the $\overline{\mathrm{S}}$-point. As the band approaches E_F it bends away and continues again to higher binding energies. This weak spectral feature (highlighted by the arrow in Fig. 8.1a is a direct result of the SDW nesting vector which results in a band re-normalisation via back folding [Rot05]. The observation of the renormalised dispersion in the data confirms the high quality of the Cr film preparation. According to previous high resolution studies [Rot08] there is also a weak surface resonance dispersing parabolically between $\overline{\Gamma}$ and k_F. This likely explains the weak intensity observed in our data in this region of k-space.

The nesting vector Q is shown in Fig. 8.1b and can be seen to join large parallel areas of the Fermi surface. The large parallel areas of the Fermi surface mean that as in quasi-1D the electronic structure is unstable towards the formation of long range order, as described in chapter 2. In contrast to the formation of CDWs, the spin susceptibility does not necessarily induce a periodic modulation of atomic core position; in a SDW it is the spin texture that varies spatially. However, one can think of the SDW as being formed of two CDWs: one of spin up, and one of spin down carrying nuclei that are π out of phase, thus the overall charge density does not vary while the spin density does [Grü94a]. This leads to an effective doubling of the unit cell due to the anti-ferromagnetic (AFM) arrangement of spins as observed by neutron scattering [Faw88] and ARPES [Rot05]. The wavevector Q is commensurate with the lattice at a film thickness of 7 nm [Rot05]. However due to the unequal sizes of the electron and hole-like Fermi surface pockets in Cr (Fig. 8.1b), the wavevector Q joining $(k,\uparrow)$ and $(k+Q,\downarrow)$ is not equal to that joining $(k,\uparrow)$ with $(k-Q,\downarrow)$ which results in an additional spatial phase between the spin up and spin down CDWs that make up the SDW. The outcome is an additional long range periodicity ($\sim$ 21

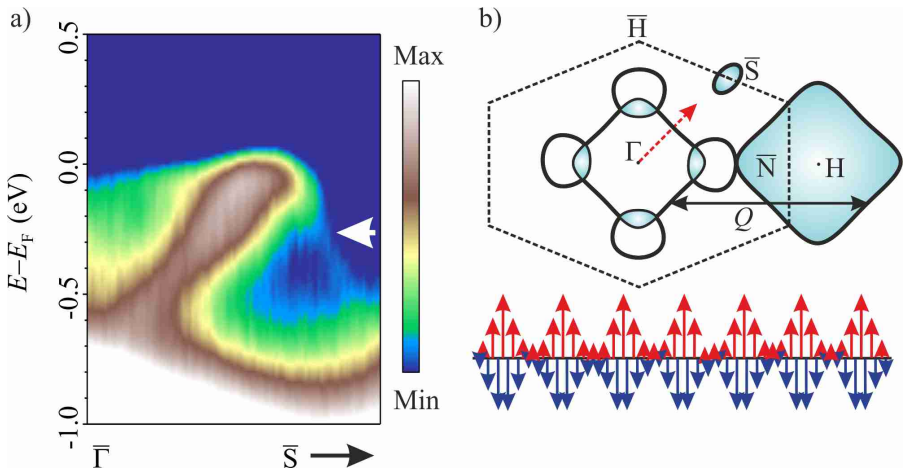

Figure 8.1: a) Electronic structure of Cr(110) thin film measured along the dotted red arrow in b). The SDW band is marked by a white arrow. b) Upper: schematic Fermi surface and surface Brillouin zone of Cr. Electron-like pockets are contained within solid black lines while hole-like pockets are coloured cyan. The dashed hexagon marks the (110) surface projected Brillouin zone. The nesting wavevector Q is marked by a double headed arrow, and joins large parallel sections of the Fermi surface. Lower: schematic SDW showing the modulation of spin magnitude, in addition to the AFM ordering.

lattice sites) over which the magnitude of the AFM ordered nuclei varies; this is shown schematically in the lower part of Fig. 8.1b. Within the simple picture of an SDW being composed of two CDWs, this extra phase shift should naturally lead to a long range modulation of charge i.e. a CDW in addition to the SDW. In fact Cr does indeed host a CDW, thought to be the second harmonic of the SDW [Faw88] although the exact relation between charge and spin order is not fully resolved.

The spectrum as described above is next obtained with pulsed XUV radiation (p-polarised) and presented in Fig. 8.2a. As expected in the SDW phase the renormalised band is observed, though it is weaker than in the He-lamp measurements due to the lower energy resolution of the high harmonics source of around 200 meV. When pump and probe beams overlap in time (Fig. 8.2b) a replica of the entire band structure is clearly observed in the unoccupied state region above E_F. This is highlighted in Fig. 8.2c by taking the difference between the images at -200 fs and 0 fs; the expanded energy range reveals a replica also *below* the original band. This signal is a result of Laser Assisted Photo-Emission (LAPE) [MA06, Saa08], already introduced in chapter 3. The LAPE signal can only be present when both pump and probe beams overlap in space and time on the sample, because the presence of the intense electric field of the pump induces new stationary solutions to the Schrödinger equation for photoelectrons. Radiation is produced by transitions between these so-called Volkov states [Ede04] which are separated by the pump photon energy. Hence the replicas in Fig. 8.2c correspond to absorption and emission of one quanta. In principle LAPE is a general effect due to the photoemission process itself, and may be observed on any sample given the correct conditions. However typically it is a weak effect, depending on the pump wavelength [Saa08]. The data obtained here shows an unusually strong signal, allowing the energy and momentum structure of both $n+1$ and $n-1$ states to be clearly observed.

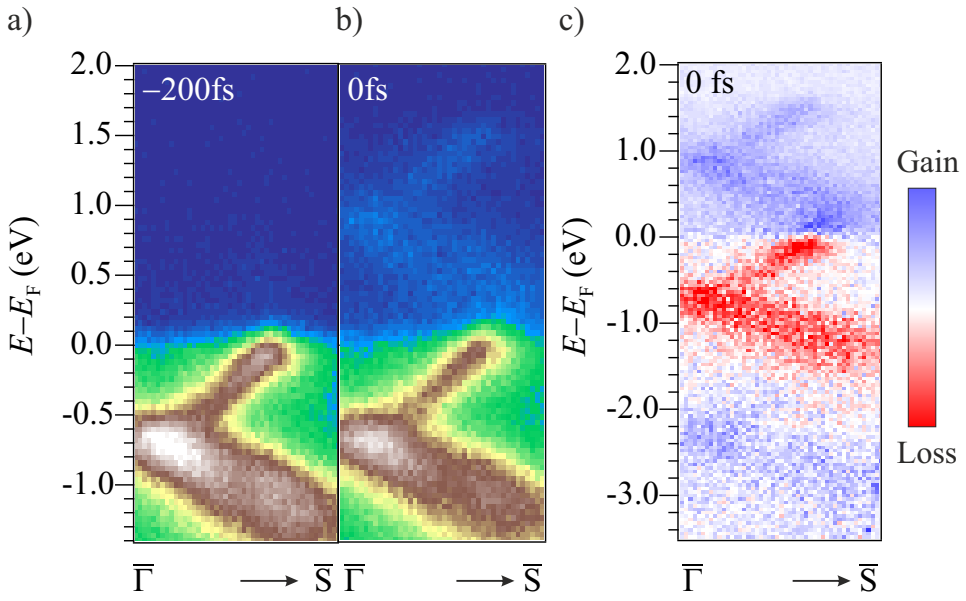

Figure 8.2: Cr/W(110) bands structure a) before excitation and b) at maximum temporal overlap, revealing a replica state due to LAPE. The difference image in c) further highlights the $n+1$ and $n-1$ photon states.

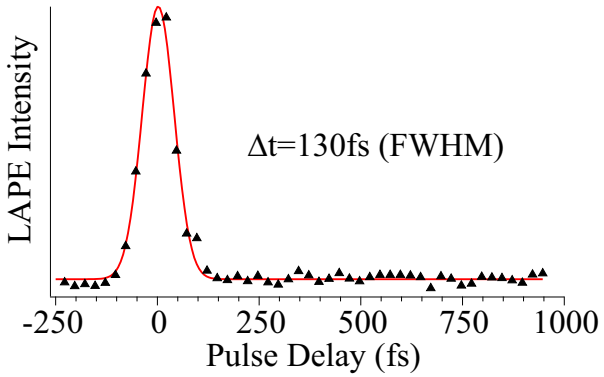

Figure 8.3: Time trace of intensity from the LAPE region above the Fermi level revealing the cross correlation of pump and probe pulse i.e. the temporal resolution of 130 fs.

A practical use of LAPE is to obtain the cross-correlation of pump and probe beams on the sample, and hence measure the total time resolution of the experiment. The integrated intensity above 500 meV are presented in Fig. 8.3 as a function of pump-probe delay. The resulting transient is fitted with a Gaussian profile, and is found to have a full-width at half mamximum of 130 fs; which is the time resolution of the experiment. Although the LAPE signal gives a clear time zero in the experiments, there is also the possibility that it overlaps and obscures real dynamics within the band structure at early times. Therefore in order to remove LAPE signal and achieve clean data for the investigation of the SDW, *s*-polarised light was used to obtain the data in which SDW dynamics were analysed.

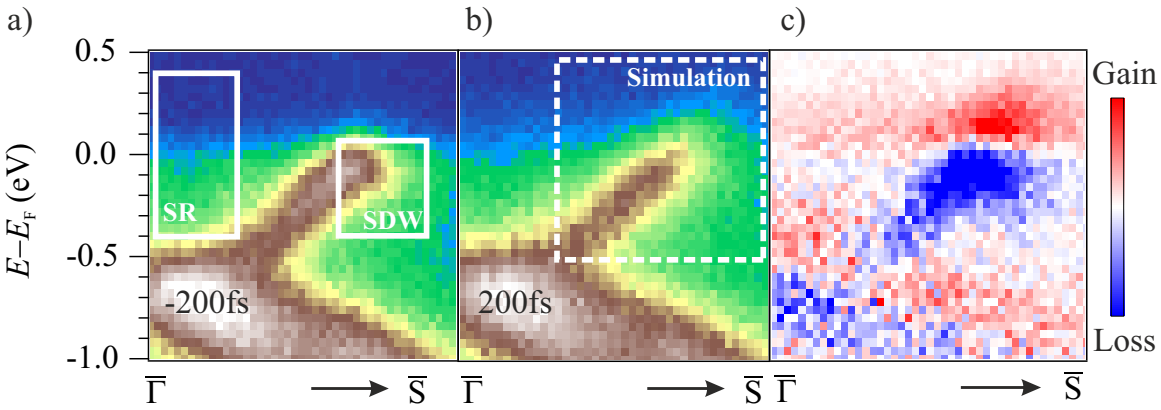

Figure 8.4: Snapshots of states near the Fermi level at a) −200 fs and b) 200 fs revealing a change in the shape of the dispersion from the back-folded shape of the SDW phase to linear, as expected for the paramagnetic phase. c) Difference image between the images shown in a) and b) highlighting the shift of spectral weight from the back-folded region into states above the Fermi level. The red intensity along the length of the band at lower energies is due to a rigid shift of the whole band structure.

8.2 Transient Electronic Structure

In order to address the dynamics of the SDW the k-space region of the back-folded band close to E_F is focussed on as presented in Fig. 8.4a. The influence of the SDW band is again visible, although still not as clearly as in the high resolution He lamp data of Fig. 8.1a. Still, a distinct deviation from a linear dispersion is clearly resolved in the region of the SDW band. Following excitation with the pump laser pulse at a fluence of 0.8 mJ cm^{-2}, the dispersion close to E_F is observed to change. As shown for 200 fs after optical excitation in Fig. 8.4b, the dispersion now linearly crosses the Fermi level, as in the paramagnetic phase [Sch99a, Rot05] in contrast to the data before excitation. It appears therefore that spectral weight is removed from the renormalised band and placed in the bare dispersion. These changes are highlighted by the difference image in Fig. 8.4c in which one clearly sees a strong reduction (blue) of spectral weight in the SDW band region, which is gained above the Fermi level (red). This reduction of the intensity in the back-folded band already suggests that the SDW phase is at the very least strongly modified, if not altogether removed due to the pump pulse. A more detailed analysis of the intensity in this region of k-space and a comparison to the expectations from a mean field description of the SDW will be presented in a subsequent section.

Also visible in Fig. 8.4c at 200 fs is a rigid shift of the entire electronic structure towards higher kinetic energies (red intensity along the length of the band). This is confirmed as a shift by extracting EDCs of the lower band as given in Fig. 8.5a. The position of the band position over time is obtained by fitting of the EDCs with a Gaussian. A maximum shift of almost 30 meV is observed; the dynamics of the shift over the time window of the experiment are presented in Fig. 8.5b. The maximum shift occurs rapidly after excitation, followed by recovery of the band position to a new equilibrium value after around 500 fs. Such dynamics are not typical of probe-induced space charge effects. The origin of this shift may be due to out-of-equilibrium chemical potential shifts as observed in Refs. [Gie13, Yan14, Mil15] induced by the

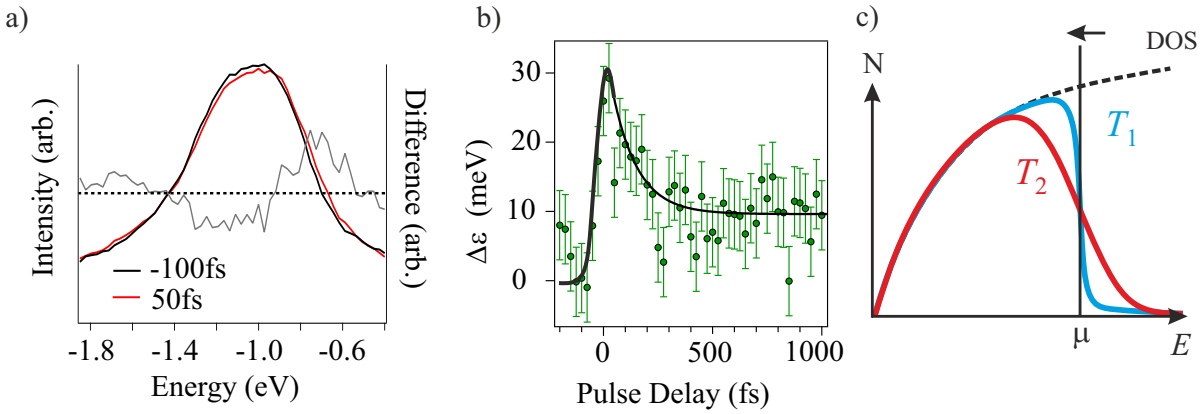

Figure 8.5: a) EDCs of the lower lying states at two delays and their difference (grey) revealing the rigid band shift. b) Dynamics of the rigid shift. c) Schematic of the number of electron states as a function of energy as an explanation for a transient rigid shift (see text). The dotted line represents the DOS.

transient electronic temperature. In principle the position of the chemical potential can be forced to vary upon heating – and therefore broadening of the Fermi-Dirac distribution – depending on the structure of the density of states. This is shown schematically in Fig. 8.5c. In the case of a DOS increasing with energy, raising the temperature from T_1 to T_2, where $T_2 > T_1$, will broaden the Fermi-Dirac distribution by $\sim 4k_B\Delta T$. As a result, more states above the Fermi level are thermally populated. Since the DOS is larger in this energy region (more energy states per interval) the total number of charges would increase for raised temperatures. Thus the chemical potential shifts, down in this example, in order to maintain constant particle number in the system. The argument would be reversed for a DOS reducing with energy. However attempts at a simple modelling of the data along these lines considering the surface states observed in the data along this cut in k-space has not reproduced the observed dynamics. A more detailed model and analysis may therefore be necessary to understand the observed behaviour; in particular the inclusion of all bands close to the Fermi level is likely to be required to capture the observed dynamics. Therefore the shift is treated as purely phenomenological in the following analysis.

8.2.1 Electronic Temperature and Two Temperature Model

A further feature in Fig 8.4c is that intensity is gained above E_F due to the broadening of the metallic states from the surface resonance [Rot08] by the Fermi-Dirac distribution in the region between the SDW band and $\overline{\Gamma}$. This broadening of metallic states – which are metallic even when the system is in the SDW phase – can be used to characterise the electronic temperature (T_e) throughout the experiment and therefore to investigate the role T_e plays in driving the SDW transition. Energy Distribution Curves (EDCs) from the metallic surface resonance region (box "SR" in Fig. 8.4a) are presented in Fig. 8.6a for multiple time delays. By fitting a Fermi-Dirac distribution convolved with the instrumental resolution, the transient T_e may be extracted. Exemplary fits before and after time zero are shown in Fig. 8.6b. It is noted that within the time resolution of 130 fs a thermal distribution of electrons is always observed. Fig. 8.6c displays the evolution of T_e up to 1000 fs following

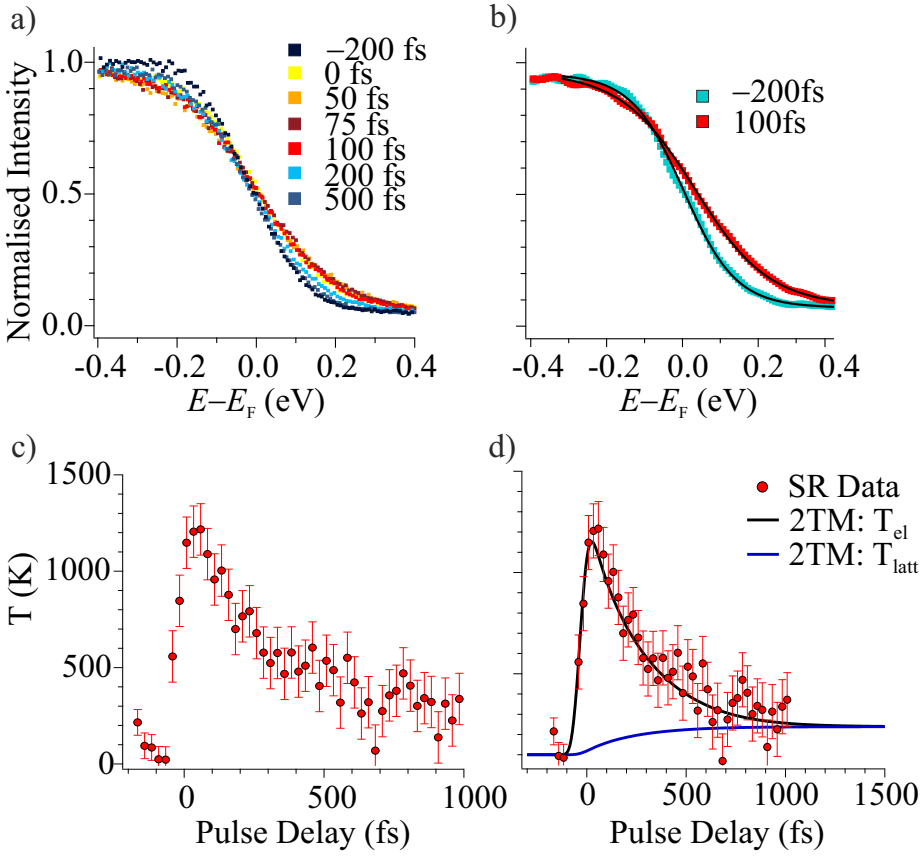

Figure 8.6: a) Integrated EDCs in the region of the metallic surface resonance for various time delays, revealing a broadening after excitation due to the increased electronic temperature. b) Two specific delays plus fits with a Fermi-Dirac distribution convolved with the experimental resolution. c) Electronic temperature extracted from the EDC fits vs. delay and d) including the two temperature model curves.

excitation. After a rapid increase to 1200 K close to time zero, T_e decreases to a new quasi-equilibrium value of around 300 K after 800 fs.

By using a two-temperature model[1] (2TM), it is in principle possible to model this transient temperature and additionally estimate the temperature of the lattice. The equations for the 2TM are two coupled differential equations:

$$C_e \frac{dT_e}{dt} = P\sqrt{\frac{2.77}{\pi\sigma^2}} \exp\left(\frac{-\ 2.77\ (t-t_0)^2}{\sigma^2}\right) - \lambda(T_e - T_{latt}) - D \tag{8.1}$$

$$C_{latt} \frac{dT_{latt}}{dt} = \lambda(T_e - T_{latt}) \tag{8.2}$$

$C_e = \gamma T_e$ and C_{latt} are the electron and lattice specific heat capacities; P is the absorbed energy density; σ is the full-width (in time) at half maximum of the laser pulse, from which the factor 2.77 is also derived; and λ is the electron-phonon coupling. It is found that in order to reproduce the experimental T_{el} it is necessary to include a diffusive term (D), in which energy is transferred to the substrate. Without such a diffusive term, the model cannot reproduce the rapid drop of T_{el} without unrealistic model values. This is perhaps unsurprising as W has a relatively high

[1]For a review see Ref. [Bov07] and references therein.

thermal conductivity [Hay03] and will therefore act as a heat sink. A simple *ansatz* for the diffusive term is therefore included. It is noted that the conclusions regarding the dynamics of the SDW do not depend on the 2TM, but rather on the electronic temperature determined directly from the experiment. The diffusive term D depends on the ordinate perpendicular to the surface normal (assuming the pump spot size is much larger than the probe spot) and can be written as:

$$D = \kappa \frac{\partial^2 T_{el}}{\partial^2 z} \tag{8.3}$$

by assuming the electron thermal conductivity κ is z-independent. κ is temperature dependent, and can be written as: $\kappa = \kappa_0 T_{el}/T_{latt}$ [Bov07]. It is assumed the diffusive term will depend on the difference between T_{el} and T_W, the substrate temperature, which is assumed to follow the lattice temperature. In the limit of $T_{el} = T_W$ there is thus no heat diffusion as the film and substrate are in thermal equilibrium. Further $T_{el} \propto z^2$ is assumed in the region of the Cr/W interface, in order that after the second derivative the z-dependence is explicitly removed. Thus:

$$D = \beta \kappa_0 \left(\frac{T_{el}}{T_{latt}} \right) (T_{el} - T_{latt}) \tag{8.4}$$

where β is a constant. The values for P = 200 J cm^{-3} and σ = 130 fs are determined experimentally; γ = 200 J m^{-3} K^{-2} is taken from the literature [Faw88] and agrees well with the Sommerfeld model [Ash76] prediction. The electron-phonon coupling λ is 0.13 [Bro90]. The temperature dependence of C_{latt} is approximated in the Debye model, with a high temperature value of C_{latt} = 0.448 J g^{-1} K^{-1} [Hay03]. The value of κ for W is taken from literature to be 173 W m^{-1} K^{-1} [Hay03]. The equations are solved numerically and reproduce the experimental data, as shown in Fig. 8.6b, which is presented over a longer delay range than Fig. 8.6a in order to show the convergence of T_{el} and T_{latt}. This rules out a strong influence of the lattice on the SDW dynamics, as the lattice temperature remains below the SDW surface transition temperature of 440 K [Sch99a] for all times.

8.2.2 Ultrafast Dynamics of the SDW Transition

In order to investigate the quantitative effect of T_e on the SDW electronic structure, the results from the mean field model presented in chapter 4 and summarised briefly here are utilised. Such a mean field description may be applied to BCS superconductors and density waves [Mah00, Grü94a], in order to describe the SDW as a renormalised dispersion with a gap. In such a model, the poles of the Green's function give the quasi-particle dispersion, which may be written as

$$E_{\pm} = \pm \sqrt{\epsilon(k)^2 + \Delta^2} \tag{8.5}$$

where ϵ is the bare band dispersion. This renormalised dispersion has two branches separated by a gap determined by Δ. The temperature dependence of the SDW order parameter (Δ) is given by

$$\Delta(T_e) = \Delta_0 \left(1 - \frac{T_e}{T_{SDW}} \right)^{\beta} \tag{8.6}$$

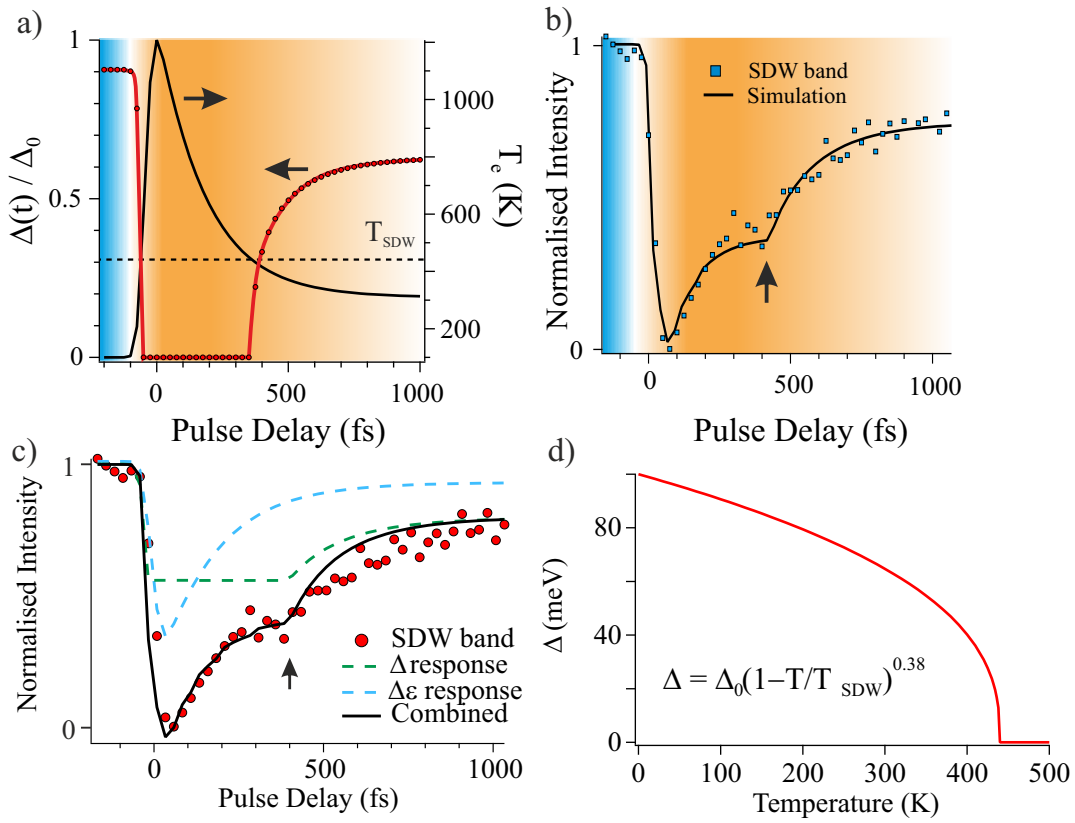

Figure 8.7: a) Dynamics of the order parameter $\Delta(t)$ compared with the electronic temperature. b) Integrated time trace intensity in the renormalised region of the SDW band structure revealing two time scales of recovery: rigid shift and SDW reformation. The solid line is from a simulation explicitly including both effects, the breakdown of which is shown in c) and again compared with the data. d) Mean field value of the order parameter for Cr/W(110) with the exponent value obtained in Ref. [Sch99a]. The functional form was used as an input to the SDW simulations outlined in the text.

where Δ_0 is half the gap measured by photoemission, and $T_{SDW} = 440$ K is the surface phase transition temperature of the SDW. The relation $\beta = 0.38$ has been determined in the previous ARPES study of Ref. [Sch99a]. In Fig. 8.7d the behaviour of the order parameter as a function of temperature is given, based on the above relation. The spectral weight in the renormalised bands is given by the coherence factors $u_{\pm}^2 = (1 + \epsilon/E_{\pm})/2$. In the experiment each time delay is associated to a particular T_e, hence time resolution is introduced into the simulation by producing snapshots of the electronic structure at the experimentally determined T_e, which subsequently determines the spectral weight in the band structure. The rigid shift dynamics are added phenomenologically on top of the SDW dynamics.

The response of the order parameter to the transient T_e is shown in Fig. 8.7a, and compared with T_e. In the region where $T_e > T_C$, Δ goes to zero, reflecting the complete closing of the SDW gap. Once T_e drops below T_C, Δ again becomes finite and assumes a value given by T_e. The resulting simulated spectral response of the renormalised SDW band is shown in Fig. 8.7b as a solid black line. The simulation assumes a single linear dispersion which is renormalised by the order parameter as in Eq. 8.5. The simulated dispersion is broadened by a Gaussian representing the

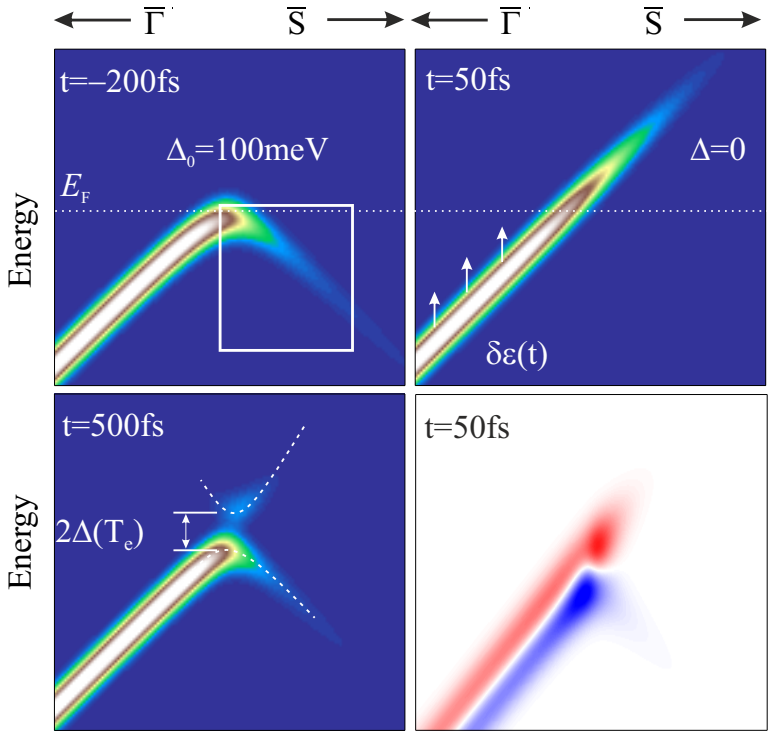

Figure 8.8: Simulated SDW dispersion data. Top left: before excitation showing the renormalised SDW band bending away from the Fermi level. Top right: following excitation the SDW gap closes and the linear dispersion appears. Bottom left: At longer times the SDW dispersion reappears as the order parameter recovers. The SDW gap reopens, but electrons are still found in states above the Fermi level due to the gradual cooling of the system. Bottom right: difference image at 50 fs highlighting the changes in the region of the renormalised band and also revealing the rigid shift along the length of the band.

energy resolution and multiplied by the Fermi-Dirac distribution. The energy and momentum region considered in the simulation is marked in Fig. 8.8 (upper left panel) by a white box, which is equivalent to that used to extract the response of the data, as marked in Fig. 8.4b.

Following excitation, two distinct regions of recovery are evident (t $>$ 100 fs). The first rapid increase in intensity is due to the relaxation of the rigid band shift presented in Fig. 8.5d, which shifts the electronic structure relative to the fixed region of interest (ROI). In principle, such an effect may be removed by considering a ROI large enough to encompass both the bands plus the shift. However doing so means the ROI includes the region in which the Fermi distribution is transiently broadened and as a result a transient change of intensity is also observed here due to changing thermal distribution: in other word the window region cannot be chosen such that the rigid dynamics are included. Indeed, the simulation shows that the rigid shift dynamics and the dynamics of the Fermi distribution (modelled by the SDW density of states multiplied by the Fermi function) give the same qualitative response. Superimposed on the rigid shift dynamics are the dynamics of the order parameter, which is saturated to zero directly following excitation due to the large T_{el}. As shown in Fig. 8.7a, the order parameter is at it's low temperatuer value before excitation and then plateaus with value zero in the time region -50 fs $<$ t $<$

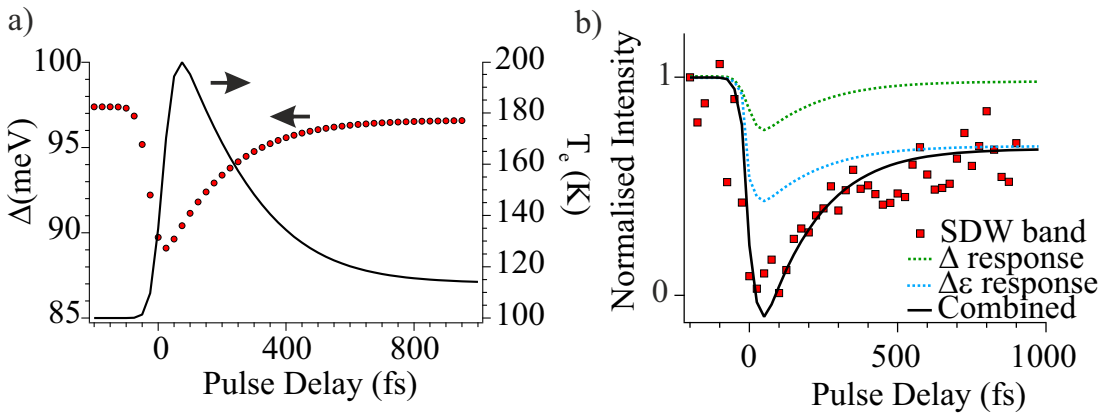

Figure 8.9: a) Electronic temperature extracted from EDCs and the corresponding order parameter for data obtained with a fluence of 0.2 mJ cm^{-2}. At this fluence the SDW gap is never completely closed, but is reduced in size. b) Breakdown of the rigid shift and SDW dynamics for this fluence.

400 fs. It again becomes finite at longer time delays. When $\Delta = 0$ the spectral weight in the SDW band is completely removed and transferred to the linear dispersion of the paramagnetic phase, as was seen in Fig. 8.4b. Once $\Delta > 0$, spectral weight is abruptly transferred back into the renormalised SDW band, resulting in a shoulder in the recovery dynamics, marked by the arrow in Fig. 8.7b. The simulated response is compared to the experimental data from the region of the SDW band (box "SDW" in Fig. 8.4a) and shows good agreement.

Snapshots from the simulation presented in Fig. 8.8 summarize the effects taking place in the electronic structure. For a given pulse delay, the magnitude of the order parameter is determined by T_e, which therefore defines both the size of the gap and the spectral weight of the renormalised band. Before time zero, when T_e is below the SDW transition temperature, the back-folded dispersion is clearly visible. Above the transition temperature, spectral weight is removed from the renormalised band and only the excited linear dispersion is observed, with states extending above the Fermi level. As the system cools, the situation in the lower left panel is reached, where a non-zero order parameter both opens a gap and places spectral weight in the renormalised band. Since the system is still excited, there are now states in both the upper and lower parts of the gapped dispersion. In principle, as this image suggests, following the gap size directly, as was shown for In/Si(111) and indeed for a number of systems [Sch08, Ret16], would be the most direct way to address the SDW dynamics. However given the energy resolution available during these experiments it has not been possible to resolve the gap. In addition the rigid band shift results in a reduction of intensity for a fixed region of the electronic structure. The separation of the two effects (the rigid band shift and order parameter dynamics) is presented explicitly in Fig. 8.7c.

Further evidence that Δ is solely governed by T_e, comes from low fluence data Fig. 8.9b. At a fluence of 0.2 mJ cm^{-2} the recovery dynamics exhibit only a single relaxation time scale as a result of a mixture of the rigid shift dynamics and the always finite order parameter shown in Fig. 8.9a. This is consistent with the extracted T_{el} curve, which reveals the electronic system does not reach the SDW transition temperature i.e. $T_e < T_{SDW}$ for all times. Thus Δ has a finite value for all time

delays at this fluence, and the system is not driven into the paramagnetic phase. This corroborates the idea that upon ultrafast optical excitation the melting and recovery of the SDW is driven by a purely electronic mechanism and that Δ can indeed be quantitatively tracked through the ultrafast phase transition.

The disappearance of the SDW signature - the renormalised band - implies the electron gas no longer experiences the SDW spin-ordering potential, which results in the disappearance of the long-range spin ordering. Since AFM ordering is present only in the SDW phase, once the SDW is removed, the magnetic order also disappears i.e. on a sub-100 fs time scale. Such a rapid demagnitisation is a result of the pure electronic origin of the SDW [Ove62]. It is thus concluded that the SDW is directly driven by the transient T_e and that even on ultra short time scales the transient heating of the electrons drives the spin-ordering of the SDW transition. The lattice plays a limited role in the SDW transition, acting as a heat sink allowing the heated electron gas to cool and the SDW ordering to re-emerge. In general trARPES is a useful tool for distinguishing the different driving mechanisms of density wave states based on time scales [Hel12]. The ultrafast melting of the SDW in Cr/W(110) is more rapid than that typically found in Peierls-like CDW materials [Sch08, Fri17], in which the lattice has to respond in order for the transition to be completed, but is more comparable to that observed in Mott [Per06, Pet11] or other electronically stabilised phases e.g. excitonic insulators [Roh11, Mon16]. The fact that the SDW melting dynamics occur on such short time scales, and additionally that the mean field model based on the T_e appears to confirm the role of electron-electron correlations as the driving force of the SDW phase.

8.3 Summary

In summary, trARPES at XUV energies has been used to investigate the excitation and recovery of the SDW in Cr(110) thin films on ultrafast time scales. It is found that that the transition to the paramagnetic state occurs promptly within the pump-pulse duration i.e. on a sub-100 fs time scale. In addition, the order parameter Δ is shown to follow the electronic temperature T_e which governs both the closing and re-opening of the SDW gap. This therefore suggests that the electrons are in quasi-equilibrium with the spin order, while out of equilibrium with the lattice. This shows that concepts from thermodynamic equilibrium can survive in the ultrafast regime for phases governed by the temperature of a single sub-system, even when not equilibrated with other degrees of freedom e.g. phonons. Such a concept should not only be true for electrons. Therefore it is speculated that such a mean-field approach may be applicable to other ordered phases which are governed by a single sub-system temperature.

9 Conclusions and Perspectives

This thesis focusses on the electronic band structure of quasi-1D materials. Confining electrons to such nanoscale structures leads to a number of intriguing emergent behaviours often involving a complex interplay between electronic, lattice and spin degrees of freedom. By utilising both high resolution ARPES to examine the ground state properties, and trARPES to investigate dynamical effects out of equilibrium, this study has provided fundamental insights into the microscopic couplings and mechanisms in a number of model quasi-1D systems.

$NbSe_3$

A dimensional crossover from 1D to 3D has been observed in the prototypical CDW compound $NbSe_3$. The coupling to a higher dimensional environment has been quantified from the quasi-1D warping of the Fermi level, and corroborated by an energy dependent analysis of the density of states. The analysis presented here is expected to be applicable to other quasi-1D systems due to the generality of finite inter-chain coupling in real materials, and will hopefully stimulate further experimental and theoretical research on the dimensional crossover. Particularly from the theoretical side, the dimensional crossover represents a fundamental challenge that is actively under investigation [Gia08, Ima09, Lak13, De 16, Fur16]. The low temperature electronic structure has been clarified, including the observation of CDW gaps in the electronic structure at the momenta indicated by x-ray diffraction. With regard to $NbSe_3$ specifically, this study has clarified the band dispersions and deepened the understanding of the effect of the CDW on the electronic structure.

Future work is likely to focus on the driving mechanism of the CDWs, which is still unclear as no gaps have been observed at the Fermi level. Ultra high-resolution measurements in the regime of a few meV or better, achievable for example with continous wave 6 eV lasers, may help shed light on this. Furthermore, the reason for the anomalous reduction in spectral weight at low temperatures, also observed in many other quasi-1D materials, remains unexplained. It may be that this behaviour is particular to the ARPES technique, or that this class of materials share some common physics that is not currently understood. In either case, future work in this direction will require a combination of high quality experimental data with theoretical modelling in order to understand the microscopic mechanisms at play. As a final perspective it is noted that trARPES measurements might allow access to a "true" 1D regime above the crossover temperature 1250 K. Since the transient electronic temperature can in principle be raised to very high values shortly after pump excitation, this could give a route to probing $NbSe_3$, or indeed other materials, above the crossover temperature. However such measurements would certainly be very challenging due to the small crystal size.

Ag/Si(557)

Metal wires on semiconducting substrates are important model systems for low dimensional materials. The Fermi surface of the 1 ML Ag/Si(557) nanowire structure has been investigated for the first time and is found to exhibit 2D metallic pockets at the Brillouin zone boundary as observed by ARPES. Filling this band by electron doping moves it to higher binding energies by several hundred meV. Evidence for a surface state is found consistent with the existence of step-edge bound residual gas atoms which dope the Ag states on the (111) terraces, supporting a previously suggested extrinsic doping mechanism. In the fully doped phase replicas of 2D Ag pockets are observed as a result of the interaction with the anisotropic substrate underlying the Ag surface. An analysis of the confining step potential suggests a regime in which confined states could be expected to be observed, however it is likely the structural inhomogeneity of the step edges masks their observation. On the other hand, by comparison to a number of other literature studies, it appears that the observation of confined plasmon states in EELS implies a more 2D environment as viewed by ARPES.

It will be interesting in future to focus on the possibility of tuning surface systems from quasi-1D to more 2D, either by systematically changing the substrate miss-cut as in Ref. [Lic16] or by tailoring the width of conduction channels via metallic coverage. Ag/Si(557) may not be the best candidate in this regard due to the structural inhomogeneity of the step edges, so the investigation of other systems including the development of new quasi-1D systems will be important. It may also be possible to approach the problem from the opposite scale and construct quasi-1D nanostructures from bulk crystals via lithographic techniques.

In/Si(111)

In/Si(111) nanowires undergo a well-known structural and electronic distortion at low temperatures, involving the interplay of multiple degrees of freedom. A detailed study of the photo-induced phase transition in In/Si(111) has been carried out with trARPES. The phase transition is found to evolve on three distinct time scales, each related to the dynamics of a specific spectral feature in momentum space. This analysis clearly reveals the temporal separation of the metal-to-insulator and structural transitions. In addition the distribution of excited states across multiple BZs is mapped, and used as an input to perform MD simulations with realistic electronic distributions and relaxation. An exceptional agreement between experiment and theory in this model system is found, which suggests that the microscopic forces and potential energy surface during the transition can be extracted with a high degree of accuracy. In particular the simulations highlight the role played by photo-excited holes localised in the Brillouin zone in the reaction mechanism. Finally a link is made from the transient electronic structure to the ultrafast formation of bonds in real space. These results provide unprecedented insights into the microscopic mechanism of a surface phase transition reaction involving electronic and structural interplay.

In future it will be interesting to investigate the influence of excitonic effects which, given the reduced dimensionality of the system, may play a central role. Such effects have been predicted to have a 10 times stronger effect at the bare Si surface than in the bulk [Roh99]. Calculations in this direction may help explain the discrepancy between the GW band structure and the experimental data in the (8x2)

phase. Additionally, changing the wavelength of the excitation pulse may provide further insights into the role of the substrate in stabilising the two phases, and to what degree coupling to the higher dimensional environment affects the dynamic phase transition. In particular an excitation below the Si band gap would be an exciting possibility. This would most likely require the implementation of a tunable pump source via a nOPA.

Cr/W(110)

The ultrafast dynamics of the SDW transition in Cr/W(110) thin films has been shown to be governed by the transient electronic temperature, thus demonstrating that equilibrium thermodynamic concepts can still survive on ultra-short time scales. This in contrast to the dynamics of many CDW materials, including quasi-1D In/Si(111), which show a strong lattice component. The electronic structure is simulated with a mean field model in order to disentangle intrinsic SDW dynamics from other non-equilibrium effects. The rapid loss of spin ordering in less that 100 fs suggests that antiferromagnetically ordered phases such as the SDW in Cr could have technological uses in future ultrafast data processing.

Directions for future work include investigation of the *charge* density wave in Cr [Faw88] thought to arise as the second harmonic of the SDW, although the exact relation between SDW and CDW order is a key open question [Jac14]. However it is not clear what, if any, signature of the CDW exists in photoemission, so it is likely that other techniques such as x-ray diffraction would be a more suitable choice. Recently the CDW has been investigated with ultrafast x-rays and was shown to have an *increased* order parameter upon excitation [Sin16]. It has also been predicted that both excitations of amplitude and phase could be excited; the latter giving rise to dynamic CDWs [Faw88].

The studies of interactions with higher dimensional environments at equilibrium have shown that ARPES can provide an efficient way to characterise the degree of one dimensionality in a material; in other words a quantification of the "quasi" in quasi-1D. On the other hand, trARPES has revealed the complex interplay of various degrees of freedom during photo-induced phase transitions. An excellent agreement between experiment and theory in these ultrafast studies reveals a microscopic understanding of quasi-1D systems out-of-equilibrium. The results presented in this work provide detailed insights into the coupling mechanisms in quasi-1D materials.

A ARPES study of the quasi-1D superconductor $K_2Cr_3As_3$

The following is a brief summary of an ARPES study of the quasi-1D superconductor $K_2Cr_3As_3$ carried out during this thesis. The work is a collaboration with the group of Dr. Moritz Hoesch, who orchestrated the project. The data was obtained at the Diamond Light Source synchrotron in the UK, and has been published in Watson *et al.*, *Phys. Rev. Lett.*, 118, 097002 (2017) [Wat17].

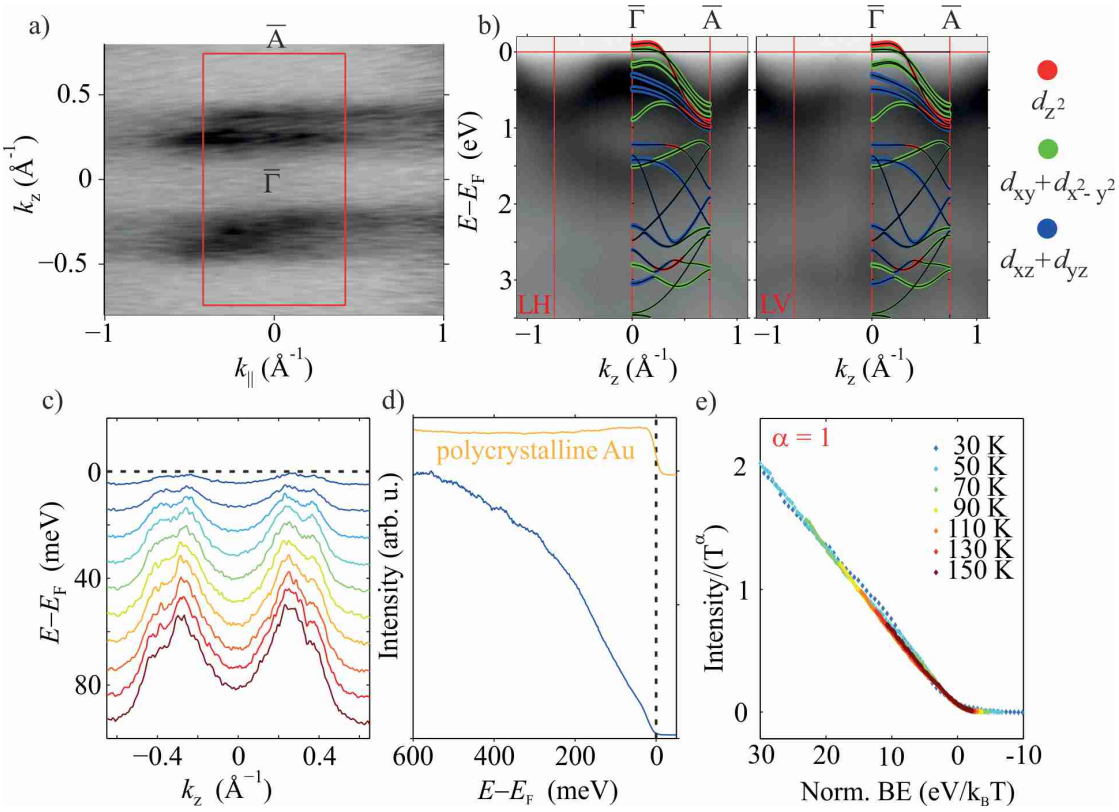

Figure A.1: a) Fermi surface and surface BZ of $K_2Cr_3As_3$. b) Band structure along the $\overline{\Gamma} - \overline{A}$ direction for linear horizontal (LH) and vertical (LV) polarisation and overlaid DFT calculations. c) Horizontal cuts through momentum at selected energies below the Fermi level showing the 4-band dispersion. d) Integrated spectral weight for the 1D bands, compared with that of polycrystalline Au. e) Scaled spectral intensity showing the spectra collapse onto a single power law curve with $\alpha = 1$, suggestive of TLL behaviour.

The recently discovered quasi one-dimensional (1D) superconductors $A_2Cr_3As_3$ (A = K; Rb; Cs) present a new opportunity for the study of the phenomena that may occur when electrons are effectively confined to 1D. The inclusion of Cr in the structure is a rare example of incorporating 3d orbitals into a quasi-1D system, as opposed to the well-known case of 4d orbitals in metallic Mo-based quasi-1D systems $Li_{0.9}Mo_6O_{17}$ and $Tl_2Mo_6Se_6$, which brings the possibility of strong correlations [Bao15]

and magnetic interactions, which may be frustrated due to the triangular Cr motifs in the structure [Wu15a]. Superconductivity is found at 6.1 K in $K_2Cr_3As_3$ [Kon15], which ranks amongst the highest T_C for quasi-1D systems, and has been suggested to be of an unconventional nature [Bao15] with some experimental [Adr15, Liu16] and theoretical [Zho15, Wu15b, Jia15] support for a triplet pairing state. Finally, the 1D nature of the system makes it a candidate for Tomonaga-Luttinger liquid (TLL) physics [Zho15, Zhi15, Mia16, Wac16]. This rich set of phenomena constitutes a very strong motivation for experimental determinations of the electronic structure by ARPES measurements.

We present a detailed study of the electronic structure of single crystals of $K_2Cr_3As_3$ using ARPES. We find a Fermi surface containing two linearly dispersing hole-like quasi-1D Fermi surface sheets (Fig A.1a). The overall bandwidth of the Cr 3d bands and Fermi velocities are comparable to DFT calculations (Fig A.1b), indicating that the correlated Fermi liquid picture is not appropriate for $K_2Cr_3As_3$. Furthermore we show that the spectral weight of the quasi-1D bands in the region of the Fermi level (Fig A.1c) decreases according to an approximately linear power law over a $\sim$200 meV energy scale up to the Fermi level (Fig A.1d), also obeying a universal temperature scaling relation (Fig A.1e). Such a temperature scaled power-law depletion of spectral weight is a signature of TLL behaviour in photoemission measurements of one-dimensional systems. We conclude that the wide range of fascinating experimental results on $A_2Cr_3As_3$ should be interpreted within the framework of a quasi-1D system close to TLL physics.

B trARPES study of the 2D-TMDC WSe_2

The following is a brief summary of a trARPES study of bulk TMDC WSe_2. A significant part of the work was completed within the framework of this thesis. The data was obtained at the Artemis user facility in the UK, and has been published in Bertoni *et al.*, *Phys. Rev. Lett.*, 117, 277201 (2016) [Ber16].

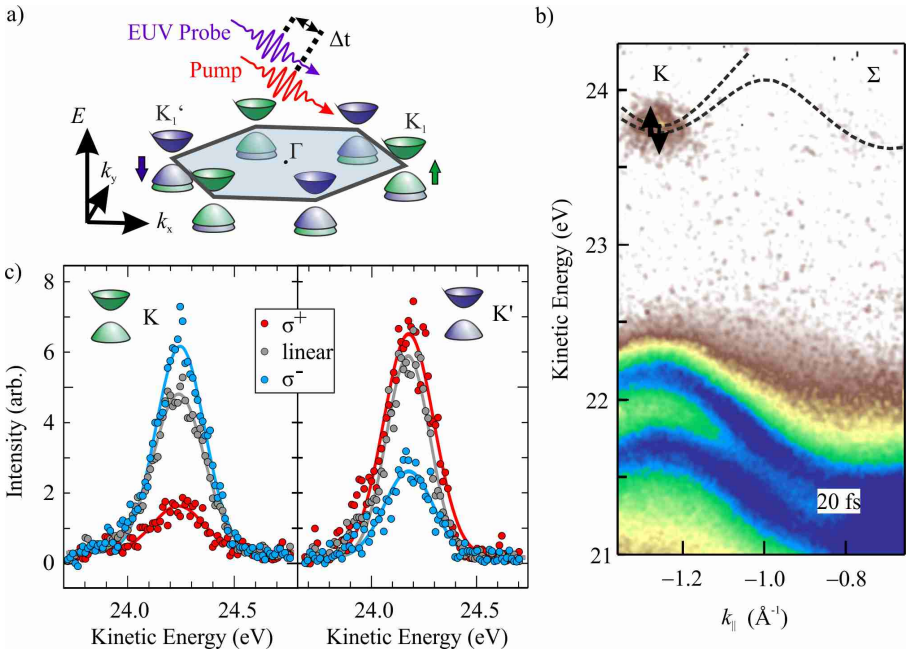

Figure B.1: a) Schematic band structure throughout the full Brillouin zone. Spin split VBs (lower parabolas) are in the occupied states, while the CB (upper parabola) is unoccupied. Moving from K to K' points reverses the spin order. A schematic pump-probe experiment is included. b) Band structure close to the K-point along the $\Gamma - K$ direction shortly after excitation. Both VBs and the bottom of the CB are observed. The initial population in the CB is rapidly transferred to the global CB minimum at the Σ-point. c) Vertical cuts in energy at the K and K'-points for excitation with positive and negative circularly polarised and linear polarised pump pulses.

Manipulation of spin and valley degrees of freedom is a key step towards realizing novel quantum technologies for which semiconducting 2D transition metal di-chalcogenides (TMDCs) have been established as promising candidates [Mak12, Zen12, Gon13, Xu14]. In monolayer TMDCs, the lack of inversion symmetry in 2H-polytypes gives rise to a spin-valley correlation of the band structure which, in combination with strong spin-orbit coupling in those containing heavy transition metals [Zhu11], lifts the energy degeneracy of electronic bands of opposite spin polarizations, allowing for valley-selective electronic excitation with circularly polarized light [Mak12, Zen12, Zhu11, Xia12, Cao12, Ber14]. While such an effect should be forbidden in inversion symmetric materials, recent theoretical work suggests that

the absence of inversion symmetry within moieties of the unit cell locally lifts the spin degeneracy [Zha14, Liu15]. The lack of inversion symmetry and the presence of in-plane dipole moments within individual TMDC layers can be seen as atomic site Dresselhaus and Rashba effects and can cause a hidden spin texture in a globally inversion symmetric material [Zha14]. This is supported by the observation of spin-polarized valence bands in 2H-WSe_2 by photoelectron spectroscopy [Yu99] and spin-resolved ARPES [Ril14]. Polarization-resolved photoluminescence experiments on inversion-symmetric bilayer samples [Mak12, Zen12, Wu13, Zhu14, Jon14] have shown varying degrees of circular dichroism. This has primarily been explained by symmetry breaking induced by applied or intrinsic electric and magnetic fields.

This study demonstrates that it is possible to generate spin-, valley- and layer-polarized excited states in the conduction band of centrosymmetric samples of bulk 2H-WSe_2. A schematic of the electronic structure in a single layer is shown in Fig. B.1a. At each of the corners of the hexagonal Brillouin zone, a spin split valence band (VB) below the Fermi level and an unoccupied conduction band (CB) is found. The spin character at the inequivalent K and K' points is reversed, as depicted by the green and blue colour scale. Layer sensitivity in the measurements is achieved by using a probe energy of 23 eV [Ril14].

A trARPES measurement of the band structure close to the K-point along the $\Gamma - K$ direction after excitation with a 1.63 eV pump pulse – slightly above the direct band gap at the K-point – is presented in Fig. B.1b. The spin split VBs in the occupied states are clearly resolved, as is the bottom of the CB in the unoccupied states. By employing circularly polarized pump pulses, spin-polarized excited state populations are observed in the K valleys, as summarised in Fig. B.1c. The population in the CB at the K-point is clearly observed to depend on the helicity of light. In addition, switching to the K'-point exactly reverses this dependence. It is found that the initial population in the K-point CB is rapidly transferred on a sub-100 fs time scale to the global minimum of the conduction band at the Σ-points. This intervalley scattering leads to a loss of valley and layer polarization as the interlayer coupling at Σ is strongly enhanced. In view of utilizing multilayer WSe_2 as a source of ultrafast spin currents, efficient electronic coupling of the acceptor states to the conduction band states at Σ is required. This suggests a strategy for the extraction of spin-polarized carriers between neighbouring layers in TMDC multilayers and heterostructures [Gei13, Wit15, Ye16] where transfer of electrons between layers is governed by the state-dependent interfacial electronic coupling, which can be controlled by an appropriate choice of materials, stacking order, and relative orientation. Such control combined with microscopic understanding of electron dynamics, as provided here, are crucial for conceiving TMD-based spintronic device concepts.

C trARPES study of the 2D-TMDC $TiSe_2$

The following is a brief summary of a trARPES study of bulk $TiSe_2$. A significant part of the work was completed within the framework of this thesis. The project has been organised and led by Dr. Claude Monney. The data was obtained at the Artemis user facility in the UK, and has been published in Monney *et al.*, *Phys. Rev. B*, 94, 165165 (2016) [Mon16].

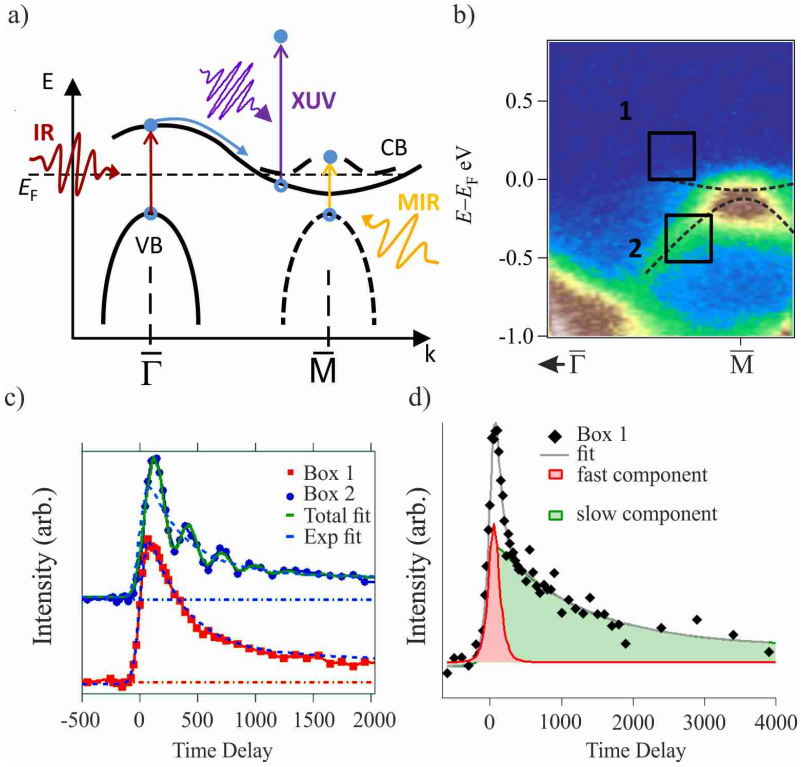

Figure C.1: a) Schematic band structure of $TiSe_2$ in the high temperature (solid) and low temperature (dashed) phases. Excitation with the two pump pulses (IR and MIR) used separately in the experiments are shown. b) Snapshot of the back-folded CDW band before excitation. Dashed lines are guides to the eye. The boxes indicate the regions integrated intensity regions presented in c). c) Dynamics in the regions marked in b) which reveal a coherent oscillation in the back-folded CDW band following excitation with a MIR pulse in the CDW phase. d) Dynamics in the high temperature phase revealing a rapid electronic component in the recovery of the system after excitation.

Materials which exhibit a metal-insulator transition occurring concomitantly with a structural phase transition naturally raise questions about the driving mechanism of the phase transition i.e. whether it is possible to single out the roles played by the electronic and lattice degrees of freedom in the transition, and how they affect the electronic structure of such materials. In the case of CDW materials the most direct approach consists of following the photoinduced changes of the CDW spectral features in the time domain, namely the closing of the CDW gap or the disappearance

of the CDW backfolded bands [Sch08, Per06, Roh11, Pet11]. Many studies have focussed on the first hundred femtoseconds following the photoexcitation, in order to figure out whether these changes occur faster or not than the movement of ions relevant to the structural distortion, the timing of which is given by the period of the relevant phonon mode. The dynamics of the recovery of the CDW order has received much less attention.

The TMDC $TiSe_2$ undergoes a peculiar second-order CDW transition [Di 76] below $T_C = 200$ K. A schematic of the band structure along the $\overline{\Gamma}$-$\overline{M}$ direction is shown in Fig. C.1a. Well above the transition temperature a hole like valence band (VB) is observed to disperse around the $\overline{\Gamma}$-point, while an electron band crosses the Fermi level at the $\overline{M}$-point. In the CDW phase a replica of the VB appears at the $\overline{M}$-point, along with a new conduction band in the unoccupied states, both shown by dashed lines. The back-folded dispersion at 30 K measured by the XUV beam before excitation is presented in Fig. C.1b. The mechanism of its CDW transition has been debated intensively over the last decades, in terms of either an electronic [Cer07, Li07] or a structural origin [Kid02, Cal11, Web11]. Time-resolved techniques seem to give a decisive answer by focussing on the ultrafast melting of the CDW and disentangling the roles of electrons and lattice on the femtosecond time scale [Roh11, Hel12, MV11]. This is consistent with a purely electronic mechanism of the CDW transition, which may be an instability towards an excitonic insulator phase [Kel65, Jér67]. On the other hand a recent ultrafast terahertz study [Por14] supports a combined scenario in which both the electrons and the lattice combine to produce the CDW instability in $TiSe_2$ [vW10, Zen13].

We focus on the femtosecond dynamics via trARPES of both the recovery of CDW phase in $TiSe_2$ at 30 K, as well as of high-temperature CDW fluctuations at 240 K, which precedes the CDW instability. We reveal the energy and momentum resolved dynamics of both the lattice and electron degrees of freedom. In the CDW phase the VB to CB transition at the $\overline{M}$-point is excited resonantly with a mid-IR pulse at 3100 nm (400 meV) (yellow pulse in Fig. C.1a). This induces a 3.4 THz coherent oscillation of the CDW amplitude mode, as shown in Fig. C.1c, observed here for the first time with trARPES. The excitation is localised to the back-folded CDW band, and is only observed for a resonant excitation at this wavelength. Above T_C, with an excitation at 1400 nm (890 meV) (red pulse in Fig. C.1a), we single out a fast component in the recovery of the CDW correlations with a relaxation time ≤ 100 fs, presented in Fig. C.1d. We interpret it as the consequence of the ultrafast recovery from the screening of the Coulomb interaction responsible for the electron-hole correlations, which precede the CDW phase transition. The observation of these two contributions, the coherent oscillations of the CDW amplitude mode at low temperature and the ultrafast electronic recovery at high temperature, support the idea that both the interband Coulomb interaction and the electron-phonon coupling stabilize cooperatively the CDW phase in $TiSe_2$.

D Details of Spectral Function Calculation for $NbSe_3$

A brief description of the method employed to calculate the spectral function of $NbSe_3$ including the CDW gaps as presented in Chapter 5 is given below. Calculations have been carried out by C. Berthod, University of Geneva.

We consider a two-dimensional, two-band model described by the Hamiltonian

$$H = \sum_{n\boldsymbol{k}} E_{n\boldsymbol{k}} c^\dagger_{n\boldsymbol{k}} c_{n\boldsymbol{k}} + V_1 \sum_{n\boldsymbol{k}} \left(c^\dagger_{n\boldsymbol{k}} c_{n\boldsymbol{k}+\boldsymbol{q}_1} + \text{h.c.} \right) + V_2 \sum_{n\boldsymbol{k}} \left(c^\dagger_{n\boldsymbol{k}} c_{n\boldsymbol{k}+\boldsymbol{q}_2} + \text{h.c.} \right) \quad \text{(D.1)}$$

on a rectangular lattice with parameters b and c. The band dispersions are $E_{n\boldsymbol{k}} = -2t_{nb}\cos(k_{\parallel \text{b}} b) - 2t_{nc}\cos(k_{\parallel \text{c}} c) - \mu_n$, $n = 1, 2$. With $t_{nb} \gg t_{nc}$, this represents a quasi-one dimensional lattice with main dispersion along the y direction. We choose parameters that mimic the two outer bands of $NbSe_3$: $(t_{1b}, t_{1c}, \mu_1) = (0.681, 0.027, -0.898)$ eV and $(t_{2b}, t_{2c}, \mu_2) = (1.88, 0.027, -3.545)$ eV. The interchain hopping $t_{nc} = 27$ meV was set to match the Fermi-surface warping for band 2 (Fig. 5.6b); we use the same value for band 1 for simplicity. The remaining parameters t_{nb} and μ_n are adjusted to reproduce the Fermi points and band minima observed in Fig. 5.6a. The last two terms in the Hamiltonian describe electrons moving in the periodic potential $V(\boldsymbol{r}) = 2V_1 \cos(\boldsymbol{q}_1 \cdot \boldsymbol{r}) + 2V_2 \cos(\boldsymbol{q}_2 \cdot \boldsymbol{r})$. This simple cosine behaviour is a minimal model for a CDW with modulation vectors $\boldsymbol{q}_1$ and $\boldsymbol{q}_2$. We focus on the CDW along the chains and fix the vectors to $\boldsymbol{q}_1 = [0, 7\pi/(16b)]$ and $\boldsymbol{q}_2 = [0, \pi/(2b)]$. We choose these values because (i) with $b = 3.48$ Å the wavevectors 0.395 Å^{-1} and 0.451 Å^{-1} are similar to the values 0.435 Å^{-1} and 0.468 Å^{-1} observed in Fig. 5.5a; (ii) these wavevectors connect $\boldsymbol{k}$ points of band 1 at energies -209 meV and -119 meV, close to the values -210 meV and -120 meV where spectral weight is suppressed in the ARPES data; and (iii) the ratio of the two wavelengths is 8/7, which leads to a commensurability with a not-too-long period of $32b$. Exact commensurability is an advantage for the calculations. The splittings of the EDC peaks due to the $\boldsymbol{q}_1$ and $\boldsymbol{q}_2$ modulations can be estimated to be 70 and 65 meV, respectively (see Fig. 5.5c of the main text). We therefore set the amplitudes to $V_1 = 70$ meV and $V_2 = 65$ meV.

The spectral function, to be compared with the ARPES intensity, is calculated as

$$A(\boldsymbol{k}, E) \;=\; \frac{1}{S} \int d^2R \left(-\tfrac{1}{\pi}\right) \text{Im} \int d^2\rho \, e^{-i\boldsymbol{k}\cdot\boldsymbol{\rho}} \times G(\boldsymbol{R} + \boldsymbol{\rho}/2, \boldsymbol{R} - \boldsymbol{\rho}/2, E). \quad \text{(D.2)}$$

$G(\boldsymbol{r}, \boldsymbol{r}', E)$ is the retarded Green's function in real space, which breaks translational invariance due to the CDW. We Fourier transform the Green's function with respect to the relative coordinate $\boldsymbol{\rho} = \boldsymbol{r} - \boldsymbol{r}'$, and perform a spatial average over the surface S with respect to the center-of-mass coordinate $\boldsymbol{R} = (\boldsymbol{r} + \boldsymbol{r}')/2$. In the absence of CDW, G is independent of $\boldsymbol{R}$ and the formula reduces to the usual definition for systems with translation invariance: $A(\boldsymbol{k}, E) = (-1/\pi)\,\text{Im}\, G(\boldsymbol{k}, E)$. The real-space Green's function is calculated as $G(\boldsymbol{r}, \boldsymbol{r}', E) = \langle \boldsymbol{r} | (E + i0 - H)^{-1} | \boldsymbol{r}' \rangle$, by expanding $(E + i0 - H)^{-1}$ on Chebyshev polynomials [Cov10]. The expansion is truncated to

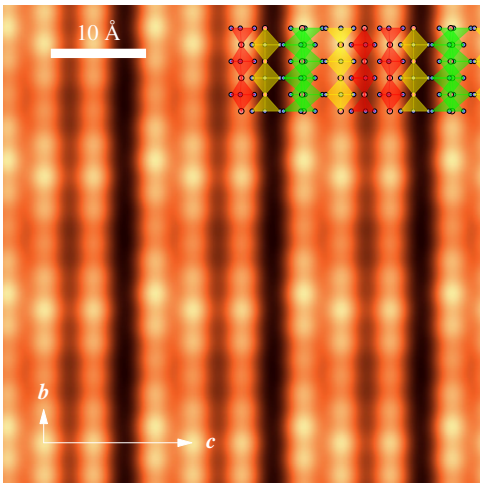

Figure D.1: Simulated STM image of the bc plane of $NbSe_3$. The projection of the crystal structure is overlaid for comparison. The CDW modulation calculated with the tight-binding model is visible along $\boldsymbol{b}$. The CDW period along $\boldsymbol{b}$ is $32b$, exceeding the size of the image.

order 1000 and terminated with the Jackson kernel [Wei06]. The real-space system size used in the calculation contains 501'001 unit cells.

For a comparison with STM measurements [Pro96, Bru10] we also compute the local density of states $N(\boldsymbol{r}, E) = (-1/\pi)\mathrm{Im}\, G(\boldsymbol{r}, \boldsymbol{r}, E)$. To mimic the STM topography, we calculate the tunneling current at -0.3 eV, $I(\boldsymbol{r}) = \int_{-0.3\ \mathrm{eV}}^{0} dE\, N(\boldsymbol{r}, E)$, for each site of the tight-binding lattice. We then attach to each Nb atom close to the cleaving plane a Gaussian function of full width at half maximum b, and weight these functions according to $I(\boldsymbol{r})$. The result presented in Fig. D.1 bears some resemblance with the STM data, in spite of the model simplicity. The most intense signal comes from the two type-III chains, one being closest to the STM tip and the second one almost exactly beneath the first one. One of the type-I chains (red) is at the surface while the second one is beneath the surface, only visible through a narrow channel, leading to a low-intensity line. Finally, the darkest regions correspond to one of the type-II (yellow) chains lying below the top Nb layer and visible through a wider channel between type-I and type-II surface chains.

Bibliography

[Abu95] T. Abukawa, M. Sasaki, F. Hisamatsu, T. Goto, T. Kinoshita, A. Kakizaki, & S. Kono. *Surface electronic structure of a single-domain Si(111)4 x 1-In surface: a synchrotron radiation photoemission study.* Surf. Sci. **325**, 33 (1995). DOI: 10.1016/0039-6028(94)00693-8.

[Adr15] D. T. Adroja, A. Bhattacharyya, M. Telling, Yu Feng, M. Smidman, B. Pan, J. Zhao, A. D. Hillier, F. L. Pratt, & A. M. Strydom. *Superconducting ground state of quasi-one-dimensional K2 Cr3 As3 investigated using μsR measurements.* Phys. Rev. B - Condens. Matter Mater. Phys. **92**, 13, 1 (2015). DOI: 10.1103/PhysRevB.92.134505.

[Ahn04] J. R. Ahn, J. H. Byun, H. Koh, E. Rotenberg, S. D. Kevan, & H. W. Yeom. *Mechanism of gap opening in a triple-band Peierls system: In atomic wires on Si.* Phys. Rev. Lett. **93**, 10, 8 (2004). DOI: 10.1103/PhysRevLett.93.106401.

[All62] F. G. Allen & G. W. Gobeli. *Work function, photoelectric threshold, and surface states of atomically clean silicon.* Phys. Rev. **127**, 1, 150 (1962). DOI: 10.1103/PhysRev.127.150.

[And72] P. W. Anderson. *More Is Different.* Science (80-.). **177**, 4047, 393 (1972). DOI: 10.1126/science.177.4047.393.

[And81] P. W. Anderson. *Basic Notions of Condensed Matter Physics.* The Benjamin/Cummings Publishing Co., California (1981).

[Arr99] Enrico Arrigoni. *Crossover from Luttinger- to Fermi-Liquid Behavior in Strongly Anisotropic Systems in Large Dimensions.* Phys. Rev. Lett. **83**, 1, 128 (1999). DOI: 10.1103/PhysRevLett.83.128.

[Åsb70] L. Åsbrink. *The photoelectron spectrum of H2.* Chem. Phys. Lett. **7**, 5, 549 (1970). DOI: 10.1016/0009-2614(70)80169-5.

[Ash76] Neil W. Ashcroft & N. David Mermin. *Solid State Physics.* Brooks/Cole, Belmont, CA (1976).

[Bao15] Jin-Ke Bao, Ji-Yong Liu, Cong-Wei Ma, Zhi-Hao Meng, Zhang-Tu Tang, Yun-Lei Sun, Hui-Fei Zhai, Hao Jiang, Hua Bai, Chun-Mu Feng, Zhu-An Xu, & Guang-Han Cao. *Superconductivity in quasi-one-dimensional K$_2$Cr$_3$As$_3$ with significant electron correlations.* Phys. Rev. X **5**, 011013 (2015). DOI: 10.1103/PhysRevX.5.011013.

[Bar57] J. Bardeen, L. N. Cooper, & J. R. Schrieffer. *Theory of superconductivity.* Phys. Rev. **108**, 5, 1175 (1957). DOI: 10.1103/PhysRev.108.1175.

[Bar82] John Bardeen, E. Ben-Jacob, A. Zettl, & G. Grüner. *Current oscillations and stability of charge-density-wave motion in NbSe3.* Phys. Rev. Lett. **49**, 7, 493 (1982). DOI: 10.1103/PhysRevLett.49.493.

[Bau04a] F. Baumberger, M. Hengsberger, M. Muntwiler, M. Shi, J. Krempasky, L. Patthey, J. Osterwalder, & T. Greber. *Localization of surface states in disordered step lattices.* Phys. Rev. Lett. **92**, May, 196805 (2004). DOI: 10.1103/PhysRevLett.92.196805.

[Bau04b] F Baumberger, M Hengsberger, M Muntwiler, M Shi, J Krempasky, L Patthey, J Osterwalder, & T Greber. *Step-lattice-induced band-gap opening at the fermi level.* Phys. Rev. Lett. **92**, January, 016803 (2004). DOI: 10.1103/PhysRevLett.92.016803.

[Bea14] P. Beaud, A. Caviezel, S. O. Mariager, L. Rettig, G. Ingold, C. Dornes, S-W. Huang, J. A. Johnson, M. Radovic, T. Huber, T. Kubacka, A. Ferrer, H. T. Lemke, M. Chollet, D. Zhu, J. M. Glownia, M. Sikorski, A. Robert, H. Wadati, M. Nakamura, M. Kawasaki, Y. Tokura, S. L. Johnson, & U. Staub. *A time-dependent order parameter for ultrafast photoinduced phase transitions.* Nat. Mater. **13**, August, 923 (2014). DOI: 10.1038/nmat4046.

[Ber64a] C. N. Berglund & W. E. Spicer. *Photoemission Studies of Copper and Silver: Experiment.* Phys. Rev. **136**, 1044 (1964). DOI: 10.1103/PhysRev.136.A1044.

[Ber64b] C. N. Berglund & W. E. Spicer. *Photoemission studies of copper and silver: Theory.* Phys. Rev. **136**, 4A, 1030 (1964). DOI: 10.1103/PhysRev.136.A1030.

[Ber10] M H Berntsen, P Palmgren, M Leandersson, a Hahlin, J Ahlund, B Wannberg, M Månsson, & O Tjernberg. *A spin- and angle-resolving photoelectron spectrometer.* Rev. Sci. Instrum. **81**, 3, 035104 (2010). DOI: 10.1063/1.3342120.

[Ber11] M H Berntsen, O Götberg, & O Tjernberg. *An experimental setup for high resolution 10.5 eV laser-based angle-resolved photoelectron spectroscopy using a time-of-flight electron analyzer.* Rev. Sci. Instrum. **82**, 9, 095113 (2011). DOI: 10.1063/1.3637464.

[Ber14] Gunnar Berghaeuser & Ermin Malic. *Analytical approach to excitonic properties of MoS2.* Phys. Rev. B **89**, 125309 (2014). DOI: 10.1103/PhysRevB.89.125309.

[Ber16] R. Bertoni, C. W. Nicholson, L. Waldecker, H. Hübener, C. Monney, U. De Giovannini, M. Puppin, M. Hoesch, E. Springate, R. T. Chapman, C. Cacho, M. Wolf, A. Rubio, & R. Ernstorfer. *Generation and Evolution of Spin-, Valley-, and Layer-Polarized Excited Carriers in Inversion-Symmetric WSe2.* Phys. Rev. Lett. **117**, 27, 277201 (2016). DOI: 10.1103/PhysRevLett.117.277201.

[Bie01] S. Biermann, A. Georges, A. Lichtenstein, & T. Giamarchi. *Deconfinement transition and Luttinger to Fermi liquid crossover in quasi-one-dimensional systems.* Phys. Rev. Lett. **87**, 27, 276405 (2001). DOI: 10.1103/PhysRevLett.87.276405.

[Bil05] Donald H Bilderback, Pascal Elleaume, & Edgar Weckert. *Review of third and next generation synchrotron light sources.* J. Phys. B **38**, 9, S773 (2005). DOI: 10.1088/0953-4075/38/9/022.

[Bla01] P. Blaha, K. Schwarz, G. Madsen, D. Kvasnicka, & J. Luitz. *An Augmented Plane Wave Plus Local Orbitals Program for Calculating Crystal Properties.* (2001).

[Blo11] T Block, C Tegenkamp, J Baringhaus, & H. Pfnür. *Plasmons in Pb nanowire arrays on Si (557): Between one and two dimensions.* Phys. Rev. B **205402**, 1 (2011). DOI: 10.1103/PhysRevB.84.205402.

[Blu11] C. Blumenstein, J. Schäfer, S. Mietke, S. Meyer, A. Dollinger, M. Lochner, X. Y. Cui, L. Patthey, R. Matzdorf, & R. Claessen. *Atomically controlled quantum chains hosting a Tomonaga–Luttinger liquid.* Nat. Phys. **7**, 10, 776 (2011). DOI: 10.1038/nphys2051.

[Bod07] M. Bode, S. Krause, L. Berbil-Bautista, S. Heinze, & R. Wiesendanger. *On the preparation and electronic properties of clean W(1 1 0) surfaces.* Surf. Sci. **601**, 16, 3308 (2007). DOI: 10.1016/j.susc.2007.06.017.

[Bog58] N. N. Bogoliubov. *On a new method in the theory of superconductivity.* Nuovo Cim. **7**, 6, 794 (1958). DOI: 10.1007/BF02745585.

[Bon95] H. P. Bonzel & Ch Kleint. *On the history of photoemission.* Prog. Surf. Sci. **49**, 2, 107 (1995). DOI: 10.1016/0079-6816(95)00035-W.

[Bos06] Aaron Bostwick, Taisuke Ohta, Thomas Seyller, Karsten Horn, & Eli Rotenberg. *Quasiparticle dynamics in graphene.* Nat. Phys. **3**, 1, 36 (2006). DOI: 10.1038/nphys477.

[Bov07] Uwe Bovensiepen. *Coherent and incoherent excitations of the Gd(0001) surface on ultrafast timescales.* J. Phys. Condens. Matter **19**, 083201 (2007). DOI: 10.1088/0953-8984/19/8/083201.

[Bov12] U. Bovensiepen & P.S. Kirchmann. *Elementary relaxation processes investigated by femtosecond photoelectron spectroscopy of two-dimensional materials.* Laser Photon. Rev. **6**, 5, 589 (2012). DOI: 10.1002/lpor.201000035.

[Bra00] K Braun, S Folsch, G Meyer, & K Rieder. *Observation of charge-density wave domains on the Cr(110) surface by low-temperature scanning tunneling microscopy.* Phys. Rev. Lett. **85**, 16, 3500 (2000). link.

[Bra09] M. Bradler, P. Baum, & E. Riedle. *Femtosecond continuum generation in bulk laser host materials with sub-microJ pump pulses.* Appl. Phys. B Lasers Opt. **97**, 3, 561 (2009). DOI: 10.1007/s00340-009-3699-1.

[Bra12] Serguei Brazovskii, Christophe Brun, Zhao-Zhong Wang, & Pierre Monceau. *Scanning-Tunneling Microscope Imaging of Single-Electron Solitons in a Material with Incommensurate Charge-Density Waves.* Phys. Rev. Lett. **108**, 9, 096801 (2012). DOI: 10.1103/PhysRevLett.108.096801.

[Bra14] J. Braun, K. Miyamoto, A. Kimura, T. Okuda, M. Donath, H. Ebert, & J. Minár. *Exceptional behavior of d-like surface resonances on W(110): The one-step model in its density matrix formulation.* New J. Phys. **16**, 001(2014). DOI: 10.1088/1367-2630/16/1/015005.

[Bro90] S. D. Brorson, A. Kazeroonian, J. S. Moodera, D. W. Face, T. K. Cheng, E. P. Ippen, M. S. Dresselhaus, & G. Dresselhaus. *Femtosecond room-temperature measurement of the electron-phonon coupling constant in metallic superconductors.* Phys. Rev. Lett. **64**, 18, 2172 (1990). DOI: 10.1103/PhysRevLett.64.2172.

[Bro15] H. Bromberger, A. Ermolov, F. Belli, H. Liu, F. Calegari, M. Chávez-Cervantes, M. T. Li, C. T. Lin, A. Abdolvand, P. St J Russell, A. Cavalleri, J. C. Travers, & I. Gierz. *Angle-resolved photoemission spectroscopy with 9-eV photon-energy pulses generated in a gas-filled hollow-core photonic crystal fiber.* Appl. Phys. Lett. **107**, 9, 1 (2015). DOI: 10.1063/1.4929542.

[Bru09] Christophe Brun, Zhao Zhong Wang, & Pierre Monceau. *Scanning tunneling microscopy at the NbSe3 surface: Evidence for interaction between q1 and q2 charge density waves in the pinned regime.* Phys. Rev. B **80**, 4, 045423 (2009). DOI: 10.1103/PhysRevB.80.045423.

[Bru10] Christophe Brun, Zhao-Zhong Wang, Pierre Monceau, & Serguei Brazovskii. *Surface Charge Density Wave Phase Transition in NbSe_{3}.* Phys. Rev. Lett. **104**, 25, 256403 (2010). DOI: 10.1103/PhysRevLett.104.256403.

[Cal11] Matteo Calandra & Francesco Mauri. *Charge-Density Wave and Superconducting Dome in TiSe 2 from Electron-Phonon Interaction.* Phys. Rev. Lett. **106**, 196406 (2011). DOI: 10.1103/PhysRevLett.106.196406.

[Cao12] Ting Cao, Gang Wang, Wenpeng Han, Huiqi Ye, Chuanrui Zhu, Junren Shi, Qian Niu, Pingheng Tan, Enge Wang, Baoli Liu, & Ji Feng. *Valley-selective circular dichroism of monolayer molybdenum disulphide.* Nat. Commun. **3**, May, 887 (2012). DOI: 10.1038/ncomms1882.

[Cas94] C. Castellani, C. Di Castro, & W. Metzner. *Dimensional crossover from Fermi to Luttinger liquid.* Phys. Rev. Lett. **72**, 3, 316 (1994). DOI: 10.1103/PhysRevLett.72.316.

[Cas09] A. H. Castro Neto, F. Guinea, N. M R Peres, K. S. Novoselov, & A. K. Geim. *The electronic properties of graphene.* Rev. Mod. Phys. **81**, 1, 109 (2009). DOI: 10.1103/RevModPhys.81.109.

[Cer07] H Cercellier, C Monney, F Clerc, C Battaglia, L Despont, M G Garnier, H Beck, & P Aebi. *Evidence for an Excitonic Insulator Phase in 1 T - TiSe 2.* Phys. Rev. Lett. **99**, 146403 (2007). DOI: 10.1103/PhysRevLett.99.146403.

[Cha93] S. Chakravarty, A. Sudbø, P. W. Anderson, & S. Strong. *Interlayer tunneling and gap anisotropy in high-temperature superconductors.* Science (80-.). **261**, 5119, 337 (1993). DOI: 10.1126/science.261.5119.337.

[Che14] Alexey Chernikov, Timothy C. Berkelbach, Heather M. Hill, Albert Rigosi, Yilei Li, Ozgur Burak Aslan, David R. Reichman, Mark S. Hybertsen, & Tony F. Heinz. *Exciton binding energy and nonhydrogenic Rydberg series in monolayer WS2.* Phys. Rev. Lett. **113**, 7, 076802 (2014). DOI: 10.1103/PhysRevLett.113.076802.

[Che15] S. V. Chernov, K. Medjanik, C. Tusche, D. Kutnyakhov, S. A. Nepijko, A. Oelsner, J. Braun, J. Minárr, S. Borek, H. Ebert, H. J. Elmers, J. Kirschner, & G. Schönhense. *Anomalous d-like surface resonances on Mo(110) analyzed by time-of-flight momentum microscopy.* Ultramicroscopy **159**, 453 (2015). DOI: 10.1016/j.ultramic.2015.07.008.

[Cor93] P. B. Corkum. *Plasma perspective on strong field multiphoton ionization.* Phys. Rev. Lett. **71**, 13, 1994 (1993). link.

[Cor07] P. B. Corkum & F. Krausz. *Attosecond science.* Nat. Phys. **3**, 381 (2007). DOI: 10.1007/978-3-642-37623-8-1.

[Cou07] A. Couairon & A. Mysyrowicz. *Femtosecond filamentation in transparent media.* Phys. Rep. **441**, 2-4, 47 (2007). DOI: 10.1016/j.physrep.2006.12.005.

[Cov10] L. Covaci, F. M. Peeters, & M. Berciu. *Efficient numerical approach to inhomogeneous superconductivity: The chebyshev-bogoliubov-de gennes method.* Phys. Rev. Lett. **105**, 16, 1 (2010). DOI: 10.1103/PhysRevLett.105.167006.

[Cra02] J. Crain, K. Altmann, C. Bromberger, & F. Himpsel. *Fermi surfaces of surface states on Si(111)-Ag, Au.* Phys. Rev. B **66**, 20, 205302 (2002). DOI: 10.1103/PhysRevB.66.205302.

[Cra04] J. Crain, J. McChesney, Fan Zheng, M. Gallagher, P. Snijders, M. Bissen, C. Gundelach, S. Erwin, & F. Himpsel. *Chains of gold atoms with tailored electronic states.* Phys. Rev. B **69**, 12, 125401 (2004). DOI: 10.1103/PhysRevB.69.125401.

[Cra05] J. Crain, M. Gallagher, J. McChesney, M. Bissen, & F. Himpsel. *Doping of a surface band on Si(111)3x3-Ag.* Phys. Rev. B **72**, 4, 045312 (2005). DOI: 10.1103/PhysRevB.72.045312.

[Cre12] A. Crepaldi, B. Ressel, F. Cilento, M. Zacchigna, C. Grazioli, H. Berger, Ph. Bugnon, K. Kern, M. Grioni, & F. Parmigiani. *Ultrafast photodoping and effective Fermi-Dirac distribution of the Dirac particles in Bi_{2}Se_{3}.* Phys. Rev. B **86**, 20, 205133 (2012). DOI: 10.1103/PhysRevB.86.205133.

[Dam03] Andrea Damascelli. *Angle-resolved photoemission studies of the cuprate superconductors.* Rev. Mod. Phys. **75**, April, 473 (2003).

[Dam04] Andrea Damascelli. *Probing the Electronic Structure of Complex Systems by ARPES.* Phys. Scr. **T109**, 61 (2004). DOI: 10.1238/Physica.Topical.109a00061.

[Dar91] B. Dardel, D. Malterre, M. Grioni, P. Weibel, Y. Baer, & F. Lévy. *Unusual photoemission spectral function of quasi-one-dimensional metals.* Phys. Rev. Lett. **67**, 22, 3144 (1991). DOI: 10.1103/PhysRevLett.67.3144.

[de 31] R. de L. Kronig & W. G. Penney. *Quantum Mechanics of Electrons in Crystal Lattices*. Proc. R. Soc. A Math. Phys. Eng. Sci. **130**, 499 (1931). DOI: 10.1098/rspa.1931.0019.

[De 16] N. De Jong, R. Heimbuch, S. Eliens, S. Smit, E. Frantzeskakis, J. S. Caux, H. J W Zandvliet, & M. S. Golden. *Gold-induced nanowires on the Ge(100) surface yield a 2D and not a 1D electronic structure*. Phys. Rev. B - Condens. Matter Mater. Phys. **93**, 23, 1 (2016). DOI: 10.1103/PhysRevB.93.235444.

[Di 76] F. J. Di Salvo, D. E. Moncton, & J. V. Wasczak. *Electronic properties and superlattice formation in the semimetal TiSe2*. Phys. Rev. B **14**, 10, 4321 (1976).

[Dro93] Richard Dronskowski & Peter E. Blöchl. *Crystal Orbital Hamilton Populations (COHP). Energy-Resolved Visualization of Chemical Bonding in Solids Based on Density-Functional Calculations*. J. Phys. Chem. **97**, 8617 (1993). DOI: 10.1021/j100135a014.

[Dud13] L Dudy, J D Denlinger, J W Allen, F Wang, J He, D Hitchcock, a Sekiyama, & S Suga. *Photoemission spectroscopy and the unusually robust one-dimensional physics of lithium purple bronze*. J. Phys. Condens. Matter **25**, 1, 014007 (2013). DOI: 10.1088/0953-8984/25/1/014007.

[Ede04] J. G. Eden. *High-order harmonic generation and other intense optical field-matter interactions: review of recent experimental and theoretical advances*. Prog. Quantum Electron. **28**, 3-4, 197 (2004). DOI: 10.1016/j.pquantelec.2004.06.002.

[Eff84] Piezoelectric Effects. *Femtosecond Laser Interaction with Metallic Tungsten and Nonequilibrium Electron and Lattice Temperatures*. Phys. Rev. Lett. **53**, 19, 1837 (1984).

[Eic14] S. Eich, A. Stange, A. V. Carr, J. Urbancic, T. Popmintchev, M. Wiesenmayer, K. Jansen, A. Ruffing, S. Jakobs, T. Rohwer, S. Hellmann, C. Chen, P. Matyba, L. Kipp, K. Rossnagel, M. Bauer, M. M. Murnane, H. C. Kapteyn, S. Mathias, & M. Aeschlimann. *Time- and angle-resolved photoemission spectroscopy with optimized high-harmonic pulses using frequency-doubled Ti:Sapphire lasers*. J. Electron Spectros. Relat. Phenomena **195**, 231 (2014). DOI: 10.1016/j.elspec.2014.04.013.

[Ein05] A. Einstein. *Ueber einen die Erzeugung und Verwandlung des Lichtes betreffenden heuristischen Gesichtspunkt*. Ann. Phys. **322**, 6, 132 (1905). DOI: 10.1002/andp.19053220607.

[Fan92] W. S. Fann, R. Storz, H. W K Tom, & J. Bokor. *Direct measurement of nonequilibrium electron-energy distributions in sub-picosecond laser-heated gold films*. Phys. Rev. Lett. **68**, 18, 2834 (1992). DOI: 10.1016/0039-6028(93)90985-S.

[Fau12] J Faure, J Mauchain, E Papalazarou, W Yan, J Pinon, M Marsi, & L Perfetti. *Full characterization and optimization of a femtosecond ultraviolet laser*

source for time and angle-resolved photoemission on solid surfaces. Rev. Sci. Instrum. **83**, 4, 043109 (2012). DOI: 10.1063/1.3700190.

[Faw88] Eric Fawcett. *Spin-Density-Wave antiferomagnetism in chromium.* Rev. Mod. Phys. **60**, 1, 209 (1988).

[Faw94] E Fawcett, H L Alberts, V Yu Galkin, D R Noakes, & J V Yakhmi. *Spin-density-wave antiferromagnetism in chromium alloys.* Rev. Mod. Phys. **66**, January 1994, 25 (1994).

[Feu72] B. Feuerbacher & B. Fitton. *Photoemission from surface states on tungsten.* Phys. Rev. Lett. **29**, 12, 786 (1972). DOI: 10.1103/PhysRevLett.29.786.

[Fle78] R. M. Fleming, D. E. Moncton, & D. B. McWhan. *X-ray scattering and electric field studies of the sliding mode conductor NbSe3.* Phys. Rev. B **18**, 10, 5560 (1978). DOI: 10.1103/PhysRevB.18.5560.

[Fri13] B. Frietsch, R. Carley, K. Döbrich, C. Gahl, M. Teichmann, O. Schwarzkopf, Ph Wernet, & M. Weinelt. *A high-order harmonic generation apparatus for time- and angle-resolved photoelectron spectroscopy.* Rev. Sci. Instrum. **84**, 7, 075106 (2013).

[Fri15] B. Frietsch, J. Bowlan, R. Carley, M. Teichmann, S. Wienholdt, D. Hinzke, U. Nowak, K. Carva, P. M. Oppeneer, & M. Weinelt. *Disparate ultrafast dynamics of itinerant and localized magnetic moments in gadolinium metal.* Nat. Commun. **6**, 8262 (2015). DOI: 10.1038/ncomms9262.

[Fri17] T. Frigge, B. Hafke, T. Witte, B. Krenzer, C. Streubühr, A. Samad Syed, V. Mikšić Trontl, I. Avigo, P. Zhou, M. Ligges, D. von der Linde, U. Bovensiepen, M. Horn-von Hoegen, S. Wippermann, A. Lücke, S. Sanna, U. Gerstmann, & W. G. Schmidt. *Optically excited structural transition in atomic wires on surfaces at the quantum limit.* Nature , 111(2017). DOI: 10.1038/nature21432.

[Fur16] Shunsuke C. Furuya, Maxime Dupont, Sylvain Capponi, Nicolas Laflorencie, & Thierry Giamarchi. *Dimensional modulation of spontaneous magnetic order in quasi-two-dimensional quantum antiferromagnets.* Phys. Rev. B - Condens. Matter Mater. Phys. **94**, 14, 1 (2016). DOI: 10.1103/PhysRevB.94.144403.

[Gao98] J. Gao, F. Shen, & J.G. Eden. *Quantum electrodynamic treatment of harmonic generation in intense optical fields.* Phys. Rev. Lett. **81**, 9, 1833 (1998). DOI: 10.1103/PhysRevLett.84.4252.

[Gao99] J Gao, F Shen, & Eden J G. *Polarization effects and the role of above-threshold ionization photoelectrons in high-order harmonic generation : comparison of experiment with quantum electrodynamic theory Polarization effects and the role of above-threshold ionization photoelectrons i.* J. Phys. B At. Mol. Opt. Phys. **32**, 4153 (1999).

[Gei13] A K Geim & I V Grigorieva. *Van der Waals heterostructures.* Nature **499**, 7459, 419 (2013). DOI: 10.1038/nature12385.

[Gia03] T. Giamarchi. *Quantum Physics in One Dimension.* Oxford University Press, Oxford (2003).

[Gia04] T Giamarchi. *Theoretical framework for quasi-one dimensional systems.* Chem. Rev. **104**, 11, 5037 (2004). DOI: 10.1021/cr030647c.

[Gia08] T. Giamarchi, Ch. Rüegg, & O. Tchernyshyov. *Bose-Einstein Condensation in Magnetic Insulators.* Nat. Phys. **4**, March, 198 (2008). DOI: 10.1038/nphys893.

[Gie13] Isabella Gierz, Jesse C Petersen, Matteo Mitrano, Cephise Cacho, I C Edmond Turcu, Emma Springate, Alexander Stöhr, Axel Köhler, Ulrich Starke, & Andrea Cavalleri. *Snapshots of non-equilibrium Dirac carrier distributions in graphene.* Nat. Mater. **12**, 12, 1119 (2013). DOI: 10.1038/nmat3757.

[Gob64] G. W. Gobeli, F. G. Allen, & E. O. Kane. *Polarization evidence for momentum conservation in photoelectric emission from germanium and silicon.* Phys. Rev. Lett. **12**, 4, 94 (1964). DOI: 10.1103/PhysRevLett.12.94.

[Gon05] C. González, J. Ortega, & F. Flores. *Metal-insulator transition in one-dimensional In-chains on Si(111): Combination of a soft shear distortion and a double-band Peierls instability.* New J. Phys. **7**(2005). DOI: 10.1088/1367-2630/7/1/100.

[Gon13] Zhirui Gong, Gui-Bin Liu, Hongyi Yu, Di Xiao, Xiaodong Cui, Xiaodong Xu, & Wang Yao. *Magnetoelectric effects and valley-controlled spin quantum gates in transition metal dichalcogenide bilayers.* Nat. Commun. **4**, May, 2053 (2013). DOI: 10.1038/ncomms3053.

[Gra86] Richard L. Graham, Danny L. Yeager, Jeppe Olsen, Poul Jorgensen, Robert Harrison, Sohrab Zarrabian, & Rodney Bartlett. *Excitation energies in Be: A comparison of multiconfigurational linear response and full configuration interaction calculations.* J. Chem. Phys. **85**, 11, 6544 (1986). DOI: 10.1063/1.451436.

[Gra11a] J. Graf, C. Jozwiak, C. L. Smallwood, H. Eisaki, R. a. Kaindl, D-H. Lee, & a. Lanzara. *Nodal quasiparticle meltdown in ultrahigh-resolution pump–probe angle-resolved photoemission.* Nat. Phys. **7**, 10, 805 (2011). DOI: 10.1038/nphys2027.

[Gra11b] A. X. Gray, C. Papp, S. Ueda, B. Balke, Y. Yamashita, L. Plucinski, J. Minár, J. Braun, E. R. Ylvisaker, C. M. Schneider, W. E. Pickett, H. Ebert, K. Kobayashi, & C. S. Fadley. *Probing bulk electronic structure with hard X-ray angle-resolved photoemission.* Nat. Mater. **10**, 10, 759 (2011). DOI: 10.1038/nmat3089.

[Gra12] A. X. Gray, J. Minár, S. Ueda, P. R. Stone, Y. Yamashita, J. Fujii, J. Braun, L. Plucinski, C. M. Schneider, G. Panaccione, H. Ebert, O. D. Dubon, K. Kobayashi, & C. S. Fadley. *Bulk electronic structure of the dilute magnetic semiconductor Ga1xMnxAs through hard X-ray angle-resolved photoemission.* Nat. Mater. **11**, 11, 957 (2012). DOI: 10.1038/nmat3450.

[Grü88] G. Grüner. *The dynamics of charge-density waves.* Rev. Mod. Phys. **60**, 1129 (1988). DOI: 10.1103/RevModPhys.60.1129.

[Grü94a] G. Grüner. *Density Waves in Solids.* Perseus Publishing (1994).

[Grü94b] G. Grüner. *The dynamics of spin-density waves.* Rev. Mod. Phys. **66**, 1, 1 (1994). DOI: 10.1103/RevModPhys.66.1.

[Gru15] Antonija Grubišić Čabo, Jill a. Miwa, Signe S. Grønborg, Jonathon M. Riley, Jens Christian Johannsen, Cephise Cacho, Oliver Alexander, Richard T. Chapman, Emma Springate, Marco Grioni, Jeppe V. Lauritsen, Phil D. C. King, Philip Hofmann, & Søren Ulstrup. *Observation of Ultrafast Free Carrier Dynamics in Single Layer MoS 2.* Nano Lett. **15**, 9, 5883 (2015). DOI: 10.1021/acs.nanolett.5b01967.

[Guo05] Jiandong Guo, Geunseop Lee, & E. W. Plummer. *Intertwined electronic and structural phase transitions in the In/Si(111) interface.* Phys. Rev. Lett. **95**, 4, 2 (2005). DOI: 10.1103/PhysRevLett.95.046102.

[Gwe04] G. H. Gweon, S. K. Mo, J. W. Allen, J. He, R. Jin, D. Mandrus, & H. Höchst. *Luttinger liquid angle-resolved photoemission line shapes from samples of Li0.9Mo6O17 grown by the temperature-gradient- flux technique.* Phys. Rev. B **70**, 15, 153103 (2004). DOI: 10.1103/PhysRevB.70.153103.

[Hai95] Richard Haight. *Electron dynamics at surfaces.* Surf. Sci. Rep. **21**, 8, 275 (1995). DOI: 10.1016/0167-5729(95)00002-X.

[Hal88] Wilhelm Hallwachs. *Ueber den Einfluss des Lichtes auf electrostatisch geladene Koerper.* Ann. Phys. **269**, 2, 301 (1888). DOI: 10.1002/andp.18882690206.

[Hal81] F D M Haldane. *'Luttinger liquid theory' of one-dimensional quantum fluids. I. Properties of the Luttinger model and their extension to the general 1D interacting spinless Fermi gas.* J. Phys. C Solid State Phys. **14**, 19, 2585 (1981). DOI: 10.1088/0022-3719/14/19/010.

[Har64] L. E. Hargrove, R. L. Fork, & M. A. Pollack. *Locking of hene laser modes induced by synchronous intracavity modulation.* Appl. Phys. Lett. **5**, 1, 4 (1964). DOI: 10.1063/1.1754025.

[Has10] M. Z. Hasan & C. L. Kane. *Colloquium: Topological insulators.* Rev. Mod. Phys. **82**, 4, 3045 (2010). DOI: 10.1103/RevModPhys.82.3045.

[Hat00] K. Hata, T. Kimura, S. Ozawa, & H. Shigekawa. *How to fabricate a defect free Si(001) surface.* J. Vac. Sci. Tech. A **18**, 1933 (2000). DOI: 10.1116/1.582482.

[Hay03] W. M. Haynes (Ed.). *CRC Handbook of Physics and Chemistry (online edition).* CRC Press, Boca Raton, Florida (2003).

[HB13] a Hanisch-Blicharski, a Janzen, B Krenzer, S Wall, F Klasing, a Kalus, T Frigge, M Kammler, & M Horn-von Hoegen. *Ultra-fast electron diffraction at surfaces: from nanoscale heat transport to driven phase transitions.* Ultramicroscopy **127**, 2 (2013). DOI: 10.1016/j.ultramic.2012.07.017.

[Hel12] S. Hellmann, T. Rohwer, M. Kalläne, K. Hanff, C. Sohrt, a. Stange, a. Carr, M.M. Murnane, H.C. Kapteyn, L. Kipp, M. Bauer, & K. Rossnagel. *Time-domain classification of charge-density-wave insulators.* Nat. Commun. **3**, 1069 (2012). DOI: 10.1038/ncomms2078.

[Her87] H. Hertz. *Ueber einen Einfluss des ultravioletten Lichtes auf die electrische Entladung.* Ann. Phys. **267**, 8, 983 (1887). DOI: 10.1002/andp.18872670827.

[Hil97] I. Hill & a. McLean. *Metallicity of In chains on Si(111).* Phys. Rev. B **56**, 24, 15725 (1997). DOI: 10.1103/PhysRevB.56.15725.

[Hir03] H Hirori, T Tachizaki, O Matsuda, & O B Wright. *Electron dynamics in chromium probed with 20-fs optical pulses.* Phys. Rev. B **68**, September, 113102 (2003). DOI: 10.1103/PhysRevB.68.113102.

[Hod78] J L Hodeau, M Marezio, C Roucau, R Ayroles, A Meerschaut, J Rouxel, & P Monceau. *Charge-density waves in NbSe , at 145 K : crystal structures , x-ray and electron diffraction studies.* J. Phys. C Solid State Phys. **11**, 4117 (1978). DOI: 10.1088/0022-3719/11/20/009.

[Hoe02] M. Hoesch, T. Greber, V. N. Petrov, M. Muntwiler, M. Hengsberger, W. Auwärter, & J. Osterwalder. *Spin-polarized Fermi surface mapping.* J. Electron Spectrosc. Relat. Phenom. **124**, 263 (2002). DOI: 10.1016/S0368-2048(02)00058-0.

[Hoe04] M Hoesch, M Muntwiler, V N Petrov, M Hengsberger, L Patthey, M Shi, M Falub, T Greber, & J Osterwalder. *Spin structure of the Shockley surface state on Au(111).* Phys. Rev. B **69**, 241401 (2004). DOI: 10.1103/PhysRevB.69.241401.

[Hoe17] M. Hoesch, T. K. Kim, P. Dudin, H. Wang, S. Scott, P. Harris, S. Patel, M. Matthews, D. Hawkins, S. G. Alcock, T. Richter, J. J. Mudd, M. Basham, L. Pratt, P. Leicester, E. C. Longhi, A. Tamai, & F. Baumberger. *A facility for the analysis of the electronic structures of solids and their surfaces by synchrotron radiation photoelectron spectroscopy.* Rev. Sci. Instrum. **88**, 013106 (2017). DOI: 10.1063/1.4973562.

[Hof87] Roald Hoffmann. *How Chemistry and Physics Meet in the Solid State.* Angew. Chemie Int. Ed. English **26**, 9, 846 (1987). DOI: 10.1002/anie.198708461.

[Hof88] R. Hoffmann. *A chemical and theoretical way to look at bonding on surfaces.* Rev. Mod. Phys. **60**, 3, 601 (1988). DOI: 10.1103/RevModPhys.60.601.

[Hof09] a. Hofmann, X. Y. Cui, J. Schäfer, S. Meyer, P. Höpfner, C. Blumenstein, M. Paul, L. Patthey, E. Rotenberg, J. Bünemann, F. Gebhard, T. Ohm, W. Weber, & R. Claessen. *Renormalization of bulk magnetic electron states at high binding energies.* Phys. Rev. Lett. **102**, May, 100 (2009). DOI: 10.1103/PhysRevLett.102.187204.

[Hüf95] S Hüfner. *Photoelectron Spectroscopy: Principles and Applications.* Springer-Verlag, Berlin (1995).

[Hüf07] S. Hüfner. *Very High Resolution Photelectron Spectroscopy*. Springer-Verlag, Berlin, Heidelberg (2007).

[Ich11] Hirohiko Ichikawa, Shunsuke Nozawa, Tokushi Sato, Ayana Tomita, Kouhei Ichiyanagi, Matthieu Chollet, Laurent Guerin, Nicky Dean, Andrea Cavalleri, Shin Ichi Adachi, Taka Hisa Arima, Hiroshi Sawa, Yasushi Ogimoto, Masao Nakamura, Ryo Tamaki, Kenjiro Miyano, & Shin Ya Koshihara. *Transient photoinduced hidden^{TM} phase in a manganite*. Nat. Mater. **10**, 2, 101 (2011). DOI: 10.1038/nmat2929.

[Ima09] Adilet Imambekov & Leonid I Glazman. *Universal Theory of Nonlinear Luttinger Liquids*. Science (80-.). **323**, 5911, 228 (2009). DOI: 10.1126/science.1165403.

[Ina04] Takeshi Inaoka. *Low-dimensional plasmons in a metallic strip monolayer on a semiconductor surface*. J. Phys. Soc. Japan **73**, 8, 2201 (2004). DOI: 10.1143/JPSJ.73.2201.

[Ing05] N. J C Ingle, K. M. Shen, F. Baumberger, W. Meevasana, D. H. Lu, Z. X. Shen, a. Damascelli, S. Nakatsuji, Z. Q. Mao, Y. Maeno, T. Kimura, & Y. Tokura. *Quantitative analysis of Sr2RuO4 angle-resolved photoemission spectra: Many-body interactions in a model Fermi liquid*. Phys. Rev. B - Condens. Matter Mater. Phys. **72**, 20, 1 (2005). DOI: 10.1103/PhysRevB.72.205114.

[Ish03] H. Ishii, H. Kataura, H. Shiozawa, H. Yoshioka, H. Otsubo, Y. Takayama, T. Miyahara, S. Suzuki, Y. Achiba, M. Nakatake, T. Narimura, M. Higashiguchi, K. Shimada, H. Namatame, & M. Taniguchi. *Direct observation of Tomonaga – Luttinger-liquid state in carbon nanotubes at low temperatures*. Nature **426**, December, 540 (2003). DOI: 10.1038/nature02199.Published.

[Ish15] Tadahiko Ishikawa, Stuart A Hayes, Sercan Keskin, Gastón Corthey, Masaki Hada, Kostyantyn Pichugin, Alexander Marx, Julian Hirscht, Kenta Shionuma, Ken Onda, Yoichi Okimoto, Shin-ya Koshihara, Takashi Yamamoto, Hengbo Cui, Mitsushiro Nomura, Yugo Oshima, Majed Abdel-Jawad, Reizo Kato, & R J Dwayne Miller. *Direct observation of collective modes coupled to molecular orbital–driven charge transfer*. Science (80-.). **350**, 6267, 1501 (2015). DOI: 10.1126/science.aab3480.

[Jac14] V. L R Jacques, E. Pinsolle, S. Ravy, G. Abramovici, & D. Le Bolloc'H. *Charge- and spin-density waves observed through their spatial fluctuations by coherent and simultaneous x-ray diffraction*. Phys. Rev. B - Condens. Matter Mater. Phys. **89**, 1 (2014). DOI: 10.1103/PhysRevB.89.245127.

[Jec16] Eric Jeckelmann, Simone Sanna, Wolf Gero Schmidt, Eugen Speiser, & Norbert Esser. *Grand canonical Peierls transition in In/Si(111)*. Phys. Rev. B - Condens. Matter Mater. Phys. **93**, 24(2016). DOI: 10.1103/PhysRevB.93.241407.

[Jér67] D. Jérome, T. M. Rice, & W. Kohn. *Excitonic Insulator*. Phys. Rev. **158**, 2, 462 (1967).

[Jia15] Hao Jiang, Guanghan Cao, & Chao Cao. *Electronic structure of quasi-one-dimensional superconductor K$_2$Cr$_3$As$_3$ from first-principles calculations*. Sci. Rep. **5**, July, 16054 (2015). DOI: 10.1038/srep16054.

[Joh89] L. S. O. Johansson. *Fermi-Level Pinning and Surface-State Band Structure of the Si(111)-(sqrt3)R30 -Ag Surface*. Phys. Rev. Lett. **63**, 19, 2092 (1989).

[Jon14] Aaron M. Jones, Hongyi Yu, Jason S. Ross, Philip Klement, Nirmal J. Ghimire, Jiaqiang Yan, David G. Mandrus, Wang Yao, & Xiaodong Xu. *Spin–layer locking effects in optical orientation of exciton spin in bilayer WSe2*. Nat. Phys. **10**, 2, 130 (2014). DOI: 10.1038/nphys2848.

[Kan64] E. O. Kane. *Implications of crytal momentum conservation in photoelectric emission for band-structure measurments*. Phys. Rev. Lett. **12**, 4, 97 (1964).

[Kel65] L. V. Keldysh. *Ionization in the field of a strong electromagnetic wave*. Sov. Phys. JETP **20**, 5, 1307 (1965). DOI: 10.1234/12345678.

[Kid02] T E Kidd, T Miller, M Y Chou, & T Chiang. *Electron-Hole Coupling and the Charge Density Wave Transition in TiSe 2*. Phys. Rev. Lett. **88**, 226402 (2002). DOI: 10.1103/PhysRevLett.88.226402.

[Kim07] Keun Su Kim, Harumo Morikawa, Won Hoon Choi, & Han Woong Yeom. *Strong Lateral Electron Coupling of Pb Nanowires on Stepped Si(111): Angle-Resolved Photoemission Studies*. Phys. Rev. Lett. **99**, 19, 196804 (2007). DOI: 10.1103/PhysRevLett.99.196804.

[Kim13] Hyun Jung Kim & Jun Hyung Cho. *Driving force of phase transition in indium nanowires on Si(111)*. Phys. Rev. Lett. **110**, 11, 1 (2013). DOI: 10.1103/PhysRevLett.110.116801.

[Kim16] Sun Woo Kim & Jun Hyung Cho. *Origin of the metal-insulator transition of indium atom wires on Si(111)*. Phys. Rev. B - Condens. Matter Mater. Phys. **93**, 24, 14 (2016). DOI: 10.1103/PhysRevB.93.241408.

[Kir85] J. Kirschner (Ed.). *Polarized electrons at surfaces*. Springer-Verlag, Berlin, Heidelberg (1985).

[Kla14] F. Klasing, T. Frigge, B. Hafke, B. Krenzer, S. Wall, A. Hanisch-Blicharski, & M. Horn-von Hoegen. *Hysteresis proves that the In/Si(111) (8x2) to (4x1) phase is first-order*. Phys. Rev. B **89**, 12, 121107 (2014). DOI: 10.1103/PhysRevB.89.121107.

[Koh59] W. Kohn. *Image of the fermi surface in the vibration spectrum of a metal*. Phys. Rev. Lett. **2**, 9, 393 (1959). DOI: 10.1103/PhysRevLett.2.393.

[Kol16] A. V. Kolobov & J. Tomoniga. *Two-Dimensional Transition Metal Dichalcogenides*. Springer International, Switzerland (2016).

[Kon15] Tai Kong, Sergey L. Bud'ko, & Paul C. Canfield. *Anisotropic Hc2, thermodynamic and transport measurements, and pressure dependence of Tc in K2Cr3As3 single crystals*. Phys. Rev. B - Condens. Matter Mater. Phys. **91**, 2, 3 (2015). DOI: 10.1103/PhysRevB.91.020507.

[Kor07] J. D. Koralek, J. F. Douglas, N. C. Plumb, J. D. Griffith, S. T. Cundiff, H. C. Kapteyn, M. M. Murnane, & D. S. Dessau. *Experimental setup for low-energy laser-based angle resolved photoemission spectroscopy.* Rev. Sci. Instrum. **78**, 5(2007). DOI: 10.1063/1.2722413.

[Kra92] F Krausz, M E Fermann, T Brabec, P F Curley, M Hofer, M H Ober, C Spielmann, E Wintner, & A J Schmidt. *Femtosecond Solid-State Lasers.* IEEE J. Quantum Electron. **28**, 10, 2097 (1992). DOI: 10.5402/2012/120827.

[Kra97] J. Kraft, M. G. Ramsey, & F. P. Netzer. *Surface reconstructions of In on Si(111).* Phys. Rev. B **55**, 8, 5384 (1997). DOI: 10.1103/PhysRevB.55.5384.

[Kri13] U Krieg, C Brand, C Tegenkamp, & H Pfnür. *One-dimensional collective excitations in Ag atomic wires grown on Si(557).* J. Phys. Condens. Matter **25**, 1, 014013 (2013). DOI: 10.1088/0953-8984/25/1/014013.

[Kri14] U Krieg, Yu Zhang, C Tegenkamp, & H Pfnür. *Tuning of one-dimensional plasmons by Ag-Doping in Ag-sqrt(3)-ordered atomic wires.* New J. Phys. **16**, 043007 (2014). DOI: 10.1088/1367-2630/16/4/043007.

[Kri15] U Krieg, T Lichtenstein, C Brand, C Tegenkamp, & H Pfnür. *Origin of metallicity in atomic Ag wires on Si(557).* New J. Phys. **17**, 4, 043062 (2015). DOI: 10.1088/1367-2630/17/4/043062.

[Kum00] C Kumpf, O Bunk, Jh Zeysing, Y Su, M Nielsen, Rl Johnson, R Feidenhans'l, & K Bechgaard. *Low-temperature structure of indium quantum chains on silicon.* Phys. Rev. Lett. **85**, 23, 4916 (2000). link.

[Lak13] B. Lake, D. A. Tennant, J. S. Caux, T. Barthel, U. Schollw??ck, S. E. Nagler, & C. D. Frost. *Multispinon continua at zero and finite temperature in a near-ideal heisenberg Chain.* Phys. Rev. Lett. **111**, 13, 1 (2013). DOI: 10.1103/PhysRevLett.111.137205.

[Lam64] W. E. Lamb. *Theory of an Optical Maser.* Phys. Rev. **134**, 1429 (1964).

[Lan57a] L. D. Landau. *Oscillations in a Fermi Liquid.* JETP **5**, 1, 101 (1957).

[Lan57b] L. D. Landau. *The theory of a Fermi liquid.* JETP **3**, 6, 920 (1957). DOI: 10.1016/B978-0-08-010586-4.50095-X.

[Lan59] L. D. Landau. *On the Theory of the Fermi Liquid.* JETP **35**, 8, 70 (1959).

[LaS96] S. LaShell, B. McDougall, & E. Jensen. *Spin Splitting of an Au(111) Surface State Band Observed with Angle Resolved Photoelectron Spectroscopy.* Phys. Rev. Lett. **77**, 16, 3419 (1996). DOI: 10.1103/PhysRevLett.77.3419.

[Lau00] R B Laughlin & D Pines. *The theory of everything.* Proc. Natl. Acad. Sci. U. S. A. **97**, 1, 28 (2000). DOI: 10.1073/pnas.97.1.28.

[Lee02] S S Lee, J R Ahn, N D Kim, J H Min, C G Hwang, J W Chung, H W Yeom, Serguei V Ryjkov, & Shuji Hasegawa. *Adsorbate-induced pinning of a charge-density wave in a quasi-1D metallic chains: Na on the In/Si(111)-(4x1) surface.* Phys. Rev. Lett. **88**, Ml, 196401 (2002). DOI: 10.1103/PhysRevLett.88.196401.

[Len95] P. Lenard. *Ueber die Absorption der Kathodenstrahlen.* Ann. Phys. **292**, 10, 255 (1895).

[Len00] P. Lenard. *Erzeugung von Kathodenstrahlen durch ultraviolettes Licht.* Ann. Phys. **307**, 6, 359 (1900). DOI: 10.1002/andp.19003070611.

[Len02] P. Lenard. *Ueber die lichtelektrische Wirkung.* Ann. Phys. **313**, 5, 149 (1902). DOI: 10.1002/andp.19023130510.

[Lév83] F. Lévy & H. Berger. *Single crystals of transition metal trichalcogenides.* J. Cryst. Growth **61**, 1, 61 (1983). DOI: 10.1016/0022-0248(83)90279-8.

[Lew94] M. Lewenstein, Ph Balcou, M Yu Ivanov, & Anne L Huillier. *Theory of high-harmonic generation by low-frequency laser fields.* Phys. Rev. A **49**, 3, 2117 (1994).

[Li07] G Li, W Z Hu, D Qian, D Hsieh, M Z Hasan, E Morosan, R J Cava, & N L Wang. *Semimetal-to-Semimetal Charge Density Wave Transition in 1 T - TiSe 2.* Phys. Rev. Lett. **99**, July, 027404 (2007). DOI: 10.1103/PhysRevLett.99.027404.

[Lic16] Timo Lichtenstein, Julian Aulbach, Jörg Schäfer, Ralph Claessen, Christoph Tegenkamp, & Herbert Pfnür. *Two-dimensional crossover and strong coupling of plasmon excitations in arrays of one-dimensional atomic wires.* Phys. Rev. B **161408**, 557, 1 (2016). DOI: 10.1103/PhysRevB.93.161408.

[Lin98] J.-L. Lin, D. Y. Petrovykh, J. Viernow, F. K. Men, D. J. Seo, & F. J. Himpsel. *Formation of regular step arrays on Si(111)7x7.* J. Appl. Phys. **84**, 1, 255 (1998). DOI: 10.1063/1.368077.

[Liu08a] Canhua Liu, Takeshi Inaoka, Shin Yaginuma, Tomonobu Nakayama, Masakazu Aono, & Tadaaki Nagao. *Disappearance of the quasi-one-dimensional plasmon at the metal-insulator phase transition of indium atomic wires.* Phys. Rev. B **77**, 20, 205415 (2008). DOI: 10.1103/PhysRevB.77.205415.

[Liu08b] Guodong Liu, Guiling Wang, Yong Zhu, Hongbo Zhang, Guochun Zhang, Xiaoyang Wang, Yong Zhou, Wentao Zhang, Haiyun Liu, Lin Zhao, Jianqiao Meng, Xiaoli Dong, Chuangtian Chen, Zuyan Xu, & X. J. Zhou. *Development of a vacuum ultraviolet laser-based angle-resolved photoemission system with a superhigh energy resolution better than 1 meV.* Rev. Sci. Instrum. **79**, 2(2008). DOI: 10.1063/1.2835901.

[Liu11] Y Liu, G Bian, T Miller, & T Chiang. *Visualizing Electronic Chirality and Berry Phases in Graphene Systems Using Photoemission with Circularly Polarized Light* **166803**, October, 1 (2011). DOI: 10.1103/PhysRevLett.107.166803.

[Liu15] Qihang Liu, Xiuwen Zhang, & Alex Zunger. *Intrinsic circular polarization in centrosymmetric stacks of transition-metal dichalcogenide compounds.* Phys. Rev. Lett. **114**, 8, 1 (2015). DOI: 10.1103/PhysRevLett.114.087402.

[Liu16] Yi Liu, Jin-Ke Bao, Hao-Kun Zuo, Abduweli Ablimit, Zhang-Tu Tang, Chun-Mu Feng, Zeng-Wei Zhu, & Guang-Han Cao. *Effect of impurity scattering on superconductivity in K2Cr3As3.* Sci. Chin. **59**, 5, 657402 (2016). DOI: 10.1038/srep16054.

[Los00] R. Losio, K. N. Altmann, & F. J. Himpsel. *Continuous transition from two- to one-dimensional states in Si(111)-(5 x 2)-Au.* Phys. Rev. Lett. **85**, 4, 808 (2000). DOI: 10.1103/PhysRevLett.85.808.

[Lüc17] A Lücke, U Gerstmann, T. D. Kühne, & W G Schmidt. *Efficient PAW-based bond strength analysis for understanding the In/Si(111) (8x2) - (4x1) phase transition.* J. Comp. Chem. **Accepted**(2017).

[Lut61] J. M. Luttinger. *Analytic properties of single-particle propagators for many-fermion systems.* Phys. Rev. **121**, 4, 942 (1961). DOI: 10.1103/PhysRev.121.942.

[Lut63] J M Luttinger. *An Exactly Soluble Model of a Many-Fermion System.* J. Math. Phys. **4**, 9, 1154 (1963). DOI: 10.1063/1.1704046.

[MA06] L. Miaja-Avila, C. Lei, M. Aeschlimann, J. Gland, M. Murnane, H. Kapteyn, & G. Saathoff. *Laser-Assisted Photoelectric Effect from Surfaces.* Phys. Rev. Lett. **97**, 11, 113604 (2006). DOI: 10.1103/PhysRevLett.97.113604.

[Mah00] G. D. Mahan. *Many-Particle Physics.* Pernum, New York (2000).

[Mai13] Stefan Maintz, Volker L Deringer, Andrei L Tchougréeff, & Richard Dronkowski. *Analytic Projection From Plane-Wave and PAW Wavefunctions and Application to Chemical-Bonding Analysis in Solids.* J. Comp. Chem. **34**, 2557 (2013). DOI: 10.1002/jcc.23424.

[Mak12] Kin Fai Mak, Keliang He, Jie Shan, & Tony F Heinz. *Control of valley polarization in monolayer MoS 2 by optical helicity.* Nat. Nanotechnol. **7**, June, 494 (2012). DOI: 10.1038/nnano.2012.96.

[Mat04] Iwao Matsuda, Masashi Ueno, Toru Hirahara, Rei Hobara, Harumo Morikawa, Canhua Liu, & Shuji Hasegawa. *Electrical resistance of a monatomic step on a crystal surface.* Phys. Rev. Lett. **93**, December, 3 (2004). DOI: 10.1103/PhysRevLett.93.236801.

[Med17] K. Medjanik, O. Fedchenko, S. Chernov, D. Kutnyakhov, M. Ellguth, A. Oelsner, B. Schönhense, T. R. F. Peixoto, P. Lutz, C.-H. Min, F. Reinert, S. Däster, Y. Acremann, J. Viefhaus, W. Wurth, H. J. Elmers, & G. Schönhense. *Direct 3D mapping of the Fermi surface and Fermi velocity.* Nat. Mater. , March, 4875 (2017). DOI: 10.1038/nmat4875.

[Mee11] W. Meevasana, P. D. C. King, R. H. He, S-K. Mo, M. Hashimoto, A. Tamai, P. Songsiriritthigul, F. Baumberger, & Z-X. Shen. *Creation and control of a two-dimensional electron liquid at the bare SrTiO3 surface.* Nat. Mater. **10**, 2, 114 (2011). DOI: 10.1038/nmat2943.

[Mer66] N. D. Mermin & H. Wagner. *Absence of ferromagnetism or antiferromagnetism in one- or two-dimensional isotropic Heisenberg models.* Phys. Rev. Lett. **17**, 22, 1133 (1966). DOI: 10.1103/PhysRevLett.17.1133.

[Mey14] S. Meyer, L. Dudy, J. Schäfer, C. Blumenstein, P. Höpfner, T. E. Umbach, A. Dollinger, X. Y. Cui, L. Patthey, & R. Claessen. *Valence band and core-level photoemission of Au/Ge(001): Band mapping and bonding sites.* Phys. Rev. B - Condens. Matter Mater. Phys. **90**, 12, 125409 (2014). DOI: 10.1103/PhysRevB.90.125409.

[Mia16] Jian Jian Miao, Fu Chun Zhang, & Yi Zhou. *Instability of three-band Tomonaga-Luttinger liquid: Renormalization group analysis and possible application to K2Cr3As3.* Phys. Rev. B **94**, 20(2016). DOI: 10.1103/PhysRevB.94.205129.

[Mil16] R.A. Millikan. *A direct photoelectric determination of Planck's "h".* Phys. Rev. **7**, 355 (1916).

[Mil15] Tristan L. Miller, Christopher L. Smallwood, Wentao Zhang, Hiroshi Eisaki, Joseph Orenstein, & Alessandra Lanzara. *Photoinduced changes of the chemical potential in superconducting BiSrCaCuO.* Phys. Rev. B **92**, 14, 144506 (2015). DOI: 10.1103/PhysRevB.92.144506.

[Min13] J. Minár, J. Braun, & H. Ebert. *Recent developments in the theory of HARPES.* J. Electron Spectros. Relat. Phenomena **190**, PART B, 159 (2013). DOI: 10.1016/j.elspec.2012.10.003.

[Mon09] C. Monney, H. Cercellier, F. Clerc, C. Battaglia, E. Schwier, C. Didiot, M. Garnier, H. Beck, P. Aebi, H. Berger, L. Forró, & L. Patthey. *Spontaneous exciton condensation in 1T-TiSe2: BCS-like approach.* Phys. Rev. B **79**, 4, 045116 (2009). DOI: 10.1103/PhysRevB.79.045116.

[Mon10a] C. Monney, E. F. Schwier, M. G. Garnier, N. Mariotti, C. Didiot, H. Beck, P. Aebi, H. Cercellier, J. Marcus, C. Battaglia, H. Berger, & a. N. Titov. *Temperature-dependent photoemission on 1T -TiSe2: Interpretation within the exciton condensate phase model.* Phys. Rev. B - Condens. Matter Mater. Phys. **81**, 1 (2010). DOI: 10.1103/PhysRevB.81.155104.

[Mon10b] C Monney, E F Schwier, M G Garnier, N Mariotti, C Didiot, H Cercellier, J Marcus, H Berger, A N Titov, H Beck, & P Aebi. *Probing the exciton condensate phase in 1T-TiSe2 with photoemission.* New J. Phys. **12**, 125019 (2010). DOI: 10.1088/1367-2630/12/12/125019.

[Mon12] Pierre Monceau. *Electronic crystals: an experimental overview.* Adv. Phys. **61**, 4, 325 (2012). DOI: 10.1080/00018732.2012.719674.

[Mon16] C. Monney, M. Puppin, C. W. Nicholson, M. Hoesch, R. T. Chapman, E. Springate, H. Berger, A. Magrez, C. Cacho, R. Ernstorfer, & M. Wolf. *Revealing the role of electrons and phonons in the ultrafast recovery of charge density wave correlations in 1T- TiSe 2.* Phys. Rev. B - Condens. Matter Mater. Phys. **94**, 16, 1 (2016). DOI: 10.1103/PhysRevB.94.165165.

[Mor08] Harumo Morikawa, Pil Gyu Kang, & Han Woong Yeom. *Electronic structure of Ag-induced atomic wires on Si(557) investigated by STS and angle-resolved photoemission.* Surf. Sci. **602**, 24, 3745 (2008). DOI: 10.1016/j.susc.2008.09.044.

[Mor10] Harumo Morikawa, C. C. Hwang, & Han Woong Yeom. *Controlled electron doping into metallic atomic wires: Si(111)41-In.* Phys. Rev. B **81**, 7, 075401 (2010). DOI: 10.1103/PhysRevB.81.075401.

[Mos16] Simon Moser. *An experimentalist's guide to the matrix element in angle resolved photoemission.* J. Electron Spectros. Relat. Phenomena **214**, 29 (2016). DOI: 10.1016/j.elspec.2016.11.007.

[Mot90] N Mott. *Metal Insulator Transitions.* CRC Press, Boca Raton, Florida (1990).

[Mou86] PF Moulton. *Spectroscopic and laser characteristics of Ti: Al203.* J. Opt. Soc. Am. B **3**, 1, 125 (1986). DOI: 10.1364/JOSAB.3.000125.

[Mou90] A H Moudden, J D Axe, P Monceau, & F Levy. *q 1 Charge-Density Wave in NbSe3.* Phys. Rev. Lett. **65**, 2, 223 (1990). DOI: 10.1103/PhysRevLett.65.223.

[Mug01] A Mugarza, A Mascaraque, V Pérez-Dieste, V Repain, S Rousset, F J García de Abajo, & J E Ortega. *Electron confinement in surface states on a stepped gold surface revealed by angle-resolved photoemission.* Phys. Rev. Lett. **87**, 788, 107601 (2001). DOI: 10.1103/PhysRevLett.87.107601.

[MV11] E. Möhr-Vorobeva, S. L. Johnson, P. Beaud, U. Staub, R. De Souza, C. Milne, G. Ingold, J. Demsar, H. Schaefer, & a. Titov. *Nonthermal Melting of a Charge Density Wave in TiSe_{2}.* Phys. Rev. Lett. **107**, 3, 036403 (2011). DOI: 10.1103/PhysRevLett.107.036403.

[Nic02] G. Nicolay, F. Reinert, S. Hüfner, & P. Blaha. *Spin-orbit splitting of the L-gap surface state on Au(111) and Ag(111).* Phys. Rev. B - Condens. Matter Mater. Phys. **65**, 3, 334071 (2002). DOI: 10.1103/PhysRevB.65.033407.

[Nic15] C. W. Nicholson, C Monney, U Krieg, C Tegenkamp, H Pfnür, K Horn, & M Wolf. *Electronic structure of self-assembled Ag nanowires on Si(557): spectroscopic evidence for dimensionality.* New J. Phys. **17**, 9, 093025 (2015). DOI: 10.1088/1367-2630/17/9/093025.

[Nic16] C. W. Nicholson, C. Monney, R. Carley, B. Frietsch, J. Bowlan, M. Weinelt, & M. Wolf. *Ultrafast spin density wave transition in Chromium governed by thermalized electron gas.* Phys. Rev. Lett. **136801**, 110, 117 (2016). DOI: 10.1103/PhysRevLett.117.136801.

[Nic17] Christopher W. Nicholson, Christophe Berthod, Michele Puppin, Helmuth Berger, Martin Wolf, Moritz Hoesch, & Claude Monney. *Dimensional Crossover in a Charge Density Wave Material Probed by Angle-Resolved Photoemission Spectroscopy.* Phys. Rev. Lett. **118**, 206401 (2017). DOI: 10.1103/PhysRevLett.118.206401.

[Nor57] Carl Nordling, Evelyn Sokolowski, & Kai Siegbahn. *Precision Method for Obtaining Absolute Values of Atomic Binding Energies.* Phys. Rev. **105**, 5, 1676 (1957). DOI: 10.1103/PhysRev.105.1676.

[Oh14] Deok Mahn Oh, S. Wippermann, W. G. Schmidt, & Han Woong Yeom. *Oxygen adsorbates on the Si (111) 4 x 1-In metallic atomic wire : Scanning tunneling microscopy and density-functional theory calculations.* Phys. Rev. B **155432**, 2 (2014). DOI: 10.1103/PhysRevB.90.155432.

[Oht04] A Ohtomo & H Y Hwang. *A high-mobility electron gas at the LaAlO 3 / SrTiO 3 heterointerface* **427**, January, 423 (2004). DOI: 10.1038/nature02308.

[Oht15] Yoshiyuki Ohtsubo, Jun-ichiro Kishi, Kenta Hagiwara, Patrick Le Fèvre, François Bertran, Amina Taleb-Ibrahimi, Hiroyuki Yamane, Shin-ichiro Ideta, Masaharu Matsunami, Kiyohisa Tanaka, & Shin-ichi Kimura. *Surface Tomonaga-Luttinger-Liquid State on Bi/InSb(001).* Phys. Rev. Lett. **115**, 25, 256404 (2015). DOI: 10.1103/PhysRevLett.115.256404.

[O'M93] J D O'Mahony, J F McGilp, F M Leibsle, P Weightman, & C F J Flipse. *Control of Terrace Width and Atomic Step Distribution on Vicinal Si(111) Surfaces by Thermal-Processing.* Semicond. Sci. Tech. **8**, 4, 495 (1993). DOI: 10.1088/0268-1242/8/4/003.

[Ong77] N.P. Ong & Pierre Monceau. *Anomalous transport properties of a linear-chain metal: NbSe3.* Phys. Rev. B **16**, 3443 (1977). DOI: 10.1103/PhysRevB.16.3443.

[Ort05] J. E. Ortega, M. Ruiz-Osés, J. Cordón, a. Mugarza, J. Kuntze, & F. Schiller. *One-dimensional versus two-dimensional electronic states in vicinal surfaces.* New J. Phys. **7**(2005). DOI: 10.1088/1367-2630/7/1/101.

[Ove62] A. W. Overhauser. *Spin Density Waves in an Electron Gas.* Phys. Rev. **128**, 1961, 1437 (1962).

[Par04] S. J. Park, H. W. Yeom, S. H. Min, D. H. Park, & I. W. Lyo. *Direct evidence of the charge ordered phase transition of indium nanowires on Si(111).* Phys. Rev. Lett. **93**, 10, 1 (2004). DOI: 10.1103/PhysRevLett.93.106402.

[Pei55] R. E. Peierls. *Quantum Theory of Solids.* Oxford University Press, Oxford (1955).

[Pen76] J. B. Pendry. *Theory of photoemission.* Surf. Sci. **57**, 679 (1976).

[Per06] L. Perfetti, P. A. Loukakos, M. Lisowski, U. Bovensiepen, H. Berger, S. Biermann, P. S. Cornaglia, A. Georges, & M. Wolf. *Time evolution of the electronic structure of 1T-TaS2 through the insulator-metal transition.* Phys. Rev. Lett. **97**, 6, 1 (2006). DOI: 10.1103/PhysRevLett.97.067402.

[Per07] L. Perfetti, P. a. Loukakos, M. Lisowski, U. Bovensiepen, H. Eisaki, & M. Wolf. *Ultrafast electron relaxation in superconducting Bi2Sr2CaCu2O8 by time-resolved photoelectron spectroscopy.* Phys. Rev. Lett. **99**, 19, 197001 (2007). DOI: 10.1103/PhysRevLett.99.197001.

[Pet11] J. C. Petersen, S. Kaiser, N. Dean, a. Simoncig, H. Y. Liu, a. L. Cavalieri, C. Cacho, I. C E Turcu, E. Springate, F. Frassetto, L. Poletto, S. S. Dhesi, H. Berger, & a. Cavalleri. *Clocking the melting transition of charge and lattice order in 1T-TaS 2 with ultrafast extreme-ultraviolet angle-resolved photoemission spectroscopy.* Phys. Rev. Lett. **107**, October, 1 (2011). DOI: 10.1103/PhysRevLett.107.177402.

[Pol76] H. D. Polaschegg. *Optimization of the Parameters of the Ideal 180deg Spherical Analyzer.* Appl. Phys. **9**, 223 (1976). DOI: 10.1126/science.1208261.

[Por14] M Porer, U Leierseder, J-M Ménard, H Dachraoui, L Mouchliadis, I E Perakis, U Heinzmann, J Demsar, K Rossnagel, & R Huber. *Non-thermal separation of electronic and structural orders in a persisting charge density wave.* Nat. Mater. **13**, 9, 1 (2014). DOI: 10.1038/nmat4042.

[Pro96] Albert Prodan, N. Ramsak, V. Marinkovic, Saw Wai Hla, F. W. Boswell, J. C. Bennett, & H. Bohm. *STM evidence of room-temperature charge instabilities in NbSe 3.* Phys. Rev. B **54**, 15, 10370 (1996). DOI: 10.1103/PhysRevB.54.10370.

[Pup15] Michele Puppin, Yunpei Deng, Oliver Prochnow, Jan Ahrens, Thomas Binhammer, Uwe Morgner, Marcel Krenz, Martin Wolf, & Ralph Ernstorfer. *500 kHz OPCPA delivering tunable sub-20 fs pulses with 15 W average power based on an all-ytterbium laser.* Opt. Express **23**, 2, 1491 (2015). DOI: 10.1364/OE.23.001491.

[Qui58] J.J. Quinn & R. A. Ferrell. *Electron self-energy approach to correlation in a degenerate elctron gas.* Phys. Rev. **112**, 3, 812 (1958).

[Rad11] I. Radu, K. Vahaplar, C. Stamm, T. Kachel, N. Pontius, H. A. Dürr, T. A. Ostler, J. Barker, R. F. L. Evans, R. W. Chantrell, A. Tsukamoto, A. Itoh, A. Kirilyuk, Th. Rasing, & A. V. Kimel. *Transient ferromagnetic-like state mediating ultrafast reversal of antiferromagnetically coupled spins.* Nature **472**, 7342, 205 (2011). DOI: 10.1038/nature09901.

[Rak98] A D Rakic, A B Djurisic, J M Elazar, & M L Majewski. *Optical properties of metallic films for vertical-cavity optoelectronic devices.* Appl. Opt. **37**, 22, 5271 (1998). DOI: 10.1364/AO.37.005271.

[Rei01] F. Reinert, G. Nicolay, S. Schmidt, D. Ehm, & S. Hüfner. *Direct measurements of the L-gap surface states on the (111) face of noble metals by photoelectron spectroscopy.* Phys. Rev. B **63**, 11, 1 (2001). DOI: 10.1103/PhysRevB.63.115415.

[Rei05] Friedrich Reinert & Stefan Hüfner. *Photoemission spectroscopy - from early days to recent applications.* New J. Phys. **7**, 97 (2005). DOI: 10.1088/1367-2630/7/1/097.

[Ret14] L Rettig, J-H Chu, I R Fisher, U Bovensiepen, & M Wolf. *Coherent dynamics of the charge density wave gap in tritellurides.* Faraday Discuss. **171**, 299 (2014). DOI: 10.1039/c4fd00045e.

[Ret16] L. Rettig, R. Cortés, J.-H. Chu, I. R. Fisher, F. Schmitt, R. G. Moore, Z.-X. Shen, P. S. Kirchmann, M. Wolf, & U. Bovensiepen. *Persistent order due to transiently enhanced nesting in an electronically excited charge density wave*. Nat. Commun. **7**, 10459 (2016). DOI: 10.1038/ncomms10459.

[Rii06] S Riikonen, A Ayuela, & D Sánchez-Portal. *Metal – insulator transition in the In/Si(111) surface*. Surf. Sci. **600**, 3821 (2006). DOI: 10.1016/j.susc.2006.01.092.

[Ril14] J M Riley, F Mazzola, M Dendzik, M Michiardi, T Takayama, L Bawden, C Granerød, M Leandersson, T Balasubramanian, M Hoesch, T K Kim, H Takagi, W Meevasana, Ph Hofmann, M S Bahramy, J W Wells, & P. D. C. King. *Direct observation of spin-polarized bulk bands in an inversion-symmetric semiconductor*. Nat. Phys. **10**, October, 835 (2014). DOI: 10.1038/nphys3105.

[Roh99] Michael Rohlfing & Steven G Louie. *Excitons and Optical Spectrum of the Si(111)- (2*1) Surface*. Phys. Rev. Lett. **83**, 4, 856 (1999). link.

[Roh11] Timm Rohwer, Stefan Hellmann, Martin Wiesenmayer, Christian Sohrt, Ankatrin Stange, Bartosz Slomski, Adra Carr, Yanwei Liu, Luis Miaja Avila, Matthias Kalläne, Stefan Mathias, Lutz Kipp, Kai Rossnagel, & Michael Bauer. *Collapse of long-range charge order tracked by time-resolved photoemission at high momenta*. Nature **471**, 7339, 490 (2011). DOI: 10.1038/nature09829.

[Roh13] G. Rohde, T. Rohwer, C. Sohrt, a. Stange, S. Hellmann, L. X. Yang, K. Hanff, a. Carr, M. M. Murnane, H. Kapteyn, L. Kipp, K. Rossnagel, & M. Bauer. *Tracking the relaxation pathway of photo-excited electrons in 1T-TiSe2*. Eur. Phys. J. Spec. Top. **222**, 5, 997 (2013). DOI: 10.1140/epjst/e2013-01901-5.

[Rot05] Eli Rotenberg, B K Freelon, H Koh, A Bostwick, K Rossnagel, Andreas Schmid, & S D Kevan. *Electron states and the spin density wave phase diagram in Cr(110) films*. New J. Phys. **7**, 114 (2005). DOI: 10.1088/1367-2630/7/1/114.

[Rot08] Eli Rotenberg, Oleg Krupin, & S D Kevan. *Surface states and spin density wave periodicity in Cr(110) films*. New J. Phys. **10**, 2, 023003 (2008). DOI: 10.1088/1367-2630/10/2/023003.

[Roy99] D Roy & D Tremblay. *Design of electron spectrometers*. Reports Prog. Phys. **53**, 12, 1621 (1999). DOI: 10.1088/0034-4885/53/12/003.

[Rug10] Eddy P. Rugeramigabo, Christoph Tegenkamp, Herbert Pfnür, Takeshi Inaoka, & Tadaaki Nagao. *One-dimensional plasmons in ultrathin metallic silicide wires of finite width*. Phys. Rev. B - Condens. Matter Mater. Phys. **81**, 1 (2010). DOI: 10.1103/PhysRevB.81.165407.

[Saa08] G. Saathoff, L. Miaja-Avila, M. Aeschlimann, M. Murnane, & H. Kapteyn. *Laser-assisted photoemission from surfaces*. Phys. Rev. A **77**, 2, 022903 (2008). DOI: 10.1103/PhysRevA.77.022903.

[Sas94] Shigemi Sasaki. *Analyses for a planar variably-polarizing undulator.* Nucl. Inst. Methods Phys. Res. A **347**, 1-3, 83 (1994). DOI: 10.1016/0168-9002(94)91859-7.

[Saw97] K. J S Sawhney, F. Senf, M. Scheer, F. Schäfers, J. Bahrdt, A. Gaupp, & W. Gudat. *A novel undulator-based PGM beamline for circularly polarised synchrotron radiation at BESSY II.* Nucl. Instruments Methods Phys. Res. Sect. A Accel. Spectrometers, Detect. Assoc. Equip. **390**, 3, 395 (1997). DOI: 10.1016/S0168-9002(97)00402-6.

[Sch93] K. Schönhammer & V. Meden. *Correlation effects in photoemission from low dimensional metals.* J. Electron Spectros. Relat. Phenomena **62**, 1-2, 225 (1993). DOI: 10.1016/0368-2048(93)80017-G.

[Sch99a] J. Schäfer, Eli Rotenberg, G. Meigs, S. Kevan, P. Blaha, & S. Hüfner. *Direct Spectroscopic Observation of the Energy Gap Formation in the Spin Density Wave Phase Transition at the Cr(110) Surface.* Phys. Rev. Lett. **83**, 10, 2069 (1999). DOI: 10.1103/PhysRevLett.83.2069.

[Sch99b] Andrew J Schofield. *Non-Fermi liquids* , August 2015(1999). DOI: 10.1080/001075199181602.

[Sch01] J Schäfer, E Rotenberg, S D Kevan, P Blaha, R Claessen, & R E Thorne. *High-temperature symmetry breaking in the electronic band structure of the quasi-one-dimensional solid NbSe3.* Phys. Rev. Lett. **87**, 196403 (2001). DOI: 10.1103/PhysRevLett.87.196403.

[Sch03] J. Schäfer, M. Sing, R. Claessen, Eli Rotenberg, X. Zhou, R. Thorne, & S. Kevan. *Unusual Spectral Behavior of Charge-Density Waves with Imperfect Nesting in a Quasi-One-Dimensional Metal.* Phys. Rev. Lett. **91**, 6, 066401 (2003). DOI: 10.1103/PhysRevLett.91.066401.

[Sch04a] J. Schäfer, D. Schrupp, Eli Rotenberg, K. Rossnagel, H. Koh, P. Blaha, & R. Claessen. *Electronic Quasiparticle Renormalization on the Spin Wave Energy Scale.* Phys. Rev. Lett. **92**, 9, 097205 (2004). DOI: 10.1103/PhysRevLett.92.097205.

[Sch04b] F. Schiller, D. Vyalikh, V. Servedio, & S. Molodtsov. *Photoemission study of the spin-density-wave state in thin films of Cr.* Phys. Rev. B **70**, 17, 174444 (2004). DOI: 10.1103/PhysRevB.70.174444.

[Sch08] F Schmitt, P S Kirchmann, U Bovensiepen, R G Moore, L Rettig, M Krenz, J-H Chu, N Ru, L Perfetti, D H Lu, M Wolf, I R Fisher, & Z-X Shen. *Transient electronic structure and melting of a charge density wave in TbTe3.* Science **321**, 5896, 1649 (2008). DOI: 10.1126/science.1160778.

[Sea79] M. P. Seah & W. A Dench. *Quantitative Electron Spectroscopy of Surfaces.* Surf. Interface Anal. **1**, 2 (1979).

[Sen13] Michael Sentef, Alexander Kemper, Brian Moritz, James Freericks, Zhi-Xun Shen, & Thomas Devereaux. *Examining Electron-Boson Coupling Using Time-Resolved Spectroscopy.* Phys. Rev. X **3**, 4, 041033 (2013). DOI: 10.1103/PhysRevX.3.041033.

[Sie67] K. Siegbahn, C. Nordling, A. Fahhnann, R. Nordberg, K. Hamrin, J. Hedman, G. Johansson, T. Bergmark, S.E. Karlsson, I. Lindgren, & B. Lindberg. *ESCA - Atomic, molecular and solid state structure studied by means of electron spectroscopy.* Almqvist and Wiksells, Uppsala (1967).

[Sie69] K. Siegbahn, C. Nordling, G. Johansson, J. Hedman, P. F. Heden, K. Hamrin, U. I. Gelius, T. Bergmark, L. O. Werme, R. Manne, & Y. Baer. *ESCA Applied to Free Molecules.* North-Holland, Amsterdam (1969).

[Sin15] A Singer, M. J. Marsh, S. H. Dietze, V. Uhlíř, Y. Li, D. A. Walko, E. M. Dufresne, G. Srajer, M. P. Cosgriff, P. G. Evans, E. E. Fullerton, & O. G. Shpyrko. *Condensation of collective charge ordering in chromium.* Phys. Rev. B **91**, 11, 115134 (2015). DOI: 10.1103/PhysRevB.91.115134.

[Sin16] A. Singer, S. K. K. Patel, R. Kukreja, V. Uhlíř, J. Wingert, S. Festersen, D. Zhu, J. M. Glownia, H. T. Lemke, S. Nelson, M. Kozina, K. Rossnagel, M. Bauer, B. M. Murphy, O. M. Magnussen, E. E. Fullerton, & O. G. Shpyrko. *Photoinduced Enhancement of the Charge Density Wave Amplitude.* Phys. Rev. Lett. **117**, 5, 056401 (2016). DOI: 10.1103/PhysRevLett.117.056401.

[Sni10] Paul C. Snijders & Hanno H. Weitering. *Colloquium: Electronic instabilities in self-assembled atom wires.* Rev. Mod. Phys. **82**, 1, 307 (2010). DOI: 10.1103/RevModPhys.82.307.

[Sob12] J. A. Sobota, S. Yang, J. G. Analytis, Y. L. Chen, I. R. Fisher, P. S. Kirchmann, & Z.-X. Shen. *Ultrafast Optical Excitation of a Persistent Surface-State Population in the Topological Insulator Bi_{2}Se_{3}.* Phys. Rev. Lett. **108**, 11, 117403 (2012). DOI: 10.1103/PhysRevLett.108.117403.

[Sob13] J. A. Sobota, S. L. Yang, A. F. Kemper, J. J. Lee, F. T. Schmitt, W. Li, R. G. Moore, J. G. Analytis, I. R. Fisher, P. S. Kirchmann, T. P. Devereaux, & Z. X. Shen. *Direct optical coupling to an unoccupied Dirac surface state in the topological insulator Bi2Se3.* Phys. Rev. Lett. **111**, 13, 1 (2013). DOI: 10.1103/PhysRevLett.111.136802.

[Spe] *SPECS GmbH He Discharge Lamp and Monochromator - Technical Manual* .

[Spe08] *SPECS GmbH manual PHOIBOS 100/150 Hemispherical Analyser Series - Technical Manual* (2008).

[Spe16] E. Speiser, N. Esser, S. Wippermann, & W. G. Schmidt. *Surface vibrational Raman modes of In:Si(111)(41) and (82) nanowires.* Phys. Rev. B **94**, 075417 (2016). DOI: 10.1103/PhysRevB.94.075417.

[SS11] A. F. Santander-Syro, O. Copie, T. Kondo, F. Fortuna, S. Pailhès, R. Weht, X. G. Qiu, F. Bertran, A. Nicolaou, A. Taleb-Ibrahimi, P. Le Fèvre, G. Herranz, M. Bibes, N. Reyren, Y. Apertet, P. Lecoeur, A. Barthélémy, & M. J. Rozenberg. *Two-dimensional electron gas with universal subbands at the surface of SrTiO3.* Nature **469**, 7329, 189 (2011). DOI: 10.1038/nature09720.

[Stö06] J Stöhr & H. C. Siegmann. *Magnetism: From Fundamentals to Nanoscale Dynamics*. Springer-Verlag (2006).

[Sto14] L Stojchevska, I Vaskivskyi, T Mertelj, P Kusar, D Svetin, S Brazovskii, & D Mihailovic. *Ultrafast switching to a stable hidden quantum state in an electronic crystal*. Science **344**, 6180, 177 (2014). DOI: 10.1126/science.1241591.

[Sun08] Y. Sun, S. Agario, S. Souma, K. Sugawara, Y. Tago, T. Sato, & T. Takahashi. *Cooperative structural and Peierls transition of indium chains on Si(111)*. Phys. Rev. B **77**, 12, 125115 (2008). DOI: 10.1103/PhysRevB.77.125115.

[Tam13] A. Tamai, W. Meevasana, P. D C King, C. W. Nicholson, A. De La Torre, E. Rozbicki, & F. Baumberger. *Spin-orbit splitting of the Shockley surface state on Cu(111)*. Phys. Rev. B - Condens. Matter Mater. Phys. **87**, 7, 1 (2013). DOI: 10.1103/PhysRevB.87.075113.

[Tan04] Takehiro Tanikawa, Iwao Matsuda, Taizo Kanagawa, & Shuji Hasegawa. *Surface-state electrical conductivity at a metal-insulator transition on silicon*. Phys. Rev. Lett. **93**, 1, 016801 (2004). DOI: 10.1103/PhysRevLett.93.016801.

[Teg05] C. Tegenkamp, Z. Kallassy, H.-L. Günter, V. Zielasek, & H. Pfnür. *Anisotropic conductance of Pb-induced chain structures on Si(557) in the monolayer regime*. Eur. Phys. J. B **43**, 4, 557 (2005). DOI: 10.1140/epjb/e2005-00090-x.

[Teg08] C. Tegenkamp, T. Ohta, J. McChesney, H. Dil, E. Rotenberg, H. Pfnür, & K. Horn. *Coupled Pb Chains on Si(557): Origin of One-Dimensional Conductance*. Phys. Rev. Lett. **100**, 7, 076802 (2008). DOI: 10.1103/PhysRevLett.100.076802.

[Tho97] J. J. Thomson. *Cathode Rays*. Philos. Mag. Ser. 5 **44**, 269, 293 (1897). DOI: 10.1080/14786449708621070.

[Tom50] Sin-itiro Tomonaga. *Remarks on Bloch's Method of Sound Waves applied to Many-Fermion Problems*. Prog. Theor. Phys. **5**, 4, 544 (1950). DOI: 10.1143/ptp/5.4.544.

[Tur10] I. C. E. Turcu, E. Springate, C. A. Froud, C. M. Cacho, J. L. Collier, W. A. Bryan, G. R. A. Jamie Nemeth, J. P. Marangos, J. W. G. Tisch, R. Torres, T. Siegel, L. Brugnera, J. G. Underwood, I. Procino, W. R. Newell, C. Altucci, R Velotta, Rb King, J. D. Alexander, C. R. Calvert, O. Kelly, J. B. Greenwood, I. D. Williams, A Cavalleri, J. C. Petersen, N. Dean, S. S. Dhesi, L. Poletto, P. Villoresi, F. Frassetto, S. Bonora, & M. D. Roper. *Ultrafast science and development at the Artemis facility*. Proc. SPIE **7469**, 746902 (2010). DOI: 10.1117/12.867540.

[Tus15] Christian Tusche, Alexander Krasyuk, & Jürgen Kirschner. *Spin resolved bandstructure imaging with a high resolution momentum microscope*. Ultramicroscopy **159**, 520 (2015). DOI: 10.1016/j.ultramic.2015.03.020.

[Uhm13] Sang Hoon Uhm & Han Woong Yeom. *Metal-insulator transition on the Si (111) 4 1-In surface with oxygen impurity.* Phys. Rev. B **165419**, 165419 (2013). DOI: 10.1103/PhysRevB.88.165419.

[Val58] J. G. Valatin. *Comments on the theory of superconductivity.* Nuovo Cim. Ser. 10 **7**, 6, 843 (1958). DOI: 10.1007/BF02745589.

[Vit15] H. Vita. *Interaction of Magnetic and Non-Magnetic Metals with Graphene.* PhD Thesis, Humboldt-Universitaet zu Berlin (2015).

[Voi93a] J Voit. *Charge-spin separation and the spectral properties of Luttinger liquids.* Phys. Rev. B. Condens. Matter **47**, 11, 6740 (1993). DOI: 10.1088/0953-8984/5/44/020.

[Voi93b] Johannes Voit. *Charge-spin separation and the spectral properties of Luttinger liquids.* Phys. Rev. **47**, 11, 6740 (1993).

[Voi94] J Voit. *One-dimensional Fermi liquids.* Reports Prog. Phys. **57**, 9, 977 (1994). DOI: 10.1088/0034-4885/58/9/002.

[Voi00] J. Voit, L. Perfetti, F. Zwick, H. Berger, G. Margaritondo, G. Grüner, H. Höchst, & M. Grioni. *Electronic Structure of Solids with Competing Periodic Potentials.* Science **290**, 5491, 501 (2000). DOI: 10.1126/science.290.5491.501.

[vW10] Jasper van Wezel, Paul Nahai-Williamson, & Siddarth S. Saxena. *Exciton-phonon-driven charge density wave in TiSe2.* Phys. Rev. B **81**, 16, 165109 (2010). DOI: 10.1103/PhysRevB.81.165109.

[Wac72] B. J. Waclawski & E. W. Plummer. *Photoemission Observation of a Surface State of Tungsten.* Phys. Rev. Lett. **29**, 12, 783 (1972).

[Wac16] Gideon Wachtel & Yong Baek Kim. *Nodal-line pairing with 1D-3D coupled Fermi surfaces: A model motivated by Cr-based superconductors.* Phys. Rev. B **94**, 10, 1 (2016). DOI: 10.1103/PhysRevB.94.104522.

[Wal12a] S. Wall, B. Krenzer, S. Wippermann, S. Sanna, F. Klasing, A. Hanisch-Blicharski, M. Kammler, W. G. Schmidt, & M. Horn-von Hoegen. *Atomistic Picture of Charge Density Wave Formation at Surfaces.* Phys. Rev. Lett. **109**, 18, 186101 (2012). DOI: 10.1103/PhysRevLett.109.186101.

[Wal12b] S Wall, D Wegkamp, L Foglia, K Appavoo, J Nag, R F Haglund, J Stähler, & M Wolf. *Ultrafast changes in lattice symmetry probed by coherent phonons.* Nat. Commun. **3**, 721 (2012). DOI: 10.1038/ncomms1719.

[Wal13] S. Wall, L. Foglia, D. Wegkamp, K. Appavoo, J. Nag, R. F. Haglund, J. Stähler, & M. Wolf. *Tracking the evolution of electronic and structural properties of VO 2 during the ultrafast photoinduced insulator-metal transition.* Phys. Rev. B - Condens. Matter Mater. Phys. **87**, 11, 1 (2013). DOI: 10.1103/PhysRevB.87.115126.

[Wal15] Lutz Waldecker, Timothy A. Miller, Miquel Rudé, Roman Bertoni, Johann Osmond, Valerio Pruneri, Robert E. Simpson, Ralph Ernstorfer, & Simon Wall. *Time-domain separation of optical properties from structural transitions in resonantly bonded materials.* Nat. Mater. **14**, July, 991 (2015). DOI: 10.1038/nmat4359.

[Wan93] K J Wan, X F Lin, & Et Al. *Surface reconstructions in the Ag/Si (111) system.* Phys. Rev. B **47**, 20, 13700 (1993). DOI: 10.1103/PhysRevB.47.13700.

[Wan06] Feng Wang, J. V. Alvarez, S. K. Mo, J. W. Allen, G. H. Gweon, J. He, R. Jin, D. Mandrus, & H. H??chst. *New luttinger-liquid physics from photoemission on Li0.9Mo6O17.* Phys. Rev. Lett. **96**, 19, 196403 (2006). DOI: 10.1103/PhysRevLett.96.196403.

[Wan12a] Qing Hua Wang, Kourosh Kalantar-Zadeh, Andras Kis, Jonathan N Coleman, & Michael S Strano. *Electronics and optoelectronics of two-dimensional transition metal dichalcogenides.* Nat. Nanotechnol. **7**, 11, 699 (2012). DOI: 10.1038/nnano.2012.193.

[Wan12b] X Wang, P Richard, Y Huang, H Miao, L Cevey, N Xu, Y Sun, T Qian, Y Xu, M Shi, J Hu, X Dai, & H Ding. *Orbital characters determined from Fermi surface intensity patterns using angle-resolved photoemission spectroscopy.* Phys. Rev. B **85**, 214518 (2012). DOI: 10.1103/PhysRevB.85.214518.

[Wan15] He Wang, Yiming Xu, Stefan Ulonska, Joseph S Robinson, Predrag Ranitovic, & Robert A Kaindl. *Bright high-repetition-rate source of narrowband extreme-ultraviolet harmonics beyond 22eV.* Nat. Commun. **6**, May, 7459 (2015). DOI: 10.1038/ncomms8459.

[Wat17] M. D. Watson, Y. Feng, C. W. Nicholson, C. Monney, J. M. Riley, H. Iwasawa, K. Refson, V. Sacksteder, D. T. Adroja, J. Zhao, & M. Hoesch. *Multiband One-Dimensional Electronic Structure and Spectroscopic Signature of Tomonaga-Luttinger Liquid Behavior in Kr2Cr3As3.* Phys. Rev. Lett. **118**, 9, 097002 (2017). DOI: 10.1103/PhysRevLett.118.097002.

[Web11] F. Weber, S. Rosenkranz, J.-P. Castellan, R. Osborn, G. Karapetrov, R. Hott, R. Heid, K.-P. Bohnen, & A. Alatas. *Electron-Phonon Coupling and the Soft Phonon Mode in TiSe2.* Phys. Rev. Lett. **107**, 26, 266401 (2011). DOI: 10.1103/PhysRevLett.107.266401.

[Wei06] Alexander Weiße, Gerhard Wellein, Andreas Alvermann, & Holger Fehske. *The kernel polynomial method.* Rev. Mod. Phys. **78**, 1, 275 (2006). DOI: 10.1103/RevModPhys.78.275.

[Wie03] H. Wiedemann. *Synchrotron Radiation.* Springer-Verlag, Berlin, Heidelberg (2003).

[Wip10] S. Wippermann & W. G. Schmidt. *Entropy Explains Metal-Insulator Transition of the Si(111)-In Nanowire Array.* Phys. Rev. Lett. **105**, 12, 126102 (2010). DOI: 10.1103/PhysRevLett.105.126102.

[Wit15] F Withers, O Del Pozo-zamudio, A Mishchenko, A P Rooney, A Gholinia, K Watanabe, T Taniguchi, S J Haigh, A K Geim, A I Tartakovskii, & K S Novoselov. *Light-emitting diodes by band-structure engineering in van der Waals heterostructures.* Nat. Mater. **14**, February, 301 (2015). DOI: 10.1038/NMAT4205.

[Wol62] E. J. Woll & W. Kohn. *Images of the fermi surface in phonon spectra of metals.* Phys. Rev. **126**, 5, 1693 (1962). DOI: 10.1103/PhysRev.126.1693.

[Wol95] L. Wolniewicz. *Nonadiabatic energies of the ground state of the hydrogen molecule.* J. Chem. Phys. **103**, 5, 1792 (1995). DOI: 10.1063/1.469753.

[Wol99] M Wolf, A Hotzel, E Knoesel, & D Velic. *Direct and indirect excitation mechanisms in two-photon photoemission spectroscopy of Cu(111) and CO/Cu(111).* Phys. Rev. B **59**, 8, 5926 (1999).

[Wu13] Sanfeng Wu, Jason S. Ross, Gui-Bin Liu, Grant Aivazian, Aaron Jones, Zaiyao Fei, Wenguang Zhu, Di Xiao, Wang Yao, David Cobden, & Xiaodong Xu. *Electrical tuning of valley magnetic moment through symmetry control in bilayer MoS2.* Nat. Phys. **9**, 3, 149 (2013). DOI: 10.1038/nphys2524.

[Wu15a] Xian Xin Wu, Cong Cong Le, Jing Yuan, Heng Fan, & Jiang Ping Hu. *Magnetism in Quasi-One-Dimensional A2Cr3As3 (A=K,Rb) Superconductors.* Chinese Phys. Lett. **32**, 5, 1 (2015). DOI: 10.1088/0256-307X/32/5/057401.

[Wu15b] Xianxin Wu, Fan Yang, Congcong Le, Heng Fan, & Jiangping Hu. *Triplet pz-wave paring in quasi-one-dimensional A2Cr3As3 superconductors (A=K,Rb,Cs).* Phys. Rev. B **92**, 10, 104511 (2015). DOI: 10.1103/PhysRevB.92.104511.

[Xia12] Di Xiao, Gui-Bin Liu, Wanxiang Feng, Xiaodong Xu, & Wang Yao. *Coupled Spin and Valley Physics in Monolayers of MoS2 and Other Group-VI Dichalcogenides.* Phys. Rev. Lett. **108**, May, 196802 (2012). DOI: 10.1103/PhysRevLett.108.196802.

[Xu14] Xiaodong Xu, Wang Yao, Di Xiao, & Tony F. Heinz. *Spin and pseudospins in layered transition metal dichalcogenides.* Nat. Phys. **10**, 5, 343 (2014). DOI: 10.1038/nphys2942.

[Yan08] Jun Yan & Shiwu Gao. *Plasmon resonances in linear atomic chains: Free-electron behavior and anisotropic screening of d electrons.* Phys. Rev. B - Condens. Matter Mater. Phys. **78**, 1 (2008). DOI: 10.1103/PhysRevB.78.235413.

[Yan14] L X Yang, G Rohde, T Rohwer, A Stange, K Hanff, C Sohrt, L Rettig, R Cortés, F Chen, D L Feng, T Wolf, B Kamble, I Eremin, T Popmintchev, M M Murnane, H C Kapteyn, L Kipp, J Fink, M Bauer, U Bovensiepen, & K Rossnagel. *Ultrafast Modulation of the Chemical Potential in BaFe 2 As 2 by Coherent Phonons.* Phys. Rev. Lett. **112**, May, 207001 (2014). DOI: 10.1103/PhysRevLett.112.207001.

[Yan15] S. L. Yang, J. A. Sobota, D. Leuenberger, Y. He, M. Hashimoto, D. H. Lu, H. Eisaki, P. S. Kirchmann, & Z. X. Shen. *Inequivalence of Single-Particle and Population Lifetimes in a Cuprate Superconductor*. Phys. Rev. Lett. **114**, 24, 1 (2015). DOI: 10.1103/PhysRevLett.114.247001.

[Ye16] Ziliang Ye, Dezheng Sun, & Tony F Heinz. *Ultrafast Manipulation of Valley Pseudospin* 1–15(2016). DOI: 10.1017/CBO9781107415324.004.

[Yeo99] H. Yeom, S. Takeda, E. Rotenberg, I. Matsuda, K. Horikoshi, J. Schaefer, C. Lee, S. Kevan, T. Ohta, T. Nagao, & S. Hasegawa. *Instability and Charge Density Wave of Metallic Quantum Chains on a Silicon Surface*. Phys. Rev. Lett. **82**, 24, 4898 (1999). DOI: 10.1103/PhysRevLett.82.4898.

[Yeo02] H. Yeom, K. Horikoshi, H. Zhang, K. Ono, & R. Uhrberg. *Nature of the broken-symmetry phase of the one-dimensional metallic In/Si(111) surface*. Phys. Rev. B **65**, 24, 241307 (2002). DOI: 10.1103/PhysRevB.65.241307.

[Yu99] S.-W. Yu, T. Lischke, R. David, N. Müller, U Heinzmann, C Pettenkofer, A. Klein, A.Ya. Perlov, E.E. Krasovskii, W. Schattke, & J. Braun. *Spin resolved photoemission spectroscopy on WSe2*. J. Electron Spectros. Relat. Phenomena **101-103**, 449 (1999). DOI: 10.1016/S0368-2048(98)00508-8.

[Zen12] Hualing Zeng, Junfeng Dai, Wang Yao, Di Xiao, & Xiaodong Cui. *Valley polarization in MoS 2 monolayers by optical pumping*. Nat. Nanotechnol. **17**, June, 490 (2012). DOI: 10.1038/nnano.2012.95.

[Zen13] B. Zenker, H. Fehske, H. Beck, C. Monney, & A. R. Bishop. *Chiral charge order in 1T-TiSe2: Importance of lattice degrees of freedom*. Phys. Rev. B **88**, 7, 075138 (2013). DOI: 10.1103/PhysRevB.88.075138.

[Zha14] Xiuwen Zhang, Qihang Liu, Jun-wei Luo, Arthur J Freeman, & Alex Zunger. *Hidden spin polarization in inversion-symmetric bulk crystals*. Nat. Phys. **10**, May, 387 (2014). DOI: 10.1038/NPHYS2933.

[Zhe95] Anatoley T Zheleznyak & Victor M Yakovenko. *"Hot Spots" in Quasi-1D Organic Conductors*. Synth. Met. **70**, 1005 (1995).

[Zhi15] H. Z. Zhi, T. Imai, F. L. Ning, Jin Ke Bao, & Guang Han Cao. *NMR investigation of the quasi-one-dimensional superconductor K2Cr3As3*. Phys. Rev. Lett. **114**, 14, 1 (2015). DOI: 10.1103/PhysRevLett.114.147004.

[Zho15] Hanting Zhong, Xiao Yong Feng, Hua Chen, & Jianhui Dai. *Formation of Molecular-Orbital Bands in a Twisted Hubbard Tube: Implications for Unconventional Superconductivity in K2Cr3As3*. Phys. Rev. Lett. **115**, 22, 1 (2015). DOI: 10.1103/PhysRevLett.115.227001.

[Zhu11] Z. Y. Zhu, Y. C. Cheng, & U. Schwingenschlögl. *Giant spin-orbit-induced spin splitting in two-dimensional transition-metal dichalcogenide semiconductors*. Phys. Rev. B **84**, 153402 (2011). DOI: 10.1103/PhysRevB.84.153402.

[Zhu14] X. Y. Zhu. *How to draw energy level diagrams in excitonic solar cells*. J. Phys. Chem. Lett. **5**, 13, 2283 (2014). DOI: 10.1021/jz5008438.

Publication List

Publications in the Framework of this Thesis

C. W. Nicholson, C. Monney, U. Krieg, C. Tegenkamp, H. Pfnür, K. Horn, M. Wolf. *Electronic structure of self-assembled Ag nanowires on Si(557): spectroscopic evidence for dimensionality.* New J. Phys. 17, 093025 (2015)

C. W. Nicholson, C. Monney, R. Carley, B. Frietsch, J. Bowlan, M. Weinelt, M. Wolf. *Ultrafast Spin Density Wave Transition in Chromium Governed by Thermalized Electron Gas.* Phys. Rev. Lett. **117**, 136801 (2016)

C. Monney, M. Puppin, C. W. Nicholson, M. Hoesch, R. T. Chapman, E. Springate, H. Berger, A. Magrez, C. Cacho, R. Ernstorfer, M. Wolf. *Revealing the role of electrons and phonons in the ultrafast recovery of charge density wave correlations in 1T-TiSe2* Phys. Rev. B **94**, 165165 (2016)

R. Bertoni, C. W. Nicholson, L. Waldecker, C. Monney, M. Puppin, H. Huebener, U. De Giovannini, M. Hoesch, R. Chapman, E. Springate, C. Cacho, A. Rubio, M. Wolf, R. Ernstorfer. *Generation and evolution of spin-, valley- and layer-polarized excited carriers in inversion-symmetric WSe2* Phys. Rev. Lett. **117**, 277201 (2016)

M. D. Watson, Y. Feng, C.W. Nicholson, C. Monney, J. M. Riley, H. Iwasawa, K. Refson, V. Sacksteder, D. T. Adroja, J. Zhao, and M. Hoesch. *Multiband One-Dimensional Electronic Structure and Spectroscopic Signature of Tomonaga-Luttinger Liquid Behavior in K2Cr3As3* Phys. Rev. Lett. (2017) **118**, 097002 (2017)

C. W. Nicholson, C. Berthod, M. Puppin, M. Wolf, M. Hoesch, C. Monney. *Dimensional crossover in charge density wave material probed by ARPES* Phys. Rev. Lett. **118**, 206401 (2017)

In Preparation

C. W. Nicholson, A. Lücke, M. Puppin, L. Rettig, W. G. Schmidt, R. Ernstorfer, M. Wolf. *Beyond the molecular movie: ultrafast dynamics of bands and bonds during a photo-induced phase transition*

M. Puppin, H. Huebener, C. W. Nicholson, L. Rettig, A. Rubio, R. Ernstorfer, M. Wolf. *Unoccupied state mapping in 2D materials*

R. Bertoni, C.W. Nicholson, C. Monney, C. Capho, R.T. Chapman, E. Springate, M. Hoesch, M. Wolf, L. Rettig, R. Ernstorfer. *Spin-Resolved excited state dynamics in centrosymmetric bulk WSe_2*

C. W. Nicholson, C. Berthod, M. Hoesch, C. Monney. *Charge density waves in $NbSe_3$ resolved by high-resolution laser ARPES*

Publications on other Topics

A. Tamai, W. Meevasana, P. D. C. King, C.W. Nicholson, A. de la Torre, E. Rozbicki, F. Baumberger.
Spin-orbit splitting of the Shockley surface state on Cu(111) Phys Rev. B, **87**, 075113 (2013)

Academic Curriculum Vitae

Christopher William Nicholson
Berlin, Germany

The curriculum vitae is omitted in this online version due to data privacy.

Acknowledgements

A single name appears on the front cover of this thesis, but a work such as this is completed only with the help and support of numerous people, to whom I give my heartfelt thanks.

First of all I would like to thank Martin Wolf, both for the opportunity to work in his group and for his role as my doctoral supervisor these past years. The encouraging and open atmosphere meant that discussions of all sizes on all topics were always possible; this has been immensely helpful in generating ideas, critically evaluating my thoughts, and bringing numerous projects to fruition. I'm particularly thankful for the independence I've been afforded to follow projects of interest and develop my own ideas for studies, but with support always available when requested. The possibility to visit a number of international conferences during my thesis work has also been a fantastic opportunity to engage with the wider scientific community.

Special thanks go to Claude Monney, particularly for helping to guide me through my first years of life as a PhD student, and for the consistent support and encouragement throughout my thesis. From the many beam times and trips to Chilton, to our wide-ranging discussions, I am lucky to have had the chance to interact so regularly with, and learn from, such an knowledgeable and friendly scientist.

I am indebted to the trARPES team at the FHI. Thanks to Ralph Ernstorfer for the many interesting discussions, ideas and support – both in and out of the lab – and for keeping us all motivated with regular visits to our friendly local restaurant. My thanks to Laurenz Rettig, whose efforts not only at the experiment but also in discussions and giving comments on my thesis have been invaluable. Particular thanks to Michele Puppin, whose tireless efforts on the laser system and support during the many long nights in Fabeckstrasse and elsewhere, have made my FHI experience both more successful and enjoyable. For offering his extensive technical expertise through both routine and exceptional circumstances in such a friendly manner, I am very thankful to Sven Kubala. Thanks also to Yunpei Deng, who patiently introduced me to working with optics and high-power lasers in general. To Jannik Malther and Johannes Feldl, your respective efforts on developing our measurement program and the laser were extremely helpful. Thanks to you all!

I would also like to warmly thank the members of Karsten Horn's group. To Karsten himself for his constant engagement and enthusiasm in the lab, even when things were difficult, and for his help in writing my first journal article. For regular support at multiple ARPES experiments I must thank Hendrik Vita, in particular for his help in trouble shooting and understanding the finer details of the machine he constructed. Thanks to Stefan Böttcher for his help at BESSY and with using the analysis software.

Thanks to Moritz Hoesch and his group at the Diamond light source for taking my ideas seriously, for the excellent technical support, and for insightful comments at all stages of our project. Thanks also to Christopher Berthod at the University of Geneva, who enlightened me on many points both of 1D theory and of his calculations with detailed and patient discussions.

Thanks also to Herbert Pfnür, Christophe Tegenkamp and Ulrich Krieg at the Leibniz University in Hanover for their help preparing Ag/Si(557) samples and understanding the measurements.

I would like to thank Martin Weinelt, for allowing the use his setup for my first trARPES experiences and for his insightful comments and excellent lectures as part of the IMPRS on semiconductors and the light-matter interaction. Thanks also to his group, in particular Robert Carley for making the laser function and giving us advice of for our own setup, and to Björn Frietsch and John Bowlan for helping us with measurements.

For all their efforts and technical support during some challenging beam times, huge thanks go to Cephise Cahco, Richard Chapman and Emma Springate at the Artemis beam line of the Central Laser Facility. We couldn't have done it without you!

To Andreas Lücke and Wolf Gero Schmidt at the university of Paderborn, my thanks for the numerous calculations and explanations, and for improving my understanding of bonding in solids.

Thanks to Martin Wolf, Tobias Kampfrath and Bettina Menzel at the International Max-Planck Research School on "Functional Interfaces in Physics and Chemistry" for encouraging regular discussions in a friendly and scientifically varied environment, and for the regular opportunities for personal development; not least by funding my German courses. Dafür bin ich sehr dankbar!

For the friendly atmosphere both in and out the office, and for the company on our regular trek from Fabeck to the Mensa, a mention has to go to my long serving office mates Sebastian, Lukas and Michele. Thanks also to all my FHI colleagues both new and old – particularly those at the Fabeckstrasse outpost of the FHI – for the great atmosphere, and for the many barbecues and outings that we enjoyed together! I've been very lucky to work in such an open and community-like environment.

Finally i'd like to thank all my friends, family, and above all Lucia, for the constant support, encouragement and understanding during the last few years. Having such a warm support network made navigating the difficulties and challenges of PhD life possible.

Selbstständigkeitserklärung gemäss der Promotionsordnung

Sämtliche verwendeten Hilfsmittel, Hilfen und Quellen sind an der entsprechenden Stelle angegeben. Ich versichere, dass ich auf dieser Grundlage diese Arbeit selbstständig verfasst habe. Diese Arbeit wurde bisher weder in gleicher noch ähnlicher Form einer anderen Prüfungskomission vorgelegt oder veröffentlicht.

Berlin, den 22.08.2017

Christopher W. Nicholson